DECENTRALIZATION OF WIRELESS MONITORING AND CONTROL TECHNOLOGIES FOR SMART CIVIL STRUCTURES

A DISSERTATION SUBMITTED TO

THE DEPARTMENT OF CIVIL AND ENVIRONMENTAL ENGINEERING

AND THE COMMITTEE ON GRADUATE STUDIES

OF STANFORD UNIVERSITY

IN PARTIAL FULFILLMENT OF THE REQUIREMENTS

FOR THE DEGREE OF

DOCTOR OF PHILOSOPHY

Jerome Peter Lynch

August 2002

© Copyright 2002 by Jerome Peter Lynch
All Rights Reserved

I certify that I have read this dissertation and that in my opinion it is fully adequate in scope and quality as a dissertation for the degree of Doctor of Philosophy.

Dr. Kincho H. Law, Principal Advisor

I certify that I have read this dissertation and that in my opinion it is fully adequate in scope and quality as a dissertation for the degree of Doctor of Philosophy.

Dr. Anne S. Kiremidjian

I certify that I have read this dissertation and that in my opinion it is fully adequate in scope and quality as a dissertation for the degree of Doctor of Philosophy.

Dr. Thomas W. Kenny

I certify that I have read this dissertation and that in my opinion it is fully adequate in scope and quality as a dissertation for the degree of Doctor of Philosophy.

Dr. Ed Carryer

Approved for the University Committee on Graduate Studies:

Abstract

A smart civil structure is defined by sensing and/or actuation technologies embedded within the system to provide insight to the structure's response and an opportunity to limit responses. The past thirty years have been characterized by a revolution in the field of smart structure technologies with sensors and actuators both reducing in size, power demands and unit costs. The efforts of this study have been chiefly focused upon two aspects of smart structure technologies: the development of a wireless monitoring system for structural health monitoring applications and decentralized structural control.

The benefits of installing a monitoring system in a structure are multiple, including opportunities to assess the health of the structural system over its expected lifespan. Historically, monitoring systems for civil structures are wire-based and employ hub-spoke system architectures; unfortunately, their high installation and maintenance costs prevent them from becoming widely adopted. Using available technologies from the marketplace, a low cost alternative to traditional wire-based sensing systems has been developed. The unit's key features include wireless communications, a 16-bit digital conversion of interfaced sensors, and a computational core that can perform various data interrogation techniques in near real-time. As a means of system validation, various performance tests were performed including installation in the Alamosa Canyon Bridge, New Mexico.

Structural control systems can be used to limit the response of structures during external disturbances such as strong winds or large seismic events. As the trend of control devices progresses towards smaller and cheaper actuators, structural control systems will be characterized by large actuation densities. The resulting large-scale dynamic system is best controlled by decentralized control approaches. Various decentralized control techniques are considered including market-based control (MBC) and energy market-based control (EMBC). Originating from the realm of econometric optimization, the structural system is modeled as a marketplace of buyers and sellers that leads to an optimal control solution. The approach, implemented in various analytical models, exhibits control performances comparable to the centralized linear quadratic regulation (LQR) controller. One distinct advantage of EMBC is its robustness qualities with respect to actuation failures in the control system.

Acknowledgments

An endeavor of this nature and magnitude cannot be attempted without the support of a wide cast of family and friends. First, I would like to thank my parents for their encouragement over the years and support during all of the challenges I have ever faced. My strength to see this task through to the end serves as a tribute to them. My brother, Stephen, and sister, Elizabeth, both have been incredibly supportive and helpful during this journey.

I will forever be indebted to my advisor and friend, Professor Kincho Law, for helping me find an area of intellectual pursuit that fit my abilities and interests perfectly. Having learned under his tutelage helped me to grow both intellectually and as a person.

Having an opportunity, while at Stanford University, to work with some of the best researchers in the world has been a real treat. Many thanks are owed to Professor Ed Carryer for unselfishly sharing with me his encyclopedic knowledge of embedded systems. I am grateful to Professor Anne Kiremidjian and Professor Thomas Kenny, for their endless contribution of ideas and insights that resulted in bettering my efforts to design wireless modular monitoring systems. I would also like to thank Professor Stephen Rock for opening my eyes to the beautiful world of control theory and control system design. Special thanks is owed to Doctor Erik Straser who laid the foundation for my research with his groundbreaking dissertation work on wireless monitoring systems for structures.

During the summer of 1998, I had the unique opportunity to study the theoretical and practical aspects of structural control in Japan through the National Science Foundation's Summer Institute in Japan program. As a visiting researcher at Kajima Corporation's Kobori Research Complex, I was honored to interact with some of the visionaries in the field of structural control, particularly Doctor Tomohiko Hatada, Mr. Akihiro Kondo and Doctor Narito Kurata, an opportunity that comes along only once in one's lifetime.

I am indebted to Doctors Charles Farrar and Hoon Sohn of Los Alamos National Labs for providing me with invaluable insight into the world of structural health monitoring and damage detection algorithms for civil structures. They are responsible for providing access to the Alamosa Canyon Bridge as a validation deployment of the wireless sensing units.

I thank Doctors Andrew Berlin and Warren Jackson, formerly of the Smart Matter group at Xerox PARC, for helping me get started with applying marketplace pricing and economic competitive equilibrium concepts to the problem of control in structural systems.

The long path I have journeyed since enrolling as a civil engineering student at Cooper Union has been brightly lighted by the passion and integrity of two role models: Doctor Robert Smilowitz of Weidlinger Associates and Doctor Therios Lefcochilos of Saudi Aramco. They serve as examples of what the noble profession of structural engineering embodies.

I thank all of my friends in the Engineering Informatics Group (EIG) for helping me with various aspects of my research, particularly David Liu, Chuck Han, Shawn Kerrigan, Gorie Lau, Yang Wang, Brian Flaherty and Arvind Sundararajan. Some of my fondest memories of Stanford will be of my time spent at the John A. Blume Earthquake Engineering Center. The intellectual and social interactions with all of the students in the Blume Center made many late nights enjoyable. I am particularly

thankful to Nicolas Luco, Ricardo Medina, Fatemeh Jalayer, Babak Alavi-Shushtari, Medji Sama, Paul Cordova, Scott Hamilton, Jackie Lai, and Racquel Hagen.

Finally, I want to express my deepest and sincerest gratitude for the support provided by Nadine Wong Shi Kam, Mishka Priven, Jun Peng, and Sam King. The entire Stanford experience would not have been the same without them.

This research is sponsored and supported by the National Science Foundation, Grant Numbers CMS-9988909 and CMS-0121842. Additional support has been provided by the National Defense Science and Engineering Graduate Fellowship provided by the U.S. Department of Defense and administered by the Department of the Navy, and the Stanford Graduate Fellowship.

Table of Contents

List of Tables

List of Figures

Chapter 1

Introduction

1.1 Smart Structure Technology

A smart structure is generically defined as a structure that has an ability to sense its external environmental loadings and have the ability to respond to these loads in order to enhance its performance and survivability. To be defined as a smart structure, it must employ a sensing system for monitoring its loading and/or a control system comprised of actuators for limiting the detrimental influence of the loading. Many applications exist in a diverse set of fields that can serve as examples of smart structures. For example, truss structures used to support solar panels on space vehicles are typically equipped with sensors to detect unwanted vibrations and active truss elements to eliminate them (Culshaw 1996).

Today, revolutionary technologies are fueling the adoption of smart structure systems in a growing number of engineering applications. Smart structures have greatly benefited from the development of micro-electro mechanical system (MEMS) sensors. MEMS sensors are comprised of mechanical sensing transducers fabricated upon silicon dies adjacent to digital circuits, resulting in accurate sensors with small form factors and low unit costs. Piezoelectric materials are widely used in smart structure applications in both sensing and actuation capacities. A piezoelectric material produces an electrical field when strained; conversely, an applied electrical field will induce strain (Srinivasan and McFarland 2001). Smart structures employing actuators require computational capabilities to process sensing data for the determination of actuation commands. The constant increase in microcontrollers' speed and functionality per unit cost make their use in smart structures increasingly popular.

Civil structures were an early adopter of smart structure technologies. By the mid-1960's, a number of civil structures were instrumented with structural monitoring systems for measuring their performance during large external disturbances such as earthquakes or large winds (Johnson 2001). In 1989, the first structure employing sensors and actuators for control of its response during dynamic loading was constructed (Kobori et al. 1991). An overview of the current state-of-practice of structural monitoring and structural control is briefly discussed below.

1.1.1 Structural Monitoring

Structural monitoring systems entail the installation of a variety of sensors in civil structures to monitor their environment and their response to loadings. The original intention of embedding monitoring systems in structures was to measure the response of structures to strong ground motions. This traditional usage led to a deeper understanding of ground motions, their effect on structures, and improvements in the design of structures in zones of high seismic activity (Shakal 2001). Early structural monitoring systems were installed in large-scale critical structures such as hospitals, dams and long-span bridges. The County Services Building serves as an example of the value associated with monitoring critical structures. During the 1979 Imperial Valley earthquake, discontinuities in the structure's time-history responses led engineers to identify drastic alterations in the structure's integrity (Bolt 2001).

Worldwide, the installation of structural monitoring systems has become increasingly popular in long-span bridges. In California, 61 long-span bridges have been instrumented with a total of 900 sensing channels (Hipley 2001). The California Department of

Transportation uses measurements to validate design models of its bridge inventory as well as to assist in emergency response efforts immediately following large earthquakes. In Europe, adoption of fiber optic strain gages to monitor structural loads and long-term deflection of concrete bridges is growing in popularity (Inaudi and Vurpillot 1999). In Asia, many large bridges have been instrumented during their initial construction such as the Akashi Kaikyo and Tatara bridges in Honshu, Japan (Tamura 2001).

To illustrate the scope of current monitoring systems designed for installation in bridges, the Tsing Ma suspension bridge in Hong Kong serves as an example. Completed in 1997, the Tsing Ma Bridge spans 1377 meters and carries 6 lanes of vehicular traffic. During its initial construction, the Tsing Ma Bridge was instrumented with a monitoring system consisting of over 350 sensors (Ni et al. 2001). Sensors selected to measure various aspects of the bridge's response include accelerometers, strain gages, anemometers, thermometers and linear displacement transducers. Anemometers are used to measure the wind speed at locations along the bridge deck and towers, thermometers are installed to log the ambient temperature of the bridge, while weigh-in-motion sensors are used to track the traffic loads. Responses to the loads are measured primarily using accelerometers. Measured dynamic responses are used for comparison to responses predicted from analytical models for modal identification purposes (Wong et al. 2001).

1.1.1.1 System Architecture

Employing hub-spoke architectures, structural monitoring systems are comprised of remote sensors wired directly to a centralized data acquisition system as shown in Figure 1-1. System sensors lack the means of processing their data and are only responsible for taking measurements. Therefore, the role of the centralized data server is to aggregate, store and process measurement data. Recent research efforts in the field have focused upon analysis techniques to assist in interrogating the acquired data and resulting decision making (Bergmeister and Santa 2001). As a consequence of hub-spoke architectures, structural monitoring systems have poor scalability properties with systems comprised of hundreds of sensors becoming increasingly expensive on a per channel basis.

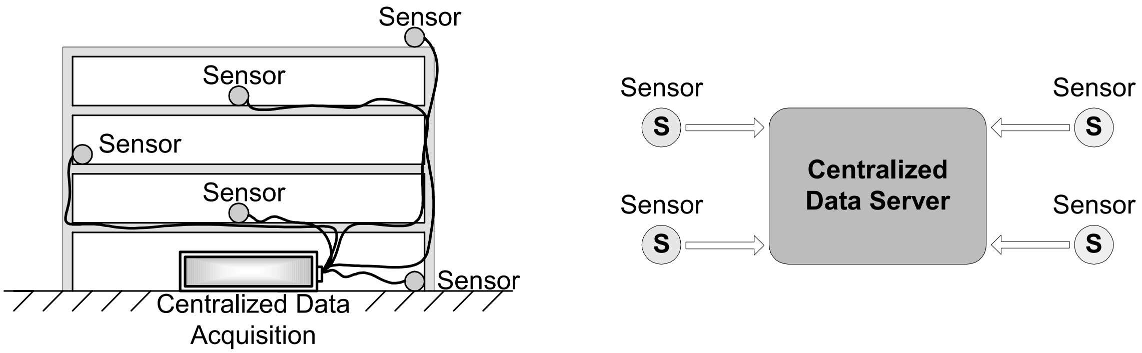

Figure 1-1: Centralized wire-based structural monitoring systems

1.1.1.2 Cost of Structural Monitoring

Today, the cost of installing structural monitoring systems in civil structures is high. For example, the cost of installing the Tsing Ma suspension bridge monitoring system was at a rate of $27,000 per sensing channel (Farrar 2001). Likewise, in Europe fiber optic monitoring systems cost between $20,000 to $100,000 for concrete bridges with spans of 200 meters (Bergmeister 2000). For bridges, annual inspections are required that visually inspect the structure for symptoms of fatigue and damage. The cost of these schedule-base inspections can range from 0.05 to 0.1% of the total construction cost of the bridge. When damage is found, repairs can cost as high as 4% of the total construction cost. By pursuing condition-based maintenance instead of scheduled maintenance, inspection costs can be drastically reduced while repair costs would be reduced by 0.1% of the bridge's total construction cost (Bergmeister 2000).

The expensive nature of structural monitoring systems is a direct result of the high installation and maintenance costs associated with system wires. Installation of the monitoring system can represent up to 25% of the total system cost with over 75% of the installation time focused solely on the installation of system wires (Straser and Kiremidjian 1998). In outdoor applications such as bridges, potentially harsh environmental conditions necessitate additional efforts spent on installing system cables in weatherproof conduits thereby raising installation costs.

1.1.1.3 Limitations of Current Structural Monitoring Systems

As a result of high installation and maintenance costs, the adoption of structural monitoring technologies in the marketplace can be characterized as sluggish. Thus far, only structures identified as critical can justify the expenses associated with installing a structural monitoring system. Today, there is a growing demand for structural monitoring systems because they represent an enabling technology for a broader set of applications. In particular, researchers have been successful in developing computational algorithms that can be used to identify the existence of damage in structures (Doebling et al. 1996). Termed a structural health monitoring system, a traditional structural monitoring system is installed for the acquisition of response measurements to ambient and forced (seismic and wind) vibrations along with computers that use the measurements to hypothesize the existence, location, and severity of damage.

The computational demands of many of the damage detection algorithms that have been developed for structural health monitoring can be high. Current monitoring systems are dependent upon highly centralized system architectures. The damage detection algorithms that will process structural response measurements are to reside in the monitoring system’s centralized data server. As the number of sensing nodes of the monitoring system increases, the centralized data server will become inundated by measurements and become overburdened in processing the data for damage detection purposes.

1.1.2 Structural Control

Civil engineering structures located in environments known for high seismic activity or large wind speeds could potentially experience structural vibrations. These vibrations can range from harmless to severe with the later resulting in serious structural damage and potential structural failure. To limit the detrimental effects of these vibrations, the concept of using a structural control system was first proposed by Yao (1972).

Structural control is defined as a mechanical system that is installed in a structure to reduce structural vibrations during external disturbances resulting in enhanced safety and habitability. The structural control system can be divided into three complementary components: a sensing system, control actuators, and a centralized controller. A graphical illustration of a generic control system is presented in Figure 1-2. The bottom three blocks represent a structure excited by an external disturbance resulting in dynamic structural responses. This is often termed the open-loop response of the system. When a control system is employed, a structural monitoring system is installed to constantly measure the magnitude of loading or the response of the structural system. Sensor measurements are then passed to a centralized controller that executes control algorithms in real-time to determine control forces to be applied to the structure. The control commands are sent to the system actuators that lead to reductions in the dynamic response of the structure. The modified response of the controlled structure is termed the closed-loop response of the system. The majority of control systems are known as feedback control systems because they only feedback sensor measurements of the dynamic state of the structure. Systems that employ sensors for measuring the external excitation are known as feed-forward control systems.

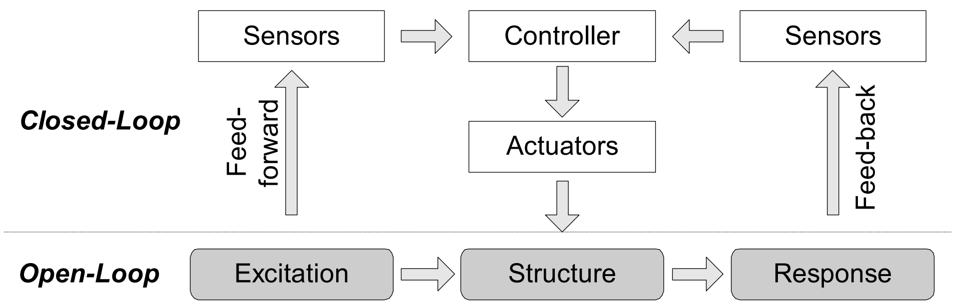

Figure 1-2: Overview schematic of the operation of a structural control system

It is common for structural control systems to be classified by their device types resulting in three general control categories: passive, active and semi-active. A passive control system is one in which structural vibrations are reduced from passive control devices that locally dissipate energy from the structural system. No sensors or actuators are used. Passive control devices are compact, require no external power and are generally considered highly reliable. Examples of passive control devices include base isolators, tuned mass dampers, viscous dampers, metallic yield dampers and friction dampers (Housner et al. 1997).

An active control system is a more complex system with electromechanical or electro-hydraulic actuators strategically installed within the structure for the application of control forces. Active control systems can attain excellent control results during moderate disturbances. However, there are some technological drawbacks to active control system designs. They are very expensive to employ during large disturbances due to the considerable amounts of power, often on the order of tens of kilowatts required for actuator operation (Symans and Constantinou 1999). As a result, the maximum control force that can be applied is generally not sufficient for large seismic disturbances. Furthermore, they occupy more space than passive control devices. Some examples of active control devices include the active mass driver system, the active tuned mass system, and the active-passive composite tuned mass damper (Culshaw 1996).

In 1989, the Kyobashi Seiwa Building in Tokyo, Japan was constructed using an active mass damper making it the first building in the world to use active structural control (Kobori et al. 1991). The control solution occupied a significant portion of the structure's roof with two actuators installed weighing 4.2 and 1.2 metric tons (representing 1% of the superstructure's weight). The system designer, Kajima Corporation, Japan, estimates the system cost to be roughly 1% of the total building construction cost (Sasaki 1998). As of 2001, there were an additional 30 buildings with active structural control systems installed in Japan (Nishitani and Inoue 2001). To date, no active structural control examples can be found in North America at least partially due to their high costs and questions regarding their reliability.

The last broad category of control is semi-active control. Passive energy dissipation devices are modified to serve as semi-active control devices. By employing mechanisms to control or assist passive control devices such as dampers, semi-active control devices utilize the motion of the structure to indirectly generate control forces. The inherent benefit of semi-active control devices is that the mechanisms only require power on the order of tens of watts (Symans and Constantinou 1999). Many semi-active devices are powered by batteries protecting them from sudden power loss during earthquakes. Furthermore, semi-active control devices are less complex mechanically than active devices and hence are highly reliable. Semi-active control devices are better suited for large-magnitude seismic applications with superior control results yielded compared to current active structural control system designs. Some examples of semi-active control devices are stiffness control devices and variable damping devices (Takahashi et al. 1998).

1.1.2.1 Active Variable Dampers

One popular type of semi-active control device is the semi-active variable damper. Variable dampers can be placed anywhere in the structure where it can dissipate energy by being connected to parts of a structure moving relative to one another. Current practice advocates placing the dampers at the apex of V-braces typically employed for lateral structural stiffening. As shown in Figure 1-3, the brace is connected to one end of the damper while the other end of the damper is connected to the floor with the variable damper directed parallel to the floor. As a structure dynamically deflects, energy is dissipated by the variable damper due to the V-brace moving relative to the floor. The defining characteristic of the variable damper is that its damping coefficient can be changed during an earthquake excitation, thereby indirectly introducing control forces into the system. At least two types of variable dampers have emerged in recent years that employ different types of mechanisms to change their damping coefficients: semi-active hydraulic dampers (SHD) and magnetorheological dampers.

The SHD, designed by Kajima Corporation, is a hydraulic damper roughly 2.3 meters long and weighs 2.4 metric tons. A flow control valve connects two adjacent hydraulic chambers in the SHD's piston. With the flow valve closed, the SHD is considered "locked". When the valve is opened, the SHD is "released" and dissipates more energy as the valve opening enlarges. During power failure of the SHD, the valves are triggered to fully open converting the semi-active variable damper to just a simple passive damper. Such a device can deliver a maximum damping force of 1000 kN using 70 W of power (Kurata et al. 1999). Eight SHD semi-active devices have recently been installed in the five-story Kajima-Shizuoka Building in Shizuoka, Japan.

The second type of variable damper is the magnetorheological damper being developed at Notre Dame University, Notre Dame, Indiana. This damper's coefficient of damping changes when a magnetic field around the damper's piston causes a change in the viscosity of an internal hydraulic fluid. This variable damper can deliver a maximum damping force of 200 kN using only 20 to 50 W of power (Spencer et al. 1998). Researchers are currently investigating the installation of magnetorheological dampers in cable stay bridges (Christenson et al. 2001).

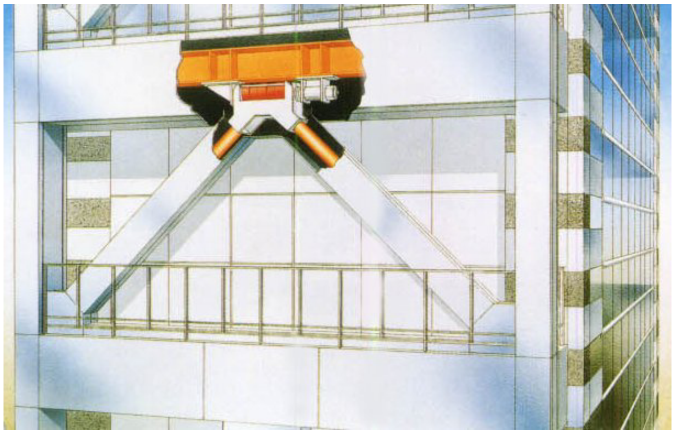

Figure 1-3: Typical semi-active variable damper installation (Kajima 1991)

1.1.2.2 Observation and Trends of Current Structural Control Approaches

In observing the shift in industry focus from active control to semi-active control devices, an evolutionary trend has been established in time; the shape factor of control devices will continue to become significantly smaller, their capital cost will be reduced and their energy consumption characteristics will be improved. Inevitably, engineers will have the opportunity to deploy larger quantities of semi-active devices throughout a single structure resulting in a large-scale control problem entailing hundreds of control devices and sensors. Current structural control systems depend upon a centralized controller for the calculation of control forces. For a large-scale complex control system, the orthodox approach of using a central computer responsible for the control of the entire system will become less desirable. The computations required by a centralized controller increase faster than at a linear rate for increases in dimensionality of the control system (Lunze 1992). The real-time demands of the control system make it necessary to be aware of the number of calculations that can be made in each operation cycle. Another inherent difficulty associated with the widely used centralized controller approach, is that one controller represents a single point of failure in the system.

1.2 Research Objectives

It is clear that the scalability of current structural monitoring and control technologies are limited as a result of their strong dependence upon centralized system architectures. The computational demands of structural health monitoring systems will overburden a centralized data server while large-scale centralized control systems are incapable of determining control commands within their allotted time steps. In response to these identified limitations, the main challenge of this thesis is the exploration of decentralized architectural concepts for adoption in smart structure systems. Decentralization entails the decomposition of a global smart structure system down to a collection of interrelated smart structure subsystems. The computational capabilities of the centralized server, located at the center of both current monitoring and control system designs, are to be distributed throughout the structural system. The distributed processing capability of a decentralized system facilitates the benefits of parallel calculations with improved system reliability as an additional advantage gained. The decentralization of both structural monitoring and control technologies are to be considered in this thesis.

1.2.1 Wireless Sensing Units for Decentralized Monitoring

A structural monitoring infrastructure optimized for decentralized system architectures is proposed for application in the civil structure arena. Drawing from the most advanced technologies commercially available, a radically new hardware platform for structural monitoring is proposed. With market adoption of structural monitoring systems slow due to high unit and installation costs, an additional research objective is to develop a low cost alternative to traditional monitoring systems.

Two innovative technologies will be included in the design of the proposed sensing units: an embedded computational core and wireless communications. The proposed computational capability of the wireless sensing unit is an important ingredient because it enables the sensing unit the freedom to locally process and interrogate measurement data. This decentralized processing capability is a significant differentiator from traditional wire-based monitoring systems where the centralized data server assumes the responsibility of executing these services. The use of wireless communications for the transfer of data between wireless sensing units accomplishes two established goals. First, it eliminates the need for extensive wiring thereby drastically reducing the cost of installation and maintenance of the novel wireless monitoring system. Second, it accommodates peer-to-peer (P2P) communications for the easy flow of data resulting in a strong interrelationship between units.

The proposed wireless sensing unit will be designed and fabricated for installation in a wireless structural monitoring system as shown in Figure 1-4. Having first investigated the adoption of autonomous wireless sensing units for structural monitoring applications, Straser and Kiremidjian (1998) have laid a firm technological foundation for this work.

The wireless sensing units proposed by Straser and Kiremidjian represent the building blocks for wireless modular monitoring systems (WiMMS) that can be deployed in a broad set of civil structures. This research improves on the previous work by embedding application software in the wireless sensing units to execute the computational tasks for system identification and structural health monitoring. The performance of the wireless sensing units in locally executing these application tasks will be validated.

1.2.2 Decentralized Control Algorithms

The field of control theory possesses a rich collection of control techniques that can be applied to a wide variety of problems. A large body of literature exists regarding general decentralized control theory with significant contribution made by Singh (1981), Lunze (1992), and Siljak (1991). However, researchers in the structural engineering field have not explored the application of decentralized control solutions to structural control systems. With a large-scale control problem at hand, an important objective of this research is to draw upon the available decentralized control methods and to explore their application to the realm of structural control. The performance of the decentralized control techniques will be compared to the widely used linear quadratic regulation (LQR) centralized control solution.

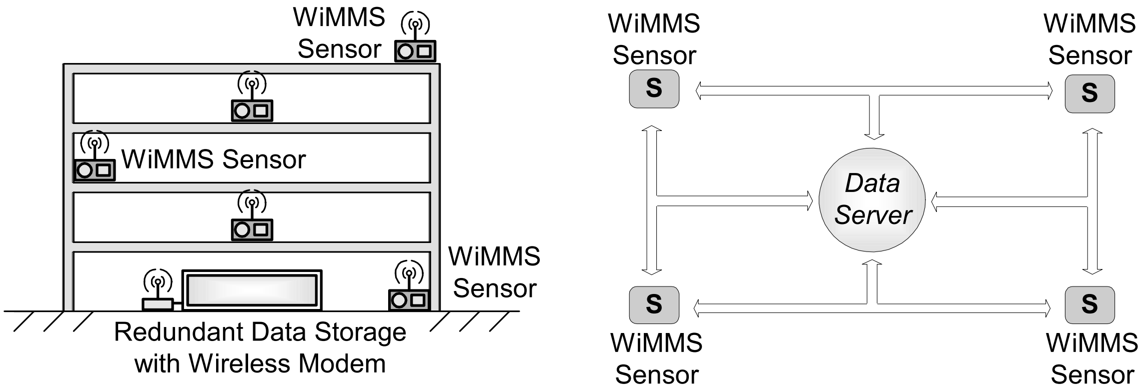

Figure 1-4: Decentralized wireless structural monitoring systems

Most recently, the explosion in development of MEMS sensing and actuation systems has resulted in many large-scale control problems. With the reliability of MEMS sensors and actuators lower than conventional counterparts, adaptive and flexible control methods have been explored. In particular, adaptive decentralized control solutions have been adopted. Researchers have explored using free-market concepts as one approach to controlling large-scale MEMS systems (Guenther et al. 1997). By modeling the control system as a free-market economy where actuators are market buyers and power source are market sellers, an adaptive and optimal control solution can result. Market-based control (MBC) methods have also been applied for controlling the computational load of server microprocessors and for load-balancing in internet networks (Clearwater 1996). A market-based control (MBC) approach specific to application in a structural control system will be derived. Performance of the MBC approach will be compared to the centralized LQR solution. The adaptive nature of the market-based controller will be explored with respect to actuation failure in the structural control system.

1.3 Organization of the Thesis

The thesis first explores the design of low cost wireless sensing units that serve as the fundamental building block of wireless structural monitoring systems. The computational capabilities embedded within the sensing unit design represent a decentralization of the computational power that resides in the centralized data servers of traditional wire-based monitoring systems. The autonomous nature of the wireless sensing units is illustrated by encoding and locally executing damage detection algorithms within the units.

The second half of the thesis explores innovative control techniques, namely decentralized control solutions, for structural control systems that employ a large number of sensors and actuators. A significant portion of the thesis explores the adaptation of static economic optimization techniques for application in structural control systems. Termed market-based control, the control system is modeled as a free market economy where the interaction of market buyers (actuators) and market sellers (power sources) yield an optimal control solution. One benefit of market-based control approaches are their robustness qualities during scenarios of actuation failures.

This thesis is organized as follows:

- Chapter 2 presents the hardware design of the wireless sensing unit. The design is presented in three parts: the sensing interface, the computational core, and the wireless communication channel.

- Chapter 3 discusses the design of embedded software for the operation of the wireless sensing unit. The software design is done in two abstraction layers. The first layer is comprised of software for the operation of hardware subsystems. An additional software layer is designed that performs analysis specific to system identification and damage detection applications.

- To validate and to quantify the performance of the proposed wireless sensing unit, Chapter 4 summarizes findings from a set of validation tests. The tests are designed to assess three aspects of the wireless sensing unit's performance. The first assesses the hardware performance of the unit's components. The second explores the ability to interface a broad collection of sensors including MEMS-based accelerometers. The last set of validation tests explores the performance of the wireless sensing unit in both the laboratory and field settings. The Alamosa Canyon Bridge in New Mexico serves as the field validation structure.

- Chapter 5 begins the thesis exploration into the use of decentralized control solutions in structural control systems. Two decentralized control approaches are considered that represent decentralized modifications of the widely used centralized linear quadratic regulator (LQR).

- Chapter 6 introduces the concept of market-based control (MBC). Static optimization techniques widely used in the field of economics are employed to serve as a decentralized solution to the control problem. Representing a piece-wise optimization solution, the approach yields control results comparable to those obtained using a centralized LQR solution.

- Energy market-based control (EMBC) is the centerpiece of Chapter 7. Based on the natural measures of energy in the dynamic structural system, the EMBC approach is a rational modification of the MBC concepts of Chapter 6. The robustness qualities of the EMBC approach are measured with respect to actuation failures in the control system.
- Chapter 8, the final chapter, serves as a thesis summary with a discussion focused towards future extensions of the research.

Chapter 2

Wireless Sensing Unit Design

The wireless sensing unit represents the fundamental building block of the wireless modular monitoring systems (WiMMS) proposed for use in civil structures. This research aims to develop an optimal hardware design that meets the requirements specified by applications envisioned for WiMMS. Cost and power consumption characteristics of hardware components are additional design criteria. The focus of this chapter is on the hardware design of a proof-of-concept prototype wireless sensing unit. The rationale and motivation for the selection of all unit components are presented.

The hardware design of the wireless sensing unit, as depicted in Figure 2-1, is partitioned into three subsystems: the sensing interface, the computational core, and wireless communications. The sensing interface is responsible for the interface of sensors to the wireless sensing unit and the conversion of their measurements to a digital format. The resulting digital measurements are then sent to the computational core where the overall operation of the wireless sensing unit is conducted. The design principle of thrusting the computational intelligence forward to the system sensors is addressed in the design of the unit's core. After the data has been logged and interrogated at the core, it is packaged for transmission on the wireless communication channel. The wireless communication channel is vital to reducing the cost and maintenance required for installation of a wireless monitoring system. In the following sections, the hardware design of each of these three functional groups is discussed in greater detail.

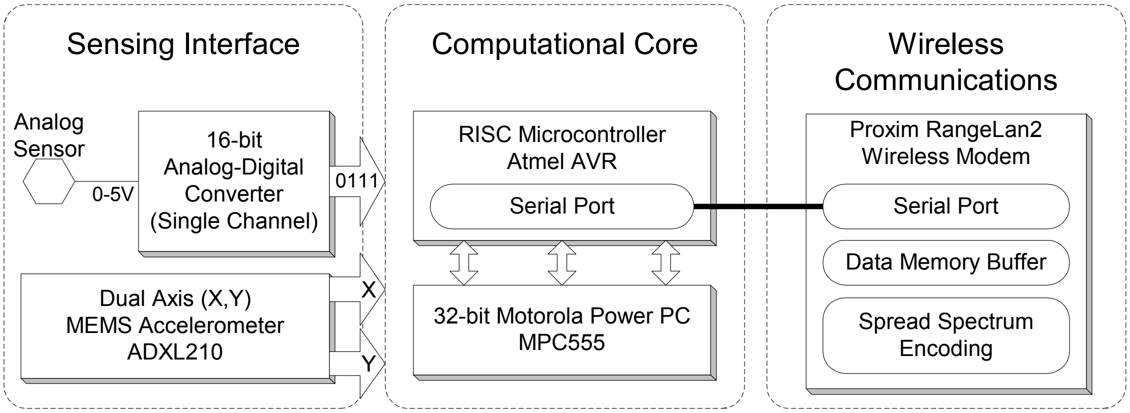

Figure 2-1: Functional layout of proposed wireless sensing unit

As will be presented in this chapter, a distinctive feature of the sensing unit's design is the use of a two-layer circuit board as a means of integrating the individual hardware components selected into a compact and cohesive unit. It is imperative that the life expectancy of the units be as long as possible. The chapter concludes with a discussion on current and potential power sources that can provide a long-term operational lifespan to the sensing units.

Finally, it should be noted that, except in the case of the tailored printed circuit board, the use of readily available off-the-shelf components is sought during the design process to keep fabrication efforts reasonable and total unit cost low. To appropriately select from the best embedded system technologies currently available, design goals for the proposed wireless sensing unit must be established. Table 2-1 summarizes the criteria used for selecting key hardware components of the prototype wireless sensing unit design. The proof-of-concept prototype wireless sensing unit represents only a first step in an iterative design process that will inevitably evolve in time to keep pace with newer hardware technologies and future application requirements.

Table 2-1: Design criteria for the prototype wireless sensing unit design

Design Parameter	Selection Criteria
Wireless Sensing Unit	
Size	Compact (less than 20 in.^{3})
Battery Life	At least 24 hours of continuous use
Cost	Less than $500
Computational Core	
Design	Dual-processor
Processor 1	Low-power 8-bit microcontroller (μC)
Processor 2	32-bit μC with hardware floating-point
Wireless Communications	
Encoding Scheme	Reliable spread spectrum technique
Radio Band	Unregulated ISM bands
Open-space Range	Over 500 ft.
Data Rate	At least 121 Kbps
Sensing Interface	
Sampling Rates	As high as 1 kHz
Channels	Multiple channels
Transducers	All analog sensors

2.1 Sensing Interface

A large number of sensors can be employed for the purpose of monitoring structures. Accelerometers are a traditional choice for monitoring the global response of structures while strain gages and crack propagation sensors are typically used for local response monitoring. To ensure a versatile and effective wireless sensing unit, the unit is designed to be sensor transparent by allowing the sensing interface to accept sensors that have analog outputs ranging in voltage from 0 to 5 V. Transduction specifications unique to each sensor, such as conversion constants, can be encoded into the computational core for the calculation of physical measurements from the sensor's analog voltage signal.

At the core of the sensing interface is an analog-to-digital (A/D) converter used to convert analog sensor outputs to a digital value. This digital value is transmitted directly to the computational core for processing. Various A/D converters are commercially available providing different levels of accuracy, speed and interfaces. To accommodate the voltage resolution of potential sensors, a 16-bit or higher resolution A/D converter is sought. The analog voltage resolution of the least significant bit of a 16-bit converter referenced at 5 V is 76.3 μV. Hence, sensors that can utilize the full potential of the 16-bit converter should have noise floors below 76.3 μV.

A single channel, low-noise, Texas Instrument 16-bit A/D converter is used for resolving the analog output of a sensor to digital form. The internal architecture of the A/D converter is a successive approximation type that internally uses an analog comparator and counting logic to perform conversions (Ball 2001). The converter employs a sample-and-hold circuit that ensures an accurate conversion by holding the input analog value constant in a buffer capacitor while the conversion is internally performed. The high speed parallel complementary metal oxide semiconductor (CMOS) architecture of the A/D converter allows for data sampling rates as high as 100 kHz (Burr-Brown 1996). Classical global response monitoring systems do not require sampling rates this high, but novel damage detection procedures based on local response data could require sampling rates in the kHz region.

The 28-pin dual-in-line package (DIP) of the ADS7821, shown in Figure 2-2, is used in the wireless sensing unit design. The chip is a mixed signal integrated circuit with analog input pins and digital output pins designed for easy interface to embedded microcontrollers. The supply voltage to power both analog and digital portions of the converter's internal circuit is done by nominally applying 5 V to pins 27 and 28. Operation and control of the ADS7821 is done through pins 23 through 25. Pin 26, connected directly to the computational core of the wireless sensing unit, gives notification to the core when a conversion has completed. The output of the sensor is connected to the converter's input pin (pin 1). After a conversion is complete, the 16-bit digital form of the sensor's output can be read from the ADS7821's digital output pins 6-13 and 15-22. These 16 output pins are connected directly to two 8-bit parallel ports of the microcontroller.

The power consumption of the A/D converter increases with an increase in the converter's sampling rate. At the maximum sample rate of 100 kHz, the ADS7821 consumes 100 mW of power drawing 16 mA of current. At the lower sampling rates envisioned for the wireless sensing unit (20-200 Hz), the A/D converter will consume less power.

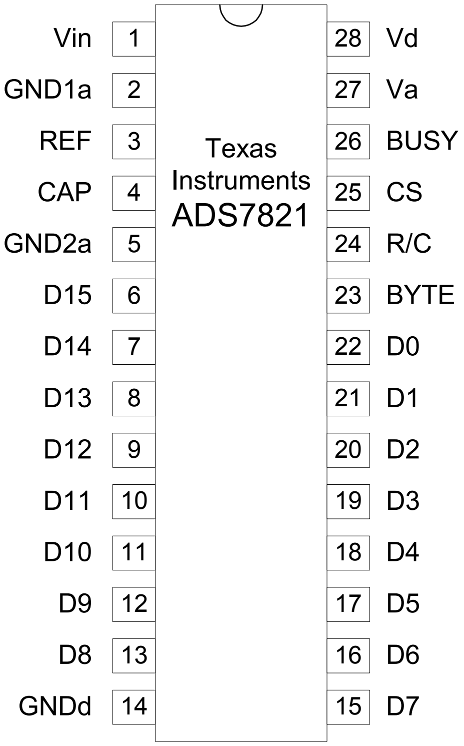

Figure 2-2: ADS7821 DIP package pin-out diagram

No internal anti-aliasing is provided by the ADS7821 A/D converter. Aliasing of the sensor input occurs when the signal contains significantly high frequency content above the Nyquist frequency (half of the sampling frequency), resulting in higher spectrum frequency content superimposing itself upon the spectrum below the Nyquist frequency. To avoid the aliasing of a sensor's signal, an anti-aliasing filter circuit is required between the sensor's output and the input of the A/D converter (Ewins 1984). An anti-aliasing filter is a low-pass filtering circuit that rejects the portion of the input signal's spectrum above the Nyquist frequency. Various types of anti-aliasing filters exist with the Butterworth filter being the most commonly used (Texas Instruments 1995).

In addition to the A/D converter, a dual axes micro-electro mechanical system (MEMS) based accelerometer is permanently interfaced to the wireless sensing unit's core. The Analog Devices' ADXL210 accelerometer was selected to interface directly to the system because it has the ability to output anti-aliased acceleration readings in a digital format that is readable by the computational core (Analog Devices 1999). Details specific to the ADXL210 operation and output will be discussed in Chapter 4. The acceleration output of the accelerometer's two orthogonal sensing axes serve as additional sensing channels included in the unit design, bringing the total number of data acquisition channels provided by the sensing interface to three.

2.2 Computational Core Design

Perhaps the most important choice in the development of the wireless sensing unit is the hardware chosen for the unit's computational core. This core will be responsible not only for aggregation of sensing data from on-board sensing transducers (i.e. accelerometers), but they will also take part in the important task of cleansing and processing the data. Various suitable alternatives are available ranging from field programmable gate arrays (FPGA) to digital signal processing (DSP) chips. The final selection was based upon the criteria of efficient power consumption characteristics of the core.

A dual microcontroller core design is used for the wireless sensing unit. The responsibilities of the computational core are classified into two functional groups: first, the overall unit operation including data acquisition from interfaced sensors and second, data processing. A separate microcontroller is selected to service each of these two functional responsibilities.

A low-power 8-bit microcontroller is selected for control of the data acquisition operation of the wireless sensing unit. In particular, the Atmel AVR AT90S8515 microcontroller is chosen. By leveraging the internal services provided by the AT90S8515, reliable acquisition of sensor data from the sensing interface can be performed in real-time. The wireless communication channel is directly accessed through the AT90S8515's serial port.

With memory and computational speed limited on the AT90S8515, a second microcontroller is selected for inclusion in the computational core. The Motorola MPC555 PowerPC, a high-performance 32-bit microcontroller, is selected for the task of local data interrogation. With significantly more read only memory (ROM) and random access memory (RAM) onboard, in addition to a faster clock rate of 40 MHz, intensive data processing not possible on the AT90S8515 can now be performed.

By employing dual processors for the computational core, a usage strategy is required for efficiently utilizing the two microcontrollers. The supply current required to operate the two microcontrollers has direct bearing on this usage strategy. Given the low-power demand of the AT90S8515, it will be responsible for the remedial task of operating the sensing interface and wireless communications. While data is acquired by the AT90S8515, the MPC555 is maintained in sleep mode, drawing very little current thereby sparing the battery. When data interrogation is required by the sensing unit, the AT90S8515 can awaken the MPC555 for the purpose of analysis. Since the MPC555, when active, requires a significant amount of supply current, it should be used sparingly to prevent the unit's power source from being drained too quickly. Table 2-2 summarizes the supply currents demanded by various components of the computation core.

Table 2-2: Supply current demand of the computational core

Operational State	Atmel AVR AT90S8515 (5V at 4 MHz)	Motorola PowerPC MPC555 (5V at 40 MHz)
Active	8 mA	110 mA
Sleep	2.5 mA	4 mA

2.2.1 Atmel AVR AT90S8515 RISC Microcontroller

The Atmel AVR microcontroller is an 8-bit architecture with a full suite of on-board services that provide convenience when used in an embedded system design. Some of the peripherals provided by the AT90S8515 include a serial communication UART (universal asynchronous receiver/transmitter), 8-bit timer/counter, 16-bit timer/counter, watchdog timer, analog comparator, serial peripheral interface (SPI), pulse width modulator (PWM), and four 8-bit input/output ports (Atmel 2001). Many of these peripherals are extensively used in the design of the wireless sensing unit. The 40-pin DIP packaging of the AT90S8515 is used in the wireless sensing unit with the package's pin-out presented in Figure 2-3.

2.2.1.1 Memory

The Atmel AVR microcontroller is a Harvard architecture microcontroller, with separate memory locations and exclusive data buses for program memory and data memory (Atmel 2001). Programs written to operate the microcontroller are stored in binary form in the AVR's read-only flash memory. Flash memory, a descendant of ROM devices, is non-volatile allowing the memory to retain content after power has been turned off (Barr 2001). The flash program memory of the AT90S8515 totals 8 Kbytes and is organized into a table of 4,000 16-bit instructions also known as 16-bit words. Data generated and employed by the execution of the program is stored in the microcontroller's data memory. Data memory is stored in volatile RAM in the form of 8-bit registers. In this case, volatile memory would lose its contents once power has been shut off.

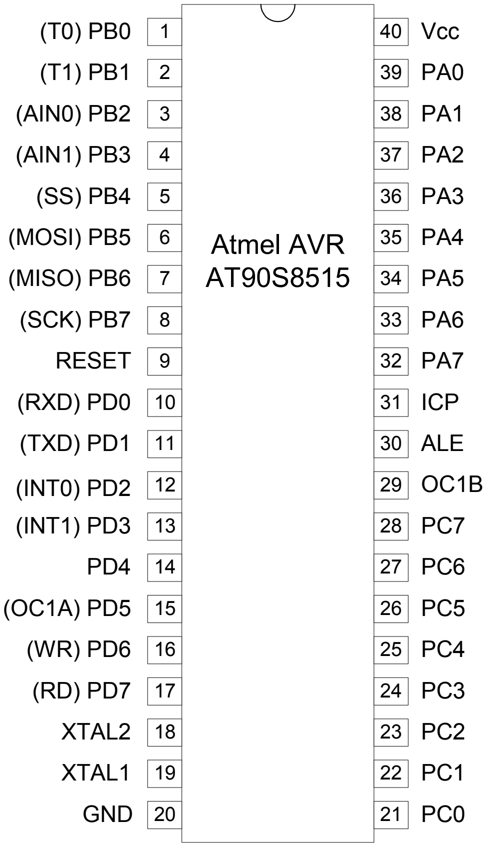

Figure 2-3: AT90S8515 DIP package pin-out diagram

Specific to the AT90S8515 internal architecture, on-board data memory is segmented into three sections: 32 general-purpose registers, 64 input/output (I/O) registers, and 512 bytes of internal static RAM (SRAM). The 32 general-purpose registers are used during execution of the microcontroller's operations and referred to by their sequential names R0 through R31. The last six general-purpose registers (R26-R31) serve dual roles as three 16-bit memory pointers termed X, Y and Z. The 64 I/O registers are memory elements used by the software for direct access to and control of the microcontroller's on-board services such as timers and parallel ports. The remaining 512 bytes of SRAM are used for temporary memory and for the implementation of the program stack. A complete memory map of the AT90S8515 is shown in Figure 2-4.

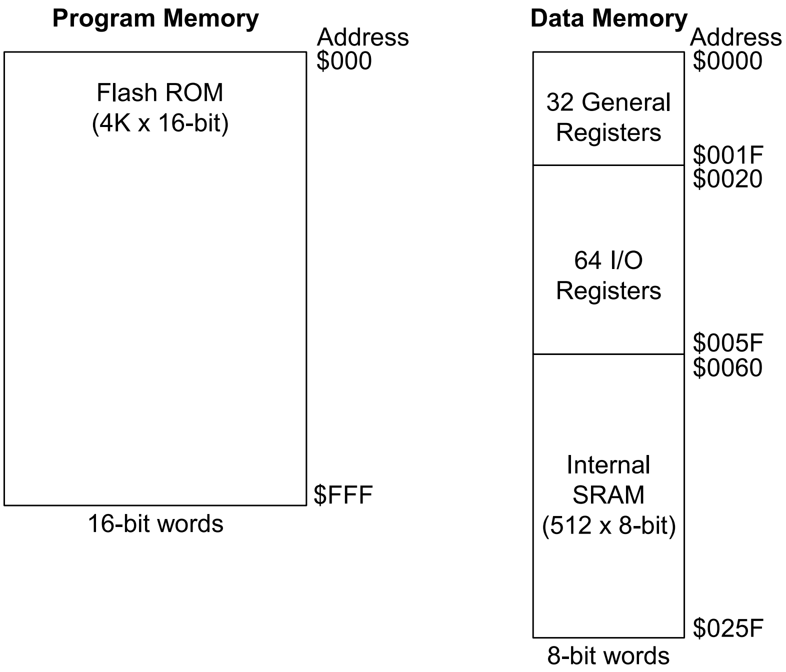

Figure 2-4: AT90S8515 memory map

2.2.1.2 Interrupts

A useful and widely exploited feature of microcontrollers is their ability to attain real-time operation requirements. Real-time requirements are those that specify completion of tasks at prescribed points in time. Interrupts are a hardware feature of the microcontroller that allows for the asynchronous interruption of the execution of a program to service a subroutine that requires completion at a certain period in time (Hintz and Tabak 1992). While servicing the interrupt, the executing code is temporarily halted. Microcontrollers provide a variety of different interrupts that can be individually enabled at the outset or during the execution of a program. Each interrupt has both a triggering event, and a respective subroutine that is serviced when the interrupt occurs. The triggering events are generally initiated by an interrupt request (IRQ) signal in hardware.

A program vector of interrupts resides in the lowest address spaces of program memory. For each interrupt in the vector, an address of the servicing software subroutine is provided. When an interrupt routine is triggered, the interrupt goes to its location in the interrupt vector where it is pointed to the entry point in program memory of the subroutine. Upon exiting the subroutine, the code is returned to its pre-interrupt location in program memory. The interrupt vector serves as a means of prioritizing the interrupts for nested interrupt handling with higher priority given to those in the lower memory locations of the vector. The initial interrupt vector, located at address $000 in program memory, is the reset interrupt. Instead of servicing a subroutine, it points to the entry point of the main program. The configuration and control of the AT90S8515 interrupts are set by various interrupt mask and flag registers located in the I/O registers in data memory. The AT90S8515's interrupt vector contains a total of 13 interrupts as documented in Table 2-3 (Atmel 2001).

Table 2-3: AVR AT90S8515 interrupt vector table

Vector Number	Memory Address	Source	Description
1	$000	RESET	Power-on and watchdog timer reset
2	$001	INT0	External interrupt request on input pin 0
3	$002	INT1	External interrupt request on input pin 1
4	$003	TIMER1 CAPT	Timer/counter 1 service on input capture
5	$004	TIMER1 COMPA	Timer/counter 1 compare match A
6	$005	TIMER1 COMPB	Timer/counter 1 compare match B
7	$006	TIMER1 OVF	Timer/counter 1 overflow
8	$007	TIMER0 OVF	Timer/counter 0 overflow
9	$008	SPI STC	Serial program interface transfer complete
10	$009	UART RX	UART completed receive character
11	$00A	UART UDRE	UART data register empty
12	$00B	UART TX	UART completed transmit character
13	$00C	ANA_COMP	Analog comparator

2.2.1.3 AVR Instruction Set

The entire family of Atmel AVR microcontrollers uses a universal Atmel RISC (Reduced Instruction Set Computer) instruction set containing 118 instructions. The instruction set can be divided into four subsets: arithmetic and logic execution, code branching, data transfer, and bit testing. Assembly programming can be used to program the AT90S8515 by writing source code that sequentially orders instructions from the RISC instruction set. Instructions and their accompanying operands, when assembled, translate directly into 16-bit words to be stored in program memory.

Architectural pipelining allows the majority of AVR instructions to be effectively executed in one clock cycle. Complementary CISC processors in the 8-bit microcontroller market require 4 to 12 times more clock cycles to complete identical tasks. Power consumption characteristics of CMOS microcontrollers are linearly proportional to their clock frequency resulting in CISC processors consuming 4 to 12 times more power per instruction than the AVR (Bogen and Wollan 1996). For the AVR microcontroller, this directly translates into a computational core that is fast as well as power efficient.

2.2.2 Motorola MPC555 PowerPC Microcontroller

The Motorola MPC555 RISC microcontroller is a PowerPC compliant processor. The 32-bit core Harvard architecture of the MPC555, with fast floating point calculations performed directly by hardware, has been designed with computationally intensive embedded applications in mind (Motorola 2000). Plenty of on-chip memory is available with 448 Kbytes of flash ROM provided for application software and 26 Kbytes of RAM for data storage. A complete memory map of the MPC55 is shown in Figure 2-5.

Similar to the AT90S8515, the MPC555 microcontroller is designed with an extensive set of peripherals. However, the complexity of the microcontroller is such that the internal architecture groups the peripherals into a collection of hardware subsystems. For example, the serial port is within the queued serial multi-channel module (QSMCM). An assortment of timers are provided on-chip in the MPC555's programmable time processor unit module (TPU3), while two 16-channel A/D converters are provided in the queued analog-to-digital converter subsystem module (QADC64). Eight pulse width modulators can be accessed from the 18-channel modular I/O subsystem (MIOS1).

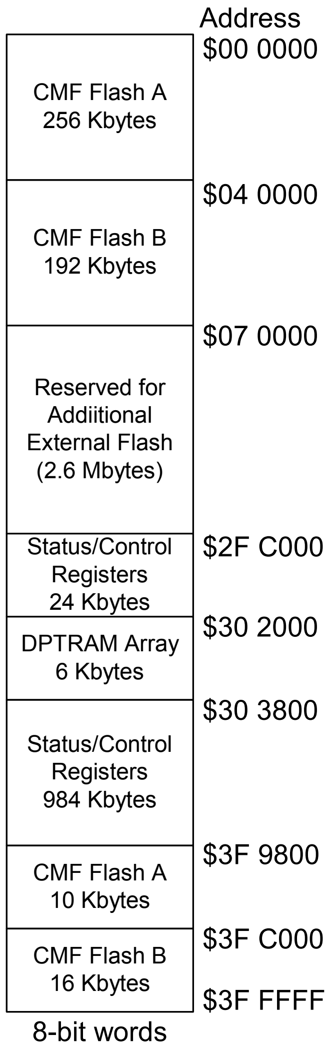

Figure 2-5: MCP555 memory map

The MPC555 microcontroller is manufactured as a 272 ball grid array (BGA) package that is 1 in. by 1 in. in area. The MPC555, purchased from Axiom Manufacturing, is already mounted on a small 3 in. by 3 in. square development board (PB555) with pin-out headers, power supply and RS232 serial ports provided. Figure 2-6 is a top view picture of the small PB555 development board from Axiom.

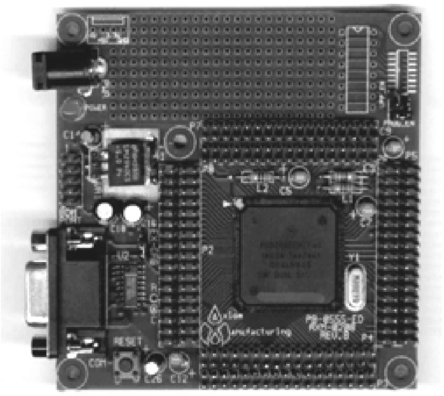

Figure 2-6: Top view of the PB555 development board

2.3 Wireless Communications

The low cost and modular installation features of the proposed WiMMS systems directly result from the use of wireless communications for data transfer in the network of wireless sensing units. However, in replacing wires as the primary means of data transfer in the system, the wireless communication technology chosen must be reliable. The commercially available wireless technologies range from inexpensive frequency modulated (FM) radios communicating on a single pre-selected frequency to complex wireless networking Ethernet cards using reliable spread spectrum techniques. For inclusion in the wireless sensing unit, a radio using spread spectrum radio techniques, consuming low-power, possessing a far transmission range, and moderately priced, is desired.

The Proxim RangeLAN2 7911 radio modem is selected to serve as the wireless technology for the sensing unit. Operating on the 2.4 GHz unregulated FCC industrial, scientific and medical (ISM) band, the RangeLAN2 communicates at a data rate of 1.6 Mbps. A standard RS232 serial port interface is provided by the modem for direct communication with the computational core. Specific features of the RangeLAN2 are summarized in Table 2-4.

Table 2-4: Summary of RangeLAN2 7911 wireless modem features

Modem Feature	Specification
Frequency Range	2.4-2.483 GHz
Modulation Technique	Frequency Hopping - Spread Spectrum (FHSS)
Channels	15
Maximum Range	1000 ft. (unobstructed exterior use)
	500 ft. (structural interiors)
Data Rate	1.6 Mbps
Output Power	500 mW
Antenna	1 dBi omnidirectional antenna
Transmit/Receive Current	160 mA
Standby Current	60 mA
Power Supply	6 to 15 V DC (2.5mm DC jack)
Package Dimensions	5.4" L x 3.3"W x 1.35"H
Operating Temperature Range	-20 °C to +60 °C
Serial Interface	16C550 UART
Serial Rate	300, 1200, 2400, 4800, 9600, 19200, 38400, 57600, and 115200 bps
Communication Mode	Packetized, Pass-through, Broadcast
Network Protocol	TCP/IP and UDP/IP

By employing a 1 dBi omni-directional antenna, open space communication ranges of over 1000 ft. can be attained which is a suitable range for the installation of sensing units upon bridges. Unfortunately, the shielding behavior of heavy construction (e.g. concrete) reduces the range to approximately 500 ft. when used on the interior of structures. Extensive empirical studies have been performed investigating the effect different building constructions has upon radio signal ranges. Path loss models of radio signals in concrete structures suggest losses increase linearly with increasing logarithmic frequency (Davidson and Hill 1997).

Powered by a 9 V direct current (DC) voltage source, the modem draws 160 mA of current during receive and transmit communications. Compared to the power consumption characteristics of the AT90S8515 microcontroller, the large power demands of the wireless modem provide additional motivation for performing as many data interrogation algorithms possible at the wireless sensing unit's core. When the modem is not needed, its current draw can be reduced to 60 mA by placing it in sleep mode. Sleep mode is important for preserving the life of the unit's battery source.

A significant amount of hardware and software engineering has gone into ensuring the reliability of wireless communications. Four naturally occurring phenomena can diminish the performance of wireless signals: noise, path loss, multipath effects, and interference (Mittag 2001). Electromagnetic waves originating from sources like the sun and fluorescent lights represent ambient white noise. At greater ranges, a wireless signal's power is naturally reduced by path loss to the power levels of the ambient white noise resulting in their loss. Multipath effects are the result of the reception of a wireless signal and various forms of its reflection. The closer the signal and its reflected counterpart are at the time of reception, the harder it is to distinguish one from the other. Interference results from other wireless devices sharing the same bandwidth.

To minimize the effects of these detrimental phenomena, encoding data and spreading the encoded data over a wide frequency band can reduce transmission and reception errors. The RangeLAN2 employs frequency hopping spread spectrum (FHSS) techniques for encoding data and spreading them on a wide frequency spectrum. Each byte of data is encoded into an equivalent 16-bit number by the transmitter. The receiver is aware of the encoding scheme and will decode every 16-bits it receives back to the original 8-bit byte. If a few of the bits of the 16-bit encoded signal are corrupted, the receiver is still capable of resolving back to the original 8-bit based signal. Once the signal has been encoded in the transmitter, it is transmitted on different frequencies by hopping from one narrow frequency band to the next within a particular channel. The receiver is synchronized to the transmitter's hopping sequence and can accurately obtain the transmitted data. The hopping of frequency bands ensures that the power of the signal is spread over a wide frequency band keeping it immune to narrow-band interference. The RangeLAN2 has 15 channels each representing 15 unique frequency hopping sequences.

2.4 Unit Packaging

To accommodate all of the individual components of the system, a two-layer printed circuit board is preliminarily designed. The printed circuit board, 4 in. by 4 in., provides a convenient means of packaging all system components in an efficient manner. In this process, a two-sided sheet of stable insulating material is used to coat thin plated circuit paths. The result is a high quality circuit package created by a reliable fabrication technique (Horowitz and Hill 1998). It should be noted that industrial production of an identical unit would require a four-layer printed circuit board design with separate power and grounding planes for the digital circuitry. The mixed signal (analog and digital) nature of the system requires that the two signal types be isolated from each other, thereby preventing digital switching from causing analog performance degradation. The four layer design approach isolates the analog and digital circuit components while a two-layer board does not. The unavoidable mixed signal limitation of the two-layer circuit board design will cause a slight reduction in the resolution of the A/D converter.

The design of the two-layered circuit board is achieved using industry-standard CAD tools intended to assist in the design, layout and simulation of circuit designs. Specifically, CircuitMaker 6 and TraxMaker 3 are used for the wireless sensing unit’s circuit board design; CircuitMaker is a component placement tool while TraxMaker is used for routing electrical connections on the circuit board.

The various circuit components, including the AT90S8515 microcontroller, ADXL210 accelerometer, ADS7821 A/D converter and all support circuitry, are laid out in CircuitMaker with packaging dimensions and respective electrical connections between components specified. CircuitMaker outputs a netlist that is a file listing parts and respective packaging as well as the interconnections between component pins. The complete circuit placement design from CircuitMaker is documented in Appendix A.

The netlist file generated from CircuitMaker is the input to TraxMaker. TraxMaker physically lays out the components on a user specified board size. With the components placed, TraxMaker can automatically route electrical connections between circuit components making use of plated pin-through-hole (PTH) to run connections from one layer of the circuit to the other. To maximize board reliability and to optimize board performance, some important design goals are kept in mind when routing circuit paths (Ginsberg 1990). Capacitive crosstalk between adjacent signal lines is reduced by adequate spacing between circuit traces. Pin to pin interconnect delay is minimized by keeping traces as short as possible. Power and ground distribution lines, well routed for close placement to component parts, are designed with wide low-impedance traces to minimize noise effects.

The resulting layer designs are output by TraxMaker as Gerber and drill files. Each Gerber file describes the dimension of all electrical traces and pads on a board layer while dimension information of the through-holes is provided in the board drill file. The design of the circuit's top and bottom layers are presented in Figure 2-7.

After the wireless sensing unit's printed circuit board is completely designed, the Gerber and drill files are sent to a circuit board manufacturer for fabrication. AP Circuits, located in Alberta, Canada, has been selected as the circuit board manufacturer. After the two-layered circuit board has been manufactured, the various electrical components are manually soldered to the board. The finished circuit board is presented in Figure 2-8. The top overlay layer provided to AP Circuits is provided in the figure for comparison to the finished board. The key circuit components are labeled in the figure for reference.

The RangeLAN2 wireless modem is externally attached to the circuit through a serial line originating from the modem's serial port. The current demonstration system can be contained within a sealed packaging unit, roughly 5 in. by 4 in. by 1 in. in dimension, as shown in Figure 2-9. The top yellow board is the completed circuit while the black entity located below it is the RangeLAN2 wireless modem.

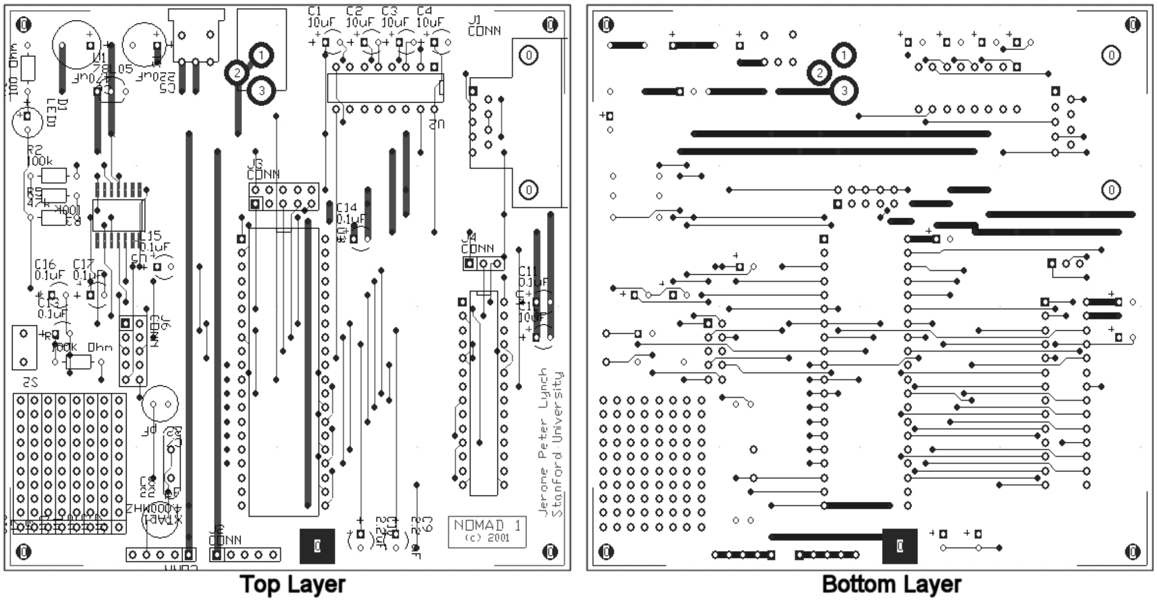

Top Layer

Bottom Layer

Figure 2-7: Printed circuit board overlay and copper layers (top and bottom)

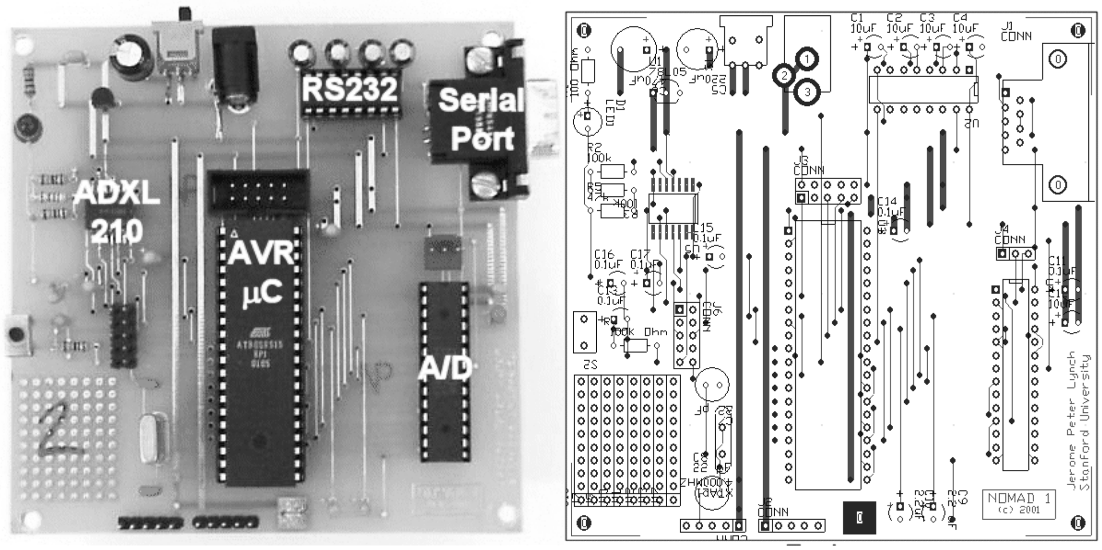

Figure 2-8: Printed circuit board (left) and top overlay layer design (right)

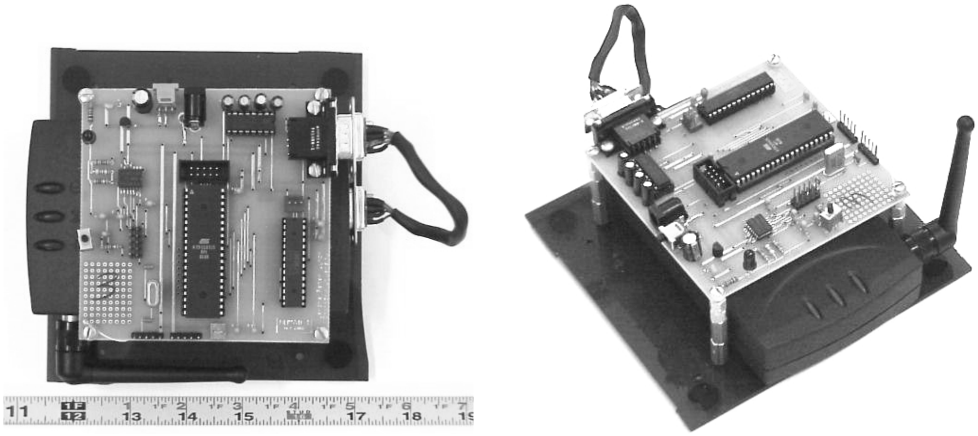

Figure 2-9: Top and perspective view of completed wireless sensing unit

2.5 Power Sources and Operational Life

The sensing unit requires a minimum 6 V DC power source. One potential source of power can originate from portable power sources such as batteries. However, the amount of power contained in a battery source is finite and will eventually run out if not recharged or replaced. If batteries are the final power source, then the design objective of the system is to extend the battery life to the order of years before replacement is required. Responsibility of battery replacement would fall upon the facility owner who would have to adopt a standard battery replacement schedule similar to ones used for smoke detector batteries. In order to avoid the added cost of replacing batteries, the system can be designed to employ rechargeable batteries and a structure’s electrical system can be used to keep the batteries fully charged. Likewise, in structural applications where sensing units are installed in the open environment, alternative power sources such as solar or wind can be considered for keeping rechargeable batteries at full capacity.

New innovative technologies are slowly making their way to the marketplace that can potentially scavenge power from a structure’s ambient vibrations. The incorporation of these technologies can make the wireless sensing units self-sufficient with respect to power. Two particular power harvesting technologies are being investigated by a large number of researchers globally. The first uses MEMS-based capacitors to derive energy from mechanical vibrations (Meninger et al. 2001). This approach is easy to attain in MEMS-sized packages but require a small voltage source to operate. The second approach is based on the charge producing strain properties of piezoelectric sheets (Glynne-Jones at al. 2001). Piezoelectrics can be mounted on structural elements undergoing cyclic strain to derive harvestable voltages. While more difficult to integrate with small electronic packages, it requires no voltage source and is currently closer to implementation in industrial applications.

Battery manufacturers provide estimates of a battery's life expectancy when powering a system at a given current. For this study, two battery technologies that represent the extreme ends of the energy efficiency spectrum are considered. The first is alkaline batteries (Zn/MnO_2) that are commonly sold as general purpose batteries for use in radios, flashlights, and other household goods. Their low cost is very attractive but their low energy density is a concern. At the other extreme, the high energy density lithium battery solutions are considered. In particular, the Li/FeS_2 cell chemistry is considered. Current costs suggest the Li-based batteries are almost three times more expensive than equivalent alkaline batteries.

Based on the electrical characteristics of the prototype unit's various components, the expected operating life of the system's power source can be estimated. The AT90S8515 data acquisition subsystem and the MPC555 are powered separately from the RangeLAN2. Two battery packs each consisting of five AA batteries (each AA battery provides 1.5 V) is used. The total volume of each battery pack is 40.5 cm^3 and outputs a total voltage of 7.5 V. The Proxim RangeLAN2 draws 160 mA when transmitting data and 60 mA when placed in sleep mode. The AT90S8515-based data acquisition circuit including all support circuitry draws 50 mA and the MPC555 microcontroller draw 110 mA when awake and 4 mA when in sleep mode. Two modes of operation are considered.

Table 2-5: Wireless sensing unit operating life for various battery chemistries

Operational State	Current (mA)	5-AA L91 (Li/FeS_2) Battery Pack (7.5 V)	5-AA E91 (Zn/MnO_2) Battery Pack (7.5 V)
AT90S8515 Circuit with MPC555 Asleep	54	50 hours	30 hours
AT90S8515 Circuit with MPC555 Active	160	15 hours	5 hours
RangeLAN2 Asleep	60	40 hours	25 hours
RangeLAN2 Active	160	15 hours	5 hours

In the first, the AT90S8515 data acquisition system is powered with the MPC555 in sleep mode. In the second, the MPC555 is awakened from sleep to perform some analysis calculations. An estimate of the RangeLAN2's battery pack is provided for both its sleep and awakened states. For the two battery chemistries considered, Table 2-5 summarizes the expected continuous operating life of the wireless sensing unit. These estimates are calculated from engineering design charts provided by Energizer, the manufacturer of the two batteries considered: the AA L91 (Li/FeS_2) and the AA E91 (Zn/MnO_2). Clearly, the Li-based cell chemistry is superior and should be used as the unit's primary battery source.

The operational life of the wireless sensing unit can be further extended by designing a trigger circuit to power the system when a certain sensor output threshold has been reached. The triggering circuit can be designed to draw a minimum of electrical current guaranteeing a long operating life. A triggering circuit with an accelerometer connected is convenient for turning on the system in a timely fashion to monitor the structure during a large seismic event (Straser and Kiremidjian 1998). In the prototype wireless sensing unit designed and fabricated, a triggering circuit is not integrated.

2.6 Summary

This chapter has presented the complete hardware design of a prototype wireless sensing unit that will act as the primary building block of wireless modular monitoring systems. Fabricated from current technologies available in the embedded system marketplace, the hardware design of the unit is an optimal combination of enabling capabilities with low power and low cost components. Some key features of the design include a sophisticated computational core that can handle the computational demands of local data interrogation algorithms. The multi-channel 16-bit sensing interface is designed to render the unit sensor transparent with a wide variety of sensors that can potentially be integrated. The wireless communication channel provides a low cost yet incredibly flexible infrastructure for means of data transfer within a network of wireless sensing units.

A defining characteristic of the embedded system market is its rapid evolution with newer and cheaper technologies constantly emerging. As a result, the hardware design of the wireless sensing unit set forth in this chapter can be modified and updated to keep pace with the embedded system market. In future design iterations, some features that will be explored further include the use of a four-layer printed circuit board to minimize mixed signal interference and the consideration of hardware options that can further reduce power demands. Furthermore, design issues not considered in this study but will be addressed in the future include design of a rugged packaging for the unit, as well as, viable renewable power sources that can last at least two years without maintenance or replacement.

Chapter 3

Embedded Software Design

With the selected hardware components of the wireless sensing unit fabricated as a single unit, software is required to manage its operation. The role of embedded software is well defined; to act as an intermediary between the physical hardware layer and the intention of the sensing unit's end user. Analogous to the role of an orchestra's conductor, embedded software is responsible for the harmonious parallel operation of various hardware components. Implementation of well-designed software will harness the full potential of the hardware. This chapter presents details associated with the complete design of the system software for embedding in the proposed prototype unit discussed in detail in Chapter 2.

The chapter begins with an explanation of the software development chain used for programming the wireless sensing unit. Software modules for the operation of the various hardware subsystems of the wireless sensing unit's AT90S8515 data acquisition system are presented next. The chapter concludes with a discussion of the development of application software for the MPC555 that utilizes the microcontroller's computational power for sophisticated local data interrogation.

3.1 The Software Development Chain

Assembly programming can be an arduous means of programming microcontrollers, particularly for large-scale software projects. Alternatively, many embedded system programmers seek the convenience provided by high-level programming languages, particularly C. The advantages of using high-level programming languages are that they provide built-in structure and abstraction. The popularity of C over other high-level languages is because it is often considered a “low-level” high-level language with data types and built-in operations for the direct handling of bits, bytes and memory addresses (Kernighan and Ritchie 1988). The C language provides defined data types such as integers, characters and floating-point numbers in addition to various mechanisms for defining new data types. New input-output data types can be made through the use of structure types. Direct access to data memory is accomplished through the use of pointers. An additional feature of great convenience is the ability to execute functions recursively (Roberts 1998).

Irrespective of the programming language, the written software must be translated into machine code before embedding in the microcontroller. The process of converting programs written in high-level languages and assembly to binary machine code is known as the software development chain. Using C as the language for writing software, the software development process begins with using a compiler to convert the C code into assembly. Compilers are specific to their target environments because assembly output files generated by the compilation process use instruction mnemonics unique to the target’s instruction set. Compilers, while designed to translate to a minimum of assembly instructions, often generate assembly code longer and less efficient than what could be programmed by an experienced assembly programmer (Morton 2001). The additional assembly code generated is an unavoidable part of the compilation process and is termed code overhead. However, the convenience provided by a high-level programming language still justifies its use over assembly programming.

The assembly code generated by the compiler is converted to a binary object file by an assembler. The object code is equivalent to machine code with relative memory addressing but information about its absolute location within the target's program memory is absent. Large-scale software programs written for embedded systems typically employ a modular programming approach with source code divided into separate source files. Each module must be compiled and assembled to derive its respective object code. In addition, some development environments provide a library of object files that contain pre-compiled and pre-assembled functions that are commonly used. The set of object files that represent the different software modules are combined into one executable binary machine code file by a linker whose role is to replace relative memory addressing of each object file with an absolute memory addressing in program memory. The entire software development chain is illustrated in Figure 3-1.

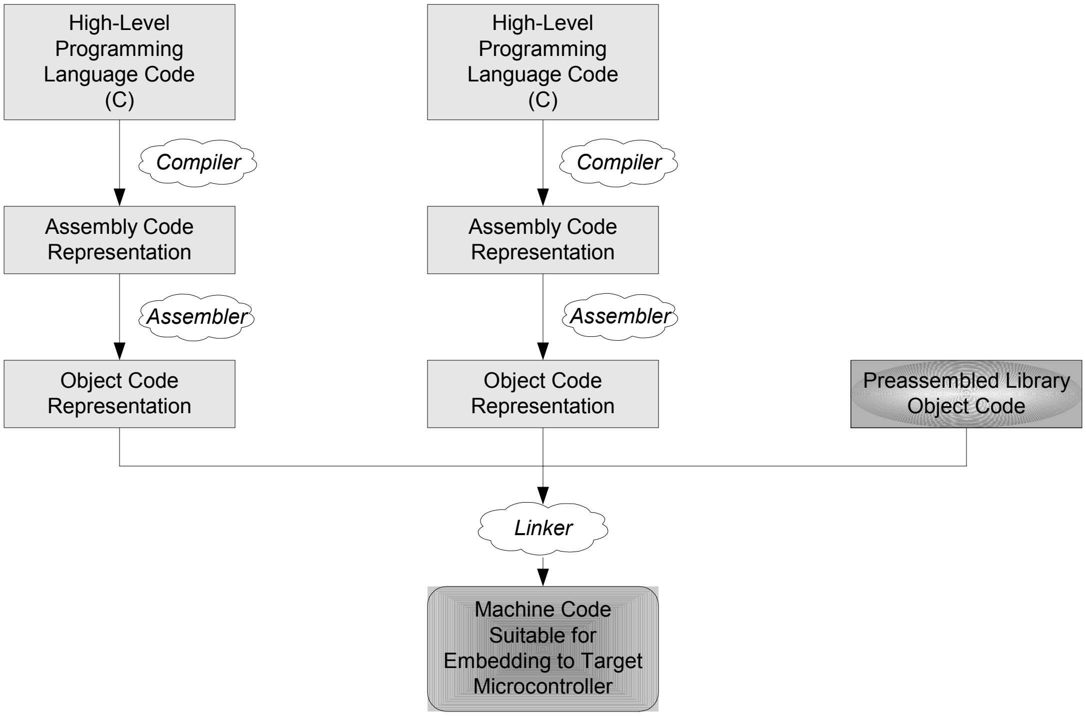

Figure 3-1: Embedded system software development chain

Fortunately, the creators of the AT90S8515 designed the AVR microcontroller family with high-level programming language users in mind. Many aspects of the microcontroller hardware design provide built-in support for high-level programming languages resulting in minimal code overhead. The 32 general-purpose registers allow C compilers the luxury of storing temporary data without being forced to move data before processing in the microcontroller's arithmetic and logic unit (ALU). Other 8-bit microcontrollers have 1 to 8 general purpose registers making moving data in and out of this limited register set necessary (Bogen and Wollan 1996). In addition, the six general-purpose registers that serve as three 16-bit pointers, allow for efficient memory addressing and indirect code jumps and calls.

The ImageCraft ICCAVR software development tools that include a C compiler, assembler and linker, all in one package, are selected for the AT90S8515. A powerful but easy to use integrated development environment (IDE) is operated on a Windows-based personal computer. Some additional features provided by the ICCAVR tools include a tailored ANSI C library optimized for the AVR microcontrollers, in-system-programming (ISP) tools for immediate download to the target controller, and code compression optimization tools (ImageCraft 2001).

Software for the Motorola MPC555 is written using the CodeWarrior PowerPC development tools from Metrowerks. Similar to the ImageCraft ICCAVR, CodeWarrior is an all-in-one package combining a C compiler, assembler and linker within a Windows-based IDE.

3.2 Software Modules

The wireless sensing unit's hardware represents the most fundamental layer of the system. To adequately operate the hardware, a software layer is required that is responsible for the operation of various hardware subsystems. This layer is a convenience often provided by an embedded real-time operating system (RTOS).

However, the complexities provided by an RTOS, such as multi-threading capabilities, is beyond the scope of what is required for this project. Therefore, this first layer of software is written for the wireless sensing unit. The role of this software layer is vital to the unit's operation since it serves as an abstraction layer hiding hardware implementation details from additional software layers that will be written for engineering applications. The software layers are presented in Figure 3-2.

The functionality envisioned for the wireless sensing unit indicates that the software required will be complex and lengthy. To ensure an efficient development process that will produce portable code of high quality, a modular software design approach is chosen for the lowest software layer. A modular approach divides the software design into separate software files called modules. Each module groups together the functions and the variables that are related to a particular hardware subsystem of the project. Given the close relationship between each module and a segment of the system's hardware, the modules are also known as hardware drivers. This logical structuring of the system software is similar to the object-oriented paradigm of C++ and Java with modules representing objects that provide information hiding, encapsulation, and portability (Morton 2001).

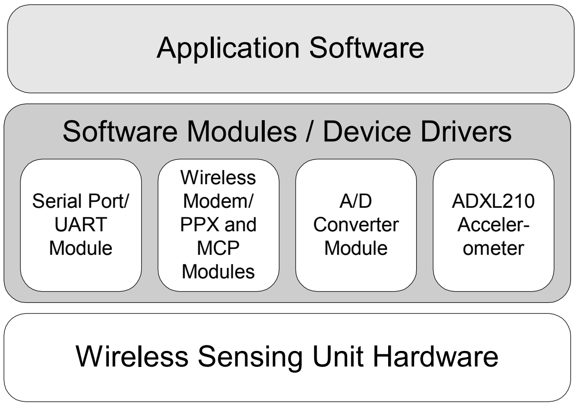

Figure 3-2: Intermediate software layer comprised of software modules

Each software module can be divided into two complementary parts: implementation and interface (Hayes 2001). Implementation of the module contains the functions and variables used in its operation. The scope of the module's functions and variables can be controlled such that they are internally private to the module or external for public use. Good programming habits support hiding as much of the implementation details as possible to reduce the ability of users to use the module incorrectly. The implementation is contained within a C source file.

The interface provides end users with information on the externally public portions of the module's implementation. As a result, the details of implementation are not shown and the external functions provided by the module appear as black box implementations. Authors of application layer software will use the interfaces to know what variables and functions they have direct access to. The interface is in the form of a C header file sharing the same name as the module's source file.

The software design of the wireless sensing unit's lowest software layer is divided into six software modules; e.g., to control communications over the serial line, a universal asynchronous receiver/transmitter (UART) module is created. Other modules control the operation of the wireless modem, obtain digital data from the A/D converter, are responsible for the collection of real-time data, and read acceleration data from the digital output of the ADXL210 accelerometer. Each of these modules will be discussed in detail in the following sections.

3.2.1 The UART Module

The serial port of the wireless sensing unit's AT90S8515 microcontroller is dedicated to the transmission of data to and from the RangeLAN2 wireless modem. A module is written that is responsible for the flow of information through the microcontroller's serial port by controlling the internal UART unit. Three functions are implemented in the module's source code and exported by the module's header file. The first, called `initUART`, initializes the UART to transmit and receive characters at a supported baud rate. The `initUART` must be called before the other two module functions since it enables the UART to work. The second module function, `transmitByte`, is for sending a single byte along the serial port. The function waits until the UART is available for transmission. Once the UART is free, the byte to be transmitted is placed in the UART's data register. At the completion of writing to the data register, the UART takes control of the byte for transmission. The last function, `receiveByte`, waits until a byte is received by the UART as notified by its enabling of the receive byte in its flag register. After receiving the byte, it is placed in the UART's data register from where the module retrieves it.

3.2.2 The Wireless Modem Modules

With a fully functional UART software module, communication with the wireless modem can now be established. The RangeLAN2 is a highly complex spread-spectrum wireless modem requiring the computational core of the wireless sensing unit to communicate with it in a controlled and precise manner. Two-way communication is established between the RangeLAN2 and the computational core with local sensor data sent to the modem for transmission. Reception of data originating from other units is passed to the core by the modem. Operating the RangeLAN2 in packetized mode, the unit's core has full control over the wireless modem by issuing commands to make changes in the modem's configuration at anytime. For the wireless unit to be able to send both data and commands to the RangeLAN2, rules for distinguishing between data packets and command packets must be established (Proxim 1998). Information transfer protocols, preprogrammed into the RangeLAN2's firmware, are employed for this purpose.

Two protocols are used for reliable operation and control of the RangeLAN2. Whether data is being sent or received or configuration commands are being issued to the modem, the Proxim packet exchange protocol (PPX-1 Layer 2 Protocol) is used for all communication between the modem and the wireless sensing unit's core. Within the packet exchange protocol, a modem command protocol (MCP) is encoded. The MCP specifies commands to the modem such as transmit data or to change configuration settings. Two software modules are written for the implementation of the PPX and MCP protocols.

3.2.2.1 Modem Command Protocol (MCP) Module

Packets encoded by the modem command protocol serve as the basis for information transfer between the modem and the wireless sensing unit's computational core. Packets specify either the transmission of local sensor measurement data or the configuration of the modem. Likewise, MCP packets received by the microcontroller from the modem can either specify incoming sensor data or the confirmation of a configuration command just issued. Table 3-1 defines the set of MCP packets that can be sent to or received from the RangeLAN2 modems.

Table 3-1: Modem command protocol (MCP) packet types

Modem Commands Packets		Modem Response Packets	
Command Byte	Packet Description	Command Byte	Packet Description
'T' = $54	Transmit Data Packet	't' = $74	Status of Transmitted Packet
		'd' = $64	Data Packet Received
'R' = $52	Request Radio Signal Strengths	'r' = $72	Signal Strength Report
'V' = $56	Request Serial Adapter Version	'v' = $76	Serial Adapter Version Report
'G' = $47	Go to Standby	'g' = $67	Standby Confirmation
'I' = $49	Initialize Serial Adapter	'i' = $69	Initialize Confirmation
'C' = $43	Set Radio Channel	'c' = $63	Radio Channel Confirmation
'S' = $53	Set Network Subchannel	's' = $73	Subchannel Confirmation
'B" = $42	Set Baud Rate	'b' = $62	Baud Rate Confirmation
'P' = $50	Get RS232 Pin Status	'p' = $70	RS232 Pin Status Report
'O' = $4F	Override Modem Parameters	'o' = $6F	Modem Parameter Confirmation
'A' = $41	Station Search	'a' = $61	Station Search Reply
'M' = $4D	Call Up Configuration Menu		

The size and structure of the actual MCP packet are unique to the command issued or response provided. The packet type is specified by its first byte. For example, an MCP packet containing sensor data for transmission would begin with a byte of the hexadecimal value $54. The MCP software module implements a function for each of the permissible MCP packet types with input variables unique to the packet's structure. Each function generates the MCP packet as an 8-bit character array.

Since the majority of information transferred between the sensor unit and the wireless modem will be measurement data, the `transmitData` function is described below in greater detail. The MCP packet for data transmission is simple in design but provides a powerful means of routing data in a network of sensing units. The first byte of the array signifies that the MCP packet is for the transmission of data by taking on the hexadecimal value $54, which is the value of the ASCII letter 'T'. The second byte is the sequence number of the data packet. This byte is very useful for ordering the packets streaming from the wireless sensing unit. The next two bytes form a 16-bit integer specifying the number of data bytes encoded in the packet while the next four bytes represent the destination address of the data with each sensor unit identified by a unique four-byte internet protocol (IP) address. For example, a unit installed within the 100.13.10 subnet could have a destination address of 100.13.10.1 to 100.13.10.254. If the sensing data is to be broadcast to the entire wireless sensing network, the broadcast address of the subnet can be used. This address is the subnet address with the value 255 placed in the last byte of the address field. For the example, the broadcast address would be 100.13.10.255. Additional bytes are used to store measurement data. Figure 3-3 is a sample MCP packet generated by the `transmitData` function of the MCP module for broadcasting three bytes of data to the 100.13.10 subnet.

84	MCP Command Byte for Transmit, 'T'
1	Sequence Number, First Packet
0	Number of Data Bytes (High)
3	Number of Data Bytes (Low)
100	Destination Address Subnet (High)
13	Destination Address Subnet (Mid)
10	Destination Address Subnet (Low)
255	Destination Address, Broadcast
1	Data
2	Data
3	Data

Figure 3-3: Example MCP packet for the broadcast of three bytes of data

The structure of the MCP transmit packet is tailored for use in the wireless sensing unit. For example, to transmit raw sensor data, the data placed in the MCP protocol is five bytes in length with the first byte representing the data point number, the next two bytes represent the time of the sample based on the microcontroller's 16-bit clock, and the last two bytes are the 16-bit sensor value as derived by the A/D converter. Previous research suggests that the functionality of the MCP packet can be enhanced by the inclusion of an additional system protocol packet implemented within the data field of the MCP transmit data packet (Straser and Kiremidjian 1998). The system protocol would uniquely specify the type of data as well as provide an ordering of the data in the MCP packet that both transmitter and receiver would understand.

3.2.2.2 Proxim Packet Exchange (PPX-1) Protocol Module

The intention of the PPX-1 protocol is to ensure a reliable means of communication over the serial line between the computational core and the wireless modem. Reliability is built in through protocol error checking and frame synchronization (Proxim 1998). The protocol is a simple list of 6 bytes that wraps an MCP packet. When the modem receives an identifiable PPX packet, it immediately unwraps the packet to reveal the MCP packet within. The modem then acts upon the information encoded in the MCP packet. Likewise, the wireless sensing unit's core receives information from the wireless modem as a PPX packet. The core then extracts the MCP packet from the PPX packet.

The PPX packet can be divided into three parts: PPX packet header, MCP packet, and the checksum tail. The header is four bytes in length. The first byte of the PPX packet is the start-of-header byte. The value of 1 is always used for this byte. The next two bytes specify the length of the enclosed MCP packet. The subsequent byte contains the sum of the Boolean "not" values of the previous high and low length bytes. Frame synchronization, performed for the assurance of reliable and accurate readings of PPX packets, is done when a byte of value 1 is received by the modem. After receiving a byte of value 1, the modem internally performs a header check to confirm the existence of a new PPX packet header. Following the header is the MCP packet. The last two bytes of the PPX packet represent the checksum tail. The bytes of the MCP packet are added with the two lowest bytes of the sum used as the checksum bytes. The checksum serves as a means for detecting errors in the receiving of PPX packets by the RangeLAN2. However, no means of error correction is provided by the wireless modem (Proxim 1998). There is a maximum PPX packet size of 1462 bytes that can be accommodated by the RangeLAN2 at one time. Figure 3-4 illustrates a PPX packet that would correctly transmit the MCP packet previously presented in Figure 3-3.

A software module is created to implement and administer the RangeLAN2's PPX packets. Two functions are provided in the implementation of the module. The first is `assemblePPX`, used to create PPX packets. The MCP packet, its array size, and a pointer to a character array for the storage of the PPX packet, serve as the inputs to the `assemblePPX` function. The character array of the resulting PPX packet is placed in memory relative to the provided memory pointer. In a similar fashion, the module's second function, `decodePPX`, is used to extract an MCP packet from an input PPX packet.

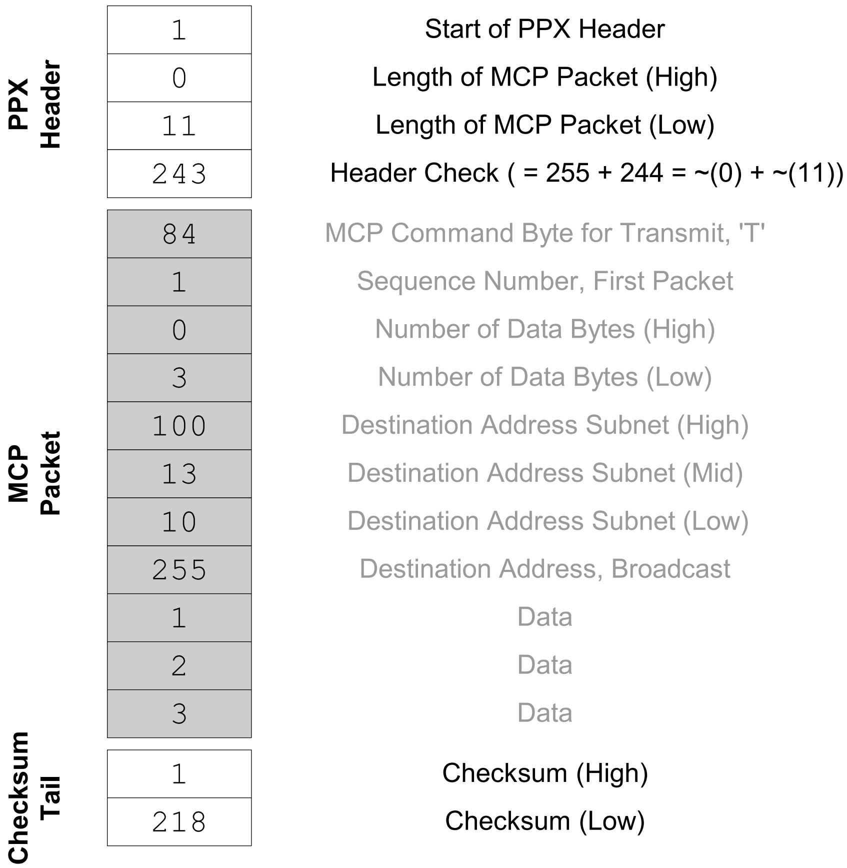

PPX Header	1	Start of PPX Header
	0	Length of MCP Packet (High)
	11	Length of MCP Packet (Low)
	243	Header Check (= 255 + 244 = ~(0) + ~(11))
MCP Packet	84	MCP Command Byte for Transmit, 'T'
	1	Sequence Number, First Packet
	0	Number of Data Bytes (High)
	3	Number of Data Bytes (Low)
	100	Destination Address Subnet (High)
	13	Destination Address Subnet (Mid)
	10	Destination Address Subnet (Low)
	255	Destination Address, Broadcast
	1	Data
	2	Data
	3	Data
Checksum Tail	1	Checksum (High)
	218	Checksum (Low)

Figure 3-4: PPX packet for the MCP packet of Figure 3-3

3.2.3 The A/D Converter Module

The Burr-Brown ADS7821 A/D converter, mounted on the wireless sensing unit's circuit board, is remotely operated by commands issued from the microcontroller. Particularly, the A/D converter is driven by a continuous square wave originating from the AT90S8515 and input to the R/C pin (pin 24 as shown in Figure 2-2). As required by the A/D converter, the square signal must be held low for a minimum of 40 ns and a maximum of 5 μs. On the rising edge of the square wave signal, the conversion of the analog signal to a 16-bit digital form is complete and exerted on the A/D converter's 16 output pins. The A/D converter provides a digital signal indicating the completion of a conversion by exerting a logical high on the converter's BUSY pin (pin 26). An inherent latency exists from the falling edge of the driving square wave and the completion of the conversion as indicated by a rising edge on the BUSY pin. In addition to the time delay from the start of conversion to the high on the BUSY pin of 8 μs, a 2 μs read time is needed to read the conversion from the converter. Therefore, the minimum time allowed between conversions is 10 μs translating to a maximum permissible sample rate of 100 kHz.

To acquire measurement data from analog sensors interfaced to the 16-bit A/D converter, a software module is written for precise operation of the converter. The design of the module must meet the stringent requirements of real-time acquisition applications. The role of the software module in operating the A/D converter is to precisely drive the A/D converter with an appropriate square wave, retrieve the converted measurement data when completed, and implement a real-time compliant data stack for the microcontroller's use.

3.2.3.1 Precision Operation of the A/D Converter

The function `initA2D` is provided for turning the A/D converter on and driving it with the appropriate square wave. The only input provided to the function is the user's desired data acquisition sampling rate. For sampling rates greater than the A/D converter's maximum rate, the user is notified that the sampling rate has been set to the unit's maximum. From the provided sampling rate, the duration of the low and high portions of the driving signal is calculated by the function. The duration of the logical low is permanently set to 4 μs while the duration of the high portion is calculated to achieve the desired sampling period.

The 16-bit counter of the AT90S8515 microcontroller is employed for generating the driving signal required by the A/D converter. The 16-bit counter provides two output compare functions that when used with the function's interrupts, will provide the precisely timed driving signal. The counter is configured to count until it attains a stored compare value determined by the linear proportional relationship that exists between the compare value and the time duration of the driving signal's high. The control register of the 16-bit counter is configured so that on a successful compare, the compare's interrupt function hidden within the module's implementation, `outputCompare`, is executed. The entry point of `outputCompare` in program memory is placed in the location of the sixth vector in the interrupt vector table shown in Table 2-3. Within the `outputCompare` interrupt function, the compare output pin, OC1B, which was previously high, is set to a logical low. The low is held for exactly 4 µs after which, it is again asserted high and the counter cleared. This process continuously repeats, generating a square wave on the OC1B pin of the microcontroller. The OC1B pin is directly interfaced to the A/D converter's R/C pin to drive the A/D converter's conversion process. The complete process of generating a driving signal for the A/D converter is shown in Figure 3-5.

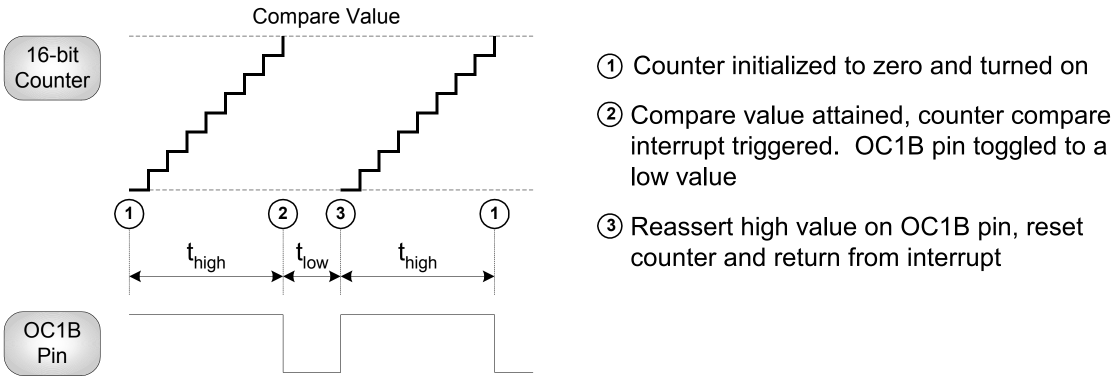

Figure 3-5: AVR microcontroller operation to generate A/D converter driving signal

3.2.3.2 Retrieval of Converted Data from the A/D Converter

The BUSY signal generated by the A/D converter, indicating when data is available for reading, is connected to the microcontroller's PD2 pin of port D. This pin is also known as the external interrupt INT0 pin. The functionality of the INT0 pin is tied directly to the second interrupt vector shown in Table 2-3. When this interrupt is enabled, the interrupt function is configured to execute upon the rising or falling edge of the pin's input signal. The BUSY pin output signal, when rising from low to high, provides the microcontroller with the exact time of when the data sample is ready for reading. The external interrupt is enabled in the general interrupt mask register and configured to trigger on a rising edge by setting two interrupt sense control bits in the microcontroller's general control register.

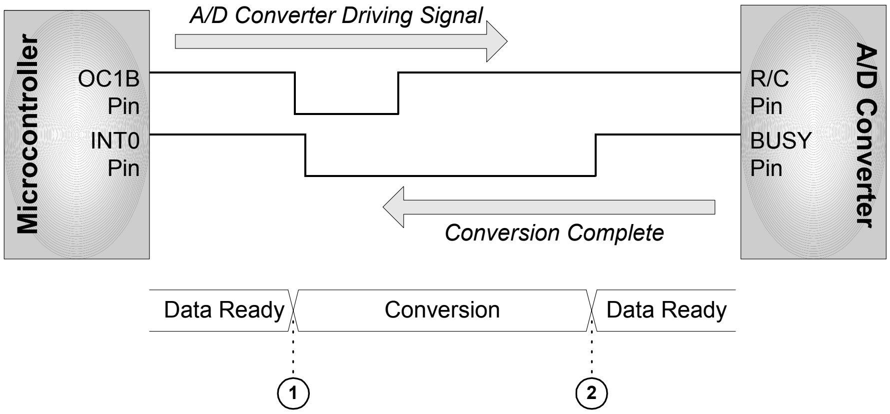

① A/D converter senses falling edge on R/C pin and starts conversion process

② Converter holds BUSY pin low until conversion completed at which time, rising edge on INT0 pin causes interrupt for fetching data to be serviced

Figure 3-6: AVR microcontroller reading measurements from the A/D converter

A second function, `fetchData`, is written in the module's implementation with its entry point in program memory written to the external interrupt of the interrupt vector table. The function, `fetchData`, executed by the servicing of the external interrupt, reads the 16-bits of data from the eight input pins of both ports A and C of the AT90S8515. The function `fetchData` is hidden from the module's interface since it is an internal function only required in the module's implementation. Figure 3-6 illustrates how the microcontroller retrieves measurement data from the A/D converter upon completion of a conversion. Once the data is retrieved by the microcontroller, the data is placed in a temporary data stack for future access.

3.2.3.3 Dual Data Stack Approach for Real-Time Constraints

Associated with each measurement are three bytes of data; the first byte being an 8-bit sample number used to sequentially order the measurements and the two other representing respectively the most significant byte (MSB) and the least significant byte (LSB) of the measurement converted by the A/D converter. After the converted measurement is read, the three bytes of data are placed within a data stack for temporary storage. Before any data is placed within the stack array, its first element is initialized to represent a count of the number of samples in the array. Each time three bytes associated with a single sample are added to the array, this first element's value is incremented.

Data placed on the data stack is simply a temporary storage location from which applications can retrieve the measurement data. Regardless of the application executing in parallel with the data acquisition process, it is imperative that its access to the recently acquired data does not hinder the module's responsibility to sample data under the constraint of strict time requirements. For example, consider the case where data placed on the temporary data stack is to be written to SRAM for permanent storage. At the outset of writing to memory, the size of the stack would be read from the array's first element. If while writing to memory an additional sample is obtained and placed on the stack, the routine writing the data to SRAM would be unaware of the new entity to the stack. When returning from the function, the stack would be cleared and the stack size reinitialized to zero. Unfortunately, any sample written to the stack during the writing to SRAM would be lost. To avoid such an undesirable situation and to ensure the integrity of each data sample obtained, a dual data stack approach is proposed.

In a dual stack approach, one stack is devoted to the real-time acquisition of measurement data from the A/D converter as described. When an application requires data from this stack, a memory pointer pointing to the current stack is switched to an alternative stack so that while the original stack is being accessed, new data points are added to the alternative stack. This dual data stack implementation is analogous to a pair of buckets used to catch water dripping from a leaky pipe. When one bucket becomes full and needs to be emptied, instead of risking water dripping on the floor due to its absence while being emptied, a second bucket held in reserve is placed under the leaking pipe to catch all the drops of water. Figure 3-7 is provided to show in more detail the operation of the dual data stack.

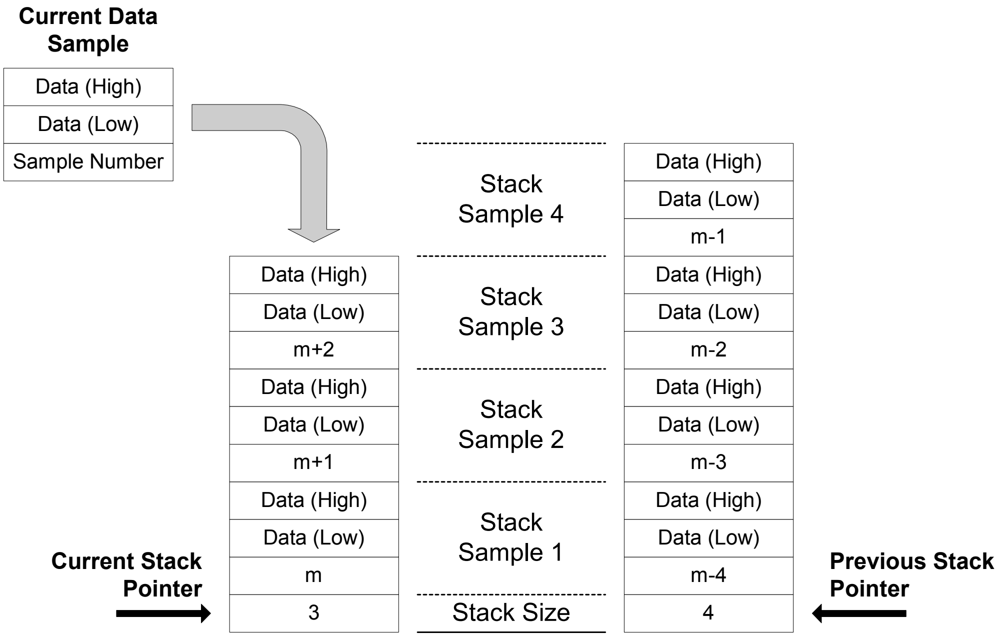

Figure 3-7: Dual stack implementation for temporary data storage

Access to the current data stack is provided in the module's interface. The function `getDataStack` takes as input a pointer variable that is used to store the address of the current data stack. As soon as this function is executed, the module's static pointer that is pointing to the current stack is switched to point to the alternative stack.

3.2.4 The ADXL210 Module

A software module is written to read measurements from an Analog Devices ADXL210 accelerometer connected directly to the wireless sensing unit. The accelerometer provides an analog and digital output signal. To avoid using the A/D converter's single input channel, the digital output of the accelerometer's two axes will be used for reading acceleration measurements. The resolution of the digital output is 14-bits and is encoded upon a duty cycle modulated output signal for each axis (Analog Devices 1999). Acceleration is linearly proportional to the duration of the high portion of the duty cycle modulated output signal. To read the acceleration measurement, the high portion of the signal needs to be precisely timed. The microcontroller provides a mechanism for timing both the high and low portions of a square wave through its input capture pin (ICP) (pin 31 in Figure 2-3). Precise time readings of the 16-bit timer are made when a rising or falling edge is sensed on the ICP.

The function `acquireData` is provided in the module's interface to utilize the ICP and the AT90S8515's timer for measuring the duty cycled modulated output of the accelerometer. The ICP is first configured through the 16-bit timer's control register to time when a rising edge of the input signal occurs. Once this occurs, the timer's value is stored in memory and the ICP is configured to sense the falling edge of the input. When the falling edge occurs, the function stores the second timer value in memory. Before returning, the time of the high portion of the accelerometer's signal is determined from the two stored times.

With the microcontroller running at 4 MHz, the 16-bit timer will overturn every 0.0164 seconds. A situation can easily be envisioned where the timer overturns during an acceleration measurement. As a result, an additional module is written for augmenting an additional 16-bit data variable to the microcontroller's 16-bit timer, yielding a 32-bit timer. When this module sees the original 16-bit timer overturning, the augmented 16-bit variable of the 32-bit timer is manually incremented. The time frame of the overturning of the 16-bit timer is slow enough to accurately detect the overturning and to manually increment the augmented timer without interfering with the time measurement of the accelerometer's output signal in the ADXL210's software module.

3.3 Application Software

The software that hierarchically sits upon the device driver modules is termed the application software layer. Application software, by utilizing the computational power of the core, is designed for fulfilling the data analysis goals of the system owner. Many analytical applications can be envisioned for the wireless sensing unit that would provide great value. For example, current wire-based monitoring systems already play a major role in performing modal analyses on the structures in which they are installed. With intelligence coupled directly with the sensor, more ambitious applications can be envisioned. Two specific application areas are proposed for investigation using the current wireless sensing prototypes, the simplest of which is the use of frequency-domain modal analyses embedded in the wireless sensing unit. The second is the use of the wireless sensing units in serving as damage detectors in an autonomous structural health monitoring system.

3.3.1 Modal Analysis

Modal testing and analysis, used to identify a mathematical model of a structure, is widely used in the civil engineering community. Often, the intent of the engineer in using modal analysis is to validate the use of finite element models that have predicted dynamic response levels of the structure. For such applications, all that is required are the natural frequencies of response and complete descriptions of the associated mode shapes. Sometimes, modal testing is used to directly calibrate an analytical model. For example, insight to the damping of the structure can be gained from modal testing, resulting in improved models better calibrated to test data. Historically, modal analysis methods have played a major role in the development of damage detection methods for structures. Significant research efforts have focused on using changes in the natural frequencies and mode shapes to identify the existence of damage in a structure. Frequency shift methods have been successful in structural environments where shifts can be measured in a precise manner such as in manufacturing machinery (Doebling et al. 1996). Unfortunately, the environmental and operational variability of civil structures is a contributor to natural frequency and mode changes rendering the changes as the basis for damage identification difficult for civil structures except in cases where extreme damage is sustained (Sohn et al. 1999).

Modal analysis theory provides a means of identifying mathematically the free response of a dynamic system by a set of frequencies and mode shapes known as the modal properties of the system. The analysis framework also provides a means of characterizing the forced response of a system through a set of frequency-domain transfer (mobility) functions relating the response of a system with its forcing function. Hence, transformation of system time-histories (response and excitation) to the frequency domain is required. Once in the frequency domain, various modal parameter extraction methods are available that find coefficients of a theoretical expression for the frequency response function (FRF) matching the FRF obtained from the measurement data (Ewins 1984).

To illustrate the possibility of using the wireless sensing unit for modal analysis of the structures in which they are installed, a software application is written that calculates the FRF from time-history measurement data. While wire-based monitoring systems would classically perform such calculations at the centralized data server, the FRF application is embedded and executed in the wireless sensing unit.

3.3.1.1 Fast Fourier Transform

The FRF of a structural system can be calculated directly from measurement data by using the computationally efficient fast Fourier transform (FFT). The discretely measured response of a system in the time domain, h_k, is converted to the response in the frequency domain, H_n, by means of a discrete Fourier transform:

$$H_n = \sum_{k=0}^{N-1} h_k e^{2\pi ikn/N} \tag{3.1}$$

where N represents the total number of time-history samples. The discrete frequencies are represented by:

$$f_n = \frac{n}{N} f_s \tag{3.2}$$

The Nyquist discrete frequency is half of the sampling frequency (f_n when n is equal to half of N).

If the discrete Fourier transform of Equation (3.1) is directly calculated by the wireless sensing unit, the calculation is an $O(N^2)$ process. Utilization of the discrete fast Fourier transform can reduce this calculation to an $O(N\log_2 N)$ process representing a significant increase in computational efficiency. Various forms of the FFT are available for use, but the Cooley-Tukey method is used (Press et al. 1992). The approach is described briefly.

Consider the use of the following notation:

$$W = e^{2\pi i/N} \tag{3.3}$$

The initial discrete Fourier transform of Equation (3.1) can be simplified using the notation proposed in Equation (3.3):

$$\begin{aligned} H_n &= \sum_{k=0}^{N/2-1} h_{2k} e^{2\pi i n(2k)/N} + \sum_{k=0}^{N/2-1} h_{2k+1} e^{2\pi i n(2k+1)/N} \\ &= \sum_{k=0}^{N/2-1} h_{2k} e^{2\pi i n k/(N/2)} + W^n \sum_{k=0}^{N/2-1} h_{2k+1} e^{2\pi i n k/(N/2)} \\ &= H_n^{\ e} + W^n H_n^{\ o} \end{aligned} \tag{3.4}$$

The result is the simplification of the initial discrete Fourier transform into a form comprised of two transforms, H_n^e and H_n^o, representing the n^{th} components of transforms made up of the even and odd components respectively. While the even and odd transforms are $N/2$ in length each, n still varies from 0 to N. In a likewise fashion, the even and odd transforms can be further reduced to even and odd components, H_n^{ee}, H_n^{oe}, H_n^{eo} and H_n^{oo}, each of size $N/4$. Assuming the initial measurement set's size N is a factor of 2, the initial discrete Fourier transform of Equation (3.1) can be further reduced to single point transforms of length 1. The single point transform is simply a copy of one of the input samples and hence, $H_n^{eooee\ldots ooeeo} = h_k$. The fast Fourier transform is required to know what input samples, h_k, corresponds with each single point transform. The value k corresponding to $H_n^{eooee\ldots ooeeo}$ can be found by reversing the even/odd notation pattern and assigning e=0 and o=1. Reordering the time-history data samples reflecting the order dictated by the order of the reversing pattern, the value of the transform H_n, is subsequently determined by recursively calculating two point transforms of adjacent data samples.

3.3.1.2 Computational Core Implementation

The FFT implemented in software for both the AT90S8515 and the MPC555 is written as a software function following a similar algorithm proposed by Press et al. (1992). The function, `fftcomplex`, takes in as input the time-history measurement data in an array ordering both real and imaginary parts of the measurement data sequentially. For N samples, a data array of size $2N$ is required for the function input. Since the measurement data of the sensors interfaced to the wireless sensing unit is comprised of real numbers, the terms representing the imaginary parts of the data are left as zero elements. If the number of samples of the input data array is not an integer power of 2, additional zero-padding elements are added to the array to produce an array that is.

The first task of the `fftcomplex` function is the bit reversal of the measurement data and a subsequent reordering of the measurement data as described in the previous section. The reordering of the measurement data is done in the original input measurement data array. After ordering the measurement data, three loops are constructed to cycle through a series of two-point discrete Fourier transforms that continuously update the real and imaginary elements of the original data array. First, the three loops algebraically combined adjacent pairs of data to form two-point transforms. Next, adjacent pairs are combined to obtain 4-point transforms. This process is continued until the first and second halves of the data set are combined to the form the final transform. Floating point number support is provided by the MPC555 in hardware, allowing the function `fftcomplex` to immediately declare data points as float types. The function returns a pointer to the original data array that has been updated with the discrete frequency response function. The first element is the complex number representation of the frequency response function at the zero frequency. The array increases in frequency up to the sampling frequency.

3.3.1.3 Additional Analysis of Frequency Response Functions

Once the frequency response function is calculated, additional analysis capabilities can be embedded in the wireless sensing unit. From a modal analysis standpoint, the frequency response function can be improved by using smoothing techniques. Smoothing is accomplished by averaging the individual frequency response functions at the same discrete frequencies derived from measurement data of the same time-history record. In addition, the finite nature of the original data set can often result in the spreading of energy from the true frequency into adjacent spectral lines, known as leakage. Leakage can be limited by using windowing techniques upon the initial time-history measurement record. Various window types exist such as rectangular, Hanning, and Hamming windows. Smoothing and windowing will result in more accurate frequency response functions that can be used by sophisticated modal analysis algorithms that will identify the natural frequencies and accompanying mode shapes.

3.3.2 Structural Health Monitoring – Damage Detection

Structural health monitoring entails the use of damage detection algorithms for the identification of damage, and to provide insight to its location and severity. Particularly for civil structures, information on the integrity of a structure in near real-time can be instrumental in assessing its safety over its operational lifespan.

A rational approach to structural health monitoring is to develop a low cost technology infrastructure for installation in a civil structure that can automate the process of detecting damage. The wireless sensing unit can serve as the fundamental building block of the automated system proposed. Using the computational power of the units, automated damage detection algorithms can be embedded that will interrogate the measurement data for the purpose of identifying and quantifying structural damage.

3.3.2.1 Statistical Pattern Recognition Paradigm

Sohn and Farrar (2001) propose using time-series analysis for the identification of damage in civil structures. It is part of a damage detection framework which consists of four-parts: evaluation of a structure's operational environment, acquisition of structural response measurements, extraction of damage sensitive features and use of statistical models for feature discrimination (Sohn et al. 2001). The time-series approach has shown promise in the identification of damage in the hull of a high-speed patrol boat as well as in several laboratory test structures. As a result of the approach addressing the environmental and operational variability of civil structures, it is selected for embedment within the wireless sensing units.

The time-history analysis begins with measurement of the structural response of the undamaged structure at a particular sensor location. Assuming the response to be stationary, an auto-regressive (AR) process model, also known as an infinite impulse response (IIR) filter, is used to fit the discrete measurement data sampled at a period of Δt:

$$x_k = \sum_{i=1}^{p} b_i^{\,x} x_{k-i} + r_k^{\,x} \tag{3.5}$$

The response of the structure at time $t=k\Delta t$, denoted by x_k, is a function of p previous observations of the response of the system, plus, a residual error term, r_k^x. Weights on the previous observations of x_{k-i} are denoted by the b_i coefficients.

The residual error of the AR model is a damage sensitive feature, but it is also influenced by the operational variability of the structure. To separate changes in the residual error resulting from structural damage and operational variability, an auto-regressive with exogenous input (ARX) time-series model is used to model the relationship between the AR model residual error, r_k^x, and the measured response, x_k:

$$x_k = \sum_{i=1}^{a} \alpha_i x_{k-i} + \sum_{j=0}^{b} \beta_j r_{k-j}^{\,x} + \varepsilon_k^{\,x} \tag{3.6}$$

Coefficients on past measurements and the residual error of the AR model are α_i and β_I, respectively. The residual of the ARX model, ε_k^x, is the damage sensitive feature used to identify the existence of damage regardless of the structure's operational state.

To implement the statistical pattern recognition approach, the structure is observed in its undamaged state under a variety of environmental and operational states to populate a database pairing AR(*p*) models of dimension *p* and ARX(*a,b*) models of dimension *a* and *b*.

After measuring the response of the structure, y_k, in an unknown state (damage or undamaged), an AR(*p*) model is fit. The coefficients of the fitted AR model are compared to the database of AR-ARX model pairs previously calculated for the undamaged structure. A match is determined by minimizing the sum of the difference of the newly derived AR model and the database AR models coefficients, b_i^y and b_i^x respectively. If no structural damage is experienced and the operational conditions of the two models are close to one another, the selected database AR model should closely approximate the measured response. If damage has been sustained by the structure, even the closest AR model of the database will not approximate the measured structural response well.

The measured response of the structure in the unknown state, y_k, and the residual error of the fitted AR model, r_k^y, are substituted in the database ARX model of Equation (3.6) to determine the residual error, ε_k^y, of the ARX model:

$$y_k = \sum_{i=1}^{a} \alpha_i y_{k-i} + \sum_{j=0}^{b} \beta_j r_{k-j}{}^{y} + \varepsilon_k{}^{y} \tag{3.7}$$

The residual of the ARX(*a,b*) model is the damage sensitive feature in the analysis. If the structure is in a state of damage, the statistics of the ARX model residual, ε_k^y, will vary from that of the ARX model corresponding to the undamaged structure. In particular, it has been shown that damage can be identified when the ratio of the standard deviation of the model residuals exceeds a threshold value established from good engineering judgment (Sohn et. al. 2001):

$$\frac{\sigma\left(\varepsilon_k{}^{y}\right)}{\sigma\left(\varepsilon_k{}^{x}\right)} \geq h \tag{3.8}$$

Establishing a threshold, h, that minimizes the number of false-positive and false-negative identifications of damage is necessary for robust damage detection.

3.3.2.2 Implementation of an Automated Damage Detection System

Using the prototype wireless sensing units, the time-series damage detection method is to be implemented. A centralized data server will be used in the system to store the database of AR(p) and ARX(a,b) models corresponding to various operational conditions of the undamaged structure. The centralized server is necessary since the memory associated with each sensing unit is not sufficient to hold the vast database.

With wireless sensing units installed throughout the system, the system response at various degrees-of-freedom is recorded. Prior to model fitting, the measurement data is normalized to have zero mean and a standard deviation of unity. A software module is written for the units' embedded application layer that determines the coefficients of an AR(p) model based on a segment of the recorded data. Multiplying both sides of Equation (3.5) by the current measurement sample, x_k, and taking the expected value of both sides, the autocorrelation function of the auto-regressive process is derived:

$$\varphi_{xx}(k) = \sum_{i=1}^{p} b_i^{\,x} \varphi_{zz}(k-i) \tag{3.9}$$

The autocorrelation function of the discrete time-history obeys the initial difference equation of the AR process. This yields a means of determining the coefficients of the AR process based on calculations of the autocorrelation of the measurement data. Resulting are the Yule-Walker equations (Gelb 1974):

$$\begin{bmatrix} \varphi_{xx}(0) & \varphi_{xx}(1) & \cdots & \varphi_{xx}(p-1) \\ \varphi_{xx}(1) & \varphi_{xx}(0) & \cdots & \varphi_{xx}(p-2) \\ \vdots & \vdots & \ddots & \vdots \\ \varphi_{xx}(p-1) & \varphi_{xx}(p-2) & \cdots & \varphi_{xx}(0) \end{bmatrix} \begin{Bmatrix} b_1 \\ b_2 \\ \vdots \\ b_p \end{Bmatrix} = \begin{Bmatrix} \varphi_{xx}(1) \\ \varphi_{xx}(2) \\ \vdots \\ \varphi_{xx}(p) \end{Bmatrix} \tag{3.10}$$

The autocorrelation values of Equation (3.10) can simply be estimated from the measurement data consisting on N samples, by:

$$\varphi_{xx}(k) \cong \frac{1}{N-k}\sum_{i=1}^{N-k} x_i x_{i+k} \tag{3.11}$$

The coefficients of the auto-regressive process are extremely sensitive to the way the autocorrelation of the process is determined. As a result, a method has been proposed by Press et al. (1992) for determining the coefficients of the auto-regressive model directly from the measurement data. The method is recursive with its order increasing during each recursive call by estimating a new coefficient b_i and re-estimating the previously calculated coefficients so as to minimize the residual error of the process.

3.3.2.3 Application Strategy

Population of the centralized database of AR-ARX models corresponding to the undamaged structure is performed first. The wireless sensing units are used to fit AR(p)-ARX(a,b) model pairs of measurement data, with the coefficients of the models transmitted for storage in the remote database.

To evaluate the structure in an unknown state (damaged or undamaged), measurement data is taken of the structure's ambient response. An AR(p) model is locally fit to the measurement data by the wireless sensing unit. After the auto-regressive model has been fit, communication is established with the centralized data server. The p coefficients of the AR(p) process are sent to the centralized server for comparison to the database. Prior to the installation of the system, the number of auto-regressive process coefficients is to be determined. The number can vary from 10 to 50 coefficients with the residual error of the auto-regressive process decreasing with an increase in the number of coefficients. Determination of the closest AR model in the database is performed in the centralized server.

Once a match has been made, the coefficients of the ARX model corresponding to the AR model are returned to the sensing unit. The measurements stored in the wireless sensing unit are then used with the ARX model to determine the time-history of the ARX residuals. The standard deviation of the ARX residual corresponding to the measurement data, $\sigma(\varepsilon_k^y)$, and that from the database, $\sigma(\varepsilon_k^x)$, are compared to check if their ratio exceeds the damage threshold, h. The process is illustrated in Figure 3-8.

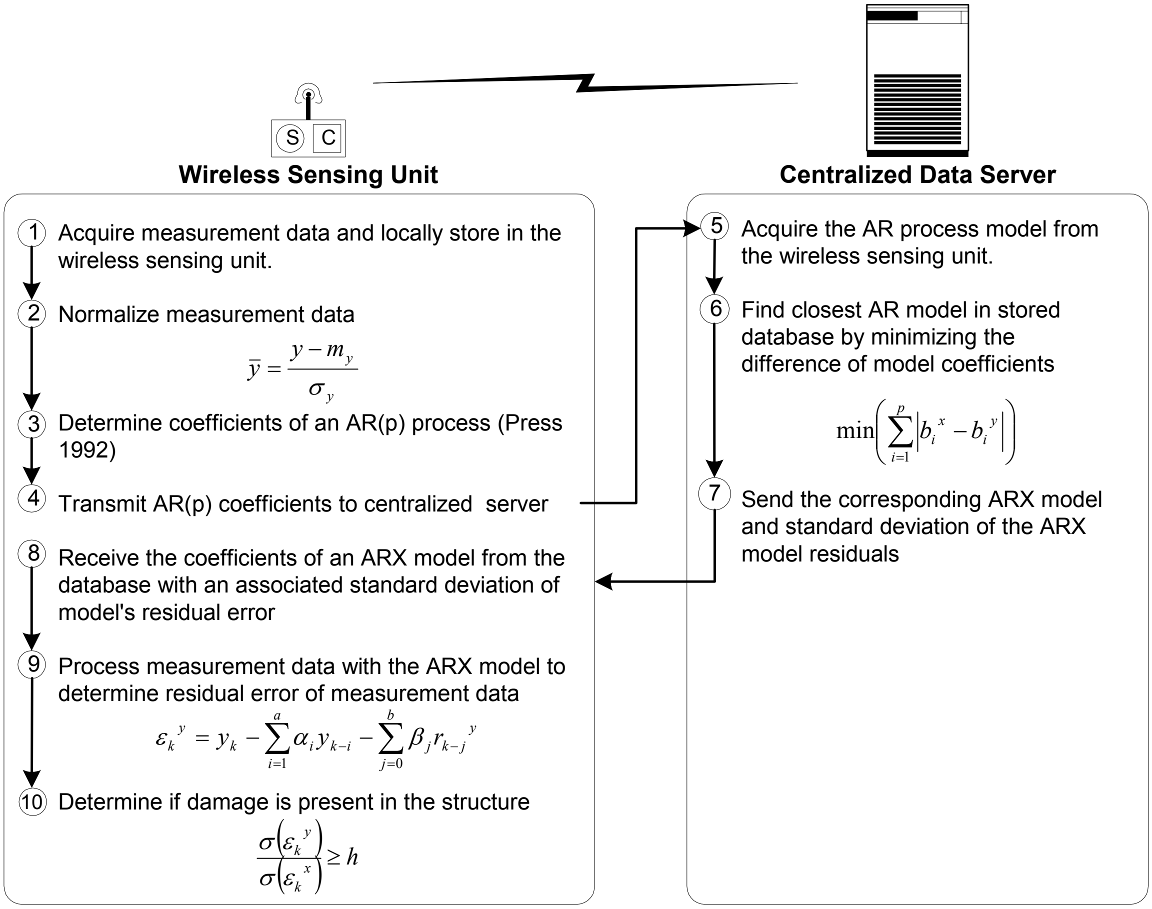

Figure 3-8: Time-series based structural health monitoring system implementation

3.4 Summary

The efforts to develop software for the wireless sensing unit can be classified into two broad categories (layers): embedded software for the device operation and application-based software. The embedded software was authored using a modular approach with distinct modules responsible for various subsystem operations. With embedded software for the operation of the unit completed, application software can be written to provide data interrogation capabilities. While many data interrogation algorithms can be incorporated, a fast Fourier transform and a statistical damage detection strategy were considered. Similarly, the computational capabilities of the core can be used to act as the controller of a structural control system with actuation forces calculated on-board from sensors interfaced to the unit and from sensor data obtained from remote wireless sensing units.

Chapter 4

Wireless Monitoring System Validation

This chapter describes a series of validation tests designed and performed to ensure the applicability of the prototype wireless sensing unit for structural monitoring applications. An assessment of the unit's performance will assist in determining if the design goals established at the outset of the project have been attained. The scope of the validation tests range from quantifying the performance of the individual hardware components of the prototype unit to the verification of a wireless modular monitoring system (WiMMS) installed in a short-span highway bridge.

The first set of validation tests is intended to provide insight to the performance of the prototype wireless sensing unit. This set of tests focuses upon empirically quantifying the analog-to-digital conversion resolution, maximum permissible sampling rates during real and near real-time applications, and limitations of the wireless communication channel.

Further verification of the wireless sensing unit's performance is done with sensors connected to the unit. Little mention has been made of the type of sensing transducers that can be interfaced to the unit for use in civil structures. With the low cost characteristic of the wireless sensing unit design, the potential synergy that could exist between the unit and the integration of low cost accurate sensing transducers is considered. In this study, two low cost sensor types are investigated for interface to the wireless sensing unit: MEMS-based accelerometers and strain gages. The sensing transducers selected are first calibrated and then mounted upon various laboratory test structures.

After monitoring the response of the test structures, data interrogation schemes embedded in the wireless sensing unit's core are locally executed. In particular, frequency response functions using fast Fourier transforms are determined in addition to the fitting of measurement data to time-series forecast models using auto-regressive modeling techniques. These two computation tasks serve as proof that coupling of computational power directly with the sensing transducer enhances the functionality and cost-benefit attribute of the wireless sensing unit.

The collection of validation tests is concluded with verification of the feasibility of easily installing wireless sensing units in civil structures for the reliable acquisition of ambient vibration measurements. The Alamosa Canyon Bridge in New Mexico is instrumented to provide a side-by-side comparison study between the wireless sensing unit and a conventional wire-based data acquisition system. Advantages and disadvantages of the current prototype unit design, as well as recommendations for future designs are addressed.

4.1 Quantification of Hardware Performance

The design of the prototype wireless sensing unit aims to select hardware subsystems that could attain the performance goals specified. During the iterative design process, a significant number of design decisions were made to attain the optimal performance of the interconnected hardware subsystems. An assessment of the impact these decisions have made on the completed prototype unit's performance is required. Specifically, tests are conducted to determine the A/D converter's effective resolution, to measure the maximum permissible sampling rate and to gain insight to the limitations of the wireless communication channel.

4.1.1 A/D Converter Resolution

The analog-to-digital conversion process that takes place in the A/D converter has many noise sources; thermal effects, quantization error, and voltage variations are classical noise contributors. Some noise sources are easy to control. For example, the voltage variation in the reference and supply voltage of the unit's on-board A/D converter is minimized by using bypass capacitors on their input. Unfortunately, the A/D converter is located on the unit's two-layer circuit board, sharing power and grounding lines with the other circuit parts including analog and digital logic components. When digital and analog integrated circuits share a common ground, ordinary switching of the digital logic can have a detrimental influence on the performance of the analog circuit (Horowitz and Hill 1998). The analog portion of the A/D converter is susceptible to some amount of corruption due to the digital switching elsewhere in the circuit. The result is manifested as a reduction in the 16-bit digital resolution of the A/D converter.

In order to assess the resolution of the wireless sensing unit's A/D converter as situated within the complete circuit, a constant noise-free voltage source is used as input to the converter. An Energizer L91 AA battery, outputting approximately 1.78 V, is used as the noise-free source for this test. After recording 15 seconds of the A/D converter's measurements at 30 Hz, an assessment of the resolution is made. The bit count of the input and its accompanying histogram are presented in Figure 4-1. The bit count of the A/D converter is determined by taking the original converter output and subtracting its integer mean value.

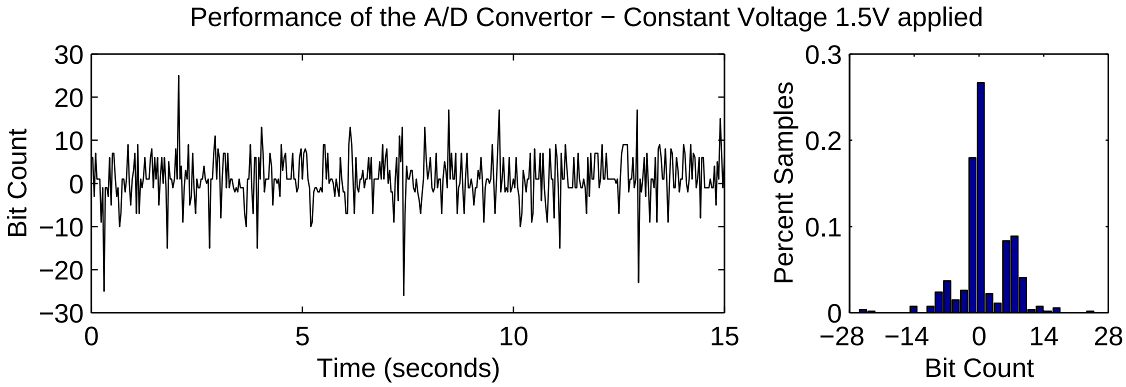

Figure 4-1: Measurement of on-board A/D converter resolution at 30 Hz

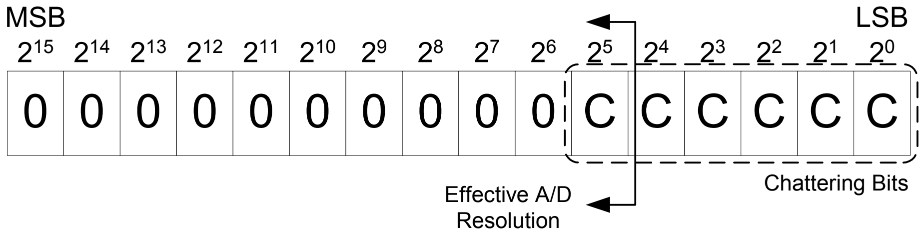

Figure 4-2: Determination of effective A/D converter resolution

The converter's output bit count varies from -26 to +25 implying the five least significant bits are chattering (randomly fluctuating to electrical noise). As illustrated in Figure 4-2, the effective resolution of the converter is determined by the most significant chattering bit which in this case is the 11th bit. Therefore, the resolution of the A/D converter is 11-bits.

It is clear that the two-layer printed circuit board design has reduced the converter's resolution by 5-bits. An attempt is made to recover the lost bits in software by internally over sampling the A/D converter and averaging the conversions. Only those noise sources that are Gaussian white noise in nature will benefit from this technique. Recommended in the literature is to increase the sampling rate by a factor of 3 or 4 for every recoverable bit sought (Staller 2001). For example, to recover one bit the A/D converter is driven at 3 times the desired sampling rate at 90 Hz with every three samples averaged and rounded to an integer value. The averaged result is output at the desired 30 Hz. Figure 4-3 presents 15 seconds of output from the wireless sensing unit after internally sampling at 90 Hz and producing the averaged time-history at 30 Hz. Immediately evident when comparing Figure 4-3 with Figure 4-1, is the improvement on the resolution of the A/D converter. The improved averaged time-history's bit count spans from -14 to 10, representing chattering in the four least significant bits. Therefore, the resolution of the A/D converter has been improved by one bit to a resolution of 12-bits, as expected.

4.1.2 Data Acquisition Sampling Rate

The wireless sensing unit can be used for both real-time and near real-time monitoring applications. For near real-time applications, the sensing unit is programmed to locally accumulate data at a given rate and to store that data for later retrieval. When the data collection is complete and all the sensor data stored in RAM, the unit can transmit that data to the other wireless sensing units in the sensing network upon demand. The delay in archiving all of the sensor data before transmission results in this approach being classified as near real-time. In contrast, for real-time applications the microcontroller is responsible for transmitting data at a precise clock time.

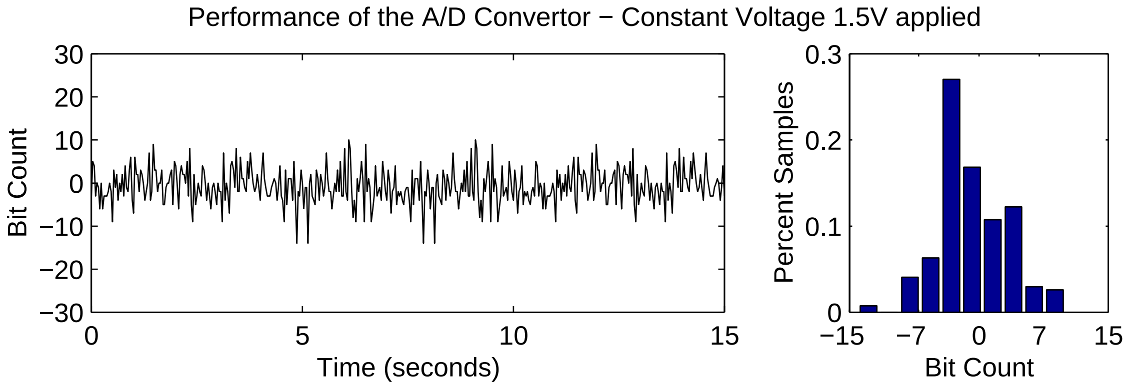

Figure 4-3: Improved resolution from oversampling at 90 Hz and averaging to 30 Hz

Prior to implementation, the sampling rate of the wireless sensing unit can be set to a desired value depending upon the monitoring application. In both modes of operation, there exist maximum sampling rates that the sensing unit can physically achieve. For real-time applications, time is required to encode each data point within the packet protocol structure of the RangeLAN2 radio modem. Once assembled in the microcontroller, additional time is required to send the packet through the serial port to the radio. The wireless sensing unit is configured to send data to the modem at a rate of 19,200 baud. Once the packet is written to the RangeLAN2's packet buffer, delays resulting from spread spectrum encoding are experienced. The time required to internally encode the data can only be determined empirically but can range from 4 to 32 ms depending upon the current wireless bandwidth usage (Proxim 1994). The limiting delay in the real-time transmission process is the time it takes to encode the data in the wireless modem.

Validation tests are performed to determine a comfortable real-time sampling rate before the RangeLAN2 begins losing packets due to an overflow of its internal packet buffer. A maximum real-time sampling rate of 33 Hz can be attained. If a sampling rate is chosen greater than the 33 Hz threshold, the safe delivery of all data points to the wireless network cannot be assured.

For near real-time applications, only the time required to attain and save the data in the wireless sensing unit's memory limits the maximum sampling rate. Empirical tests indicate that for near real-time, a maximum sampling rate of 20 kHz can easily be attained.

4.1.3 Wireless Communication Access Limitations

Limitations exist in the selected wireless communication infrastructure not found in conventional wire-based data acquisition systems. First, the range of communications between wireless sensing units is limited by the 500 mW output power of the RangeLAN2 radios. The line of sight range of the RangeLAN2 modems is over 1000 ft., but inside structures the range is reduced to approximately 500 ft. There also exist multiple access limitations of the wireless communication channel when using the sensing network for real-time applications. The real-time sampling rate of the wireless sensing unit is controlled by the RangeLAN2's speed of operation. For communication between one wireless sensing unit and another, the maximum speed at which one unit can sample and transmit data limits the effective sampling rate to 33 Hz. Symmetrically, the 33 Hz represents the speed which a receiving radio can internally decode the wireless data packets. This 33 Hz reception rate is independent of the number of units which transmit packets to the receiving radio. Therefore, if more than one wireless sensing unit is trying to communicate to another unit, the rate they send data to the receiving unit must be throttled accordingly. It has been empirically determined that two sensing units sending data to a third unit can stream data comfortably at 18 Hz each before the receiving unit's internal packet buffer overflows. In a similar fashion, three units can transmit at 10 Hz while four must reduce their transmission down to 7 Hz. For near real-time applications, this is not a major concern since bandwidth usage rules can be followed ensuring that one unit has exclusive access to another during information transfers.

4.2 Laboratory Validation of Sensing Transducers

Many sensors can be envisioned for integration with the wireless sensing unit providing valuable measurements of a structure's response or environment. For measuring a structure's response, current state-of-practice uses accelerometers for measuring the absolute acceleration response of a structure while strain gages are widely used for tracking stress and strain levels in major structural components. To ascertain the environmental impact on long span suspension bridges and tall skyscrapers, they are often instrumented with anemometers (for measuring wind speeds), thermometers and humidity sensors. Humidity and temperature are measured since a structure's modal properties exhibit sensitivity to these ambient parameters.

For this study, MEMS-based accelerometers and strain gages are considered for integration with the wireless sensing unit for validation in the laboratory. Both sensor types are relatively inexpensive and complement the low cost nature of the proposed wireless sensing unit.

4.2.1 MEMS-Based Accelerometers

There exist many different accelerometer architectures with varied performance characteristics in the market. By tradition, the force balanced accelerometer architecture is extensively used for structural monitoring applications because of its accuracy and high-level output (Kinemetrics 2002). The principle of operation of a force balanced accelerometer is an internal mass of the accelerometer prevented from moving from its null position by a series of control actuators that are commanded by a feedback loop signal. This feedback loop signal is proportional to the acceleration (Norton 1982). The market prices of force balanced accelerometers are high resulting in a search for viable accelerometer alternatives that are low cost.

The field of micro-technologies is fabricating small micrometer sized mechanical transducers upon the same silicon die used for integrated circuits, yielding low cost and precise micro-electro mechanical system (MEMS) sensors in form factors unimaginable years ago. Answering the high volume and low cost needs of the automotive market, sensor manufacturers fabricate precise MEMS accelerometers capable of measuring low accelerations (Soloman 1998).

Two distinctly different MEMS accelerometer architectures are considered in this laboratory validation study: capacitive and piezoresistive designs. The Analog Devices ADXL210 and Bosch SMB110 accelerometers are selected from the family of capacitive designs while a new piezoresistive accelerometer design, fabricated at Stanford University, is investigated. Validation of a low-noise MEMS accelerometer (Crossbow CXL01LF1) will be performed during validation of a WiMMS system installed on a full-scale bridge structure. The internal architectural design of the CXL01LF1 is classified as capacitive-based, identical to that of the ADXL210 and SMB110 accelerometers.

4.2.1.1 Capacitive Accelerometers

Employing advanced photolithography and etching techniques during manufacturing, a three dimensional polysilicon structure consisting of a released proof mass can be fabricated (Weinberg 1999). The proof mass is connected to the silicon substrate through linear springs. Capacitive plates are etched into the perimeters of both the proof mass and substrate, forming balanced differential capacitors that are used to directly measure acceleration. The substrate's capacitor plates are driven at 180° out of phase with voltage square waves. As the capacitive plate of the proof mass displaces between the two plates of the substrate, it unbalances the differential capacitor resulting in a square wave signal whose amplitude is proportional to the displacement. A synchronous demodulator is then used to generate an analog signal from the differential capacitor proportional to the acceleration of the sensor. Some capacitive accelerometer designs modulate the output on a duty cycle modulated digital signal for easy interface to a microcontroller. Figure 4-4 serves as a conceptual illustration of the capacitive architecture's operation.

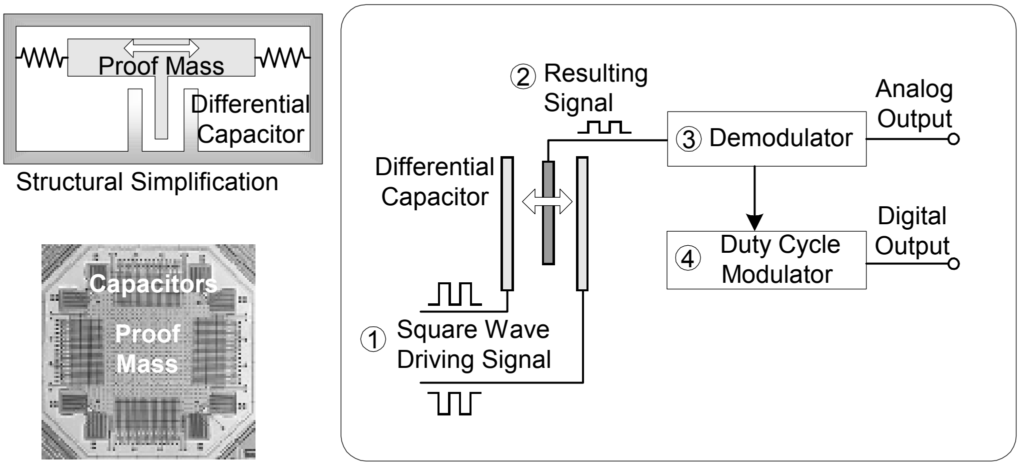

Structural Simplification

ADXL210 Internal MEMS Structure

Capacitive Accelerometer Functionality

Figure 4-4: Illustration of capacitive accelerometer's architecture and operation

The characteristics of the accelerometer's performance such as bandwidth and resolution can be set by connecting a capacitor on the analog output completing a first-order RC low pass filter. In general, a tradeoff exists between the bandwidth and resolution of the accelerometer with greater bandwidths causing reduced resolution. The noise inherent to capacitive accelerometers is characteristically Gaussian and is therefore constant over the entire bandwidth of the sensor.

In the capacitive accelerometer family, two accelerometers are considered for interfacing with the sensing unit: Bosch SMB110 and Analog Devices ADXL210. Variations exist in the design of the two accelerometers; in particular, the SMB110 is a single axis accelerometer while the ADXL210 measures acceleration in two planar axes. While an ADXL210 sensor is permanently interfaced to the microcontroller on the unit's printed circuit board, an additional ADXL210 is externally connected through the A/D converter for this study. When interfaced directly to the microcontroller, the advantage of using the optional digital output of the ADXL210 accelerometer is exploited. The ADXL210 encodes its acceleration upon a continuous square wave by varying the time duration of the wave's high portion. The resolution of this duty cycle modulated signal is 14-bits. Unlike the ADXL210, the Bosch accelerometer has no digital output. Both accelerometers employ low-pass filters on-chip to provide anti-aliasing of the output signal. The performance properties of the two capacitive accelerometers as configured for integration to the wireless sensing unit are summarized in Table 4-1.

Table 4-1: Performance specifications of the capacitive accelerometers

Sensor Property	Analog Devices ADXL210	Bosch SMB110
Measurement Range	0 ± 10 g	0 ± 2.3 g
Sensitivity	100 mV/g	780 mV/g
Bandwidth	50 Hz	56.4 Hz
RMS Resolution	4.33 mg	6.79 mg
Operating Voltage	5 V	5 V
Offset at 0g	2.5 V	2.5 V
Anti-aliased Output	Yes	Yes

4.2.1.2 High Performance Piezoresistive Accelerometer

Piezoresistive materials change resistance when placed under tensile or compressive strain. This property has been exploited for well over 20 years in the design of piezoresistive accelerometers (Roylance and Angell 1979). Classical piezoresistive accelerometers are generally used for out-of-plane acceleration with a proof mass connected to a short flexure upon which a piezoresistive material has been implanted. A new high-performance design of a piezoresistive accelerometer for measurement of in-plane acceleration is proposed by Professor Thomas Kenny's group at Stanford University (Partridge et al. 2000). An accelerometer with a planar cantilevered proof mass is fabricated upon a silicon die using deep reactive ion etching (DRIE) techniques. The cantilever is a single short flexure that is slender in the in-plane direction limiting the out-of-plane response of the proof mass. Oblique ion implantation is used for the formation of piezoresistors upon the side walls of the cantilevering element where a region of highly focused strain exists. A Wheatstone bridge, intended for temperature compensation of the piezoresistive implants, is embedded in the die to complete the accelerometer design. Over the full dynamic range, the accelerometer exhibits nearly constant sensitivity resulting in a linear transfer function of the sensor. A scanning electron microscope (SEM) image and design illustration of the piezoresistive accelerometer design are presented in Figure 4-5.

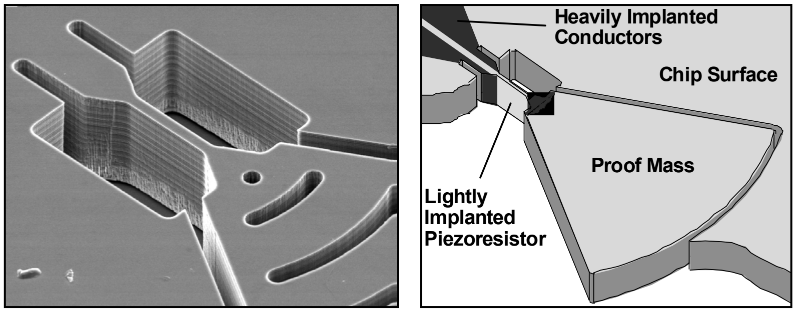

Figure 4-5: HPPA SEM image (left) and design illustration (right) (Partridge et al. 2000)

Performance characteristics of the high-performance piezoresistive accelerometer (HPPA) can be tuned to a specific application through the resizing of the cantilever dimensions. For example, to maximize the sensor's sensitivity, the width of the flexure should be minimized while the radial length of the proof mass maximized. Similar to the capacitive architecture, there exists a design tradeoff between the sensor's bandwidth and resolution; for greater resolution, the resonant frequency and bandwidth decrease. The maximum range of the accelerometer is determined by how far the proof mass can transverse before it is arrested by its housing. This arresting design ensures the survivability of the accelerometer when mechanically shocked. This is a major advantage of the accelerometer since the capacitive designs sustain damage when shocked. The end stops of the proof mass also prevent the flexural element from entering a nonlinear response regime.

Two dominant noise sources are present in the accelerometer design. In lower frequency regions, roughly below 100 Hz, noise is attributed to the inverse frequency (*1/f*) Hooge electrical noise of the piezoresistive elements (Hooge 1994). Above approximately 100 Hz, Johnson noise is the dominate noise source and is constant over the applicable frequency region (Partridge et al. 2000). Johnson noise is a direct result of the thermal agitation of electrons in a conductive element.

When compared with commercially available piezoresistive accelerometers, the experimental results of the high-performance piezoresistive accelerometer are superior. One set of accelerometers is designed and fabricated for specific adoption within the wireless structural sensing unit. These particular accelerometers have a radial length of 1 mm and a flexural width of 5 μm. The full dynamic range of the accelerometers is well above 10 g with a resolution of 20 μg at an acceleration bandwidth of 650 Hz.

The accelerometer samples fabricated are packaged in an eight pin DIP package as shown in Figure 4-6. The internal circuit of the accelerometer is a Wheatstone bridge circuit configuration with the piezoresistive elements of the cantilever serving as variable resistors of the bridge between pins 1 and 2 and pins 5 and 6. Between pins 2 and 3 and pins 6 and 7 are fixed resistors with nominal values of a few kilo-ohms.

The accelerometer outputs a low voltage differential output and therefore requires a low-noise differential amplification circuit. Figure 4-7 documents the complete circuit required for the proper interface of the HPPA to the wireless sensing unit. The differential output of the accelerometer's Wheatstone bridge is connected to a differential amplifier (AD620) where the signal is converted to a single voltage and amplified by 50. The output of the amplifier is referenced by the output of an operational amplifier (OP27) to ensure the zero gravity acceleration of the accelerometer's output is at 2.5 V.

Unlike the commercially produced capacitive accelerometers, the output from the high performance piezoresistive accelerometer, which is fabricated experimentally, is not anti-aliased. To avoid aliasing of the accelerometer spectrum above the Nyquist frequency, it is necessary to filter the accelerometer's output before interfacing to the wireless sensing unit. A four pole Butterworth low-pass anti-aliasing filter circuit, as shown in Figure 4-8, is designed with a cutoff frequency at 30 Hz.

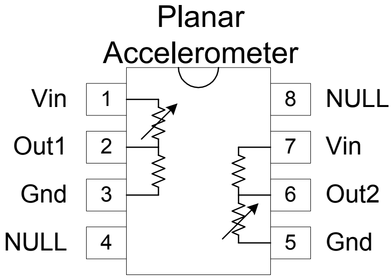

Figure 4-6: DIP package of the high-performance piezoresistive accelerometer

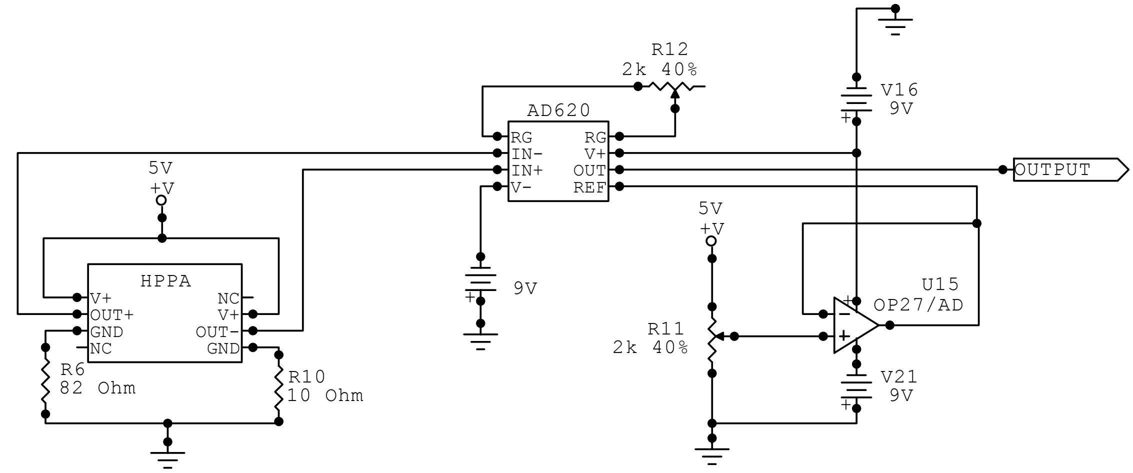

Figure 4-7: Support circuit to complete piezoresistive accelerometer interface

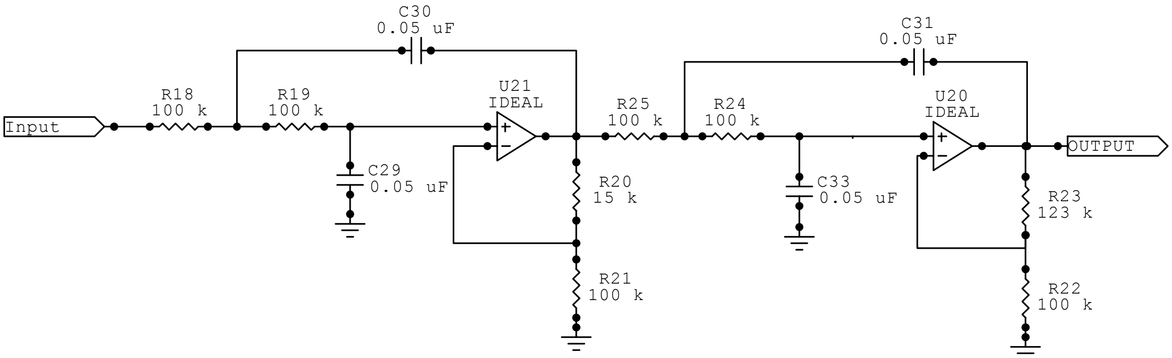

Figure 4-8: Four-pole Butterworth anti-alias filter with 30 Hz cutoff frequency

4.2.2 Strain Gages

Sensing transducers used to measure strain in structural members are known as strain gages. A strain gage is an alloy foil acting as a variable resistor embedded in a thin film. The film is easily mounted to the face of a structural member using epoxy glue. The properties of the strain gage are determined by the alloy selected to act as the variable resistive foil. In this study, constantan alloy foils are selected for their high strain gage factors and insensitivity to temperature and strain level. The sensitivity of the strain gage is measured by its gage factor (*GF*), defined as:

$$GF = \frac{\Delta R / R_{init}}{\varepsilon} \tag{4.1}$$

The change in resistance, ΔR, from the strain gage's initial resistance, R_{init}, is due to the strain, ε, in the structural member's surface.

Specifically, a Micro-Measurement EP-08-250BG-120 strain gage is selected to interface to the wireless sensing unit. The strain gage's initial resistance is 120 Ω with a gage factor of 2.055 (Measurements Group 2000). The constantan foil is embedded in a polymide film approximately 0.001 in. thick. For measuring strain, a three-wire Wheatstone bridge circuit is constructed around the strain gage. Three 120 Ω resistors are selected to serve as the fixed resistors of the bridge circuit as shown in Figure 4-9.

A relationship for the output differential voltage of the Wheatstone bridge, V_{OUT}, and strain, ε, can easily be derived for a bridge powered by a regulated voltage, V_{IN} that is nominally 5 V:

$$\varepsilon = \frac{1}{GF}\left(\frac{4V_R}{1-2V_R}\right) \tag{4.2}$$

where V_R is given as:

$$V_R = \frac{V_{OUT}(strained) - V_{OUT}(initial)}{V_{IN}} \tag{4.3}$$

A differential amplifier is required to convert the differential voltage output of the Wheatstone bridge circuit to a single amplified voltage. Strong similarities exist between the strain gage and the piezoresistive accelerometer architecture, resulting in a strain gage circuit similar to the one used for the accelerometer output. Figure 4-10 documents the circuit designed to interface the strain gage to the wireless sensing unit.

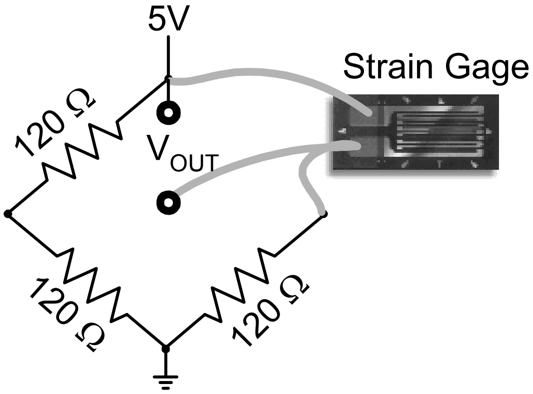

Figure 4-9: Wheatstone bridge configuration for 120 Ω strain gage

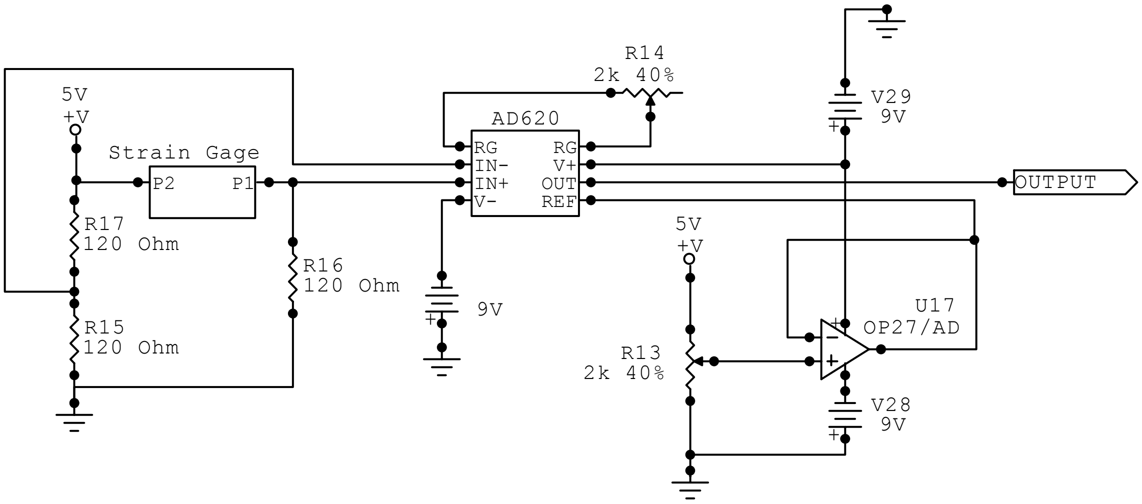

Figure 4-10: Circuit schematic to interface strain gage to wireless sensing unit

4.3 Accelerometer Calibration Tests

The three accelerometers (ADXL210, SMB110, HPPA) are interfaced to the wireless sensing unit for validation of their performance specifications. In particular, the sensitivity and resolution of the sensors are to be validated experimentally. Sensitivity is calculated by placing the accelerometers upon a vibration isolated laboratory surface in the 0 g and 1 g gravity fields. The change in mean voltage of the two readings provides the sensitivity measure (voltage change per unit acceleration). The steady state time-history readings of the accelerometers acquired from the sensitivity tests are then used to characterize the resolution of the sensors. The root mean square of the 0 g signal deviation from its mean (standard deviation) is determined. This measurement serves as a suitable means of quantifying the noise inherent in the acceleration readings of the capacitive accelerometers. Although the noise in the high-performance accelerometer is not necessarily Gaussian, the standard deviation value of the signal noise is still a convenient vehicle of quantifying the noise in the sensor. Figure 4-11 summarizes the results of the calibration tests conducted on the Analog Devices ADXL210, Bosch SMB110, and high performance piezoresistive accelerometers. The figure shows both the sensitivity results and the histograms of signal deviations.

The measured sensitivities of the ADXL210 and SMB110 accelerometers are in good agreement with their data sheet values of 100 mV/g and 780 mV/g respectively. The accelerometer sensitivities measured from the results presented in Figure 4-11 indicates the ADXL210 sensitivity is 103 mV/g while the SMB110 sensitivity is 795 mV/g. The sensitivity of the piezoresistive accelerometer is measured to be 90 mV/g. The sensitivity of the SMB110 accelerometer is roughly 8 times larger than that of the ADXL210 and the piezoresistive accelerometer because it has a smaller acceleration range of 2.3 g compared to the 10 g range of the other two.

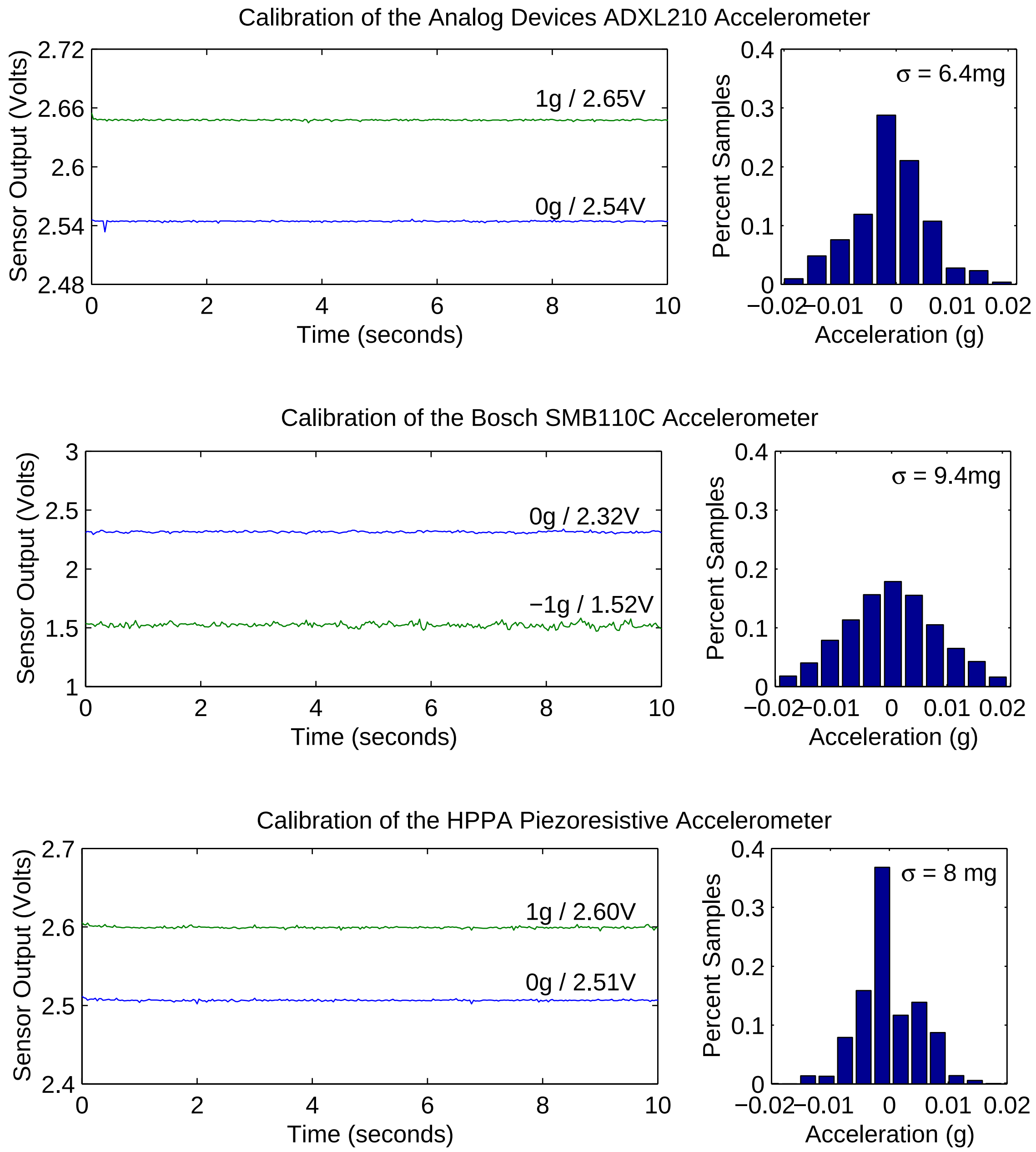

Figure 4-11: Calibration of accelerometers: sensitivity (left) and resolution (right)

The noise distributions of both capacitive accelerometers portray a rather Gaussian distribution with standard deviations of 6.4 mg and 9.4 mg respectively. For the ADXL210 accelerometer, this resolution is down near that of the A/D converter. The 9.4

mg deviation of the SMB110 signal is in good agreement with that stated in the datasheet. The noise distribution of the high-performance piezoresistive accelerometer is not as Gaussian as the capacitive accelerometers and exhibits a standard deviation value of 11.9 mg. In applications where accelerations are characterized by high frequency content, the noise in the high-performance piezoresistive accelerometer will be better than that of the capacitive accelerometers (Partridge et al. 2000).

4.4 Laboratory-Based Validation Tests

To validate the performance of the wireless sensing unit in applications similar to those envisioned in the field, two tests are set up in the laboratory. The first test utilizes the wireless sensing unit for monitoring the level of strain in a steel rod subjected to tensile and compressive loads. The second test installs the three accelerometers upon a five degree-of-freedom shear structure fastened to a shaking table. The structure is excited at its base by the horizontal movement of the shaking table.

4.4.1 Tensile Strain Test

To measure the cyclic stress-strain behavior of high strength steel, a 4 in. long, 1 in. diameter steel rod is selected for testing. The rod is mounted in a 22 kip load cell that will apply a tensile and compressive force along the rod's axis. The load cell is part of a laboratory MTS 3116-20K Test Frame. Provided the maximum force of the load cell, the center section of the rod is machined to a diameter of 0.52 in. to ensure yielding of the steel. A square pad region is milled to two sides of the rod for mounting the strain gage. The pads are 0.75 in. long and machined 0.02 in. into the surface of the rod. The Micro-Measurement EP-08-250BG-120 strain gage is bonded to the steel using epoxy. The complete rod is illustrated in Figure 4-12. An MTS 643.12F-24 extensometer with a gage length of 25 mm (0.98 in.) is attached to the rod to measure strain in the sample in parallel. The extensometer is connected to a traditional wire-based data acquisition system. Figure 4-13 is a picture of the steel rod mounted in the 22 kip load cell with the strain gage mounted to the rod surface and the extensometer clipped the side of the rod.

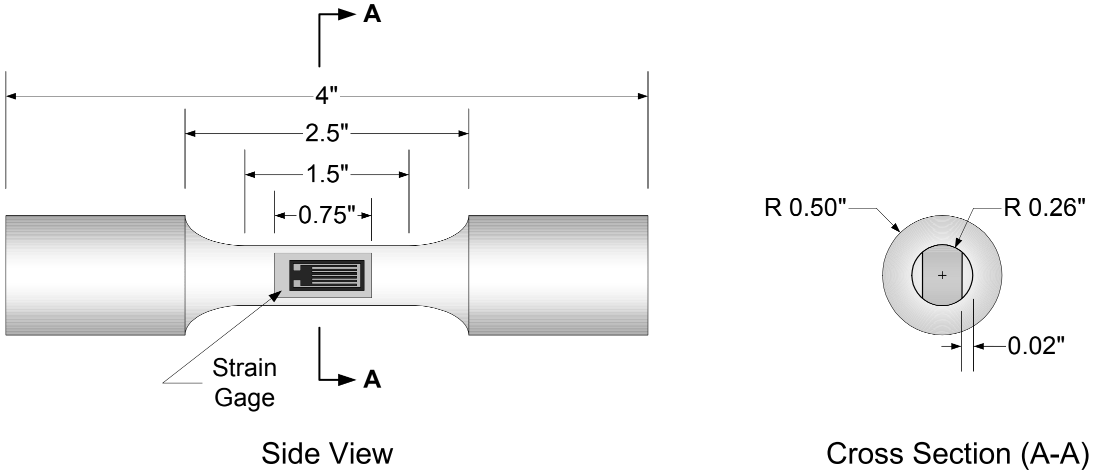

Figure 4-12: Steel rod with the EP-08-250BG-120 strain gage attached

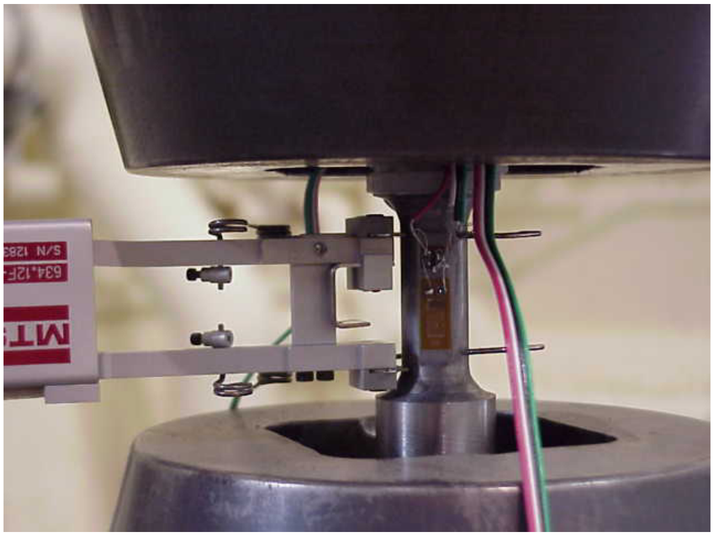

Figure 4-13: Test setup of steel rod with strain gage and extensometer attached

A cyclical loading is applied to the steel rod by the load cell with the loading increasing in time with a maximum load of 11 kips applied. The cyclical loading test occurs for over 16 minutes. Figure 4-14 presents a graph of the actual load applied to the steel rod by the load cell.

The rod's strain during the cyclic test is measured by the extensometer and the strain gage that is interfaced to the wireless sensing unit. The strain response of the rod and loading are logged at 0.5 Hz. The results of the test are presented in Figure 4-15. The graphs on the left present the time-history strain response of the rod while the graphs on the right present the strain response as a function of the applied axial force. When comparing the strain response measured by the strain gage interfaced to the wireless sensing unit with the strain measured by the extensometer, the results are nearly identical. It can be concluded that the strain gage interfaced to the unit is a reliable and accurate means of using the wireless sensing unit for measuring strain in structural members.

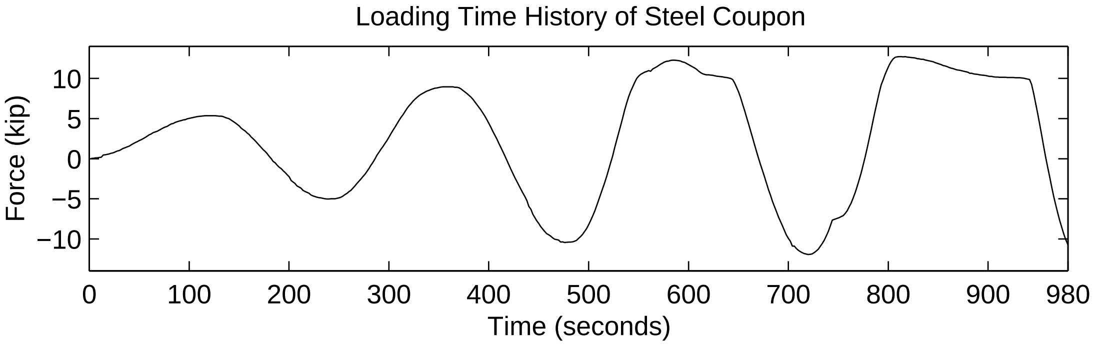

Figure 4-14: Time-history of the axial load applied to the steel rod

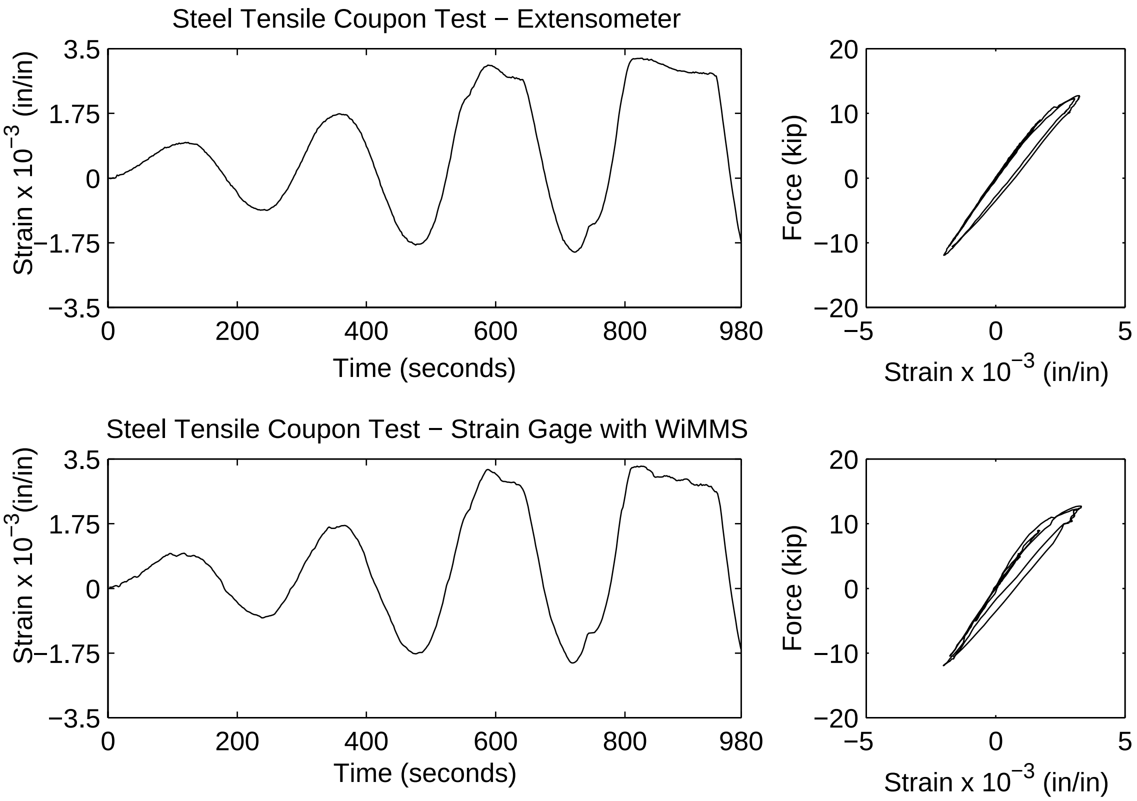

Figure 4-15: Measured strain response of steel rod to cyclic axial loading

4.4.2 Five Degree-of-Freedom Structure

To validate the performance of the wireless sensing unit, a validation test upon a laboratory test structure is devised. A five-story shear frame structure, made from aluminum, is employed as shown in Figure 4-16. The lateral stiffness of each floor originates from the four vertical aluminum columns, 0.5 in. by 0.25 in. in cross sectional area. Each floor represents 16 lb. of weight. From log-decrement calculations of free vibration tests, the damping of the structure is approximated to be 0.5% of critical damping. The wireless sensing unit is securely fastened to the fourth story while the MEMS-based accelerometers are mounted upon the fifth story adding additional mass to the structure. The entire structure is fastened to the top of a one-directional lateral shaking table driven horizontally by an 11 kip actuator. Various excitations are applied at the base of the structure to dynamically excite the system.

For this set of validation tests, the use of MEMS-based accelerometers in conjunction with the wireless sensing unit for measuring the real-time response of a structure is to be illustrated. A swept-frequency sine, also known as a chirping excitation, is applied to the base of the structure in order to excite the lower modes of response of the system. The chirping excitation has a constant displacement amplitude of 0.075 in. with a linearly varying frequency of 0.25 to 3 Hz over 60 seconds. During the excitation, the acceleration response of the fifth story is monitored using all three accelerometers mounted to the structure. The measurement data is sampled at 30 Hz, well above the primary modes of response of the system analytically determined to be 2.96, 8.71, 13.70, 17.47, and 20.04 Hz.

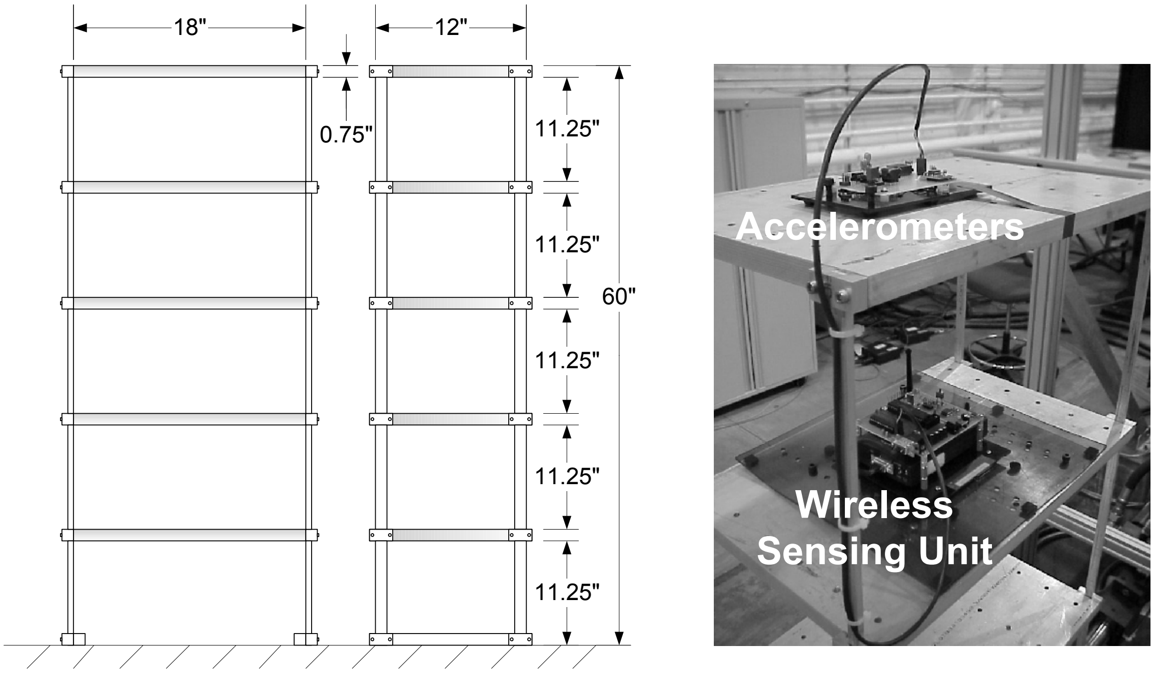

Figure 4-16: Five-story structure with accelerometers and sensing unit attached

Figure 4-17 presents the absolute acceleration response of the shear structure to the input excitation generated by the shaking table. The absolute acceleration responses measured using the three accelerometers (ADXL210, SMB110, and HPPA) are in very good agreement with the theoretical response determined analytically. The agreement is evident in both the amplitude and phase of the structural response. Some minor discrepancies might exist that can be easily attributed to the test structure not behaving exactly within the assumptions of the over generalized analytical system.

4.5 Local Data Interrogation

Attention is now turned to the validation of embedding data interrogation schemes within the computational core of the wireless sensing units. The first local data interrogation scheme is performed using the time-history response of the test structure recorded by the three accelerometers. The second data interrogation scheme uses time-history measurement data for the generation of an auto-regressive time-series model.

4.5.1 Calculation of Frequency Response Functions

The frequency response function of the three recorded time-histories is calculated by the wireless sensing unit using an embedded FFT algorithm. The FFT is performed on 1024 consecutive time points of the response between 10 and 44 seconds. The first three modes of response of the structure, at 2.87, 8.59, and 13.54 Hz, can easily be visually identified from the response functions as shown in Figure 4-18. The frequencies of the calculated modes are within 3% of those calculated from the theoretical model. At 12.84 Hz, there appears to be an additional mode that can be attributed to a torsion response mode resulting from minor geometric imperfections in the model. It should be noted that the frequency response function from the high-performance piezoresistive accelerometer is slightly noisier than those calculated from the capacitive accelerometers. This was expected because of the dominance of the *1/f* Hooge noise inherent to the accelerometer's design at low frequencies.

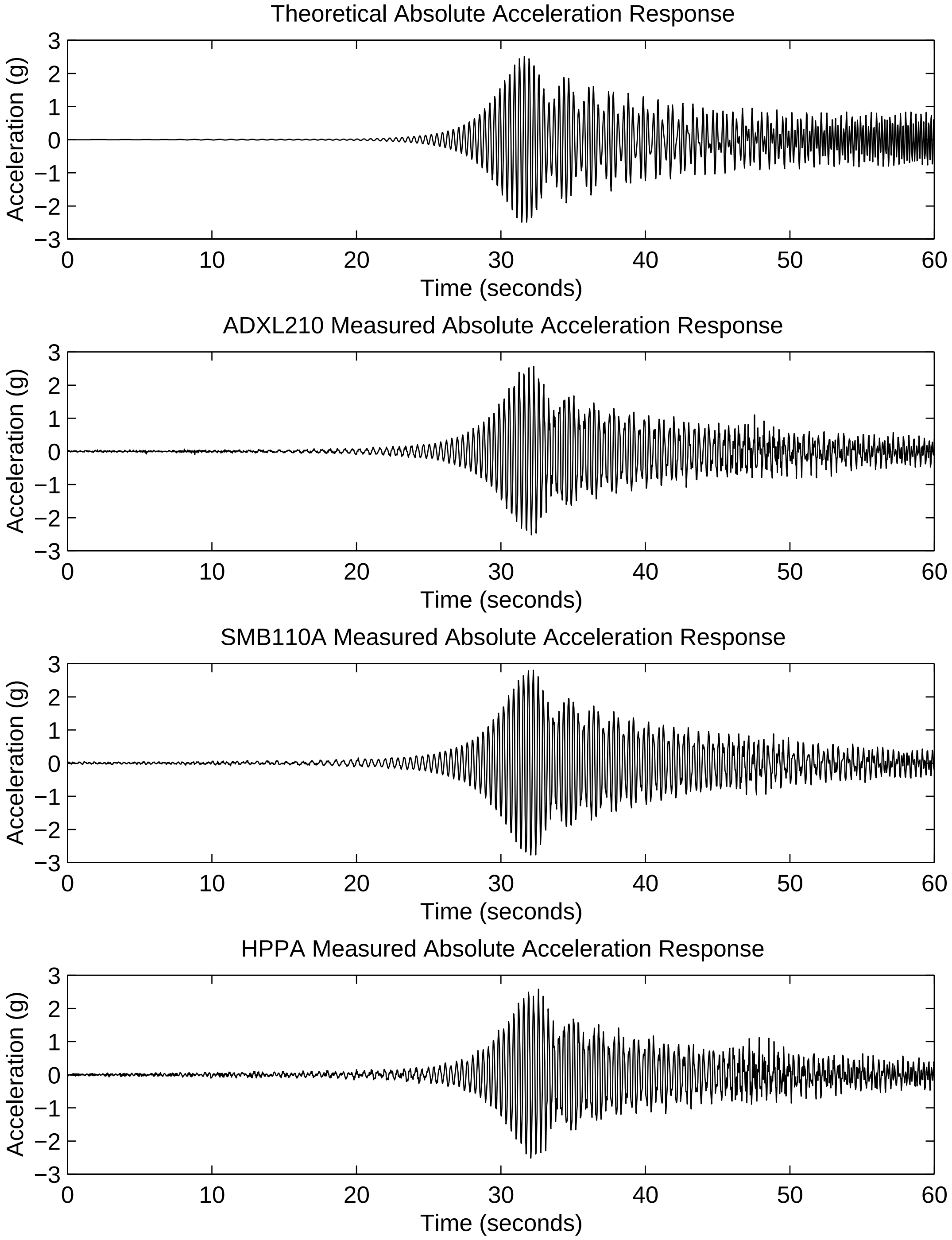

Figure 4-17: Absolute acceleration response of five-story structure to sweep signal

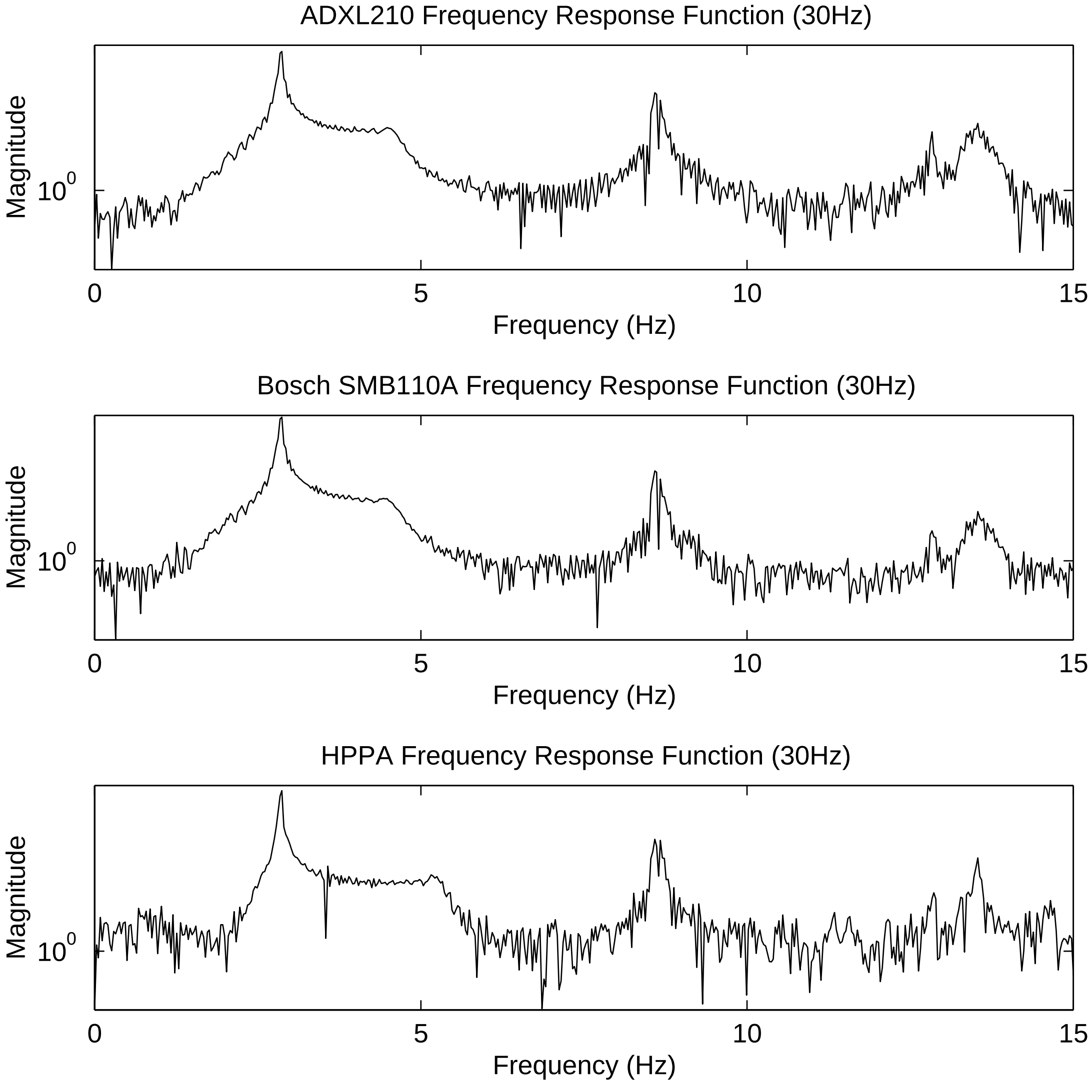

Figure 4-18: FRF calculated from five-story structure acceleration response

The frequency response functions can be improved by employing smoothing techniques. The frequency response function is calculated ten times with a different time offset for each response measurement time-history. The ten responses are then averaged to yield a smoothed frequency response function. The smoothed frequency response functions will make the identification of the structure's primary modes easier to identify. The smoothed functions presented in Figure 4-19 are calculated remotely on a computer, but can easily be embedded in the computational core for local execution.

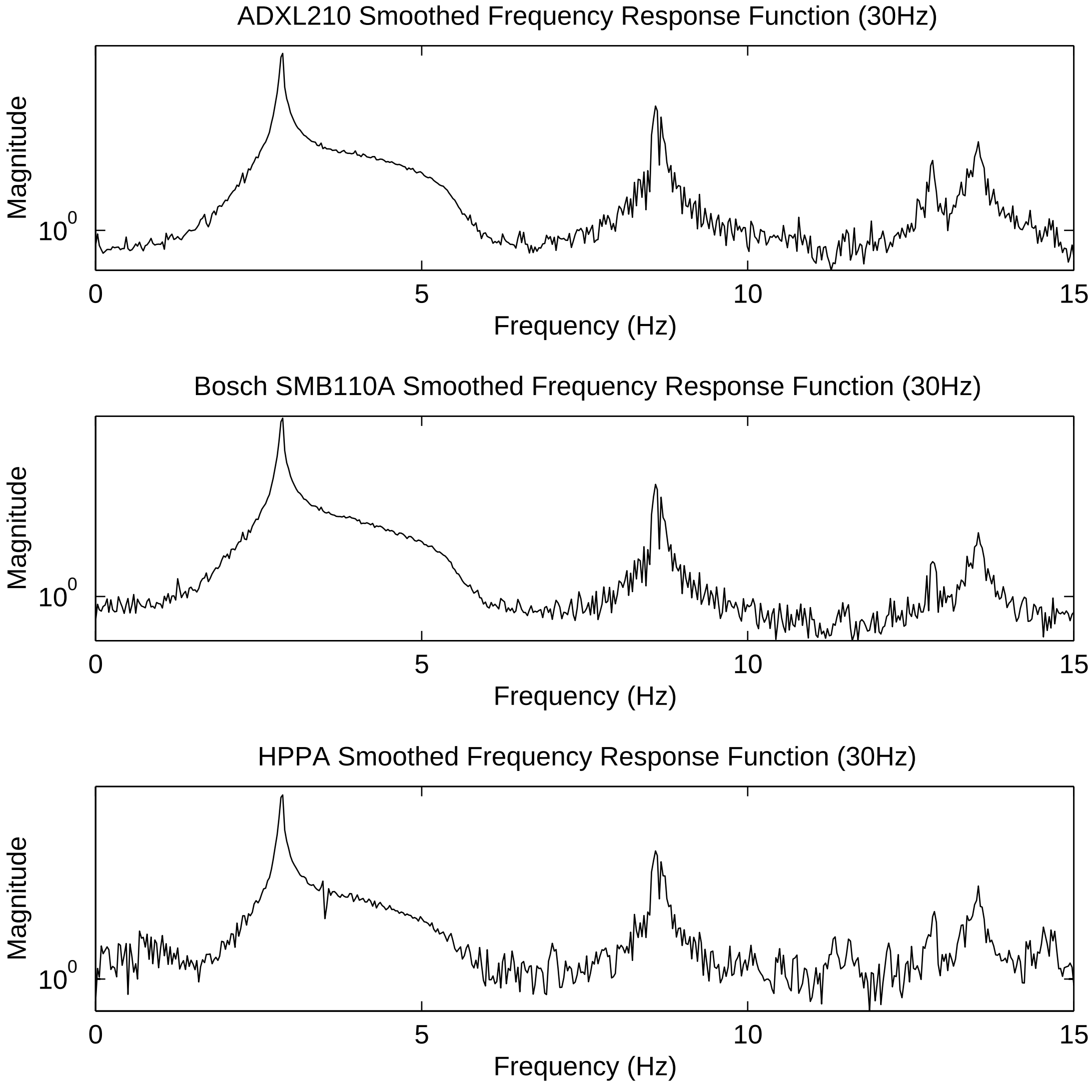

Figure 4-19: Smoothed FRF from five-story structure acceleration response

4.5.2 Auto-Regressive Time-history Modeling

The five degree-of-freedom test structure is instrumented with an ADXL210 accelerometer on its fifth story to measure the response of the structure to a white noise input. A white noise displacement record is created with zero mean and a standard deviation of 0.05 in. The response of the system to the designed disturbance is presented in Figure 4-20.

To determine if the time-history response is stationary, the recorded response is decimated into 10 segments, each 6 seconds in duration. The mean and standard deviations of the portions are measured. Table 4-2 summarizes the statistical findings. The time-history acceleration response of the structure as measured in this manner is relatively stationary with zero mean and a standard deviation of approximately 1.1 g. Therefore, the record is suitable to fitting an auto-regressive time-series model.

Table 4-2: Statistical properties of test structure response to white noise

Time-History Portion	Mean	Standard Deviation
1	-0.0015 g	1.3929 g
2	0.0001 g	1.2030 g
3	-0.0069 g	1.0268 g
4	0.0083 g	1.1174 g
5	0.0148 g	1.0829 g
6	0.0138 g	1.0091 g
7	0.0008 g	1.2397 g
8	0.0068 g	1.1058 g
9	-0.0027 g	1.1947 g
10	0.0028 g	1.0075 g

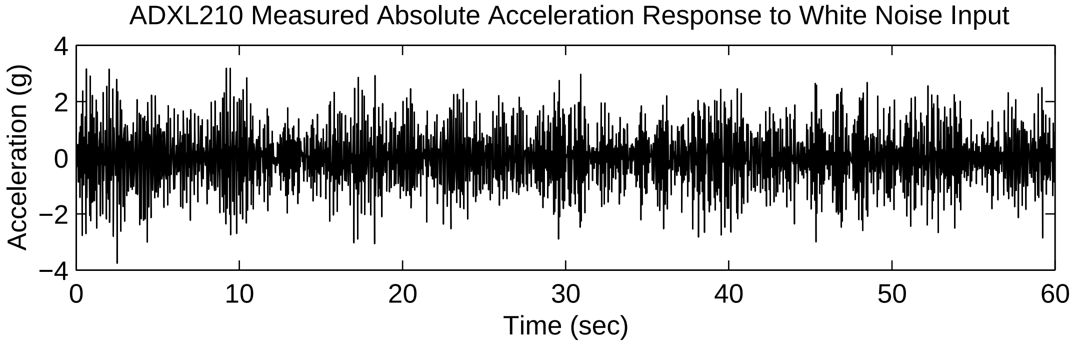

Figure 4-20: Absolute acceleration response of five-story structure to white noise

The Burg method of solving the Yule-Walker equations shown in Equation (3.10) has been embedded within the computational core of the wireless sensing unit. In particular, the hardware floating point capabilities of the MPC555 are extensively used in solving the Yule-Walker equations. After recording the acceleration response of the test structure, an auto-regressive model is fit for models of various sizes. In particular, three auto-regressive models of 10, 20 and 30 coefficients are fit to the measurement data of Figure 4-20. After logging the coefficients, an identical analysis is performed using Burg's auto-regressive function provided by MATLAB to ensure the accuracy of the coefficients determined. The coefficients as determined by the wireless sensing unit and MATLAB are tabulated in Table 4-3. It is evident that the results are identical.

Using the computational power of the wireless sensing unit to fit auto-regressive time-series models to stationary data is the first step towards the time-series based structural health monitoring system set forth in Figure 3-8.

Table 4-3: Auto-regressive coefficients for test structure recorded response

Coefficient, b_i	AR_{10}		AR_{20}		AR_{30}	
	MPC555	MATLAB	MPC555	MATLAB	MPC555	MATLAB
b_{1}	1.6650	1.6650	1.5915	1.5915	1.5853	1.5853
b_{2}	1.3009	1.3009	1.2415	1.2415	1.2471	1.2471
b_{3}	0.4752	0.4752	0.5293	0.5293	0.5369	0.5369
b_{4}	0.1171	0.1171	0.0624	0.0624	0.0652	0.0652
b_{5}	0.6756	0.6756	0.2754	0.2754	0.2648	0.2648
b_{6}	1.5212	1.5212	0.8377	0.8377	0.8064	0.8064
b_{7}	1.2646	1.2646	0.5392	0.5392	0.5062	0.5062
b_{8}	0.5989	0.5989	0.1494	0.1494	0.0870	0.0870
b_{9}	0.1498	0.1498	-0.1833	-0.1833	-0.2283	-0.2283
b_{10}	0.0891	0.0891	-0.2473	-0.2473	-0.2882	-0.2882
b_{11}			-0.4464	-0.4464	-0.4679	-0.4679
b_{12}			-0.5422	-0.5422	-0.5005	-0.5005
b_{13}			-0.3261	-0.3261	-0.2722	-0.2722
b_{14}			-0.1971	-0.1971	-0.1289	-0.1289
b_{15}			-0.0715	-0.0715	0.0354	0.0354
b_{16}			0.2227	0.2227	0.2475	0.2475
b_{17}			0.1912	0.1912	0.1760	0.1760
b_{18}			0.2397	0.2397	0.2276	0.2276
b_{19}			0.2360	0.2360	0.2900	0.2900
b_{20}			0.0134	0.0134	0.1397	0.1397
b_{21}					0.0871	0.0871
b_{22}					-0.0268	-0.0268
b_{23}					-0.1818	-0.1818
b_{24}					-0.2119	-0.2119
b_{25}					-0.0666	-0.0666
b_{26}					0.0093	0.0093
b_{27}					0.0366	0.0366
b_{28}					-0.0262	-0.0262
b_{29}					-0.1236	-0.1236
b_{30}					-0.0504	-0.0504

4.6 Alamosa Canyon Bridge Validation Test

In order to validate the feasibility of using the proposed wireless sensing units within a large civil structure, the sensing units are instrumented upon a full-scale bridge for ambient and forced vibration monitoring. The Alamosa Canyon Bridge, located in Truth or Consequences, New Mexico is selected. A benefit gained from using the Alamosa Canyon Bridge for validation tests is that the bridge's modal properties are well documented from past benchmark tests (Farrar et al. 1997). Installation in the Alamosa Canyon Bridge is instrumental in assessing the ease of installation of the units in addition to quantifying their performance during the monitoring of the structure's response under various excitations.

4.6.1 Structural Details of the Alamosa Canyon Bridge

The Alamosa Canyon Bridge is located 10 miles north of Truth or Consequences and serves as a traffic bridge spanning a small portion of the Alamosa Canyon. The bridge is part of a local two lane service road that runs parallel and adjacent to Interstate 25. Constructed in 1937, the Alamosa Canyon Bridge is comprised of seven independent spans, each 50 ft. long and 24 ft. wide. A 7 in. concrete deck is supported by six W30x116 steel girders whose centerline separation is 58 in. apart. To provide additional lateral strength to the bridge, four single channel braces are installed between adjacent girders. The load from the spans is transferred from the girders to shared concrete piers situated at the girder ends. At the girder-concrete pier interface is a standard roller acting as a classical pin support for the span.

For this set of validation experiments, the third span from the northern end of the bridge is selected for instrumentation. Figure 4-21 is an illustration of the span's structural details. Figure 4-22 is a picture of the top view of the bridge looking south with a view of Interstate 25 on the bridge's left side. Figure 4-23 is a side view of the Alamosa Canyon Bridge with the cows grazing under the third span of the bridge.

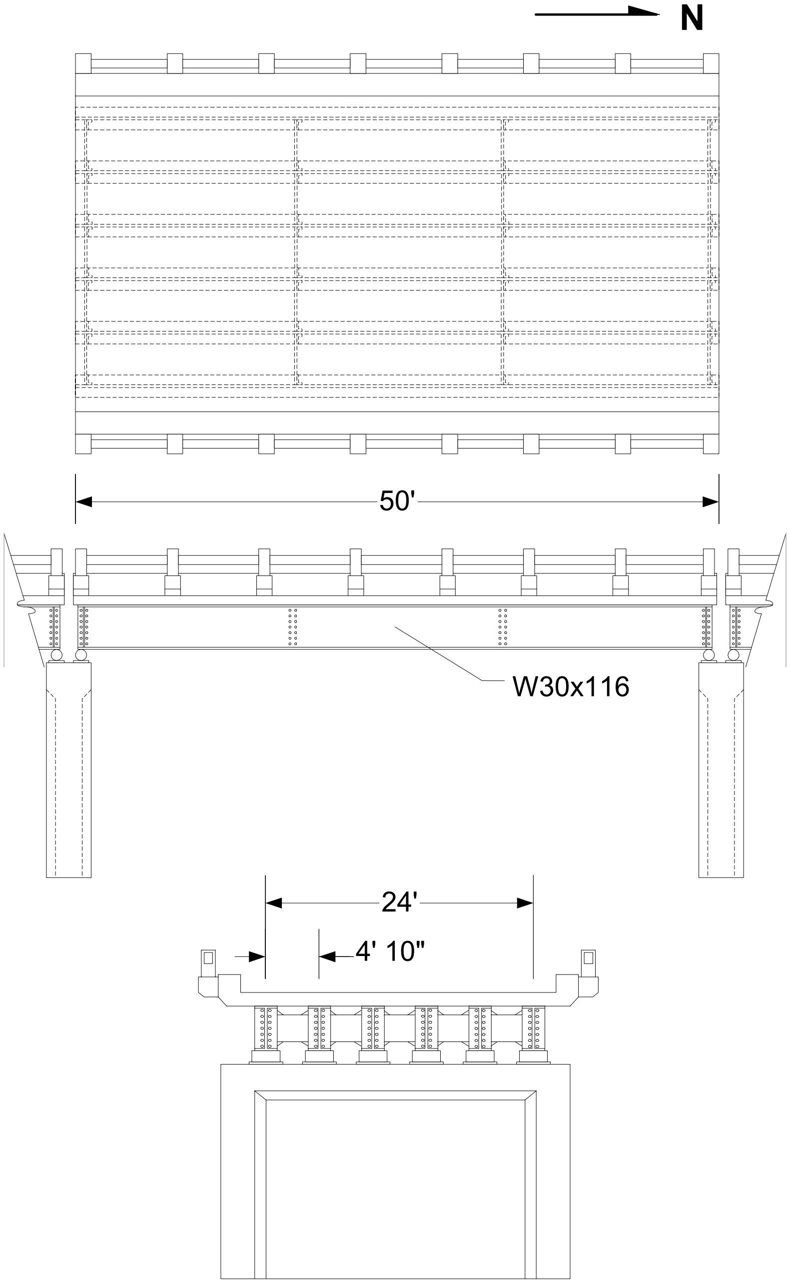

Figure 4-21: Structural details of the third span of the Alamosa Canyon Bridge

Figure 4-22: Southward top view of the Alamosa Canyon Bridge

Figure 4-23: Side view of the third northern span of the Alamosa Canyon Bridge

4.6.2 Sensing Transducers for Field Validation

The MEMS accelerometers previously tested in the laboratory are well suited for applications involving the measurement of high acceleration responses such as those experienced by the laboratory validation structure and those envisioned for structures responding to large seismic disturbances. However, their noise levels are too high for use in low-response structural monitoring applications. For example, the standard deviation of the ADXL210 accelerometer's noise floor when interfaced to the unit's A/D converter is 6.4 mg, while the SMB110 and piezoresistive accelerometers' noise floor are slightly higher at 9.4 mg and 8 mg respectively. The response of the Alamosa Canyon Bridge will fall within the noise floor of the accelerometers. As a result, different accelerometers are considered for instrumentation upon the Alamosa Canyon Bridge.

To measure the dynamic response of the bridge to a broad set of ambient and forced vibrations, two different accelerometers will be installed. The first set of accelerometers, the Piezotronics PCB336C, is used exclusively with a wire-based data acquisition system. The PCB336 is not a MEMS sensor and is part of the piezoelectric accelerometer family. The PCB336 is capable of recording vibrations within a 1 to 2000 Hz dynamic range. With a sensitivity of 1 V/g, the amplitude range of the accelerometer is ± 4 g with a noise floor of 60 μg.

Interfaced to the wireless sensing units are Crossbow CXL01LF1 accelerometers. These accelerometers are MEMS-based accelerometers internally using capacitive-based transduction systems similar in design to the Bosch SMB110 and Analog Devices ADXL210 accelerometers. The CXL01LF1 is selected because of its high 2 V/g sensitivity and its low 0.5 mg noise floor. When compared to the lowest noise accelerometer previously considered, the Analog Devices ADXL210 (4.33 mg), the noise floor of the CXL01LF1 represents a 90% reduction. The amplitude range of the accelerometer is ± 1 g with a bandwidth of 50 Hz. The accelerometer is internally anti-aliased with a low-pass filter. Table 4-4 summarizes the performance attributes of the two accelerometers selected for installation in the Alamosa Canyon Bridge.

Table 4-4: Specifications of the Alamosa Canyon Bridge accelerometers

Sensor Property	Crossbow CXL01LF1	Piezotronics PCB336
Measurement Range	0 ± 1 g	0 ± 4 g
Sensitivity	2 V/g	1 V/g
Bandwidth	50 Hz	2000 Hz
RMS Resolution	0.5 mg	60 μg
Offset at 0g	2.5 V	-
Anti-aliased Output	Yes	No

4.6.3 Alamosa Canyon Bridge Validation Test Setup

The experimental test of the Alamosa Canyon Bridge is performed over three consecutive days. At the beginning of each day, two data acquisition systems are installed upon the selected span of the Alamosa Canyon Bridge. The first system is comprised of the proposed wireless sensing units while the second system is a classical wire-based system. The two systems are installed in parallel to allow for a direct comparison of the prototype wireless sensing unit’s performance to that of a commercially available wire-based data acquisition system.

The commercially available data acquisition system selected is the Dactron SpectraBook dynamic signal analyzer. Collaborators from Los Alamos National Laboratory installed the system in the Alamosa Canyon Bridge for this study. The SpectraBook accommodates 8 simultaneous input channels with sampling rates as high as 21 kHz. The internal sensing interface of the Dactron system employs a 24-bit analog-to-digital converter providing a range of 120 dB. Accelerometers mounted upon the structure are interfaced directly to the data acquisition system through one of the channels of the SpectraBook. A Windows-based laptop with RT Pro Signal Analysis software installed is interfaced to the SpectraBook in order to control the system and to obtain data. Once data is obtained, modal analysis tools provided by RT Pro can be used for modal identification of the test structure.

A wireless modular monitoring system is installed on the Alamosa Canyon Bridge. Multiple prototype wireless sensing units are installed within the structure with accelerometers directly interfaced. The wireless communication channel of the wireless sensing units is used to transfer data from the sensing units to a centralized data server. A Linux-based laptop running a custom designed data acquisition system is employed for controlling the wireless sensing units and to transfer data from the units to the laptop.

The first accelerometer, the Piezotronics PCB336C, is used exclusively with the wire-based Dactron system. The sensors are attached to a magnetic mounting block that is then mounted by magnetic force to the steel girder's web. Interfaced to the wireless sensing units are Crossbow CXL01LF1 accelerometers. The Crossbow accelerometers are mounted to 2 in. by 3 in. mounting plates that are machined from a 0.25 in. thick aluminum bar. The aluminum mounting plates are permanently attached to the structure using high strength, fast-setting epoxy glue.

Locations for mounting the accelerometers to the span's steel girders are determined. The locations are distributed throughout the structure to provide good spatial separation for identification of the lower modes of response of the structure. To make identification of the sensor locations easy, the girders of the span are numbered 1 through 6. In total, seven locations are selected with each location denoted by a unique location number such as S1, S2, etc. Except for location S4, all accelerometers are mounted at the midpoint of the girder's web. The accelerometers installed at location S4 are situated 4 in. above the bottom flange surface of the girder. Figure 4-24 documents the location of the seven accelerometers installed. Figure 4-25 is a picture of the accelerometers mounted at sensor location 6. At the center of the girder's web are the accelerometers with the PCB336 installed on the left and the CXL01LF1 on the right. A 30 ft. long wire is used to connect the PCB336 to Dactron SpectraBook. The CXL01LF1 is interfaced to the wireless sensing unit that is sitting upon the girder flange.

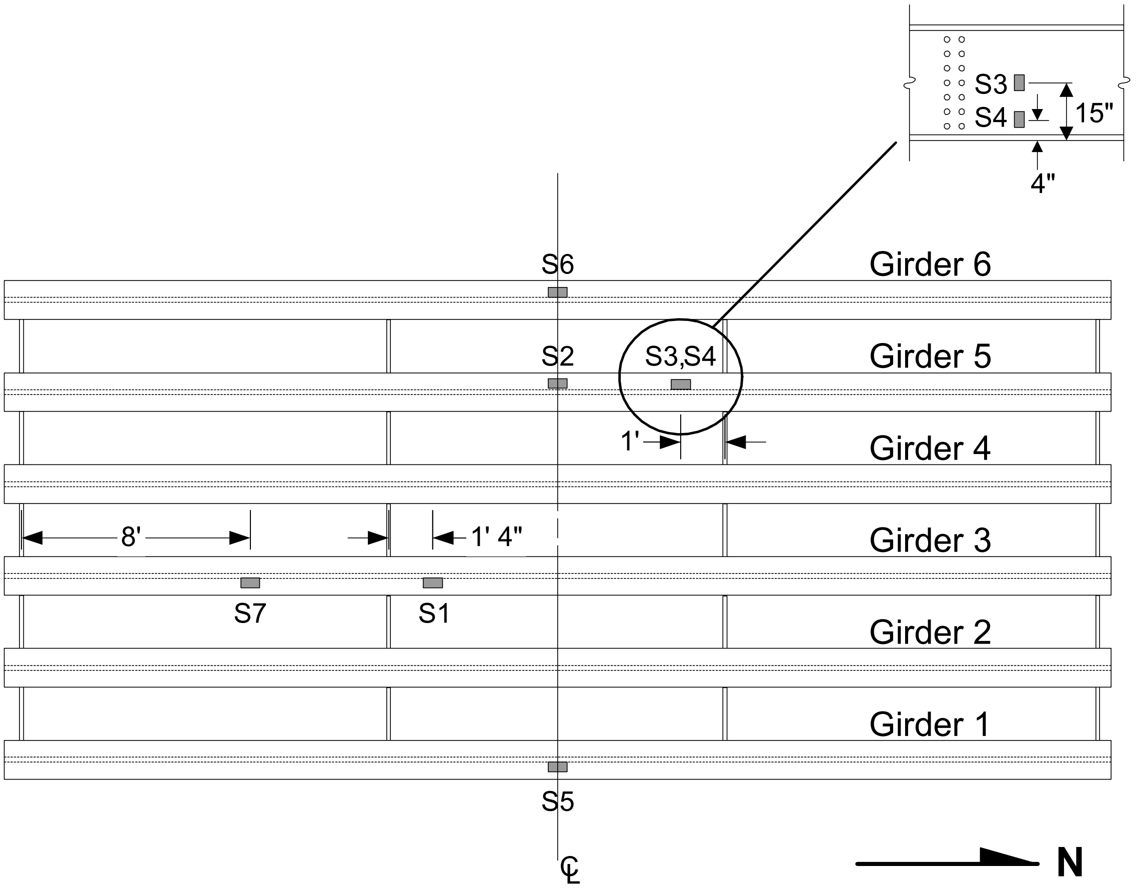

Figure 4-24: Top view of accelerometer installation locations

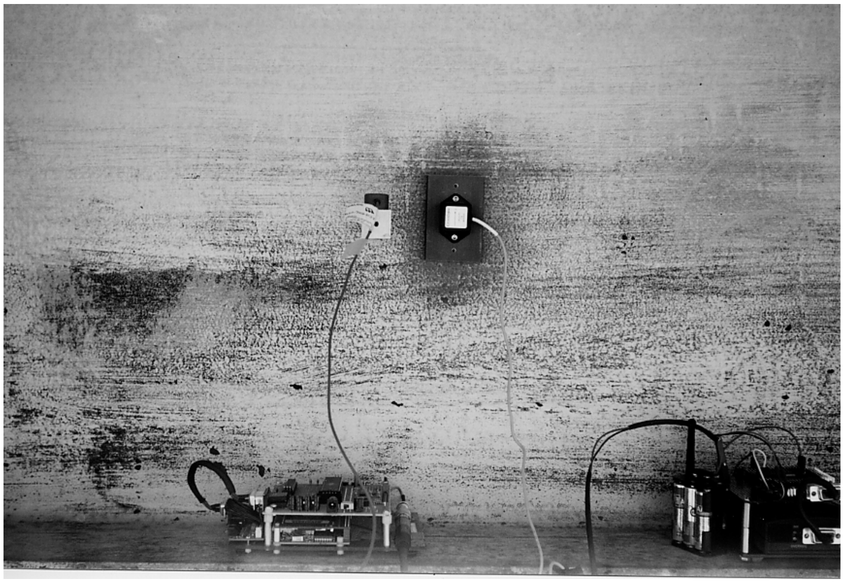

Figure 4-25: PCB336 (left) and CXL01LF1 (right) accelerometers at S6

4.6.4 Forced Vibration Tests

To produce a sizable vibration response of the selected span of the Alamosa Canyon Bridge, two excitation inputs are considered. The first excitation source selected is an impact blow to the span from a modal hammer. As a second excitation source, a large four wheel truck is used to drive over a wood stud strategically placed in the center of the span. Both excitation levels yield reasonably high structural responses that are measured and logged. These recorded time-histories yield frequency response functions that are used to identify the primary modes of response of the bridge span.

4.6.4.1 Modal Hammer Impact Test

A nearly perfect low level impulse force can be exerted to a structure through the use of a modal hammer. The visual appearances of a modal hammer are similar to that of a large sledge hammer. The head of the modal hammer can be customized to deliver impacts of various magnitudes and frequency ranges. The tip of the hammer head is instrumented with a load cell to directly measure the force imparted to the structure.

Figure 4-26: Modal hammer used to deliver an impact force to the bridge deck

For the Alamos Canyon Bridge, a 12 lb. Piezotronics PCB86C50 modal hammer is selected. A soft head tip is attached to the modal hammer to provide a long time duration response and to concentrate imparted energy within the lower modes of response of the structure. For the modal hammer tests, the point of impact is at the midpoint of the selected bridge span in both the length and width directions. As shown in Figure 4-26, the blow from the modal hammer is directed perpendicular to the bridge deck.

The modal hammer is used to deliver a hard blow to the center of the deck of the third bridge span. The blow delivered by the hammer represents an impact force as documented by Figure 4-27. Considering the response of the bridge span over 4.5 seconds, the impact force is delivered at approximately 1 second. A valuable quality of the modal hammer's impact force is that in the frequency domain, it has a nearly constant magnitude over a broad spectrum greater than 0.75 Hz as shown in Figure 4-28. This is in agreement with a perfect impulse force whose frequency response function would be of a constant magnitude over the complete frequency range. The constant magnitude feature of the modal hammer impact force implies that the frequency response functions of the acceleration time readings will be nearly identical to the magnitude plot of the bridge transfer function relating the hammer force at the point of impact with the response experienced at the location of the sensor. One shortcoming of the modal impact test is the inability to perfectly repeat each impact excitation.

The time-history response of the structure is recorded from accelerometers mounted at sensor location S3. The time-history response obtained from the wire-based Dactron system sampling the PCB336 accelerometer at 320 Hz is presented in Figure 4-29. Similarly, the response of the bridge is recorded by a wireless sensing unit situated at sensor location S3. Sampling the recorded data at 976 Hz, the data is temporarily stored for 5 seconds in random access memory and then wirelessly transmitted for permanent storage on a Linux-based laptop. Figure 4-30 documents the response measured by the wireless sensing unit.

To consider the performance of the two data acquisition systems, a 1.7 second period of the structural response is magnified for examination. Figure 4-31 and Figure 4-32 are graphs of the magnified response for the Dactron system and the wireless modular monitoring system (WiMMS) respectively.

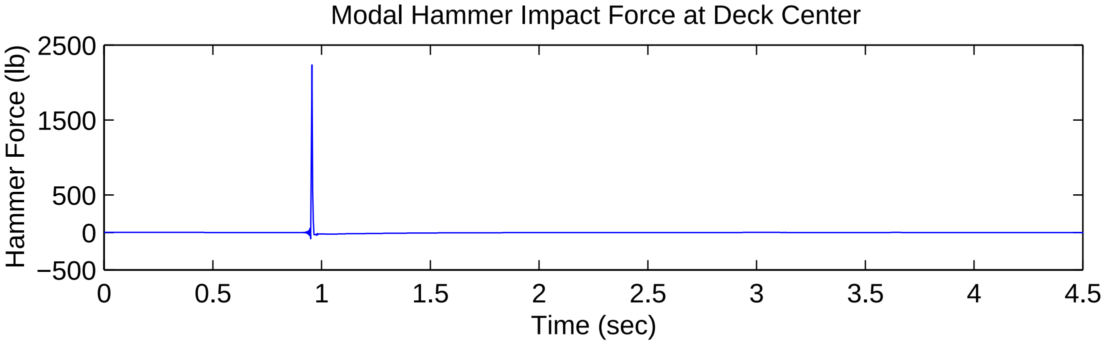

Figure 4-27: Time-history measurement of the modal hammer impact force

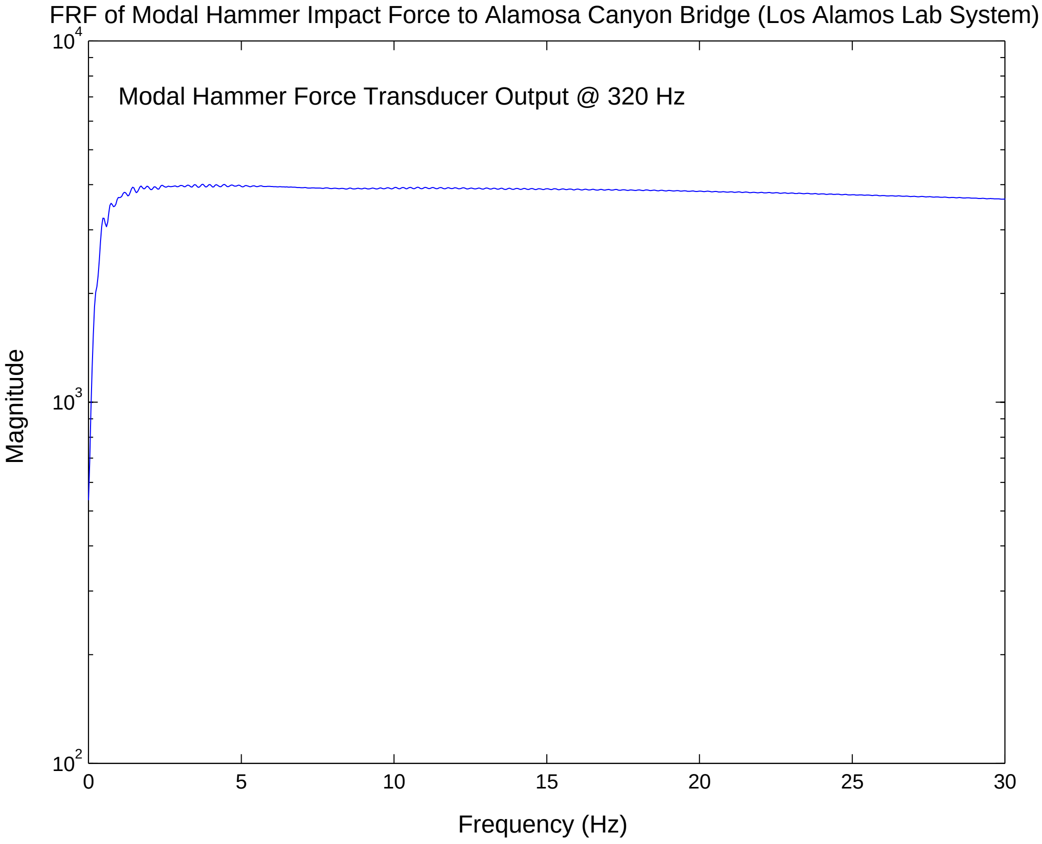

Figure 4-28: FRF of the modal hammer impact force

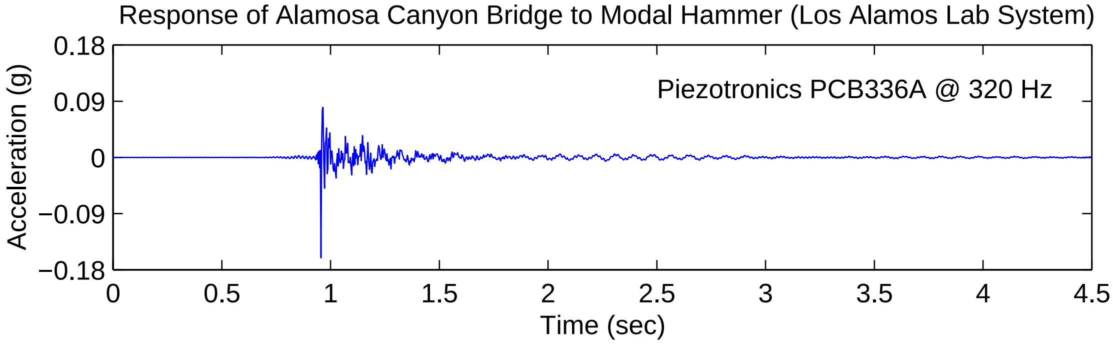

Figure 4-29: Response at S3 to a modal hammer impact force (Dactron)

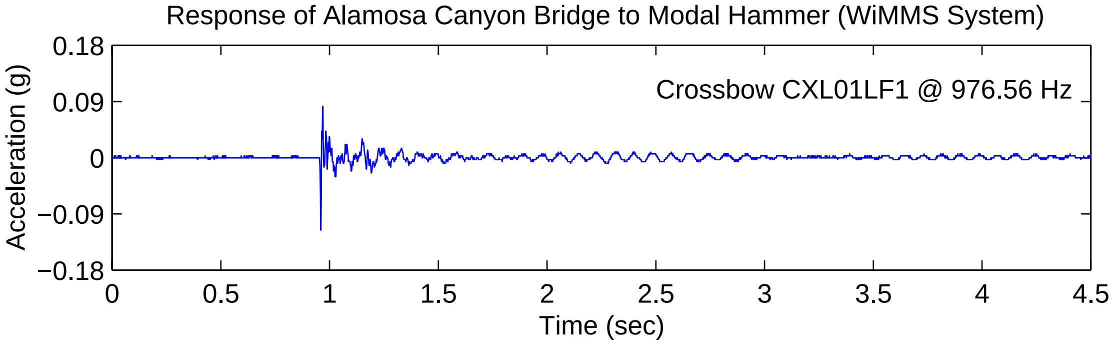

Figure 4-30: Response at S3 to a modal hammer impact force (WiMMS)

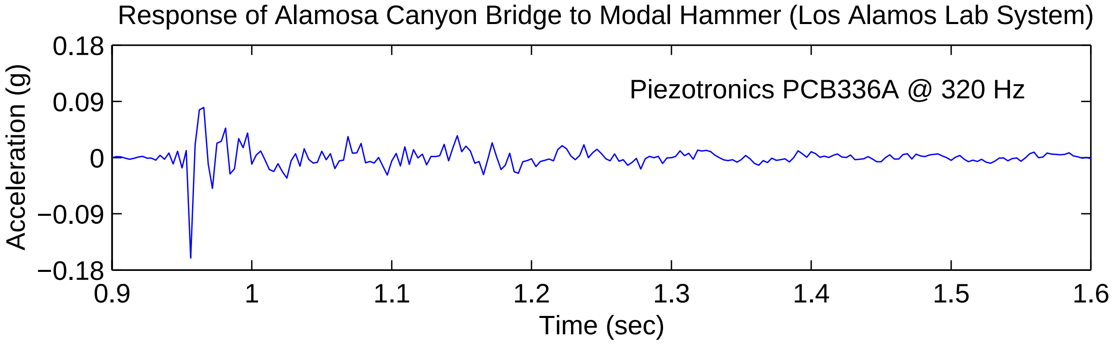

Figure 4-31: Magnified response at S3 to modal hammer impact (Dactron)

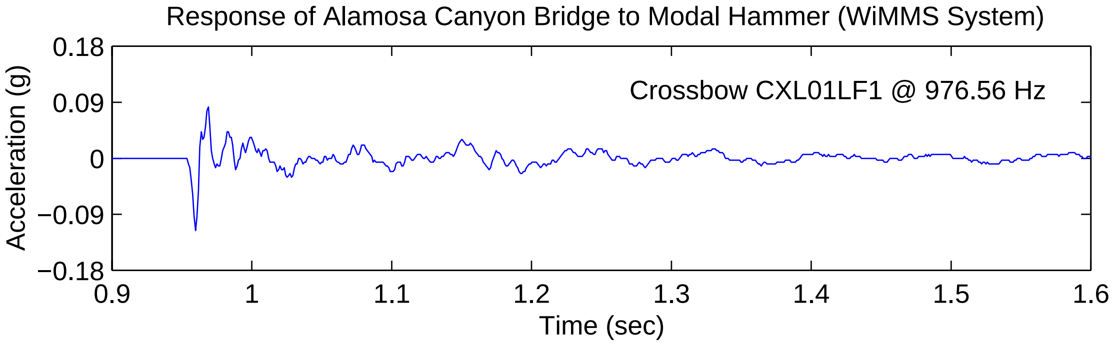

Figure 4-32: Magnified response at S3 to modal hammer impact (WiMMS)

In comparing the recorded time-history response of the system to the same modal hammer impact force, strong agreement exists in both amplitude and frequency between the two different data acquisition systems. Minor discrepancies exist between the initial peak acceleration responses measured by the two systems. The Dactron system indicates that the peak response is roughly 0.17 g while the WiMMS data acquisition system measures it closer to 0.12 g. This minor discrepancy can be due to the response nearing the maximum measurable acceleration of the CXL01LF1 accelerometer where sensor nonlinearities are more prevalent. However, the amplitudes of the acceleration peaks of the system's free response after the impact are in complete agreement. Furthermore, the alignment of acceleration peaks along the time axis match. In considering the time-history response of the system to the modal hammer impact force, it can be concluded that the performance of the wireless sensing unit is reliable and accurate when compared to a conventional wire-based data acquisition system.

Having obtained two time-history records of the same structural response at sensor location S3, frequency response functions are obtained from the recorded data. The frequency response functions are useful in identifying the primary modes of response of the structural system. Figure 4-33 depicts the 0-30 Hz region of the 8192 point frequency response function (FRF) derived from data recorded by the Dactron system. Figure 4-34 is the 4096 point FRF calculated from data obtained by the wireless sensing unit. Only 5000 data points could be stored on the unit at one time limiting the size of the FRF.

In comparing the two frequency response functions, strong agreement exists, particularly in the shape and location of the peaks and valleys of the functions. The FRF derived from the Dactron system data is smoother compared to the one derived from the WiMMS measured data. This can be attributed to two observations. First, over the 0-30 Hz frequency region, the density of points used to define the frequency response functions is six times greater for the Dactron measured data. Second, the lower 11-bit resolution of the wireless sensing unit introduces quantization noise that is not introduced by the 24-bit Dactron data acquisition system. To improve the quality of the frequency response function obtained from the prototype wireless sensing unit, two improvements can be made: more memory should be integrated to the unit to provide ample space for longer recorded time-histories and the A/D resolution should be improved to at least 16-bits to limit the effects of quantization.

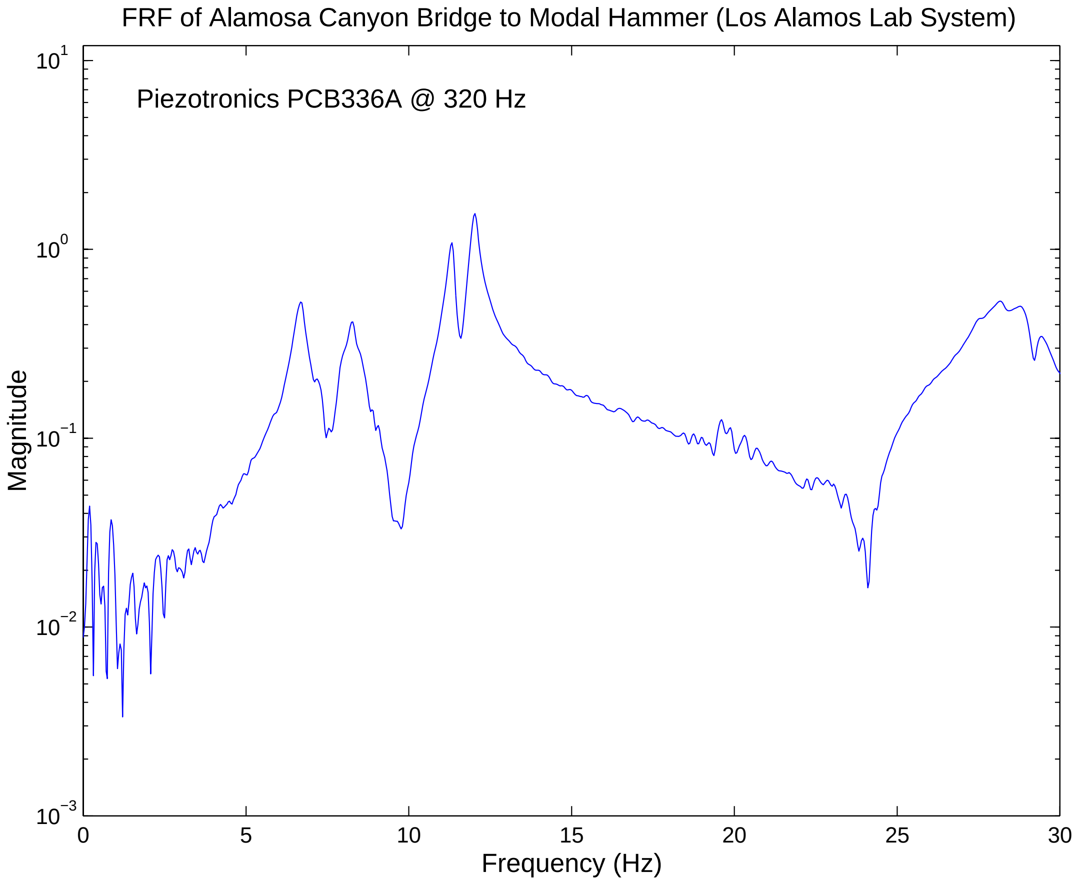

Figure 4-33: FRF of acceleration response to modal hammer at S3 (Dactron)

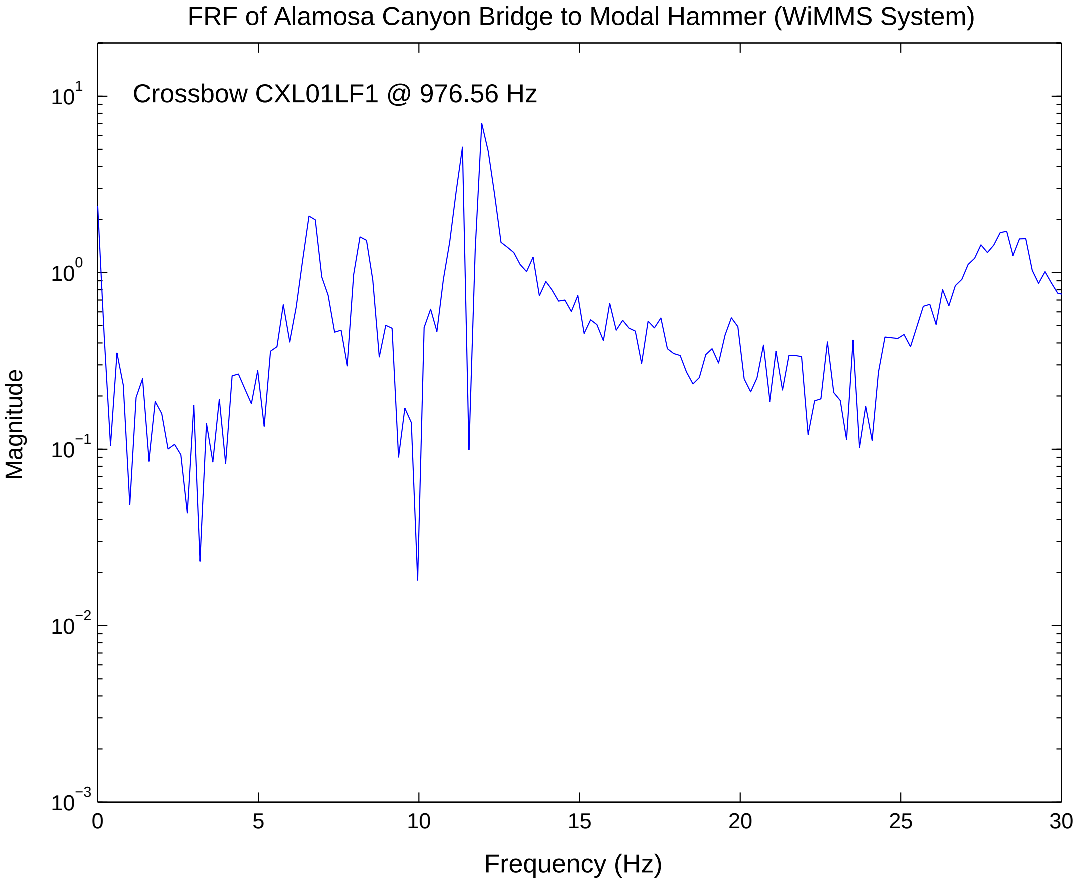

Figure 4-34: FRF of acceleration response to modal hammer at S3 (WiMMS)

The first two modes of response of the structure are easily identified by the first two peaks of the frequency response function at roughly 6.7 and 8.2 Hz. This is in good agreement with modal properties of the northern-most span of the Alamosa Canyon Bridge previously tested by Farrar, et al. (1997) where the fist two modes of response were identified at 7.38 and 8.04 Hz. The next two peaks of the frequency response function could potentially represent the third and fourth modes of response at 11.4 and 12 Hz. Farrar, et al. (1997) has documented the third mode to be at 11.48 Hz which is consistent with what is observed in our frequency response function, but the fourth mode of the first span was determined to be at 19.55 Hz which is further away from our identified fourth mode. Even though the two spans selected for the two independent studies are geometrically similar, they have distinctly different boundary conditions that make direct comparison between the two sets of modal properties difficult. Hence, the large discrepancy that exists in the location of the fourth mode of response can be a possible manifestation of the two different boundary conditions.

4.6.4.2 Dynamic Traffic Test

The second set of forced vibration tests to be performed is the response of the Alamosa Canyon Bridge to a large dynamic truck loading. To provoke a greater response from the third span of interest, a wood studding post is laid down in the center of the span as shown in Figure 4-35. When the truck transverses the bridge at approximately 40 miles per hour, the force exerted by the truck as it drives over the wood stud will be significantly greater than the load imparted by the modal hammer.

Figure 4-35: Forced vibration test of a speeding truck driving over a wood stud

For the dynamic truck loading test, the accelerometers mounted at sensor location S7 are employed. The acceleration response of the Alamosa Canyon Bridge at this sensor location is recorded by both the Dactron and WiMMS data acquisition systems. Figure 4-36 and Figure 4-37 presents the acceleration response of the structure over a 10 seconds interval due to the passing truck as monitored by the Dactron and WiMMS systems respectively. Similar to the modal hammer test, the wireless sensing unit is configured to first locally store the data and to then transmit the data upon demand after the completion of the test. Different from the modal hammer test, the wireless sensing unit is configured to sample at 244 Hz.

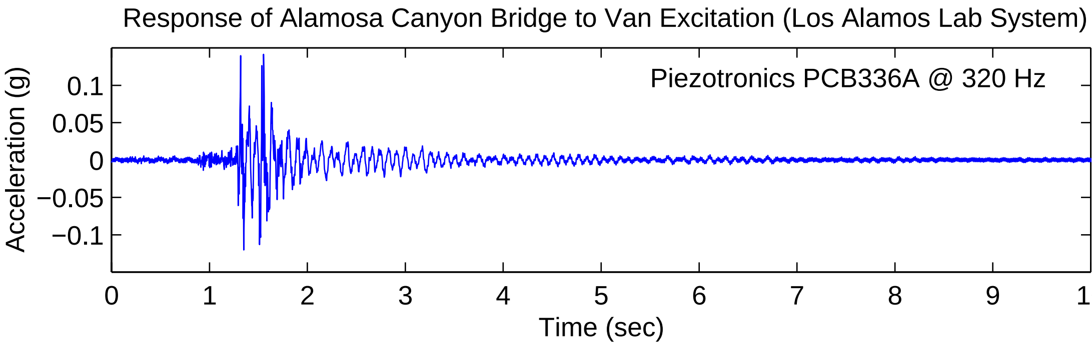

Figure 4-36: Response at S7 to a speeding truck (Dactron)

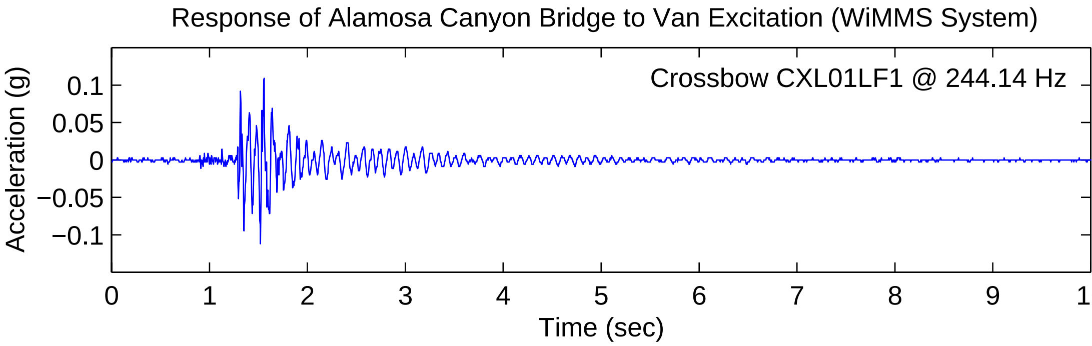

Figure 4-37: Response at S7 to a speeding truck (WiMMS)

To provide a clearer picture of the measured response for comparison analysis, a 2 seconds interval capturing the truck loading is magnified for both the Dactron and WiMMS acquired time-history data. Figure 4-38 and Figure 4-39 plot the 2 seconds magnified portion of the time-history response measured by the Dactron and WiMMS data acquisition systems.

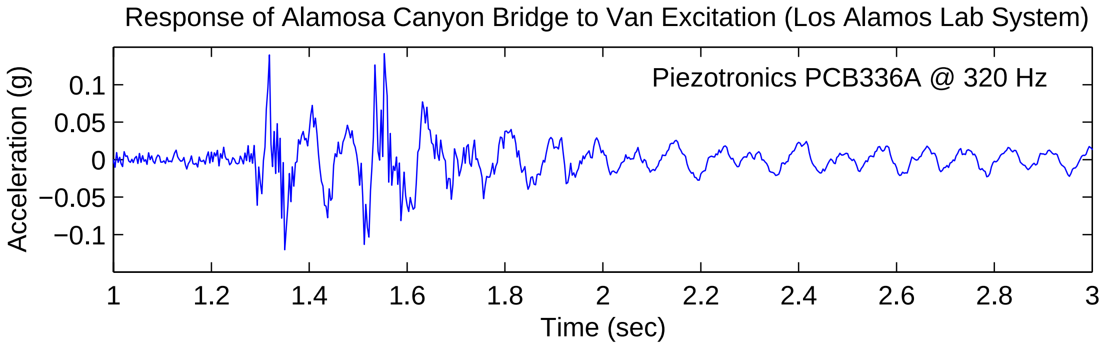

Figure 4-38: Magnified response at S7 to speeding truck (Dactron)

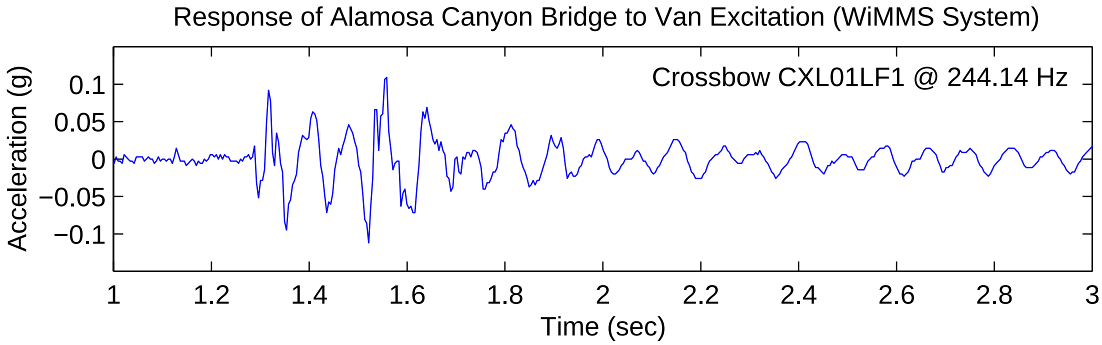

Figure 4-39: Magnified response at S7 to speeding truck (WiMMS)

In comparing the two recorded responses, the amplitude of the acceleration peaks from the wireless sensing unit recorded data is slightly lower than those obtained using the Dactron system. In the case of the speeding truck load, the subtle differences in the acceleration peaks can be attributed to the slower sampling rate of the wireless sensing unit with peaks potentially occurring between sampling points. It is obvious that the signal recorded by the wireless data unit has the appearance of less noise as denoted by the smoother appearance of the time-history response data of Figure 4-39.

The recorded time-histories are converted to the frequency domain using a fast Fourier transform deriving the frequency response function of the bridge span. The load transmitted to the structure from the speeding truck is not monitored as was conveniently done with the modal hammer. Hence, the truck's dynamics will be manifested within the frequency response functions derived. This makes identification of the structure's modes of response a harder task when visually inspecting the frequency response functions.

Using the data derived from the response of the bridge to the speeding truck, the frequency response function is determined from both recorded data sets. Presented in Figure 4-40 is the 8192 point FRF derived from the Dactron system while Figure 4-41 presents the 4096 point FRF determined from the WiMMS measured response data. Good agreement exists in the two frequency response functions indicating the accuracy and reliability of the prototype wireless sensing unit design. The improvement in smoothness of the FRF obtained from the wireless sensing unit data from the modal hammer test to the dynamic truck test is attributed to a greater density of points defining the FRF over the 0-30 Hz frequency band. However, quantization noises can still be viewed in the wireless sensing unit's FRF when compared to the FRF derived from the Dactron system.

The functions are well defined making identification of the first two modes of response at 6.75 and 8.1 Hz easy. These two modes are in agreement with those obtained during the modal hammer test with only minor differences present. The minor difference in the second mode can be attributed to changes in the modal properties of the bridge as a function of temperature. The bridge was almost 10 °F warmer during the van test than when the bridge was tested earlier in the day using the modal hammer. It is difficult looking at the frequency response function of Figure 4-40 and Figure 4-41, to determine if the peak present at 11.3 Hz represents one or two modes. Based on observations made during the modal hammer test, the two peaks are still identified as the third and fourth modes at 11.2 and 11.9 Hz respectively. These two identified modes are slightly different from those obtained during the modal hammer tests.

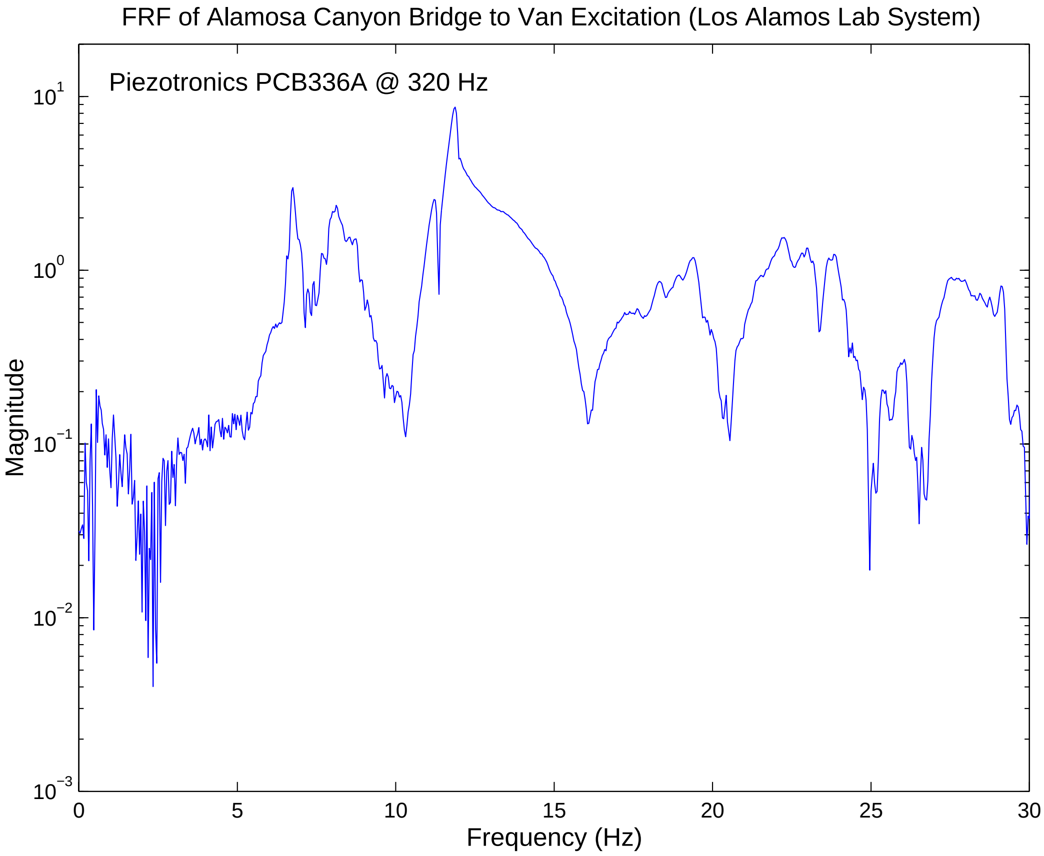

Figure 4-40: FRF of acceleration response to speeding truck at S7 (Dactron)

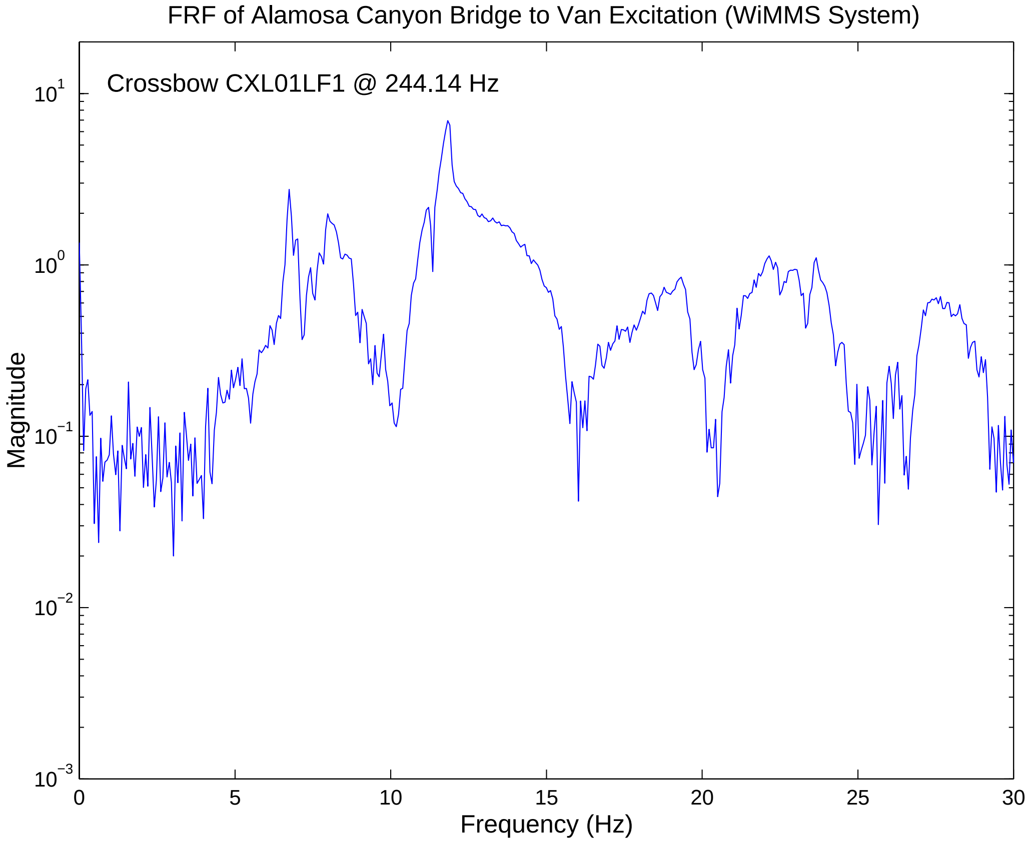

Figure 4-41: FRF of acceleration response to speeding truck at S7 (WiMMS)

4.6.5 Ambient Vibration Monitoring

During the last set of tests, the accelerometers located at sensor location S5 are used to monitor the ambient vibrations induced in the bridge structure from passing traffic on Interstate 25, located only 50 ft. away. Interstate 25 is comprised of two parallel reinforced concrete bridges that carry north and south bound traffic across the Alamosa Canyon. When a large 18 wheels truck passes over one of the Interstate 25 bridges, their loads are transmitted through the site soil and indirectly imparted into the Alamosa Canyon Bridge. To measure these ambient excitations, the wireless sensing unit is used. The wireless sensing unit is configured to locally obtain data and to transmit it in real-time. The Linux-based laptop is responsible for the logging of the data. The ambient response of the Alamosa Canyon Bridge is monitored using the CXL01LF1 accelerometer sampled at 30 Hz. Figure 4-42 represents a 130 seconds time-history record of the ambient response of the bridge due to truck traffic on Interstate 25. A total of 3 trucks are identified during this 130 seconds interval as denoted in the time-history plot of Figure 4-42. The other apparent responses between trucks 2 and 3 could be from passing car traffic.

The ambient time-history data is used to derive the frequency response function of the bridge. Figure 4-43 illustrates the frequency response function of sensor location S5 to the ambient excitations. It is observed that the frequency response function has a significant level of noise not seen in previous frequency response functions. This noise originates from the noise present in the accelerometer, which is only slightly lower that the low acceleration response of the ambient vibrations. However, the first two modes of response of the system are easily identified at 6.7 and 8.98 Hz. The ambient test was performed in the very late morning when the structure is still relatively cool at 90 °F. The low bridge temperature is most likely the cause for the large discrepancy in the second mode with those obtained from the forced vibration tests. The forced vibration tests were performed when the bridge temperature was approximately 120 °F.

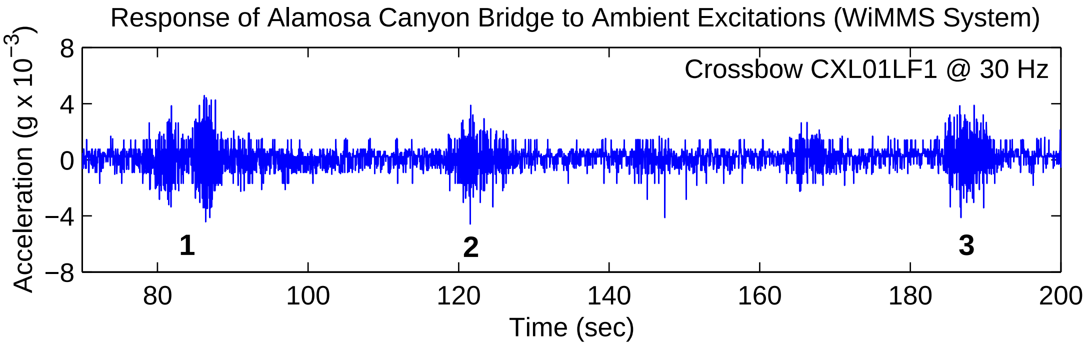

Figure 4-42: Ambient response at S5 due to truck traffic on Interstate 25 (WiMMS)

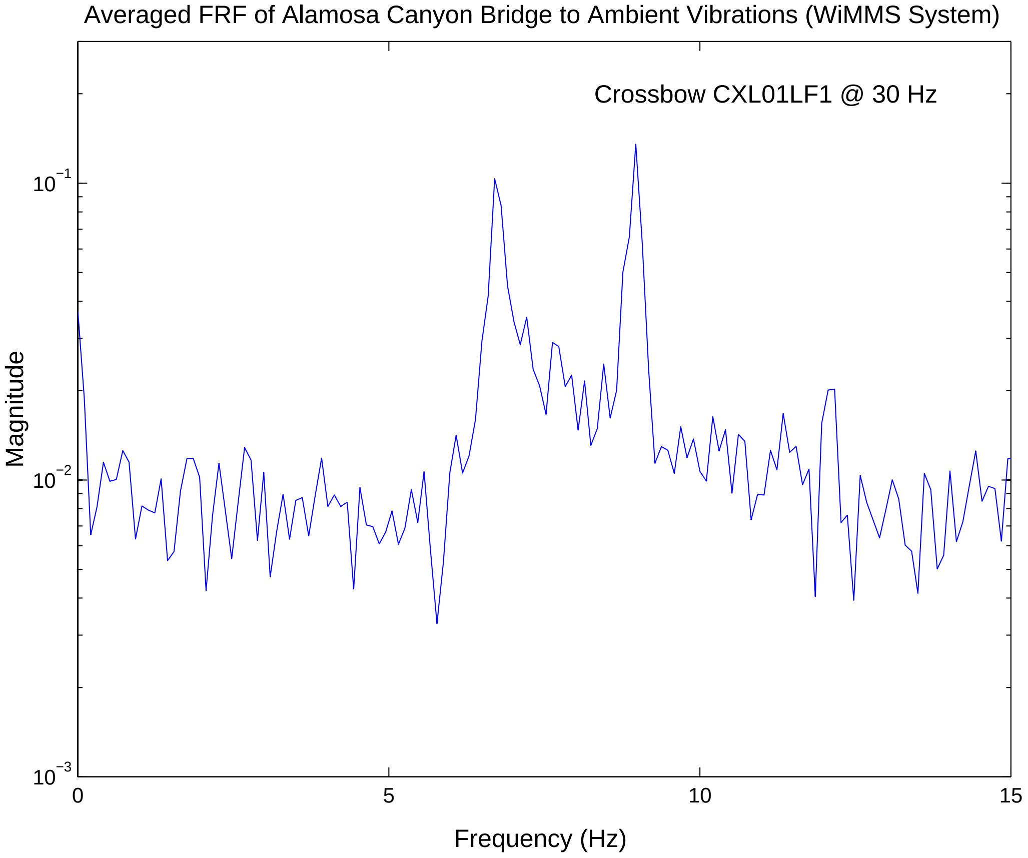

Figure 4-43: FRF of acceleration response at S5 to ambient excitations (WiMMS)

4.7 Summary

The collection of validation tests performed on the prototype wireless sensing unit varied in scope from quantifying the performance of various hardware subsystems to testing the units within a full scale civil structure. In reviewing the validation test results, it can be concluded that the design of the wireless sensing unit has meet all design goals established at the outset of the study.

The validation of the wireless sensing unit in the laboratory began with the interfacing of three MEMS-based accelerometers. Two of the accelerometers are commercially available and are of capacitive architectures. The third accelerometer is a high performance piezoresistive accelerometer experimentally fabricated at Stanford University. All three accelerometers were successful in monitoring the high acceleration response of a laboratory test structure. The noise floors of the three accelerometers were sufficiently small to permit the accurate calculation of frequency response functions for the identification of the test structure's modes of response. To illustrate the computational power of the wireless sensing unit, the time-history data obtained from the test structure was used to find the frequency response function by calculating a fast Fourier transform local to the unit. To illustrate one component of the proposed structural health monitoring approach, the time-history data of the test structure is used to fit an auto-regressive time-series model.

Next, the wireless sensing unit is taken to the field for validation upon a full-scale bridge structure. After installing and uninstalling the system three times, significant time savings associated with using a wireless monitoring system is evident. In the absence of wires, the installation of the wireless monitoring system entails the placement of wireless sensing units on girder flanges adjacent to mounted accelerometers. Conversely, the wire-based Dactron system requires the temporary installation of wires connecting the installed accelerometers to the SpectraBook channel box. The taping of wires to girders to ensure they do not get stepped on required a significant portion of the installation time. While not precisely timed, the time savings gained in using the wireless monitoring system is estimated to be roughly two thirds of the time required to install the conventional wire-based system.

The performance of the wireless modular monitoring system installed in the Alamosa Canyon Bridge was accurate and reliable when compared against a commercially available wire-based data acquisition system. The value of field validation was underscored by two important observations made regarding the limitations of the current prototype design. First, the need for a larger allocation of memory on the sensing unit was made obvious. More memory would provide flexibility in size of the frequency response functions calculated. Second, improvements need to be made in the resolution of the A/D converter. The 11-bit resolution injected quantization noise in the calculated frequency response functions. A 16-bit A/D resolution is the minimum acceptable resolution for low acceleration measurements as observed during validation on the Alamosa Canyon Bridge, especially when the structure was excited by modal hammer impacts.

As the design of the wireless sensing unit progresses further towards field implementation, additional field testing should be performed. In particular, the scalability of the wireless modular monitoring system paradigm needs to be addressed. The Alamosa Canyon Bridge entailed only seven sensor locations with all units within radio contact to each other. One question to be addressed is how the wireless sensing units perform in high density deployment applications where hundreds of sensing units are installed in the same structure with spatial separations that result in units only in radio contact with a portion of the sensor network. Some additional issues to be considered in the future include structural tests that assess the appropriate amount of information to be transmitted on the limited wireless bandwidth before a situation of data inundation results.

Chapter 5

Decentralized Structural Control

Current structural control systems are designed using approaches that are characterized by their centrality. A single centralized controller bears the responsibility of coordinating in real-time the reading of measurements from all system sensors and determining the magnitude of control forces to be applied by system actuators. In the majority of applications, the controller is designed as a linear quadratic regulator (LQR) representing an optimal control solution. While success has been enjoyed by the centralized LQR approach in systems with sensors and actuators numbering less than a dozen, it does not represent a scalable control solution.

As the state of structural control technology evolves towards smaller, more power efficient and less expensive control devices, future structural control systems are likely to be deployed with large numbers of control devices and sensors. The result is a large-scale control problem characterized by high sensor and actuation densities. Such systems are better suited for decentralized control. Decentralized control techniques decompose the global system to a set of local sub-systems for which local controllers are designed.

This chapter serves as an introduction to two decentralized control approaches. In order to better understand the decentralized control architectures, the classical LQR control approach is presented first. Next, the centralized LQR control approach is modified to accommodate decentralized system architectures, which produce suboptimal control solutions. The chapter concludes with an investigation of a decentralized approach that yields an optimal control solution for specific constrained decentralized system architectures. A 20-story analytical structure employing semi-active control devices is used as the benchmark structure for comparing the performance and power consumption characteristics of the various control techniques considered.

5.1 Centralized Linear Quadratic Regulation Control

In designing a linear control system, the most effective and widely used approach is the centralized linear quadratic regulator (LQR). The LQR approach derives an optimal control solution, meaning, the control results are the best attainable for the amount of control effort exerted. Let us first consider a linear time invariant structural system whose equation of motion is posed in state space form.

$$\dot{\boldsymbol{X}}(t) = \boldsymbol{A}\boldsymbol{X}(t) + \boldsymbol{B}\boldsymbol{U}(t) + \boldsymbol{D}\boldsymbol{W}(t) \tag{5.1}$$

The state of the system, ***X(t)***, contains the displacement and velocity response terms of the system. Since displacement and velocity sensing transducers are not installed at each degree-of-freedom of the system, the full state is often calculated using estimation algorithms that use measurements derived from system accelerometers as inputs (Soong 1990). The system is externally loaded by a dynamic disturbance, ***W(t),*** and controlled by control forces, ***U(t)***. The matrix ***A*** represents the system matrix and encapsulates the open-loop dynamic properties of the system. The matrices, ***B*** and ***D,*** represent the locations of the system actuators and external loads, respectively.

The dynamic response of the structural system is defined by the system matrix, ***A***. The eigenvalues of the system matrix characterize the uncontrolled dynamic response of the system. When plotted on the complex plane, these eigenvalues, often termed poles of the system, will all fall in the left half side of the plane if the dynamic system is stable. The right half side of the complex plane represents instability, such that if any system pole is located there, the entire system is dynamically unstable. Graphically, the natural frequency and damping coefficients of each mode of the system can be determined from the location of the poles in the complex plane. The absolute distance from the origin to the pole is the natural frequency of that pole's mode while the sine of the angle between the pole and the positive imaginary axis is the damping ratio of the mode. Figure 5-1 depicts the graphical relationship that exists between a system pole and its corresponding modal frequency and damping ratio.

The introduction of control forces to the system is an opportunity to improve the system response when subjected to external disturbances. As the end result of controls, the poles of the system are moved to more desirable locations on the complex plane. While many pole placement techniques exist, LQR has emerged as a reliable systematic guide to pole placement that allows for the weighting of control response against control effort (Stengel 1994).

The LQR method provides an optimal control solution through the minimization of a cost function that encapsulates the system's control objectives. The cost function, *J*, contains two control objectives; the minimization of structural response, ***Y(t)***, and the minimization of the input control forces, ***U(t)***, required to attain those responses.

$$J = \int_0^\infty \left(\boldsymbol{Y}^T \boldsymbol{Y} + \boldsymbol{U}^T \boldsymbol{R} \boldsymbol{U} \right) dt \tag{5.2}$$

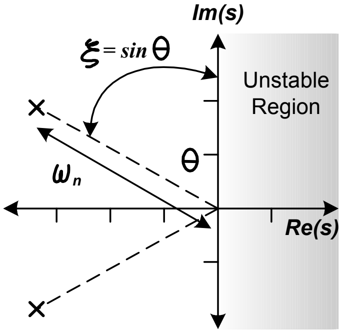

Figure 5-1: Relationship between system poles and corresponding modal properties

A weighting matrix, ***R***, is included in the cost function to vary the proportional emphasis on the control force vector relative to the system response. The regulated response vector, ***Y(t)***, can be representative of any structural response as long as it can be written as a linear function of the system state, ***X(t)***, with ***C*** representing a transformation from the full system state.

$$\boldsymbol{Y}(t) = \boldsymbol{C}\boldsymbol{X}(t) \tag{5.3}$$

Therefore, we are afforded more flexibility in choosing the desired structural response to be controlled. For example, inter-story drifts can now be a control objective rather than trying to indirectly control drifts by controlling absolute structural displacements. As a result, the cost function can be written in terms of the state vector where $\boldsymbol{Q}=\boldsymbol{C}^T\boldsymbol{C}$.

$$J = \int_0^\infty \left(\boldsymbol{X}^T\boldsymbol{Q}\boldsymbol{X} + \boldsymbol{U}^T\boldsymbol{R}\boldsymbol{U}\right)dt \tag{5.4}$$

To ensure that a minimum of the cost function can be found, the weighting matrices, ***Q*** and ***R***, must both be positive definite. The positive definite criterion guarantees that the surface of the cost function is upward convex. Furthermore, the quadratic form of the cost function is necessary to avoid the minimum point existing as a cusp and thus unobtainable.

The minimum of the cost function is found by adjoining the cost function, *J*, and the constraining equation of motion of the system with a time dependent Lagrangian multiplier, *λ(t)*.

$$J = \int_0^\infty \left(\boldsymbol{X}^T\boldsymbol{Q}\boldsymbol{X} + \boldsymbol{U}^T\boldsymbol{R}\boldsymbol{U} + \lambda^T\left\{\dot{\boldsymbol{X}} - \boldsymbol{A}\boldsymbol{X} - \boldsymbol{B}\boldsymbol{U} - \boldsymbol{D}\boldsymbol{W}\right\}\right)dt \tag{5.5}$$

The result of the minimization of the cost function is a static gain matrix, ***K***, that when multiplied by the full state of the system, ***X(t)***, yields the optimal control force vector.

$$\boldsymbol{U}(t) = -\boldsymbol{R}^{-1}\boldsymbol{B}^{T}\boldsymbol{P}\boldsymbol{X}(t) = -\boldsymbol{K}\boldsymbol{X}(t) \tag{5.6}$$

The Ricatti matrix, ***P***, represents the solution of the algebraic Ricatti equation, shown in Equation (5.7), which results in the minimization procedure.

$$\boldsymbol{P}\boldsymbol{A} + \boldsymbol{A}^{T}\boldsymbol{P} + \boldsymbol{Q} - \boldsymbol{P}\boldsymbol{B}\boldsymbol{R}^{-1}\boldsymbol{B}^{T}\boldsymbol{P} = 0 \tag{5.7}$$

Substituting Equation (5.6) into Equation (5.1), a revised state equation of the system can now be expressed as:

$$\dot{\boldsymbol{X}}(t) = (\boldsymbol{A} - \boldsymbol{B}\boldsymbol{K})\boldsymbol{X}(t) + \boldsymbol{D}\boldsymbol{W}(t) \tag{5.8}$$

The new pole locations of the closed-loop system are the eigenvalues of the modified system matrix, $\overline{\boldsymbol{A}} = (\boldsymbol{A} - \boldsymbol{B}\boldsymbol{K})$.

Key to understanding the location of the closed-loop poles is the understanding of the influence of the individual terms of the LQR cost function. The route the migrating poles take from their initial uncontrolled position to their final LQR closed-loop locations is dependent upon the variable, ***Y(t)***, chosen to be regulated (Stengel 1994). If ***Y(t)*** is equal to the vector of displacements of the system nodes, the poles will migrate in a manner consistent to increased system stiffness. Increased system stiffness is synonymous with poles migrating outward as shown in Figure 5-2a. On the other hand, if the regulated response is system velocities, the resulting control solution will cause poles to migrate with increased system damping. Poles rotation about the origin towards the negative real axis is consistent with increased system damping, as shown in Figure 5-2b. A combination of displacement and velocity in the regulation variable would result in a pole migration pattern that would be influenced by both increased system stiffness and damping. How far the final poles result on these generalized trajectory paths is dependent upon the weighting matrix, ***R***. If ***R*** is near infinity, the poles will not move because control effort is expensive relative to the system response. As ***R*** decreases towards zero, control becomes inexpensive and poles result in positions far from their open-loop positions.

While LQR represents an excellent mechanism for the design of centralized control systems, some limitations of the LQR controller exist. In particular, the optimality of the LQR solution is dependent upon the assumption of a linear time invariant system model. For structures excited by large seismic events, the assumption of system linearity is often invalid. While beyond the scope of this study, numerous nonlinear control approaches can be taken such as feedback linearization, gain scheduling, and sliding mode control, just to name a few (Sastry 1999). Another inherent weakness of the LQR method is its heavy dependence upon the assumption of perfect knowledge of the system. If the model used in the design of the controller is incorrect, the LQR solution is no longer optimal and could potentially be destabilizing. The performance of the LQR controller is dependent upon system parameter uncertainties which can be significant for civil structures. The field of robust structural control can be consulted for control techniques offering superior control performance in light of plant uncertainties (Housner et al. 1997). One motivation for considering the decentralization of the control problem is that it might have the benefit of better addressing the performance of a controller, making controllers more robust to uncertainties in the models of the structural system.

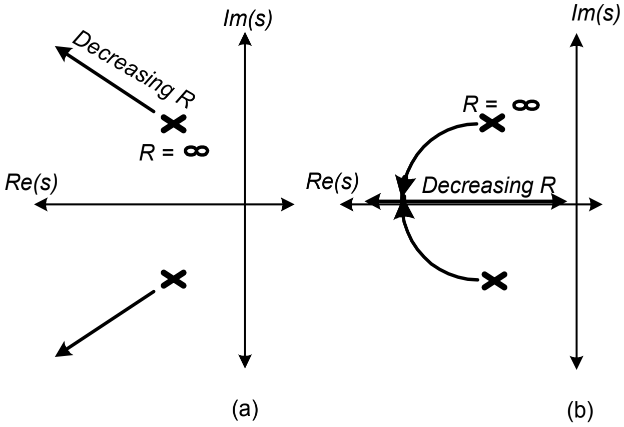

Figure 5-2: Influence of the system cost function on closed-loop pole locations

5.2 Decentralization of the Control Problem

As the field of structural control continues to evolve, the size and cost of actuation and sensing devices will continue to decrease. The result will be an overall increase in the number of actuators and sensors used by structural engineers, which will increase the complexity of the structural control system. Introducing a dense array of actuators and sensors into an already complex structure results in a control system characterized by high system dimensionality and is often termed a large-scale control problem. As the system dimensionality increases, the computations required by a centralized controller increase faster than at a linear rate (Lunze 1992). The real-time demands of the control system make it necessary to be aware of the number of calculations that can be made in each operation cycle. An additional failure of centrality occurs when considering the spatial separation of system sensors. Cost and reliability of communication links between system sensors and a controller need to be considered (Sandell et al. 1978). As a result, the division of the control problem into a collective set of smaller sub-systems that can be controlled on a local level by decentralized controllers is a possible alternative to the centralized controller. Control computations can now be performed in parallel using decentralized distributed control architectures. The control approach of decomposing the global system into a set of sub-systems is termed decentralized control or distributed control (Singh 1981).

The information structure of the control system defines the class of the control approach (centralized versus decentralized). In the centralized approach, complete knowledge of the system plant (*a priori* information) and a complete set of state data (*a posteriori* information) is assumed during implementation. In decentralized control, local controllers only have access to a portion of the global information. The amount and type of information available to each sub-system controller define the non-classical information structure of the decentralized control approach. Three types of decentralized information structures can be identified: total, partial and hierarchical decentralized control structures (Drouin et al. 1991).

A totally decentralized control structure provides local *a posteriori* information to each controller with no information exchange between local controllers permitted. Knowledge of how the control actions of the local controller affect the overall system response is not available. If information transfer is permitted between local controllers, the result is a partially decentralized control solution. While the amount of information exchange is kept as low as possible, it provides a way of ensuring partial knowledge of how the local controller is affecting the remainder of the global system. The last decentralized architectural type, hierarchical decentralized control, adds an additional layer of vertical information flow serviced by additional controllers situated above that of the local controllers. The principal role of the additional high level controller is to ensure concordant behavior between the lower local controllers leading to improved overall global performance. Figure 5-3 illustrates the three decentralized information structures.

The mathematical representation of the structural system presented by Equation (5.1) is modified to reflect the decentralization of the control problem. The responsibility of the centralized global controller is divided into *N* subsystem controllers.

$$\dot{\boldsymbol{X}}(t) = \boldsymbol{A}\boldsymbol{X}(t) + \sum_{i=1}^{N} \boldsymbol{B}_i \boldsymbol{U}_i(t) + \boldsymbol{D}\boldsymbol{W}(t) \tag{5.9}$$

The feedback of sensor measurements used to track the response of the subsystems is represented in a decentralized fashion.

$$\boldsymbol{Y}_i(t) = \boldsymbol{C}_i \boldsymbol{X}(t) \tag{5.10}$$

For this study, only total decentralized system architectures will be investigated. In particular, two decentralized control approaches will be pursued. The first is a direct modification of the centralized feedback controller gain to fit the decentralized system architecture. The modified LQR approach would represent a suboptimal solution, but its ease of implementation might outweigh any reduced optimality. The second decentralized control approach is a reformulation of the centralized optimal control solution with the optimization procedure constrained by a total decentralized architecture. These two approaches are only a small sampling of techniques readily available for adoption in structural control. Other decentralized control techniques that can be considered include, decentralized proportional-integral control and degenerate control, just to name a few (Siljak 1991).

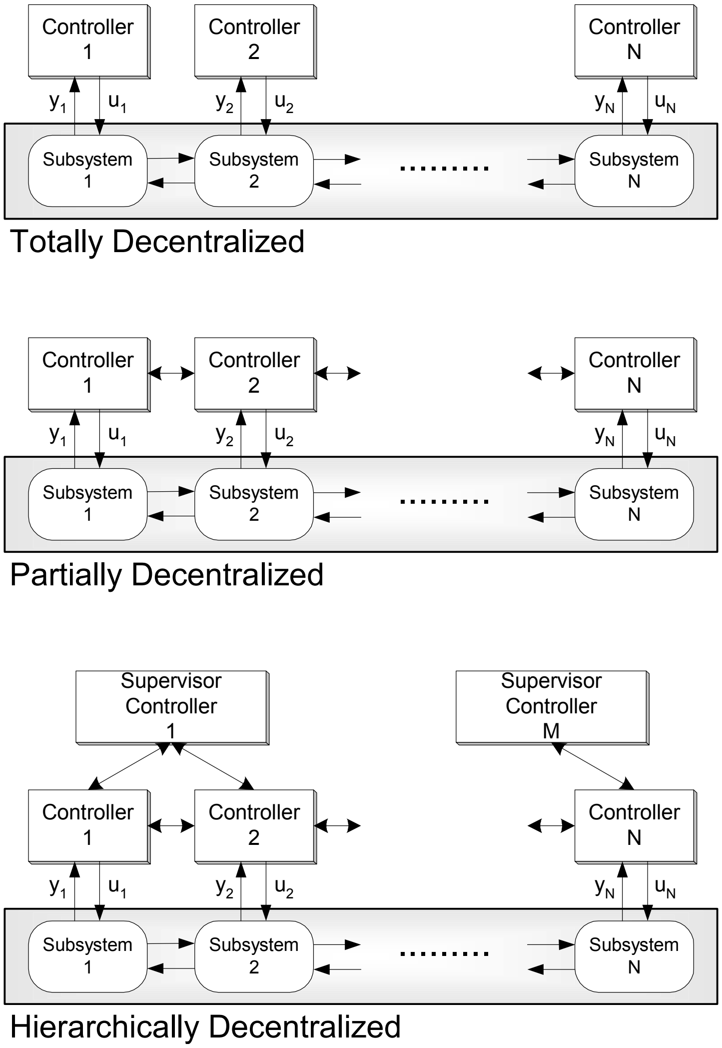

Figure 5-3: Decentralized information structures

5.3 Benchmark Structure

For comparison of the selected distributed control techniques, a benchmark structure is selected. The 20-story steel structure designed for the Structural Engineers Association of California (SAC) project is selected (Spencer, Christenson, and Dyke 1998). Having been designed using current seismic building design codes, the building represents a realistic design for the southern California region. The benchmark structure is depicted in Figure 5-4.

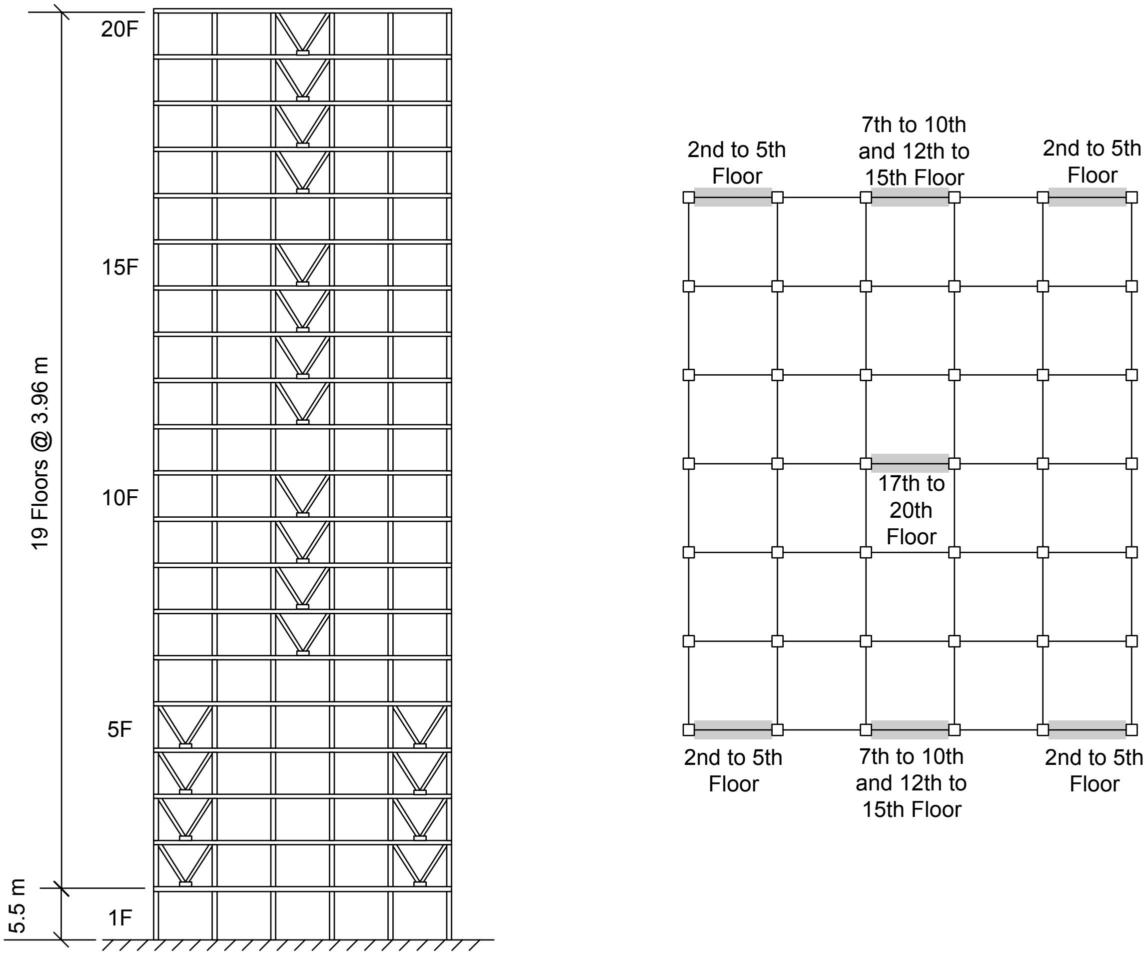

Figure 5-4: 20-story steel benchmark structure

Table 5-1: Structural properties of the 20-story benchmark structure

Floor	Seismic Mass	Story Stiffness	Number of SHD Devices
1	1.126×10^6 kg	862.07×10^3 kN/m	-
2	1.100×10^6 kg	862.07×10^3 kN/m	4
3	1.100×10^6 kg	862.07×10^3 kN/m	4
4	1.100×10^6 kg	862.07×10^3 kN/m	4
5	1.100×10^6 kg	862.07×10^3 kN/m	4
6	1.100×10^6 kg	554.17×10^3 kN/m	-
7	1.100×10^6 kg	554.17×10^3 kN/m	2
8	1.100×10^6 kg	554.17×10^3 kN/m	2
9	1.100×10^6 kg	554.17×10^3 kN/m	2
10	1.100×10^6 kg	554.17×10^3 kN/m	2
11	1.100×10^6 kg	554.17×10^3 kN/m	-
12	1.100×10^6 kg	453.51×10^3 kN/m	2
13	1.100×10^6 kg	453.51×10^3 kN/m	2
14	1.100×10^6 kg	453.51×10^3 kN/m	2
15	1.100×10^6 kg	291.23×10^3 kN/m	2
16	1.100×10^6 kg	291.23×10^3 kN/m	-
17	1.100×10^6 kg	291.23×10^3 kN/m	1
18	1.100×10^6 kg	256.46×10^3 kN/m	1
19	1.100×10^6 kg	256.46×10^3 kN/m	1
20	1.170×10^6 kg	171.70×10^3 kN/m	1

In simplifying the analysis, the structure is modeled as a lumped mass shear model sustaining elastic deformations. The mass and stiffness properties of the structure are presented in Table 5-1. The structure's natural damping is chosen to be 5% of critical damping in the first mode. The first five horizontal modal frequencies of the structure are 0.28, 0.74, 1.23, 1.66, and 2.09 Hz, respectively.

5.3.1 Semi-Active Variable Damping Control Devices

To control the structure during seismic disturbances, a total of 36 semi-active hydraulic damping (SHD) devices are strategically placed throughout the structure as shown in Table 5-1. In particular, SHD devices designed and manufactured by the Kajima Corporation, Japan are considered. The Kajima SHD devices are capable of applying a maximum control force of 1,000 kN to the structure with the SHD damper typically installed between the low point of a stiff K-brace and the floor. Given a command control force, the SHD calculates the damping coefficient by dividing the command force by the relative velocity between the two floors to which the SHD is connected. If the relative velocity between the two floors is in the opposite direction of the desired control force, then the control force is applied. If the response is in the same direction, no control force is applied and the damper is set to its default minimum damping setting. A typical installation of an SHD control device in a structure is documented in Figure 5-5.

The steel bracing used to connect the SHD to the structure is not perfectly rigid. As a result, the stiffness of the brace is geometrically in series with the damper of the SHD. In the idealized lumped mass model, the spring and dashpot series are analyzed as a Maxwell damping element (Hatada et al. 2000). The forced response of the Maxwell element, *p(t)*, is characterized by a second order differentiable equation.

$$\dot{p}(t) + \frac{k_{eff}}{c_{SHD}} p(t) = k_{eff}\dot{x}(t) \tag{5.11}$$

The combined stiffness of the SHD damper in series with the brace represents the effective stiffness, k_{eff}, of the Maxwell element.

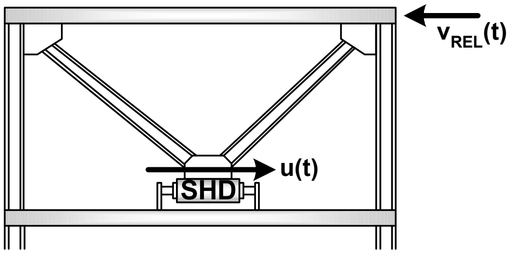

Maximum Control Force	1,000 kN
Maximum Displacement	+/- 6 cm
Stiffness of the SHD	400,000 kN/m
Maximum Damping Coefficient	200,000 kN-s/m
Minimum Damping Coefficient	1,000 kN-s/m
Maximum Shaft Velocity	25 cm/s
Power Consumption	70 Watts

Figure 5-5: Application of the Kajima semi-active hydraulic damper (SHD)

5.3.2 Input Ground Motions

To evaluate the effectiveness of the decentralized control strategies, three earthquake records are considered for external excitation of the analytical benchmark structure. In particular, the El Centro (1940 NS) and Taft (1952 NS) earthquakes, representing far field records, and the Northridge (1994 NS – Sylmar County Hospital) earthquake, representing a near field record, are selected. To normalize the maximum kinetic energy input of the three records, the earthquake time-histories are scaled so that their maximum absolute velocities are 50 cm/s. The peak ground acceleration of the three earthquake records are 3.07, 1.53 and 8.27 m/s^2, respectively.

5.3.3 Centralized LQR Solution

The performance of the proposed decentralized control techniques will be compared to the performance of a centralized LQR controller designed for the 20-story benchmark structure. The LQR solution, representing a controller designed by current state-of-practice methods, can be considered the most optimal solution. No constraints are imposed on the structure of the feedback gain matrix that will be used by the centralized controller to calculate control forces.

At the outset of the analysis, the $\boldsymbol{Q}$ and $\boldsymbol{R}$ weighting matrices of Equation (5.4) are chosen. The selection of the state weighting matrix, $\boldsymbol{Q}$, is selected to reflect the objective of the controller; regulate the absolute displacement and velocity response of the system. A weight of 10 is placed upon the velocity of the state relative to the displacement response.

$$\boldsymbol{Y}_{regulate} = \boldsymbol{CX} = \begin{bmatrix} \boldsymbol{I} & 10\boldsymbol{I} \end{bmatrix} \begin{Bmatrix} \boldsymbol{x} \\ \dot{\boldsymbol{x}} \end{Bmatrix} \tag{5.12}$$

The state weighting matrix is derived from the $\boldsymbol{C}$ matrix of Equation (5.12) through the relationship $\boldsymbol{Q}=\boldsymbol{C}^T\boldsymbol{C}$, resulting in a 40 by 40 square matrix.

$$\boldsymbol{Q} = \begin{bmatrix} \boldsymbol{I} & 10\boldsymbol{I} \\ 10\boldsymbol{I} & 100\boldsymbol{I} \end{bmatrix} \tag{5.13}$$

The actuation weighting matrix, ***R***, is a 20 by 20 square matrix selected to be:

$$\boldsymbol{R} = 1x10^{14}\left[\boldsymbol{I}\right] \tag{5.14}$$

The result of the LQR analysis is the system gain matrix, ***K***, of Equation (5.6). The gain is a 20 by 40 matrix with zero row vectors on the 1st, 6th, 11th, and 16th rows reflecting the absence of actuation at those degrees-of-freedom of the system. In calculating the LQR controller gain, it is assumed that the full state is measured at each time step with sensors located at each degree-of-freedom. The result of the collocation of the system sensors with system actuators is a strong dominance of the diagonal terms of the gain matrix.

Figure 5-6 is a three-dimensional representation of the resulting gain matrix with the value of matrix elements plotted upon the z-axis. The x-axis represents the degree-of-freedom of the system with system displacements corresponding to the first 20 columns and velocities corresponding to the last 20 columns. The y-axis corresponds to the actuation applied at each respective degree-of-freedom. The figure serves to illustrate the dominance of the diagonal terms.

Figure 5-7 plots the maximum absolute interstory drift response obtained from an analysis of the structure when no control devices are installed, when the variable dampers are set to minimum and maximum passive damping settings and when LQR control is applied. Maximum interstory drifts are used as the response characteristic for comparison since they serve as good indication of structural elastic displacement. It is clear from the results that the LQR controller provides an effective means of reducing the response of the system during seismic disturbances.

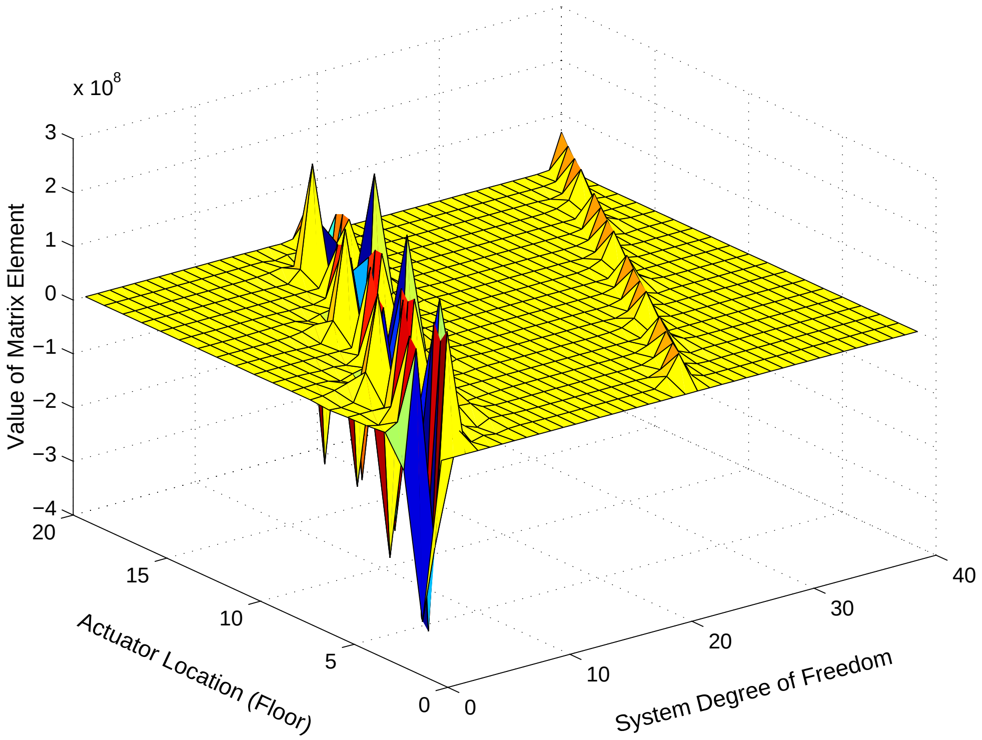

Figure 5-6: Terms of the centralized LQR feedback controller gain matrix

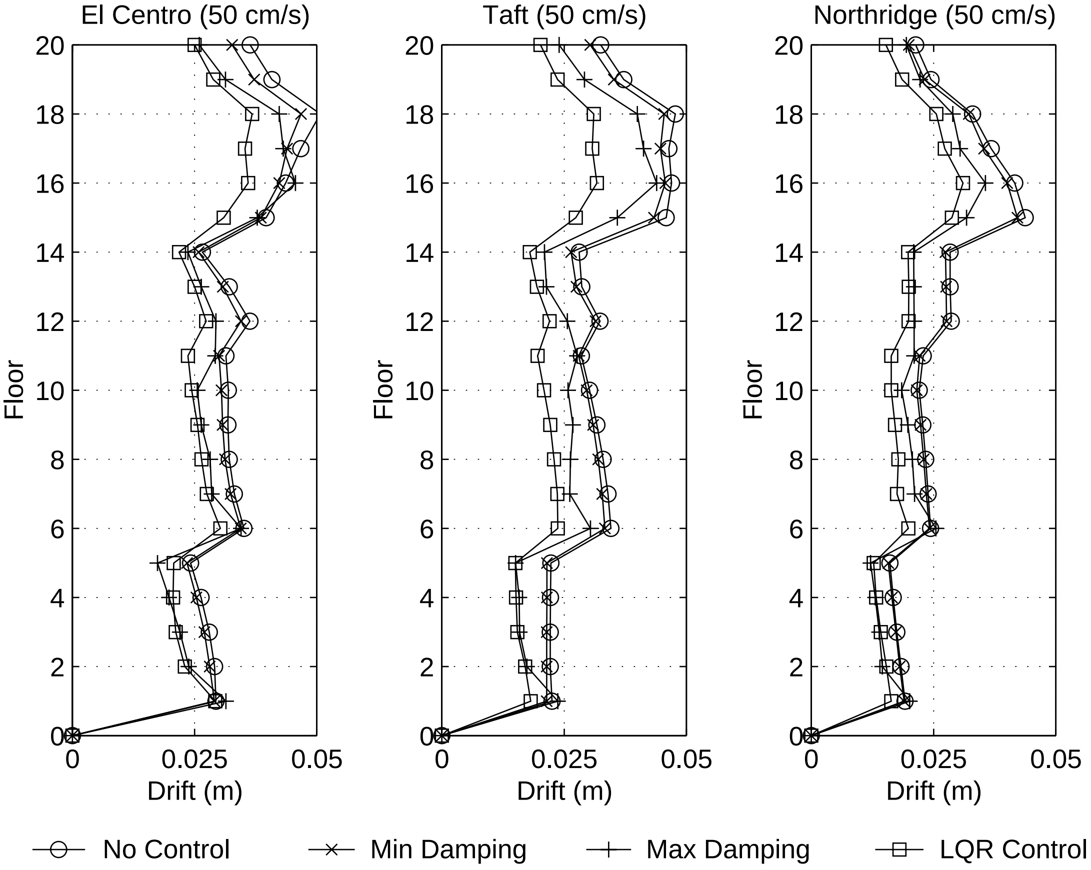

Figure 5-7: Benchmark structure maximum interstory drifts (LQR)

The passive control response of the structure is obtained by running an analysis with SHD devices set at a fixed damping value. Two different analyses have been conducted with the damper fixed at both minimum and maximum damping settings. From Figure 5-7, the structural response while using LQR control is superior to the control attained when the dampers are set to their maximum damping settings. It can been shown that the choice of effective stiffness of the K-brace is important in the performance of the active control system relative to the performance of the SHD devices when set to their maximum damping coefficients. When the ratio of SHD bracing stiffness to lateral structural stiffness, also known as the stiffness rate, is high, the damper operated by the control system will not perform better than when the damper is fixed at its maximum damping value. When the stiffness rate is low, as is typical of SHD installations in high rise structures, the controlled damper will perform better than the damper fixed at its maximum damping coefficient.

5.4 Decentralized Extensions of the Centralized Controller

In totally decentralized control architectures, the control system is divided into subsystems. The control system used to control the 20-story benchmark structure can be divided into four subsystems along the same lines as the clusters of SHD devices: 2nd to the 5th floor representing one subsystem, devices on the 7th to the 10th, 12th to the 15th, and 17th to the 20th comprising the other three subsystems. State information available to each subsystem controller is the response of the structure at the degrees-of-freedom geometrically located within the subsystem's physical boundaries. Structural responses outside of a particular subsystem remain unknown to the subsystem controller when determining control forces. Control forces calculated by the subsystems will be done using linear feedback gain matrices.

The form of the global gain matrix resulting from the centralized LQR analysis is convenient and can be exploited with minor modifications to provide a control solution compatible with the decentralized control architecture. All gain terms outside of the four subsystems of the 20-story structure are zeroed, as shown in Figure 5-8. The zeroing of these terms logically represents the inability of the subsystems to transfer state information to each other. This control solution represents a sub-optimal controller that is a close approximation of the optimal centralized controller. However, as the dominance of the off-diagonal terms increase, the decentralized extension of the centralized controller diverges further from optimality and degradation in the control system's performance is experienced.

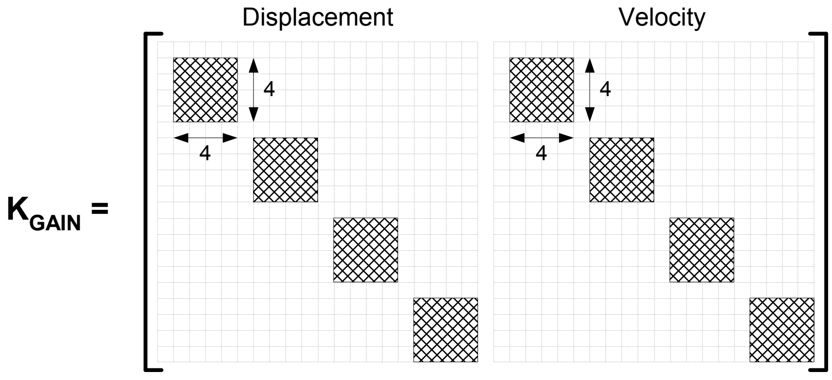

Figure 5-8: Modified LQR gain matrix to accommodate total decentralization

When the modified gain matrix is applied to the benchmark structure, excellent control results are obtained. Figure 5-9 plots the maximum absolute interstory drift results of the structure for the three seismic disturbances considered. For comparison purposes, the results of the decentralized extension of the LQR controller are presented along with the drift response of the structure when LQR control and no control are used. It is evident that the decentralized modified LQR controller is as effective as the original centralized LQR solution with marginal performance degradation. This is a direct result of the largest terms of the LQR feedback gain matrix being retained by the subsystem controllers of the decentralized system architecture.

5.5 Optimal Decentralized Control

The decentralized extension of the centralized LQR controller, while yielding suitable performance, does not represent an optimal solution. A reformulation is necessary to derive an optimal decentralized controller. The derivation of a decentralized linear optimal controller presented by Lunze (1992) is used for application to the structural control problem.

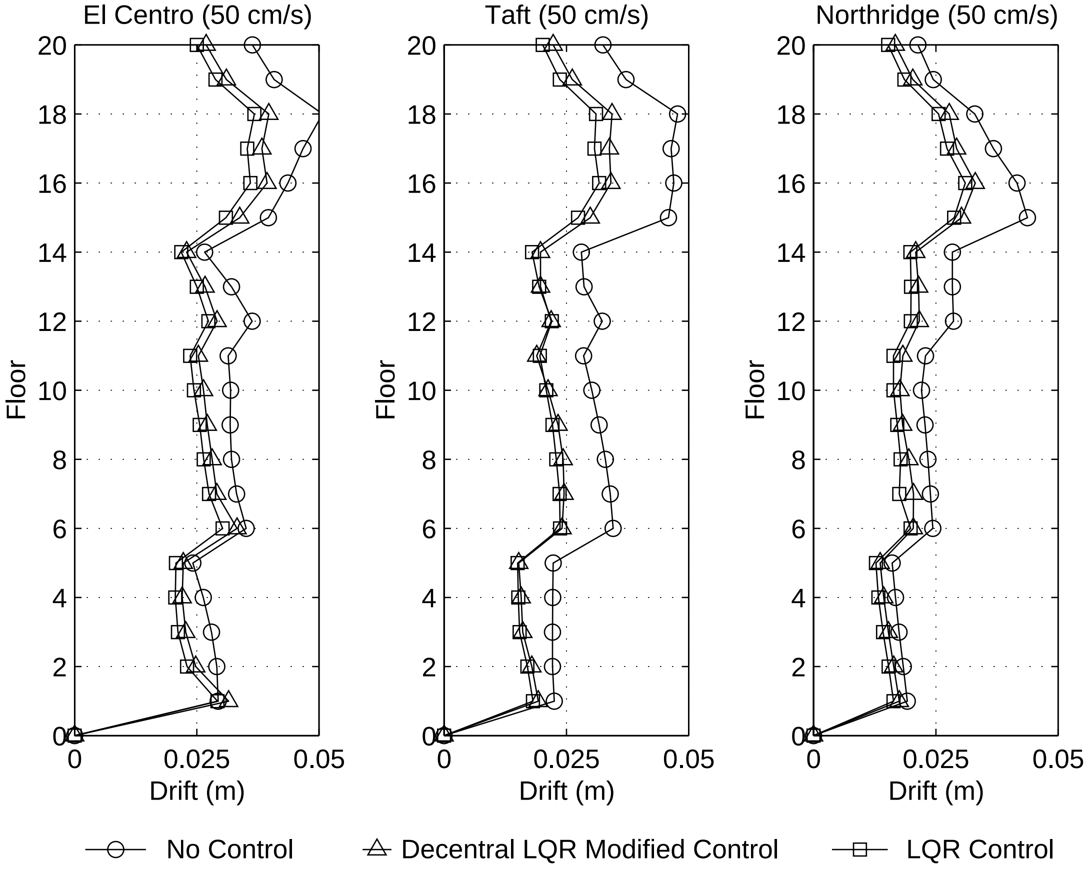

Figure 5-9: Benchmark structure maximum interstory drifts (modified LQR)

5.5.1 Cost Function Derivation

The original cost function of Equation (5.4), previously used in the derivation of the LQR controller, is now minimized subjected to the architectural constraints of total decentralization specified by Equation (5.9) and Equation (5.10). The solution to the minimization of the cost function can yield a nonlinear function $\boldsymbol{U}_i(\boldsymbol{Y}_i)$. Intuitively, this nonlinear control solution can be interpreted as the subsystem controllers using the structural system response as a means of information flow between isolated controllers. To avoid the use of nonlinear control solutions, the feedback controller is forced to remain linear by explicitly defining a linear constant control gain at the outset of the optimization procedure. This feedback gain, ***K'***, is a block diagonal matrix comprised of the various subsystem displacement and velocity gain matrices, $\boldsymbol{K}_{Di}$ and $\boldsymbol{K}_{Vi}$. The optimization of the cost function is constrained by Equation (5.15), ensuring that a linear feedback controller results.

$$\boldsymbol{K}' = \begin{bmatrix} \boldsymbol{K}_{D1} & & & \boldsymbol{K}_{V1} & & \\ & \ddots & & & \ddots & \\ & & \boldsymbol{K}_{DN} & & & \boldsymbol{K}_{VN} \end{bmatrix} \tag{5.15}$$

Consider the state trajectory solution of the closed-loop system. It is a function of the initial state of the system.

$$\{\boldsymbol{X}(t)\} = e^{(\boldsymbol{A}-\boldsymbol{BK'C})t}\{\boldsymbol{X}_o\} = \boldsymbol{\Phi}(t)\{\boldsymbol{X}_o\} \tag{5.16}$$

The state trajectory is substituted within the original cost function to reflect the dependence of the solution on the initial state vector.

$$\begin{aligned} J &= \boldsymbol{X}_O{}^T \int_0^\infty \left(\boldsymbol{\Phi}(t)^T \boldsymbol{Q}\boldsymbol{\Phi}(t) + \boldsymbol{\Phi}(t)^T \boldsymbol{C}^T \boldsymbol{K}'^T \boldsymbol{RK}'\boldsymbol{C}\boldsymbol{\Phi}(t)\right) dt \boldsymbol{X}_O \\ &= \boldsymbol{X}_O{}^T \boldsymbol{P}\boldsymbol{X}_O \end{aligned} \tag{5.17}$$

The integral portion of the modified cost function of Equation (5.17) is simplified as the matrix, ***P***, which represents the solution to the Lyapunov stability equation:

$$(\boldsymbol{A} - \boldsymbol{BK'C})^{\boldsymbol{T}} \boldsymbol{P} + \boldsymbol{P}(\boldsymbol{A} - \boldsymbol{BK'C}) + \boldsymbol{C}^{\boldsymbol{T}} \boldsymbol{K}'^{\boldsymbol{T}} \boldsymbol{RK'C} + \boldsymbol{Q} = \boldsymbol{0} \tag{5.18}$$

The solution of the Lyapunov stability equation assures that the matrix ***P*** is symmetric. Given this symmetry, the cost function of Equation (5.17) can be further simplified:

$$J = \boldsymbol{X}_O{}^{\boldsymbol{T}} \boldsymbol{P}\boldsymbol{X}_O = trace\left(\boldsymbol{P}\boldsymbol{X}_O \boldsymbol{X}_O{}^T\right) \tag{5.19}$$

The initial state of the system remains unknown. To determine an optimal feedback gain, ***K'***, compliant with the structure of Equation (5.15), the dependence of the cost function on the initial state needs to be eliminated (Levine and Athans 1970). To minimize the cost function independently of the system's initial state, the expected value is equivalently minimized. The expected value of the cost function over a set of linearly independent initial states is considered.

$$\tilde{J} = E\left[trace\left(\boldsymbol{P}\boldsymbol{X}_O\boldsymbol{X}_O^{\ T}\right)\right] \tag{5.20}$$

With the initial state assumed to be a random variable uniformly distributed over the *n*-dimensional space of the state, the equivalent cost function of Equation (5.20) can be further simplified because the expected value of the initial state times its transpose is known.

$$E\left[\boldsymbol{X}_O\boldsymbol{X}_O^{\ T}\right] = \frac{1}{n}\boldsymbol{I} \tag{5.21}$$

Hence, the cost function of Equation (5.20) can now be rewritten independently of the initial state of the system.

$$\tilde{J} = \frac{1}{n}trace(\boldsymbol{P}) \tag{5.22}$$

5.5.2 Minimization of the Constrained Cost Function

The cost function of Equation (5.22), constrained by the initial equation of motion of the system and the gain structure of Equation (5.15), is to be minimized. As presented by Levine and Athans (1970), the gradient of the cost function can be calculated.

$$\frac{d\tilde{J}}{d\boldsymbol{K}'} = 2\left(\boldsymbol{R}\boldsymbol{K}'\boldsymbol{C} - \boldsymbol{B}^T\boldsymbol{P}\right)\boldsymbol{L}\boldsymbol{C}^T \tag{5.23}$$

The positive definite matrix, ***L***, representing the solution to Equation (5.24), exists if the closed-loop system is stable.

$$(\boldsymbol{A}-\boldsymbol{BK'C})\boldsymbol{L}+\boldsymbol{L}(\boldsymbol{A}-\boldsymbol{BK'C})^T+\boldsymbol{I}=0 \tag{5.24}$$

Setting the gradient of Equation (5.23) to zero, the following condition on the decentralized gain matrix is established:

$$\boldsymbol{K'}=\boldsymbol{R}^{-1}\boldsymbol{B}^T\boldsymbol{PLC}^T\left(\boldsymbol{CLC}^T\right)^{-1} \tag{5.25}$$

The decentralized controller gain that minimizes the cost function of Equation (5.22) must satisfy the conditions set forth by Equations (5.25), (5.24), and (5.18). An iterative procedure known to converge to a solution is used to determine the decentralized feedback gain, ***K'*** (Lunze 1992).

5.5.3 Application to the Benchmark Structure

Using the same ***Q*** and ***R*** used to derive the LQR feedback gain matrix, an optimal decentralized controller is determined following the iterative procedure proposed by Lunze (1992). The resulting feedback gain of Figure 5-10 can be decomposed into four controllers suitable for implementation in the subsystem controllers. One interesting observation is how the optimal decentralized controller compensates for its decentralization with a heavier emphasis upon the feedback of the state's velocity terms when compared to the gain matrix of the centralized controller of Figure 5-6.

As presented in Figure 5-11, the results of the optimal decentralized controller are compared against those obtained by the centralized LQR controller. The results of the decentralized controller are quite similar to those of the centralized controller with only a slight degradation of performance at the higher levels of the structure when excited by the Taft record. However, the controller represents an optimal solution subjected to the limitations of information flow in the system infrastructure set forth at the outset of the solution derivation.

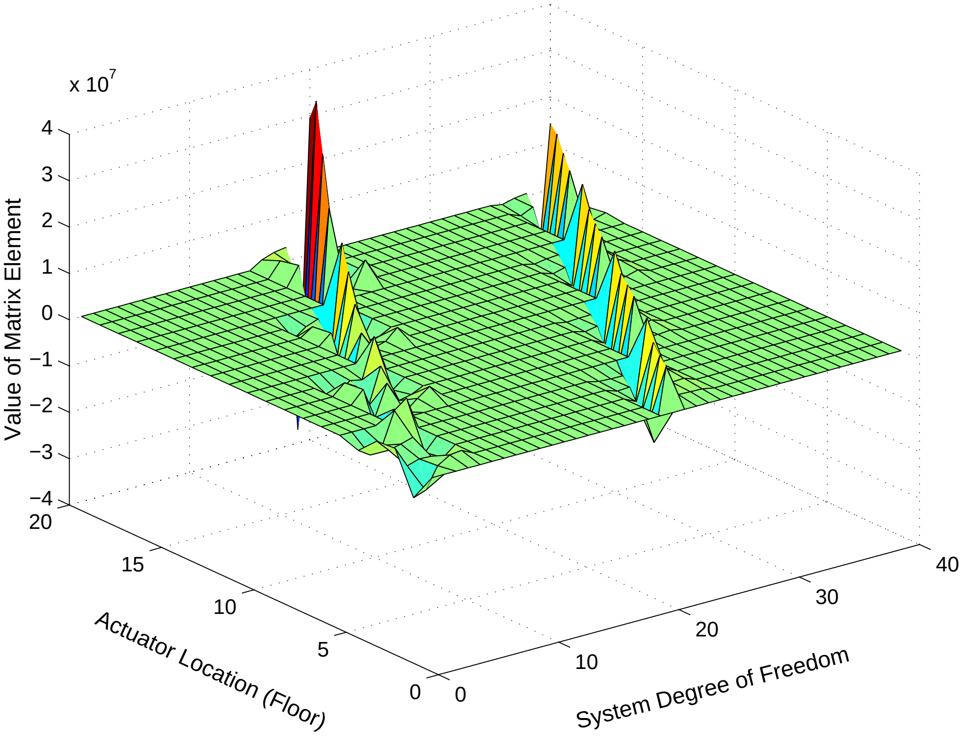

Figure 5-10: Terms of the optimal decentralized controller gain matrix

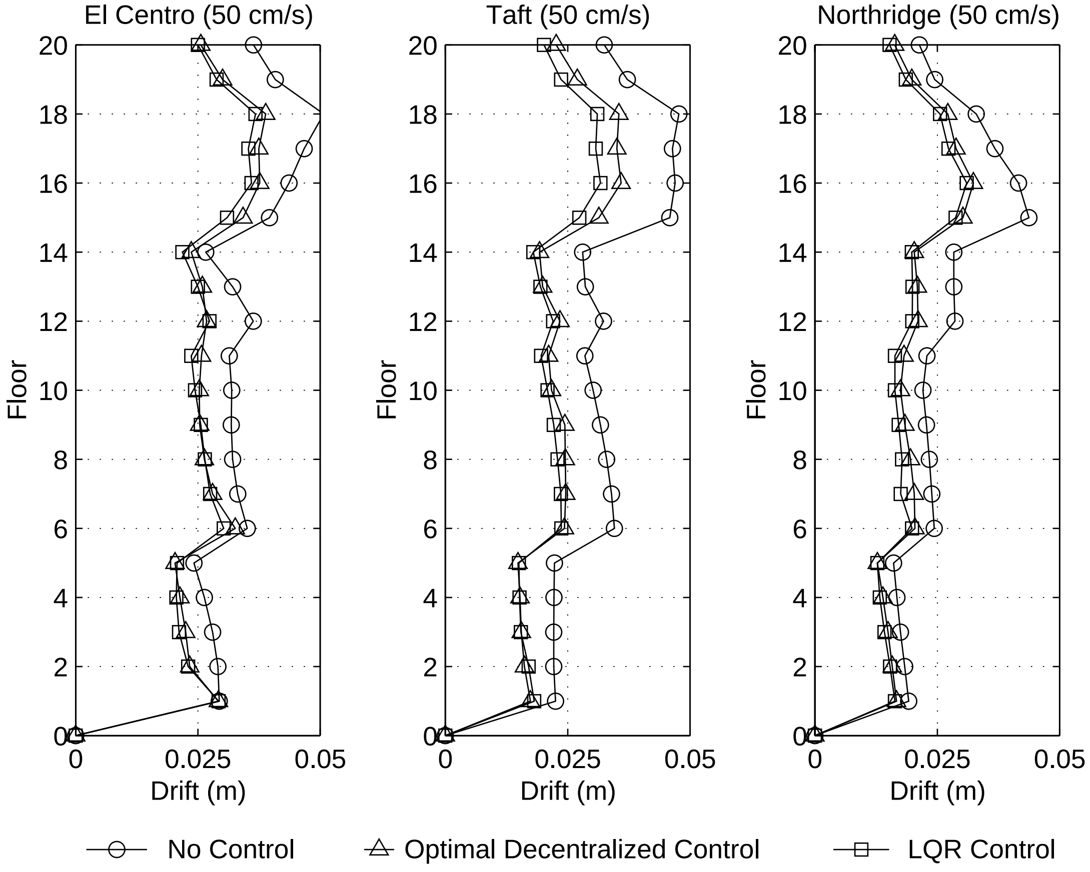

Figure 5-11: Benchmark structure maximum interstory drifts (optimal decentralized)

5.6 Summary

This chapter began with a discussion of the centralized LQR controller that represents the current state-of-practice approach to structural control. After exploring the scalability of the centralized control approach, two decentralized control techniques were derived and implemented in an analytical structure. Both decentralized controllers exhibited suitable global performance with the optimal decentralized controller yielding the best reduction in system responses. In favor of the decentralized extension of the centralized optimal controller is its easy implementation with sub-optimal performance close to that of the optimal decentralized controller.

Having only addressed two decentralized control approaches, other decentralized techniques exist that can be considered for application in the large-scale complex problem of controlling a structure during an earthquake. Inevitably, as structural control systems employ large numbers of small and inexpensive controllers and sensors, the vast field of decentralized control will play a more prominent role. Furthermore, given their flexible frameworks, decentralized control approaches can be extended to handle significantly more complex systems such as nonlinear structures. Many methods of nonlinear structural control depend upon the reduction or the linearization of the system model to a point where classical control approaches can be applied. Alternatively, the complexity of the nonlinear control problem can be best tackled with a distributed control framework with increased complexity being dealt with by each subsystem.

The importance of decentralized control will continue as a theme for the remainder of this study with investigations into additional decentralized control approaches continued. Furthermore, the performance of decentralized control in the context of solution robustness will be evaluated. While a centralized controller represents a single point of failure, the redundant nature of control decision in a decentralized control system makes it inherently more robust if failures occur.

Chapter 6

Market-Based Control

Structures excited by large external disturbances are complex systems characterized by high dimensionality, nonlinear behavior and significant plant uncertainty. Introducing a large number of sensors and control devices results in a large information network, rendering the control problem even more complex. New ideas are needed for decomposing the overall system into independent sub-systems that can be handled locally by decentralized controllers. The control devices in a decentralized system act as independent decision makers within the global system. The goal of the system is to allocate system resources (i.e. input device power) in a distributed and efficient manner. Chapter 5 has discussed two decentralized control techniques that show success in controlling the global response of a large-scale civil structure subjected to seismic disturbances. An alternative decentralized control approach is pursued that is decentralized in the knowledge of the system plant (*a priori* information) rather than in the knowledge of the state (*a posteriori* information).

A strong parallel exists between the operational goal of a decentralized control system and a free market economy. Both seek to attain an efficient distribution of scarce system resources. In the case of an economic market, goods and services serve as the scarce resources in the market while power is the scarce resource in a control system. Using the rules observed in a free market for the operation of control devices in a control system, market-based control emerges as a potentially novel approach to the control problem.

Market-based control (MBC) is a multi-objective optimal control technique that exploits the efficiencies of a marketplace for determining the allocation of power in a control system. The focus of this chapter will center on the modeling of an MBC system for application in civil structures. The discussion begins with an investigation of optimization techniques used for economic systems since the origin of MBC finds itself within this discipline of theoretical economics. The implementation of an MBC solution is presented for a single degree-of-freedom system in addition to multiple degree-of-freedom systems such as the five-story Kajima-Shizuoka building and the 20-story benchmark structure used in Chapter 5.

6.1 Review of Econometric Optimization

Economics is a study of the allocation of scarce resources between competing parties. There exist two optimization methods widely used by economists in determining optimal allocation solutions: static optimization and dynamic optimization. Each technique is well suited for a given archetype economic problem. Static optimization techniques are useful for finding optimal magnitudes of choice variables with no concern for sequential action. Dynamic optimization techniques solve for the optimal magnitudes within a prescribed period of time with the solution presented as an optimal time trajectory (Chiang 1992).

6.1.1 Static Optimization

The optimal solution for the allocation of scarce resources at an instant in time can be found using static optimization techniques. The static optimization problem can be posed as essentially a mathematical programming problem (Intriligator 1971). Static optimization entails the maximization of a real scalar valued objective function, $F(\mathbf{x})$, constrained by solutions found within a prescribed opportunity set, X.

$$\max F(\boldsymbol{x}) \text{ subject to } \boldsymbol{x} \in X \tag{6.1}$$

The vector representing the state of the system, $\boldsymbol{x}$, is in n-dimensional Euclidean space. The general mathematical programming problem can be further defined by the constraints placed on the solution opportunity set. The classical programming problem constrains the solution using m nonlinear functions.

$$\boldsymbol{x} \in X: \qquad \boldsymbol{g(x)} = \begin{pmatrix} g_1(x_1, x_2, \ldots, x_n) \\ g_2(x_1, x_2, \ldots, x_n) \\ \vdots \\ g_m(x_1, x_2, \ldots, x_n) \end{pmatrix} = \begin{pmatrix} b_1 \\ b_2 \\ \vdots \\ b_m \end{pmatrix} \tag{6.2}$$

The general static optimization problem of Equation (6.1) can be written to reflect the classical programming problem with equality constraints:

$$\max F(\boldsymbol{x}) \text{ subject to } \boldsymbol{g}(\boldsymbol{x}) = \boldsymbol{b} \tag{6.3}$$

The nonlinear programming problem is defined by constraint functions that are constrained by inequalities. Furthermore, the state can be further constrained to be positive in the nonlinear programming problem.

$$\max F(\boldsymbol{x}) \text{ subject to } \boldsymbol{g}(\boldsymbol{x}) \le \boldsymbol{b}, \quad \boldsymbol{x} \ge 0 \tag{6.4}$$

The linear programming problem is characterized by linear constraint functions. The linearity of the constraint functions is mathematically defined by the m x n matrix, $\boldsymbol{A}$.

$$\boldsymbol{Ax} = \begin{bmatrix} a_{11} & a_{12} & \cdots & a_{1n} \\ a_{21} & a_{22} & & a_{2n} \\ \vdots & & \ddots & \vdots \\ a_{m1} & a_{m2} & \cdots & a_{mn} \end{bmatrix} \begin{Bmatrix} x_1 \\ x_2 \\ \vdots \\ x_n \end{Bmatrix} \le \begin{Bmatrix} b_1 \\ b_2 \\ \vdots \\ b_n \end{Bmatrix} \tag{6.5}$$

Therefore, the linear programming problem can be stated as:

$$\max F(\boldsymbol{x}) \text{ subject to } \boldsymbol{Ax} \le \boldsymbol{b}, \quad \boldsymbol{x} \ge 0 \tag{6.6}$$

The maximization of the scalar objective function, $F(\mathbf{x})$, is performed to find the optimum solution, $\mathbf{x}$. For all three programming problems (Equations (6.3), (6.4), and (6.6) respectively), a graphical interpretation of the problem can be given. First, the objective function is projected upon the *n*-dimensional plane of the opportunity set. Figure 6-1 illustrates the projection for a hypothetical objective function upon a 2-dimensional opportunity set. The result of the projection is the contours representing equal values of the objective function.

Using the objective function contours of Figure 6-1, classical programming optimization can be thought of as a line representing the constraint of the system intercepting the contour plot. The optimal solution is represented by the maximum value of the objective function along the line. This can be graphically interpreted as the point of tangency between the constraining line and a contour line corresponding to the maximum value of the objective function along the constraint. The optimal solution of the classical programming problem is illustrated in Figure 6-2a.

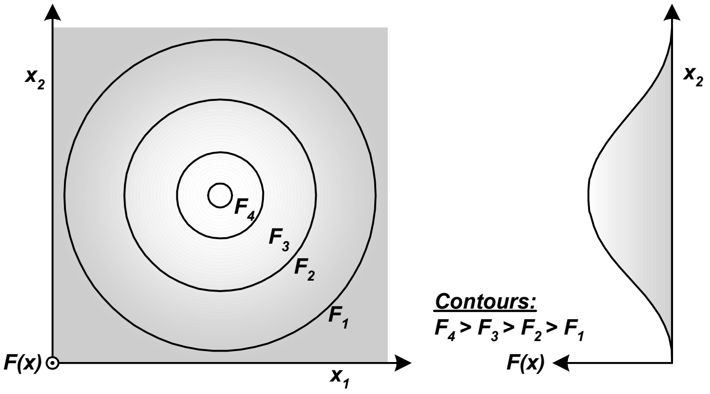

Figure 6-1: Objective function's projection upon the opportunity set

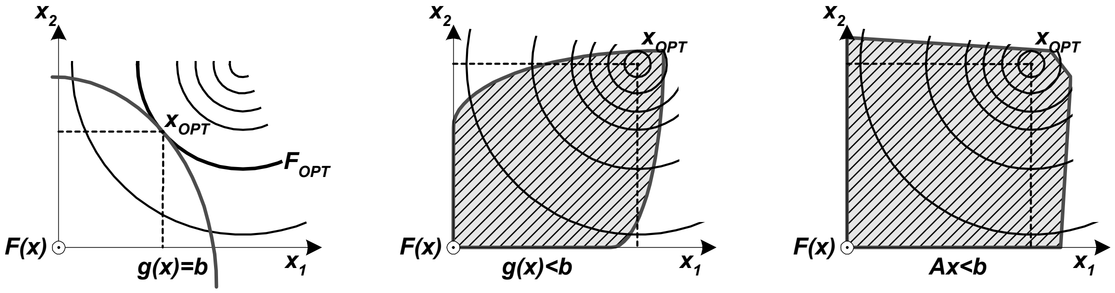

(a) (b) (c)

Figure 6-2: Mathematical programming: (a) classical, (b) nonlinear, and (c) linear

The constraints of the nonlinear programming problem would be represented by the hashed region within the nonlinear boundaries of Figure 6-2b. The optimal solution of *x* is the maximum value of *F(**x**)* within or along the nonlinear boundary. Likewise, the solution of the linear programming problem is contained within or along the linear boundaries of Figure 6-2c.

The mathematical methods for determining the optimal solution for all three problems are often based on the Lagrange multipliers. As an example, consider the objective function of the classical programming problem stated by Equation (6.3). The Lagrangian function of the original objective function can be formulated using the Lagrange multiplier vector, $\boldsymbol{\lambda}$, of *m* elements.

$$L(\boldsymbol{x},\boldsymbol{\lambda}) = F(\boldsymbol{x}) + \boldsymbol{\lambda}^T(\boldsymbol{b} - \boldsymbol{g}(\boldsymbol{x})) \tag{6.7}$$

The optimal solution is found by locating where first-order partial derivatives of the Lagrangian vanish (Intriligator 1971).

$$\begin{aligned}\frac{\partial L}{\partial \boldsymbol{x}}(\boldsymbol{x},\boldsymbol{\lambda}) &= \frac{\partial F}{\partial \boldsymbol{x}} - \boldsymbol{\lambda}\frac{\partial \boldsymbol{g}}{\partial \boldsymbol{x}} = \{\boldsymbol{0}\} \\ \frac{\partial L}{\partial \boldsymbol{\lambda}}(\boldsymbol{x},\boldsymbol{\lambda}) &= \boldsymbol{b} - \boldsymbol{g}(\boldsymbol{x}) = \{\boldsymbol{0}\}\end{aligned} \tag{6.8}$$

A second condition on the existence of the objective function's maximum is that the Hessian matrix of the Lagrangian function, presented in Equation (6.9), be negative semi-definite.

$$\frac{\partial^2 L}{\partial \boldsymbol{x}^2}(\boldsymbol{x}) = \begin{bmatrix} \frac{\partial^2 L}{\partial {x_1}^2} & \frac{\partial^2 L}{\partial x_1 \partial x_2} & \cdots & \frac{\partial^2 L}{\partial x_1 \partial x_n} \\ \frac{\partial^2 L}{\partial x_2 \partial x_1} & \frac{\partial^2 L}{\partial {x_2}^2} & & \frac{\partial^2 L}{\partial x_2 \partial x_n} \\ \vdots & & \ddots & \vdots \\ \frac{\partial^2 L}{\partial x_n \partial x_1} & \frac{\partial^2 L}{\partial x_n \partial x_2} & \cdots & \frac{\partial^2 L}{\partial {x_n}^2} \end{bmatrix} \tag{6.9}$$

The Lagrange multiplier, λ, is a valuable variable introduced during the optimization procedure because it provides a direct measure of the sensitivity of the optimization solution. The nonlinear and linear programming problem solutions also make extensive use of the Lagrange multiplier method with some minor variations specific to each problem constraint.

6.1.1.1 Static Optimization of the Household and Firm

Households, firms, federal governments and trade unions, all represent institutions that serve as the fundamental building blocks economists use to model markets. The behavior of each of these entities can be defined using constrained or unconstrained objective functions. Static optimization methods are extensively used to determine the optimal behavior of each of these institutions at a fixed point in time.

The household represents a marketplace participant that uses its income to purchase goods and services. The objective function governing its behavior is termed a utility function, *U(**x**)*. The utility function is a mathematical convenience for measuring how much utility a household obtains in purchasing a particular set of goods or services. To determine the optimal amount of goods and services a household should buy, the utility function of the household is statically optimized. The optimization of the utility function can be constrained by the household's budget. The budget prevents the purchasing of more goods than what the household's income can support. If the vector of goods, $\boldsymbol{x}$, can be purchased at prices contained within the price vector, $\boldsymbol{p}$, and the household's available income is the scalar r, the budget of the household would constrain the maximization of the utility function by $\boldsymbol{p}^{\mathrm{T}}\boldsymbol{x} \le r$. The static optimization of the household's utility therefore is a linear programming problem.

$$\max U(\boldsymbol{x}) \text{ subject to } \boldsymbol{p}^{T}\boldsymbol{x} \le r, \quad \boldsymbol{x} \ge 0 \tag{6.10}$$

Provided that the optimization is dependent upon the price vector, p, and the solution is unique, the maximization of the utility of Equation (6.10) results in the household demand function of each commodity as a function of price (Luenberger 1995).

$$\boldsymbol{x}_{OPT} = f(\boldsymbol{p}, r) \tag{6.11}$$

The firm represents the manufacturing engine of the economy with goods and services produced for consumer consumption. Similar to the household, the behavior of a firm is determined by its objective function. The objective function for the firm is also known as the profit function, Π, and is simply the revenue, R, minus production costs, C.

$$\Pi = R - C \tag{6.12}$$

Revenue is a function of the level of production, $\boldsymbol{q}$, of the firm. The production level is likewise a function of the firm's inputs, $\boldsymbol{x}$. The production function can be of various forms ranging from linear to nonlinear functions. Hence, revenue is simply the price charged by the market for each of the firm's outputs.

$$R = \boldsymbol{p}^T \boldsymbol{q}(\boldsymbol{x}) \tag{6.13}$$

The production costs of the firm are the sum of the cost of the individual inputs, w_i, times the amount of input, x_i.

$$C = \sum_{i=1}^{n} w_i x_i = \boldsymbol{w}^T \boldsymbol{x} \tag{6.14}$$

The output of the firm is determined by maximizing the profit function. In the long-term, the maximization of the cost function is unconstrained except by a condition of the inputs selected to be greater than or equal to zero. In the short term, the firm is constrained by a technology function, also termed the production function, with output a nonlinear function of the factor inputs (Intriligator 1971). The result is a classical programming problem.

$$\max \Pi(\boldsymbol{x}) = \boldsymbol{p}^T \boldsymbol{q}(\boldsymbol{x}) - \boldsymbol{w}^T \boldsymbol{x} \text{ subject to } \boldsymbol{g}(\boldsymbol{x}) \le \boldsymbol{b}, \quad \boldsymbol{x} \ge 0 \tag{6.15}$$

The solution of the optimization problem posed by Equation (6.15) yields the firm's supply function for each of its outputs.

$$\boldsymbol{q}_{OPT} = f(\boldsymbol{p}, \boldsymbol{w}) \tag{6.16}$$

6.1.1.2 Competitive Equilibrium

Households and firms are two competing elements within a free market economy. Firms are directly buying labor from the households to generate goods. In turn, the goods are purchased by the households from wages they earn from the firms. The result of the dependent interaction of the two economic institutions is the formation of two parallel markets: a goods market and a production factor market. The goods market is where the products generated by the firms are sold to households while the production factor market is where firms buy household labor with wages. Figure 6-3 illustrates the competitive mechanisms of both marketplaces.

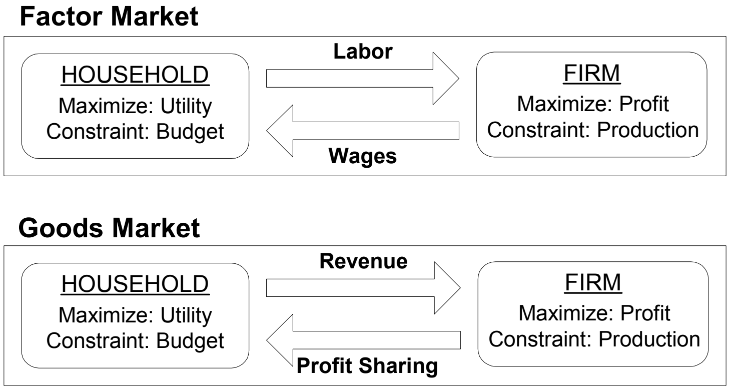

Figure 6-3: Mechanisms of the goods and factor marketplaces

An economy is generally comprised of a large number of firms and households all competing with each other for a variety of goods and services. The result of direct competition is price equilibrium for the goods and services exchanged. Mathematically, the optimal allocation of the scarce resources is provided by the simultaneous solution of Equation (6.10) and (6.15) for all firms and households of the market. In addition, market-clearing constraints exist within the market with the sum of all demands equaling the sum of supplies of a particular good (Intriligator 1971). The general equilibrium solution can be solved using static optimization techniques. For example, if the production function of Equation (6.15) is linear, the optimization problem reduces to a linear mathematical programming problem. The solution yielded is often termed a Pareto optimal solution. Pareto optimal is defined by a market in competitive equilibrium where no market participant can reap the benefits of higher utility or profits without causing harm to other participants when a resource allocation change is made (Mas-Colell et al. 1995).

6.1.2 Dynamic Optimization

Dynamic optimization differs from the static optimization problem by considering optimality within the context of time. The solution to the dynamic optimization problem is an optimal time trajectory of the system. Borrowing many concepts from the engineering discipline of control theory, the dynamic optimization has grown in popularity in the past two decades as a valuable tool used by economists to model macroeconomic models. Arnold Tustin, in 1953, is the first to propose using the extensive mathematics of dynamic system and control theory to the realm of economic models (Aoki 1976).

The definition of the dynamic optimization problem is analogous to that of the static optimization problem. Dynamic optimization centers on the maximization of a prescribed objective function, *J*, which is an integral of an instantaneous objective function defined over a desired time interval. The objective function is generally a function of the state of the model, ***x***, control variables, ***u***, and time, *t*.

$$J = \int_{t_0}^{t_1} I(\boldsymbol{x}(t), \boldsymbol{u}(t), t)dt + F(\boldsymbol{x}_1, t_1) \tag{6.17}$$

The last term of the generic objective function represents the dependence of the dynamic optimization upon the final state of the system.

The opportunity set of the potential trajectory solutions is constrained by a set of differentiable equations known as the equations of motion of the economic system.

$$\dot{\boldsymbol{x}} = f(\boldsymbol{x}(t), \boldsymbol{u}(t), t) \tag{6.18}$$

Additional constraints can be applied to the system in the initial and final state of the system, $\boldsymbol{x}_o$ and $\boldsymbol{x}_1$, respectively. The maximization of Equation (6.17) constrained by Equation (6.18) is the dynamic optimization problem.

$$\max J = \int_{t_0}^{t_1} I(\boldsymbol{x}(t), \boldsymbol{u}(t), t)dt + F(\boldsymbol{x}_1, t_1) \text{ subject to } \dot{\boldsymbol{x}} = f(\boldsymbol{x}, \boldsymbol{u}, t),\ \boldsymbol{x}_o, \text{ and } \boldsymbol{x}_1 \tag{6.19}$$

Figure 6-4 serves as a graphical interpretation of the dynamic optimization problem for a single state variable (Intriligator 1971). The hashed region indicates trajectory regions outside of the equation of motion opportunity set.

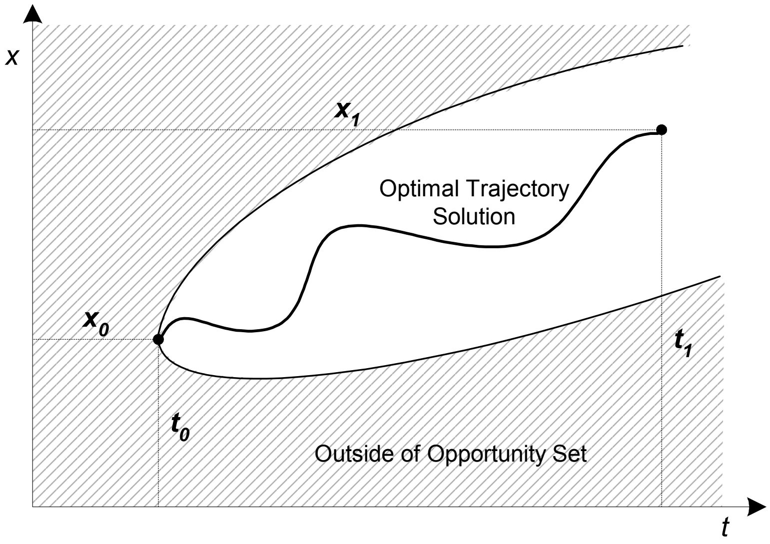

Figure 6-4: Graphical interpretation of dynamic optimization problem

The dynamic optimization problem can be further classified by modifications of Equation (6.19). For example, for objective functions independent of final state scalar function, $F(\boldsymbol{x}_1,t)$, the dynamic optimization problem is known as a Lagrange problem.

$$\max J = \int_{t_0}^{t_1} I(\boldsymbol{x}(t),\boldsymbol{u}(t),t)dt \text{ subject to } \dot{\boldsymbol{x}} = f(\boldsymbol{x},\boldsymbol{u},t),\ \boldsymbol{x_o}, \text{ and } \boldsymbol{x_1} \tag{6.20}$$

If the control variable, $\boldsymbol{u}$, of the Lagrange problem is equal to the time differential of the state, then the problem reduces to the classical calculus of variations problem.

$$\max J = \int_{t_0}^{t_1} I(\boldsymbol{x}(t),\dot{\boldsymbol{x}}(t),t)dt \text{ subject to } \boldsymbol{x_o} \text{ and } \boldsymbol{x_1} \tag{6.21}$$

Directly borrowing terminology from the control discipline, an economic model can be said to be open-loop or closed-loop controlled. In open-loop control, the optimal control trajectory is predefined and is a function of time, $\boldsymbol{u}(t)$. Closed-loop control is a function of the state trajectory, $\boldsymbol{u}(\boldsymbol{x}(t))$, requiring feedback of the state in real-time. An example borrowed from the realm of macroeconomics is used to illustrate these two control concepts. Consider the federal government and its role in controlling economic growth through a federal interest rate. In an open-loop control system, the federal government would employ a predetermined interest rate table to determine when and how much to change the current interest rate. In a closed-loop control model, the federal government would adaptively change the interest rate as a function of certain market indicators (Intriligator 1971).

It is not surprising to immediately see the striking similarities that exist between the objective function of the Lagrange type dynamic optimization problem, Equation (6.20), and that of the linear quadratic regulator (LQR), Equation (5.4). The LQR controller represents a Lagrange dynamic optimization problem constrained by the dynamic system's equation of motion, Equation (5.1). The controls community has specified the LQR objective function in a manner that ensures a stable solution always exists. The generality of the econometric dynamic objective function provides economists with flexibility in the type and scope of dynamic problems they can consider.

The number of econometric problems that benefit from dynamic optimization are many. To just name a few from the area of microeconomics would include the profit maximization of monopolistic firms, the optimal labor adjustment of a firm with changes in employment costs, and the optimal long-term investment strategy of firms and households. From the area of macroeconomics, an evaluation of the federal government's options in trading off inflation for unemployment and the determination of an optimal anti-pollution fine strategy for municipalities are two examples (Chiang 1992).

6.2 Static Econometric Optimization Applied to Controls

The growing complexity of structural control systems is one motivation for considering decentralized control approaches for application to the control of civil structures. The decentralization of the control solution is defined with respect to the available *a priori* and *a posteriori* information of the system. The decentralized control techniques discussed in Chapter 5 were defined by decentralization of *a posteriori* information (state measurements of the system) with complete *a priori* information (a precise system model) readily available.

A complex system elegantly controlled in a decentralized fashion is the free market economies. In a free market system, scarce societal resources are distributed based on the local interactions of buyers and sellers who obey the laws of supply and demand as set forth by Adam Smith (1776). In the free markets, what is optimally "controlled" is the price that is paid for goods and the salary workers receive for their services. The market naturally determines optimal pricing solutions in a decentralized fashion with no *a priori* information available. The historically poor performance of centrally controlled economies, where complete *a priori* information is assumed by market custodians, is additional evidence of the difficulty associated with controlling a complex system such as a market.

The competitive mechanisms of the decentralized free markets are considered for application to the control paradigm. The resulting control approach, termed market-based control (MBC), models the complex dynamic system as a market whose operation is akin to financial markets. A scarce system resource, such as power, is identified and is optimally distributed in a decentralized manner. Researchers have only recently begun to consider using market concepts for the control of complex systems. The majority of applications are found within the realm of computer architecture systems where the market paradigm is useful in modeling a bidding system for control of computer memory usage or network traffic (Clearwater 1996). Baker (1992) has applied the market-based control concepts to distributed computer architectures for the control of automated manufacturing processes. Engineers have investigated the use of market-based control techniques to MEMS (Micro-electro mechanical systems) where hundreds of actuators and sensors are employed in system plants of high uncertainty with high likelihood of actuation failure. Guenther, et al. (1997) have made use of classical economic static optimization theory to derive market-based control concepts to MEM systems.

The static econometric optimization techniques used by economists will be adopted for use in the design and modeling of a competitive marketplace explicitly intended for adoption in a control system. The task is made easier by only having to model the goods market around one scarce resource, power. Control devices and power sources represent agents in the marketplace of power. In particular, control devices would represent the household buyers while the power sources used to supply power to the system represent the market selling firms. The behavior of control devices acting as market households are modeled using utility functions. In a similar fashion, the selling behavior of the system firms is determined from their profit function. The static utility and profit functions of the market buyers and sellers are designed around the dynamic response of the system and hence change at every time step. The utility and profit functions are statically optimized at each time step in order to determine the optimum price of power in the control system's market. The myopic feature of this recursive static optimization approach serves as a crude approximation to an alternative dynamic optimization solution where time is explicitly modeled.

A dynamic optimization approximation using static optimization approaches is supported by the general Weierstrass theorem. The general Weierstrass theorem states that dynamic optimization is equivalent to static optimization in an infinite dimensional space (Intriligator 1971). As an illustration, simply consider an initial dynamic optimization objective function defined over the $[t_0, t_1]$ time interval for a single scalar variable.

$$\max J = \int_{t_0}^{t_1} I\big(x(t), u(t)\big)dt \text{ subject to } \dot{x} = f\big(x,u\big) \tag{6.22}$$

The time interval is evenly divided into N portions and the objective function of Equation (6.22) is likewise written in its discrete form.

$$\max \tilde{J} = \sum_{i=1}^{N} I\big(\big(x(i\Delta t), u(i\Delta t)\big)\Delta t$$
$$\text{subject to } x((i+1)\Delta t) = x(i\Delta t) + f\big(x(i\Delta t), u(i\Delta t)\big) \tag{6.23}$$

As N nears infinity, Equation (6.23) asymptotically converges to Equation (6.22). The discrete form of the dynamic optimization procedure represents a static optimization problem in N dimensions. Hence, continuous dynamic optimization is equivalent to a static optimization in an infinite dimensional space.

Associated with each seller of power is a profit function, Π, that is a function of the amount of power produced, P_S, and the price of power, p, at each time step. The seller's cost function is a representation of the amount of profit the seller obtains when selling power at the market price. Likewise, for each buyer there is an associated utility function, U_B, that is a function of the system response of the buyer's subsystem, $y_B(t)$, the amount of power sought, P_B, and the price of power, p.

In a decentralized fashion, individual buyers and sellers seek to simultaneously maximize their associated profit and utility functions at each time increment of the dynamic system. The market buyers are constrained by their instantaneous wealth, W, while market sellers are constrained by their limited power supply, P_{MAX}.

$$\begin{aligned}
&\max \Pi_{S1}\left(P_{S1}, p\right) \text{ subject to } P_{S1} \le P_{MAX1}\\
&\max \Pi_{S2}\left(P_{S2}, p\right) \text{ subject to } P_{S2} \le P_{MAX2}\\
&\qquad\qquad\vdots\\
&\max U_{B1}\left(P_{B1}, p, y_{B1}(t)\right) \text{ subject to } pP_{B1} \le W_1\\
&\max U_{B2}\left(P_{B2}, p, y_{B2}(t)\right) \text{ subject to } pP_{B2} \le W_2
\end{aligned} \tag{6.24}$$

The marketplace modeled is a goods market centered on control power. It is assumed to be in perfect competition. In a marketplace defined by perfect competition, all market participants must buy and sell at the equilibrium price established. All firms are price takers since no firm can sell at a price higher than the equilibrium price without losing all of its sales (Luenberger 1995). Power is conserved in the marketplace where *m* system buyers purchase all the power produced by the system's *n* suppliers.

$$\sum_{i=1}^{n} P_{Si} = \sum_{j=1}^{m} P_{Bj} \tag{6.25}$$

Each buyer's utility function is maximized with respect to power to determine the demand function of the buying agent. For the selling agents, the profit function is also maximized with respect to power to derive the seller's supply function.

The marketplace aggregates the demand functions of the individual buyers to obtain the demand function of the market. In a likewise manner, the market aggregates the supply functions of the sellers to determine the market's supply function. At each point in time, the demand function and supply function of the market share a point where they intercept. This point represents the state of competitive equilibrium of the system that sets the price of power. With the equilibrium price of power found, the static optimization of the marketplace is complete and a transfer of power can exist between the market sellers and market buyers. This solution is a Pareto optimal solution in the multi-objective optimization sense. Figure 6-5 serves as an illustration of the role the marketplace plays in the determination of system control forces, ***u****(t)*.

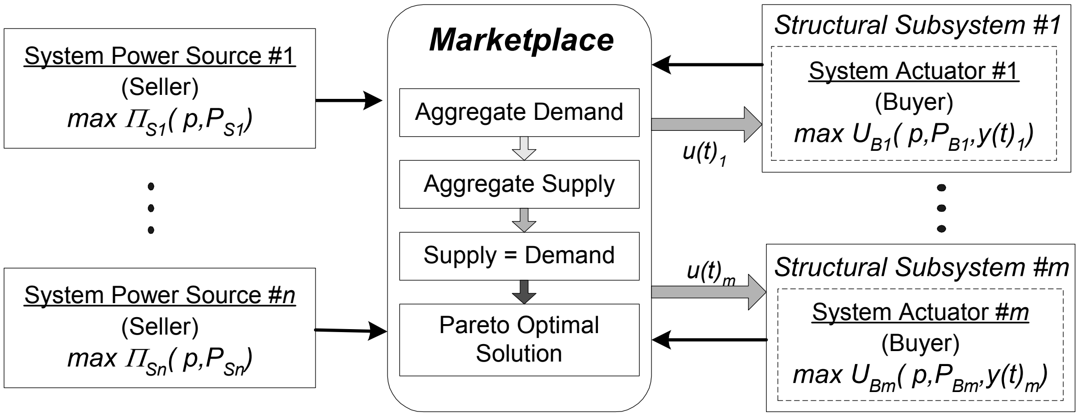

Figure 6-5: Overview of the market-based control system's control objectives

At each time step the goods market is optimized to determine an efficient control solution. When the power is purchased by the market buyers, it transfers some of its wealth to the market sellers. In this study, a production factor market is not modeled. Instead, the money obtained by the market sellers is evenly distributed to the households to represent income for their future purchases.

6.3 Derivation of MBC for a Single Degree-of-Freedom

First, a single degree-of-freedom system is considered in the derivation of market-based control for implementation in structural control systems. Utility and profit functions for the actuators and power sources are proposed with demand and supply functions derived from them. Later, these single degree-of-freedom demand and supply functions are extended with minimal modification to their multiple degree-of-freedom form.

No strict rules exist on the form of the control devices' utility functions as long as they represent some measure of utility derived by the actuators for the purchases of power (Lynch and Law 2000). As a result, the utility function's form is selected to ensure a linear demand function results when the utility function is optimized.

$$U(P,p) = -C_1 pP + C_2 P - \frac{1}{2}P^2 \tag{6.26}$$

The first term on the right-hand side of Equation (6.26) is the total cost of the power consumed. The negative sign on the term's coefficient implies the utility is reduced when the actuator has to spend money for the power purchased. The remaining two terms indicate that when C_2 is greater than half of the power purchased, the utility increases when greater power is used for applying control forces to the dynamic system. C_2 is chosen to ensure this is always the case. Differentiating the utility function of Equation (6.26) and setting it to zero, the demand function of the market buyer is yielded.

$$P_{DEMAND} = -C_1 p + C_2 \tag{6.27}$$

The linear form of the demand function obtained is convenient since it has a negative slope and a positive intercept. The negative slope expresses the sensitivity of consumer demand to price of power. When the price of power is low, system control devices are inclined to purchase more power at the market price. On the other hand, when the price of power rises, devices will purchase less.

The demand function designed will also be directly influenced by structural responses so that when the response of a structure increases, so will the demand of the control devices. For the linear demand function of Equation (6.27), the slope and *y*-axis intercept are chosen to be functions of the dynamic response of the system.

$$P_{DEMAND} = -\left|f(x,\dot{x})\right|p + \left|g(x,\dot{x})\right| \tag{6.28}$$

The slope and intercept point of a device's demand function, *f* and *g*, will vary with the displacement, *x*, and velocity, $\dot{x}$, of the control device's node. An absolute value is taken of the functions relating system response to slope and intercept since these values must be positive to maintain the form of the demand function shown in Equation (6.27). When the structure's displacement and velocity increase, it is natural to expect the demand for power to grow proportionally. Allowing the *y*-axis intercept to increase with increasing structural responses can attain an increase in demand. Likewise, reducing the demand function's slope also attains increased demand. The slope and *y*-intercept of the demand function take the following form:

$$f(x,\dot{x}) = \frac{1}{Tx + Q\dot{x}} \tag{6.29}$$

$$g(x,\dot{x}) = Rx + S\dot{x} \tag{6.30}$$

where T, Q, R, and S, represent the various constants used for tuning the market based controller. Figure 6-6 depicts how the selection of the intercept and slope of the demand function influence its growth.

The profit functions of the market power suppliers follow the form introduced in Equation (6.12).

$$\Pi = R - C = pP - \frac{1}{2}\beta P^2 \tag{6.31}$$

The revenue derived by the sellers is reflected by the first term of Equation (6.31) where the price of power is multiplied by the amount of power sold. The second term is the cost of production and is chosen to be quadratic. A quadratic cost function is chosen to ensure that a linear supply function results. The profit function of Equation (6.31) is maximized to derive the seller's supply function.

$$P_{SUPPLY} = \frac{1}{\beta} p \tag{6.32}$$

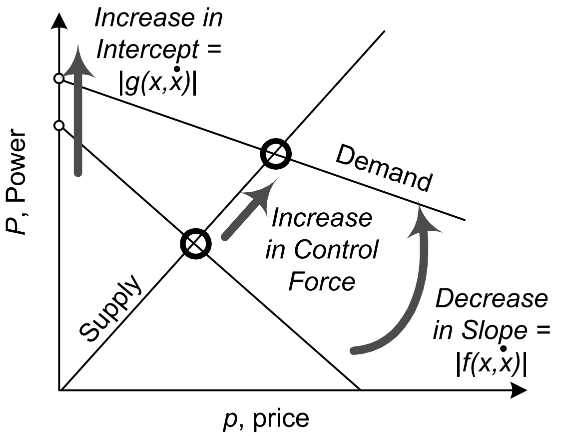

Figure 6-6: Behavior of the buying agent's demand function

The linear supply function reflects the behavior of the market firms well. When the price of power rises, the firms produce more power in order to reap greater revenues. With the intercept at the origin, when the price of power is zero, no producer can gain revenue and therefore no power is produced. The slope of the supply function is the inverse of the coefficient, β.

For a single degree-of-freedom system, the point of competitive equilibrium is where the supply and demand functions intersect. For the selected supply and demand functions, the resulting equilibrium price of power can be found by equating Equations (6.28) and (6.32). Using this equilibrium price, the amount of power purchased by the control device can be determined using Equation (6.28). The control force, *u*, is proportional to the amount of power purchased by the proportionality constant, *K*.

$$u = K\left(\frac{|Rx + S\dot{x}|}{|Tx + Q\dot{x}| + \beta}Tx + \frac{|Rx + S\dot{x}|}{|Tx + Q\dot{x}| + \beta}Q\dot{x}\right) \tag{6.33}$$

The resulting control force is significantly different in form to one traditionally obtained from a centralized LQR analysis. The control law from LQR is linear while for market-based control, the control law of Equation (6.33) is nonlinear. The coefficients of the displacement and velocity terms of the market-based control law vary in relation to the structural response causing a constant movement in the closed-loop system poles (Lynch and Law 2001). This is in contrast to the fixed pole locations of an LQR control law.

6.3.1 Application to a Single Degree-of-Freedom Structure

To illustrate the effectiveness of the market-based control method, a single degree-of-freedom system is considered. A linear lumped mass shear model of a one-story structure is considered subjected to the full scale El Centro (1940, NS) seismic disturbance. Both an LQR and market-based control algorithm are implemented for comparison of control system performance. The structure's natural period is 0.5 seconds with a mass of 158,000 kg and a stiffness of 25,000 kN/m. The structure's damping ratio is assumed to be 5%. For this illustrative structure, no specific control device (active or semi-active) is specified in order to allow the designed LQR and MBC controllers to implement control forces without concern to device limitations. However, a maximum allowable control force of 1,000 kN is imposed on the system actuator. The uncontrolled response of the structure exhibits a maximum absolute displacement of 4.43 cm.

First, an LQR controller is designed and implemented. For the design of the controller, the weighting matrix, ***Q***, is selected with weight applied only on the velocity term of the state vector to cause an increase of damping in the system. The weighting term on actuation effort, ***R***, is varied until the actuator exceeds its capacity. They are given as:

$$\boldsymbol{Q} = \begin{bmatrix} 0 & 0 \\ 0 & 1 \end{bmatrix} \text{ and } \boldsymbol{R} = 1x10^{-13} \tag{6.34}$$

The result is a linear feedback gain matrix presented by Equation (6.35).

$$\boldsymbol{G} = \begin{bmatrix} -1.1257x10^{6} & 2.8255x10^{6} \end{bmatrix} \tag{6.35}$$

Figure 6-7 shows the time-history response of the LQR controlled structure subjected to the El Centro earthquake. The LQR controller is effective in reducing the peak absolute displacement of the single degree-of-freedom structure from 4.43 cm to 1.51 cm.

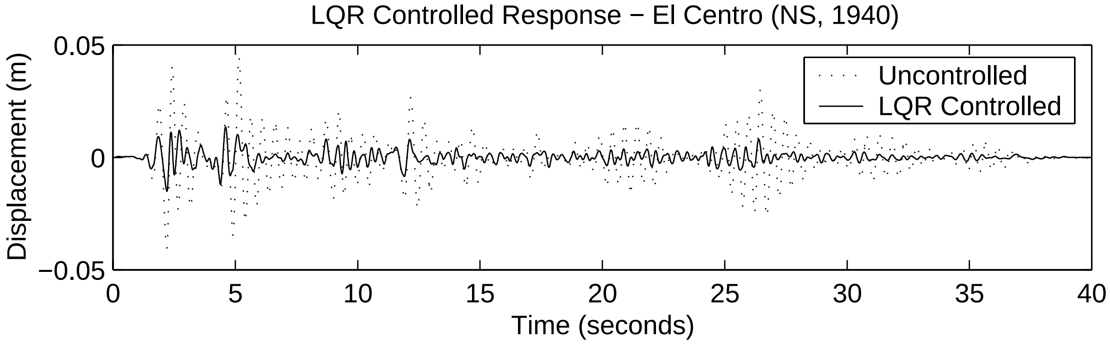

Figure 6-7: Time-history response of LQR controlled SDOF structure

Next, a market-based controller is implemented in the system. The goal of the MBC controller is to attain the same level of response reduction as the LQR controller. The control system designer is free to determine how to select the weighting terms of the market functions. For example, selection of the controller's weighting terms, Q, R, S, T, and β, could be made from a detailed parameter study of the controlled response of the system to various seismic records under a plethora of different weighting terms. However, for this study, the weighting terms are chosen based on engineering judgment of the expected response of the system. To maintain a perspective of how the market mechanism is operating, the weighting terms are selected to normalize the slope and intercept of the demand function at the root mean square values of the uncontrolled system response. This way, large incomprehensible values of power and price do not cloud our visibility of the market's operation. The root mean square value of the uncontrolled response is a convenient normalizing point due to its representation of energy contained in the uncontrolled system.

Considering the response of the uncontrolled structure, the root mean square of the system's uncontrolled displacement and velocity is 0.01 m and 0.12 m/s respectively. Scaling these values to 1, the scaling factors on displacement and velocity are 100 and 8 respectively. These scaling factors serve as our starting point for the values of T and Q, except that Q is increased to 12 to represent an increased importance placed on system velocities. The slope of the supply function, β, is set to 1. To allow for significant variation of the coefficients of the displacement and velocity terms of Equation (6.33), R and S are both selected to be 1. With the weighting factors of the market defined, the control weighting term, K, is to be determined. The actual price of power and the amount purchased based upon the supply and demand functions of the system, will both be less than 1. Therefore, K is varied until desired control results are attained. A scaling factor of $2.2 x 10^6$ is selected for K.

The market-based control solution, with the chosen coefficients, is implemented in the single degree-of-freedom structure. The result is a reduction of the system response to a maximum absolute displacement of 1.50 cm. Figure 6-8 shows the time-history response of the system with an MBC controller implemented. The results clearly indicate that a market-based controller is as effective as the LQR controller in reducing the system response to seismic disturbances.

Consider the two control solutions within the complex domain. As seen in Figure 6-9, the result of the LQR controller is the relocation of the system's open-loop poles (eigenvalues) to new locations in the left half side of the complex plane. The new locations correspond to increased system damping (0.79) with the original natural frequency held nearly constant. This is consistent with the selection of the LQR weighting matrix ***Q***. Different from the LQR's static closed-loop pole locations, the eigenvalues of the MBC controlled system change with the system response measurements. If structural responses are large, the poles migrate further to the left side of the complex plane. The trajectory pattern is consistent with the weighting terms chosen. We select the weight on state response, *Q*, to weigh the system velocities more than displacements. The result is a trajectory that is consistent with greater damping during large system responses with a small increase in the natural frequency of the system. If only increased damping was desired as is the case with the LQR controller designed, then the weighting term on displacement, *T*, should be set to 0.

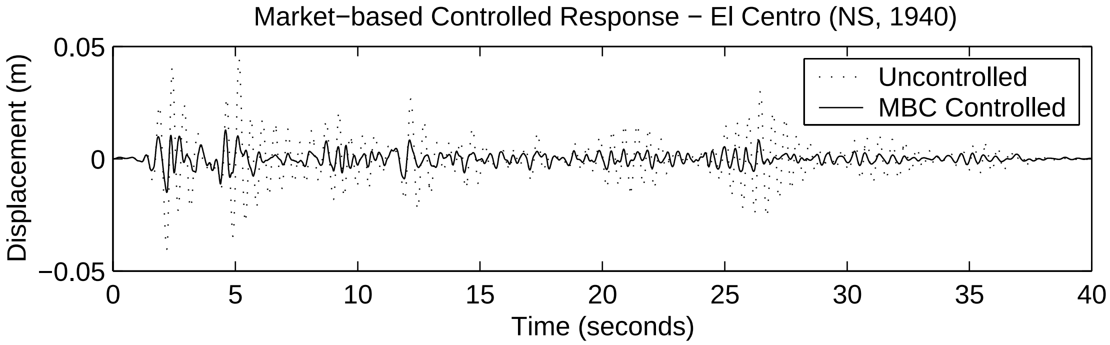

Figure 6-8: Time-history response of market-based controlled SDOF structure

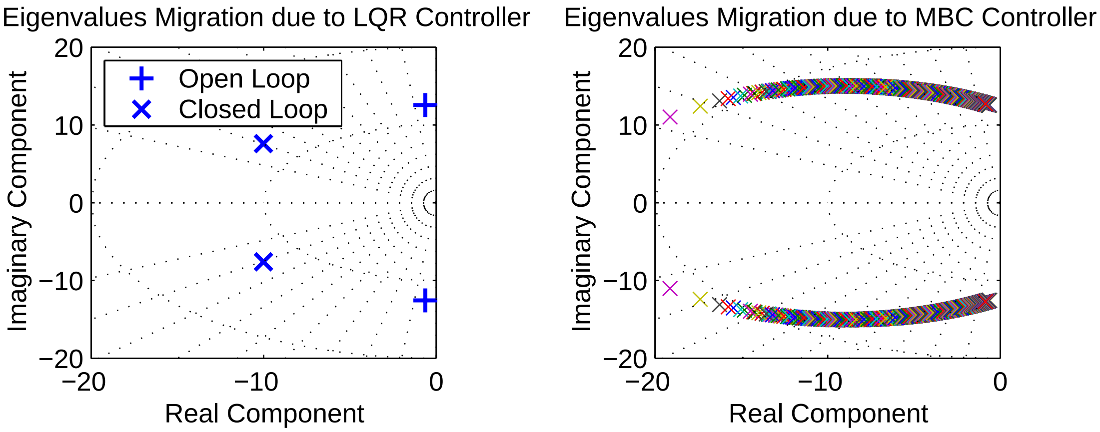

Figure 6-9: Migration pattern of closed-loop poles of the LQR and MBC controllers

While the performances of the two controllers are similar, does one control methodology require more control effort than the other? In consideration of this question, the absolute value of the control force of each controller is added in time. As shown in Figure 6-10, a plot of the accumulated control effort of both controllers reveal that for the single degree-of-freedom system, the MBC controller attains the same control performance with 40% less total control effort. The reduced control effort of the market-based controller can be attributed to the adaptive nature of the controller's feedback coefficients shown in Equation (6.33). Unlike the LQR controller, when system responses grow, the feedback coefficients of the market-based controller increase, providing greater control as needed.

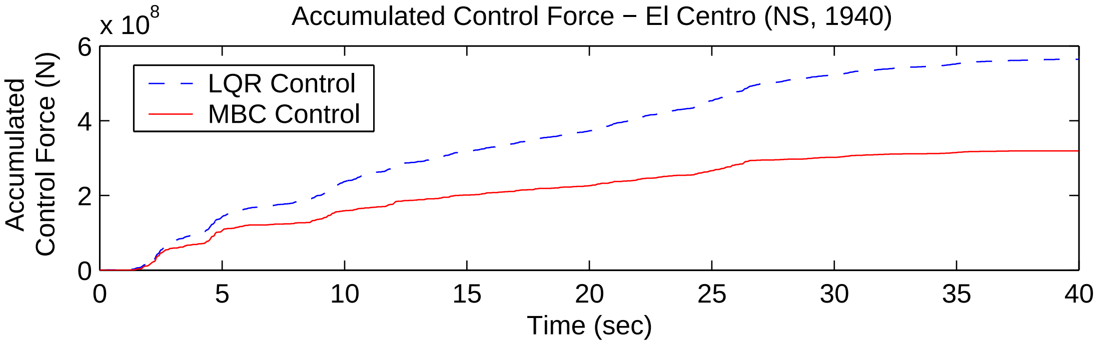

Figure 6-10: Accumulated control force of the LQR and MBC controllers

6.4 Derivation of MBC for Multiple Degrees-of-Freedom

While the results from the single degree-of-freedom system are evidence of the merits of the market-based control algorithm, it represents a simplification since the realistic application of market-based control is in large-scale systems. In this section, the basic laws of supply and demand developed for the single degree-of-freedom system are extended to multiple degrees-of-freedom systems.

In large-scale systems comprised of multiple control devices acting in the role of buyers and system power sources representing market sellers, a true marketplace appears. Not considered in the discussion of the single degree-of-freedom case, but necessary in an environment of multiple buyers and sellers, the concept of wealth is introduced. Each buying agent of the system has an allocation of wealth, W_i, with the subscript i denoting the i^{th} agent of the market. Wealth is a direct measure of the amount of money available to consumers for the purchasing of control power. It represents the budget constraint placed on the household's utility function. Total wealth in the system, W_{TOTAL}, is assumed constant in time throughout the market competition process.

$$W_{TOTAL} = \sum_{i=1}^{m} W_i \tag{6.36}$$

The demand function of each agent will be influenced by the amount of wealth the agent possesses. If a buying agent possesses a large amount of saved wealth, then its demand for power would naturally increase, just as affluent consumers spend more than destitute ones in a real economy. To depict this, the demand function used in the single degree-of-freedom system is augmented with the agent's wealth in the following manner:

$$P_{D_i} = \left(-\left| \frac{1}{Tx_i + Q\dot{x}_i} \right| p + \left| Rx_i + S\dot{x}_i \right| \right) W_i \tag{6.37}$$

To keep the market control system easy to implement, market sellers are not permitted to maintain corporate wealth. Therefore, no modifications of the firms' supply functions are necessary. Rather, the market wealth of the economy is contained solely within the hands of the market buyers. At each step in time, after the equilibrium price of power is established, the market buyers purchase power from the market sellers with a portion of their wealth. Since no production factors market is modeled, the money obtained by the power sellers from the market buyers, is distributed back to the buyers. Each buyer receives an equal share of the total profit made by the market sellers, regardless of the amount of power purchased by that buyer. This is analogous to the labor payment made to workers who are also potential consumers in the marketplace.

The total market demand at each time step is determined by aggregating the demand functions of all *m* buying agents of the market. In a similar fashion, the supply functions of the system's *n* selling agents are aggregated to form a global market supply function. The competitive equilibrium price of power is obtained from the point where the demand of the market equals supply. The result is the equilibrium price of power at each time step.

$$p_{eq} = \frac{\sum_{i=1}^{m} W_i \left| Rx_i + S\dot{x}_i \right|}{\dfrac{n}{\beta} + \sum_{i=1}^{m} \dfrac{W_i}{\left| Tx_i + Q\dot{x}_i \right|}} \tag{6.38}$$

Again, *T, Q, R,* and *S,* are weighting terms of the system buyers' demand functions while β is the inverse proportionality constant of the sellers' supply function. Once the market price is established, each control device will only buy power if the market price at that time step does not exceed its wealth. Once all actuators have purchased power, the amount paid is subtracted from their total wealth.

6.4.1 Stability of the Market-based Control Solution

Stability is defined by a system's tendency to grow or decay in response to an input disturbance to the system. If the response decays, the system is considered stable. However, if the response grows in time, then the system is defined as unstable. The stability of a dynamic system is characterized by the location of the system poles in the complex plane. Given the existence of at least one pole in the right half part of the complex plane, the system is considered unstable and will exhibit growing system response to input disturbances. If all poles are located in the left half part of the complex plane, the system is stable. Various tests for linear system stability exist such as the Routh's Stability Criterion and the Nyquist Stability Criterion (Franklin et al. 1994).

For the LQR controller, closed-loop system stability is guaranteed if two criteria are met; first, the system matrix, ***A***, and the control location matrix, ***B***, of Equation (5.1) must be a controllable pair and second, the weighting matrices ***R*** and ***Q*** of Equation (5.4) are both positive definite (Stengel 1994). The controllability criterion ensures that the controller has influence on all modes, particularly unstable modes, of the system. The positive definite criterion on ***R*** allows for control effort to have a positive effect on the cost function, *J*, while the positive definite criterion on ***Q*** provides penalty on system responses, particularly unstable responses.

Unlike the LQR controller, the current controller derived in the market-based control method has not been shown to be mathematically stable in closed form. Further work is needed to consider the limitations of the controller with regard to stability concerns. However, when applied in systems that utilize semi-active control devices, stability is less of a concern since the devices do not add mechanical energy directly to the system and therefore the system is bounded-input bounded-output (BIBO) stable (Housner et al. 1997).

6.5 Application of MBC to Large-Scale Structures

Market based control is applied to two multiple degree-of-freedom systems. The first structure considered is the Kajima-Shizuoka Building recently constructed in Shizuoka, Japan (Kurata et al. 1999). The structure is a five story steel structure employing 8 semi-active hydraulic dampers (SHD) on the first 4 stories of the structure. The second system is the benchmark structure of Chapter 5 with 36 SHD dampers installed throughout the twenty-story steel structure. In simplifying the analysis, each structure is modeled as a lumped mass shear model that sustains perfect elastic deformations. The hydraulic dampers selected are modeled as Maxwell damping elements in the linear structural system. Major reductions of displacements are sought from the uncontrolled to the controlled response of the linear structures utilizing an MBC controller. The MBC control solution is compared to one obtained from a centralized LQR controller.

6.5.1 The 5-Story Kajima-Shizuoka Building

The Kajima-Shizuoka Building is a five story steel structure roughly 19 m in height. With plan dimensions of 11.8 m by 24 m, the structure has significant flexibility in the direction of its short plan dimension (Kurata et al. 1999). Figure 6-11 illustrates the structural design of the Kajima-Shizuoka Building while Table 6-1 is a summary of the structure's stiffness and mass properties. The first five horizontal modal frequencies of the building in the weak transverse direction are 1.01, 2.86, 4.55, 5.88 and 6.67 Hz respectively.

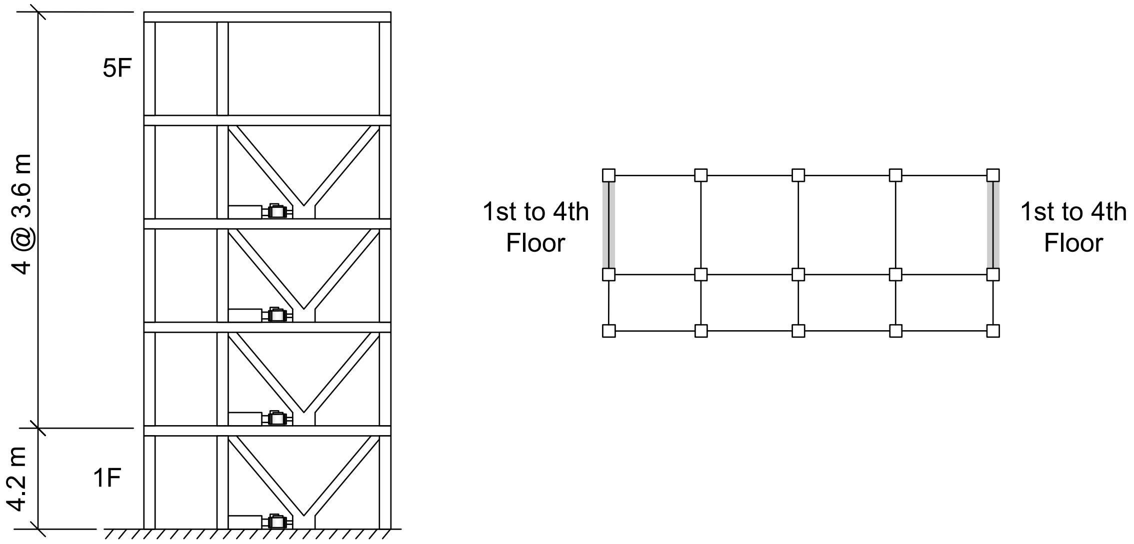

Figure 6-11: Kajima-Shizuoka Building, Shizuoka, Japan

Table 6-1: Structural properties of the Kajima-Shizuoka Building

Floor	Seismic Mass	Story Stiffness	Number of SHD Devices
1	215.2 x 10^3 kg	147.0 x 10^3 kN/m	2
2	209.2 x 10^3 kg	113.0 x 10^3 kN/m	2
3	207.0 x 10^3 kg	99.0 x 10^3 kN/m	2
4	204.8 x 10^3 kg	89.0 x 10^3 kN/m	2
5	266.1 x 10^3 kg	84.0 x 10^3 kN/m	-

The designed lateral resisting system for the structure in the weak transverse direction is augmented with a total of 8 semi-hydraulic dampers upon the first four floors of the structure. Two semi-active hydraulic dampers (SHD) are used per floor and are placed at the apex of K-braces. The associated stiffness of the K-braces are chosen to ensure deformation is dominated by the dampers resulting in better performance when the dampers are controlled as compared to using them in a passive capacity. The stiffness of the K-braces on the first floor is 438 kN/mm each while the stiffness of all braces upon the second through fourth story is 565 kN/mm.

The intention of the structural designers was to effectively reduce structural displacements by operating the system's SHD dampers through a centralized control system. Kurata et al. (1999) have designed and implemented an LQR strategy for the Kajima-Shizuoka Building and have shown its effectiveness in attaining the control objective of reducing inter-story drifts. In this study, a market-based controller will be designed and implemented. To assess the benefits of the decentralized MBC controller, a centralized LQR controller will also be utilized in controlling the Kajima-Shizuoka building. Both controllers will be designed with respect to their performance during the El Centro seismic disturbance. Once implemented, the two controllers are analyzed using the El Centro, Taft and Northridge records that have been normalized to a peak absolute ground velocity of 50 cm/s.

The design of an MBC controller is considered first. Its design is dependent upon the prudent selection of the weighting coefficients of the supply and demand functions depicted in Equations (6.32) and (6.37). Drawing on the success of the selection process used for the single degree-of-freedom system, the weighting terms of the supply and demand functions are selected in a similar fashion. First, given that the fifth story displacement and velocity responses of the uncontrolled system are greatest, they are considered in the tuning of the weighting terms. Under the scaled El Centro disturbance, the root mean square of the uncontrolled fifth story displacement and velocity time-histories are determined to be 0.07 m and 0.34 m/s. The root mean square values will be used to determine the weighting terms of the demand function's slope, *Q* and *T*. To scale the root mean square values to 1, the weighting term on the slope function's displacement and velocity are about 14 and 3, respectively. This will in effect set the slope of the demand function to 1 for the root mean square response of the fifth story. However, to give more emphasis to the control system's velocity solution versus letting the control system be dependent upon increasing system stiffness, the *Q* term is increased three-fold to 9. Considering the weighting terms of the demand function intercept, *R* and *S*, they are scaled to give an intercept of 1 for the root mean square values of displacement and stiffness. A weight of 8 is given to *R* and a weight of 2 to *S*. The slope of the supply function for the one market seller is set to one. The conversion factor between power and control force, *K*, is used to tune the system to ideal performance. The following summarizes the MBC controller's weighting terms:

$$R = 8; \quad S = 2; \quad T = 15; \quad Q = 10; \quad \beta = 1; \quad K = 1x10^{5} \tag{6.39}$$

In the Kajima-Shizuoka Building, each degree-of-freedom (floor) is modeled as a market buyer and therefore has control over the two control devices at that floor. Hence, the first market buyer corresponds to the first floor, the second buyer corresponds to the second floor, and so on. Since one battery is provided by the control system for power, only a single market seller is modeled.

Given the dominance of the first mode of response of the system, maximum structural responses under disturbances are assumed to increase in increasing height of the structure. To give buying agents in the upper stories more initial wealth for purchasing power from the system sellers, the following initial wealth distribution is used:

$$W_1 = 100; \quad W_2 = 150; \quad W_3 = 300; \quad W_4 = 400; \quad W_5 = 0 \text{ (no control device)} \qquad (6.40)$$

Roughly speaking, the Pareto optimal price of competitive equilibrium of the system that results will be centered close to 1. In light of this fact, the values of the initial wealth for the buyers are chosen such that the buyers will not deplete their wealth too quickly during a seismic disturbance.

For the design of the LQR controller, the weighting matrix on state response, ***Q***, is selected with the objective of reducing system velocity responses. The weighting on control, ***R***, is increased to a point of actuation saturation.

$$\boldsymbol{Q} = \begin{bmatrix} 0 & \boldsymbol{I} \end{bmatrix} \text{ and } \boldsymbol{R} = 1x10^{-13}\left[\boldsymbol{I}\right] \qquad (6.41)$$

As can be seen in Figure 6-12, a significant reduction of the structure's maximum absolute inter-story drifts are significant for both the LQR and MBC controller when compared to the uncontrolled and passively controlled response. In comparing the performance of the MBC and LQR controllers, it can be safely concluded that both yield similar reductions of structural response. In the case of the Taft and Northridge earthquakes, the MBC controller is marginally better while for the El Centro record, the LQR controller is marginally better.

In considering the market mechanism, it is interesting to consider the variation of the Pareto optimal solution over time. To do so, let us consider the variation in the market price in Figure 6-13 for the El Centro analysis. A strong relationship exists between the equilibrium price of power and the input ground motion to the structure. As the structural responses of the system increase with respect to the input ground acceleration, the demand for control power increases. Given the fixed nature of the supply function, the result is an increase in the equilibrium price of power.

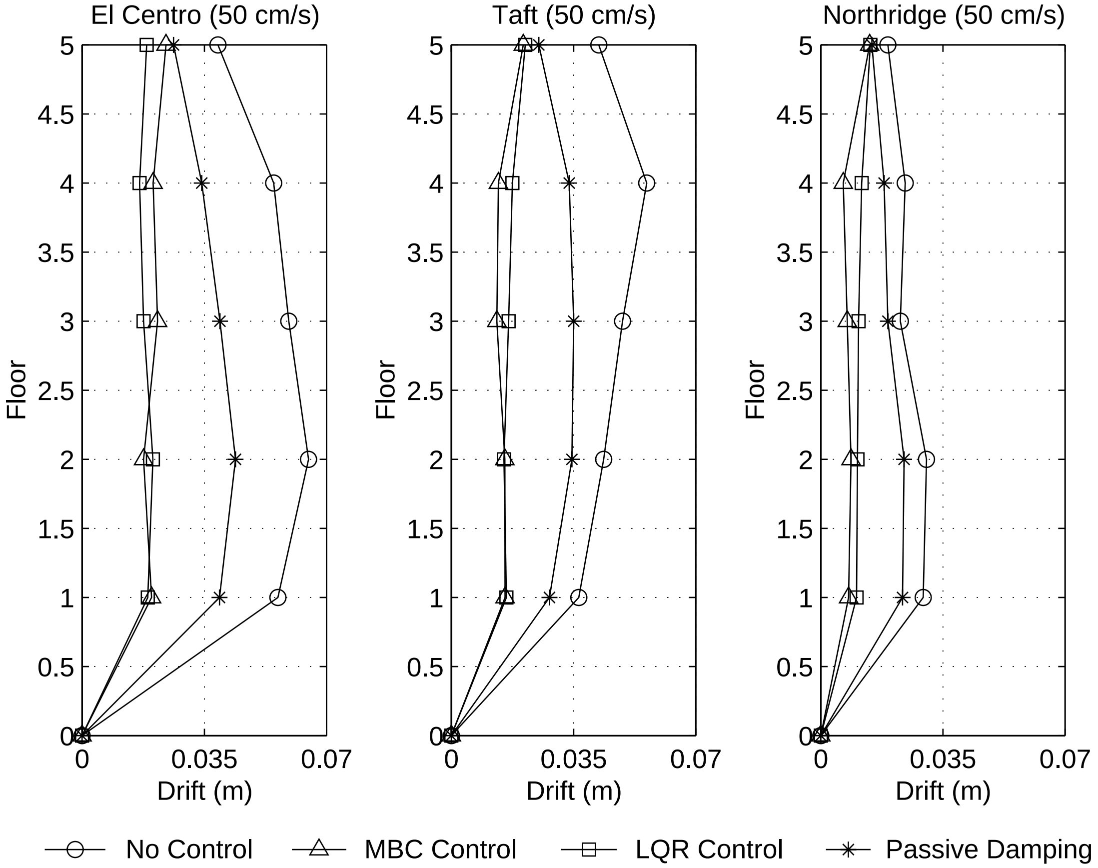

Figure 6-12: Shizuoka Building maximum absolute interstory drifts (LQR, MBC)

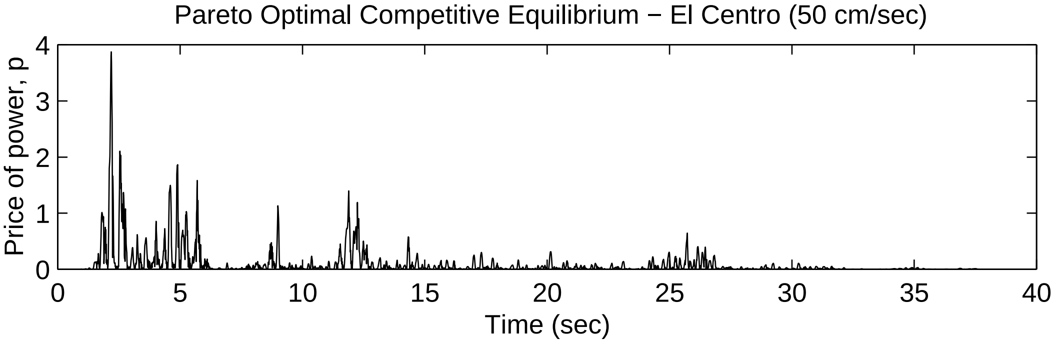

Figure 6-13: Time-history of the MBC Pareto optimal pricing solution

Again, the total control effort of the control system is considered to ensure that the MBC controller is not using excessive amounts of control energy to remain competitive with the LQR solution. As seen in Figure 6-14, the MBC controller is using approximately 25% more control effort during all three seismic disturbances. With a different approach to tuning the MBC market function's coefficients, the control effort of the solution could be reduced to levels similar to those of the LQR solution.

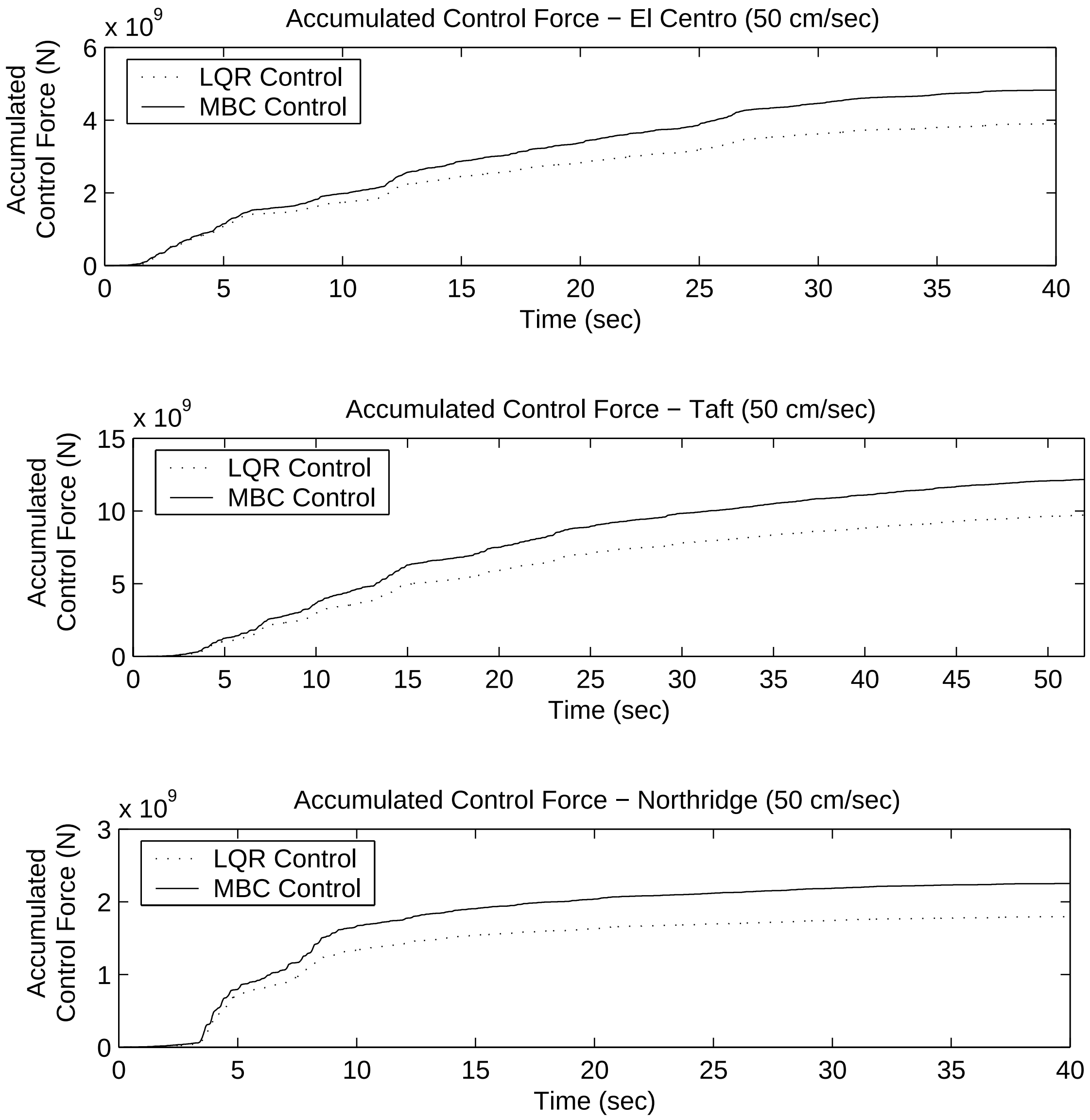

Figure 6-14: Shizuoka Building accumulated control effort (LQR, MBC)

6.5.2 Benchmark 20-Story Steel Structure

To illustrate the effectiveness of the market-based control method, the large benchmark structure of Chapter 5 is used. A total of 36 semi-active SHD devices are installed in the analytical model using the same location configuration used for the analysis of the decentralized control techniques. This distribution should be sufficient in reducing the uncontrolled lateral response of the structure during large earthquakes. Given the size of the structure and the large number of system control devices in use, the associated benefits of pursuing a decentralized control approach makes market-based control a prudent control choice.

The top story response is considered in the determination of the weighting coefficients used in the MBC controller design. The root mean square displacement of the uncontrolled response to the El Centro seismic record is determined to be 0.1353 m while the root mean square velocity of the top story is 0.3195 m/s. As a result, *T* and *Q,* are initially chosen to be 8 and 3 respectively. To emphasize that the controller increases damping instead of stiffness, the *Q* term is increased to 6. To normalize the intercept of the demand function to the root mean square values of displacement and velocity, the *R* and *S* weights are chosen to be 4.5 and 1.5 respectively. Again, the slope of the supply function is fixed to 1. *K* is varied until desirable control results are obtained and the control effort of the MBC controller is within 5% of the LQR controller. The resulting weighting terms are presented in Equation (6.42).

$$R = 4.5; \quad S = 1.5; \quad T = 8; \quad Q = 6; \quad \beta = 1; \quad K = 2x10^5 \tag{6.42}$$

Similar to the Kajima-Shizuoka Building, only one market seller is modeled and each floor of the structure is represented by a market buyer. Therefore, a market buyer determines the control force for all of the control devices situated upon its floor. The wealth distributed to the market buyers at the outset of the analysis is:

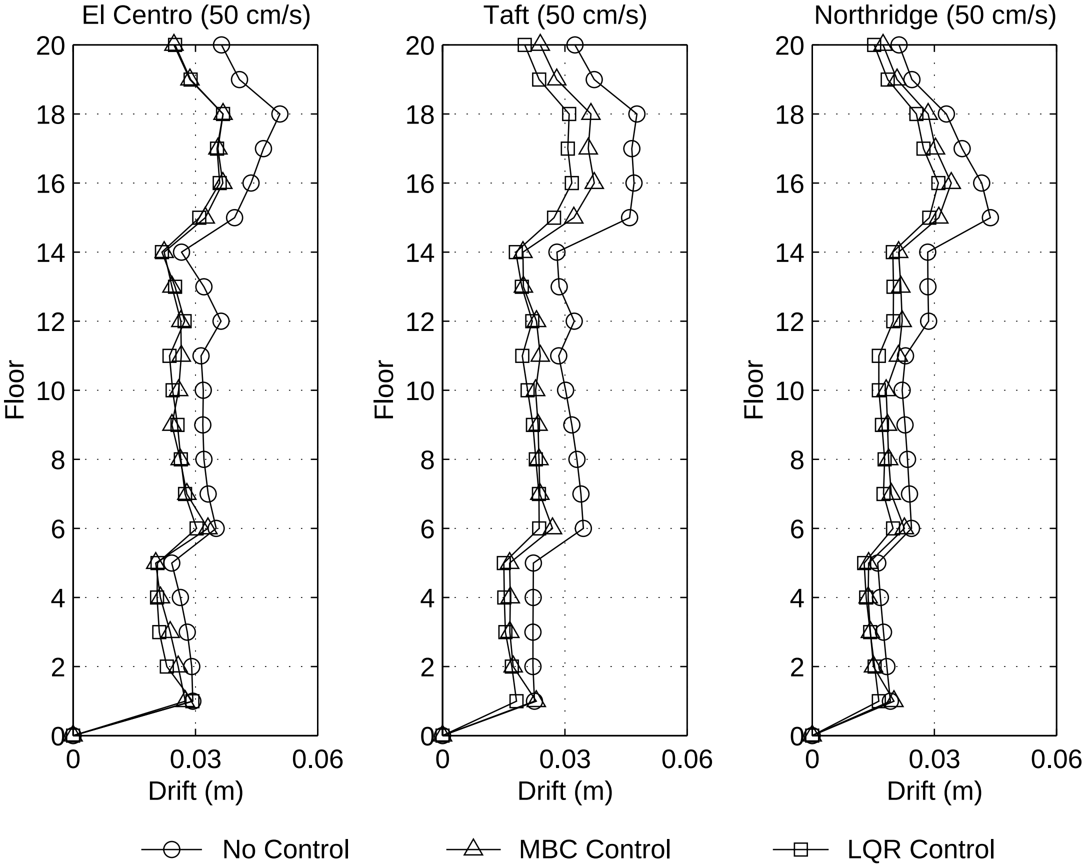

Figure 6-15: Benchmark structure maximum absolute interstory drifts (LQR, MBC)

$$\begin{gathered} W_1 = 0; \quad W_2 = W_3 = W_4 = W_5 = 600; \quad W_6 = 0; \\ W_7 = W_8 = W_9 = W_{10} = 220; \quad W_{11} = 0; \quad W_{12} = W_{13} = W_{14} = W_{15} = 220; \\ W_{16} = 0; \quad W_{17} = W_{18} = W_{19} = W_{20} = 100; \end{gathered} \tag{6.43}$$

The LQR controller already designed in Chapter 5 will be used for comparison with the market-based control performance where the weighting matrices selected are:

$$\boldsymbol{Q} = \begin{bmatrix} \boldsymbol{I} & 10\boldsymbol{I} \\ 10\boldsymbol{I} & 100\boldsymbol{I} \end{bmatrix} \text{ and } \boldsymbol{R} = 1x10^{14}[\boldsymbol{I}] \tag{6.44}$$

Figure 6-15 depicts the effectiveness of the LQR and MBC controllers. As can be seen from the results, the responses obtained from both controllers are again nearly identical.

They are both effective in reducing the response of the structure by as much as 50% for some floors of the system. Not only has the selected gain, *K,* attained suitable performance levels, but as shown in Figure 6-16, it has also been correctly tuned to keep

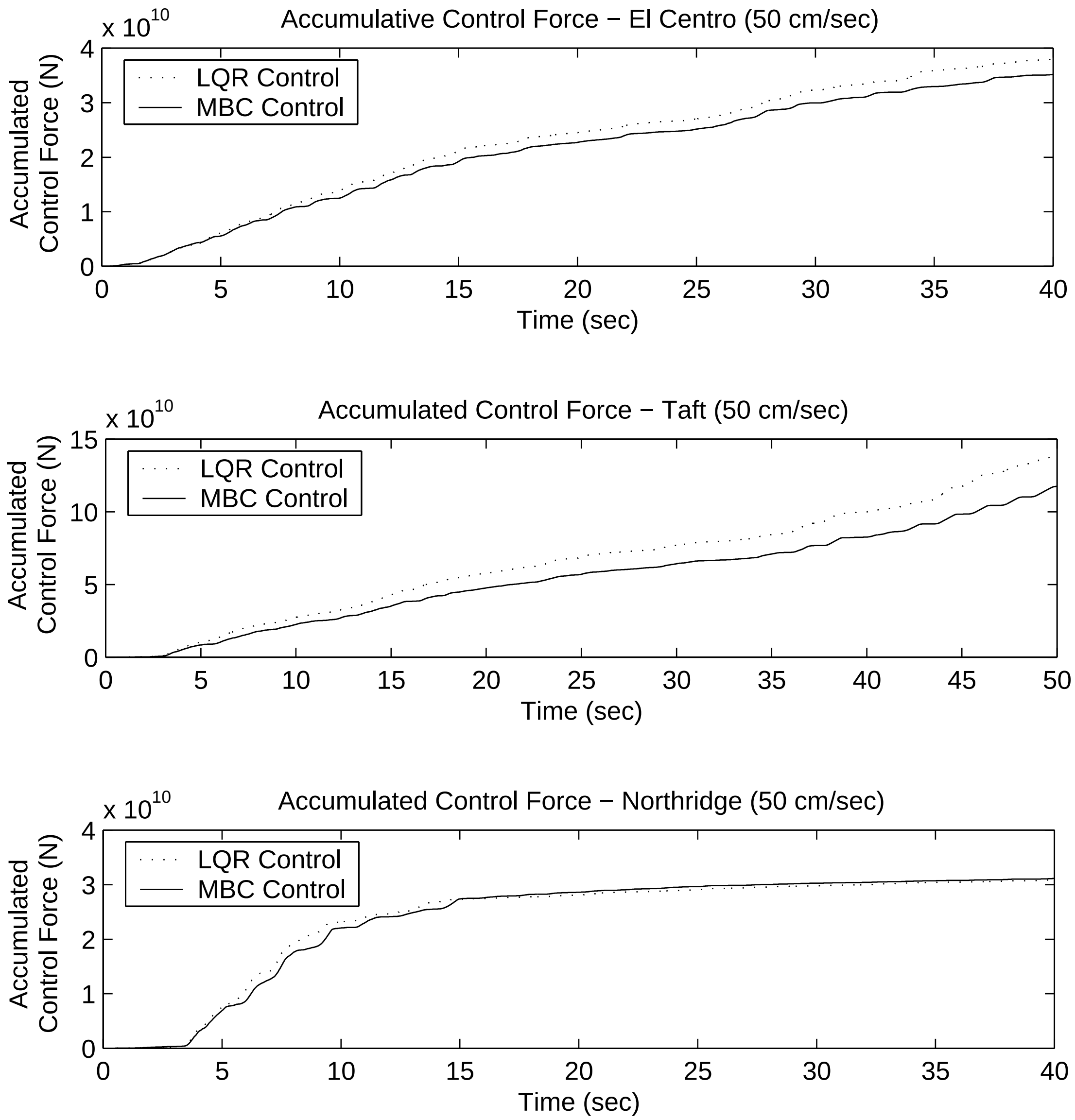

Figure 6-16: Benchmark structure accumulated control effort (LQR, MBC)

the MBC control effort within 5% of the LQR control effort. For both the El Centro and Taft seismic records, the LQR controller requires as much as 3% more effort than the MBC controller. For the Northridge disturbance, the control efforts of both controllers are within 1% of each other.

6.6 Summary

The origins of market-based control are from the realm of static econometric optimization. By solving the static optimization problem at each discrete time step, a solution results that approximates a solution yielded by a dynamic optimization problem. Adaptation of the static optimization approach for application in a structural system renders the approach an effective control technique for limiting structural deflections during earthquakes. For the one-degree-of-freedom system, the market-based method yields results nearly identical to the LQR results. For the Kajima-Shizuoka Building and the 20-story benchmark structure, significant story drift reductions were attained with market-based control. The results of the market-based control solution illustrate the potential applicability of the approach to structural control. In conclusion, this chapter represents a significant advancement of the market-based control approach.

Many interesting research issues still remain for market-based control. First, the selection of utility and profit functions was governed by our desire to ultimately yield linear demand and supply functions for the market participants. Furthermore, a large number of tuning constants (R, S, T, and Q) were provided in the market demand function to allow for flexibility of the approach during implementation. A better derivation is required that would be more rational in its selection of demand and supply functions and would be less dependent upon tuning constants. This issue will be addressed in Chapter 7 where a new approach to market-based control is explored using naturally occurring energy measures of the dynamic system.

A second research issue to address is the development of a means of inter-device communication that would allow marketplace information to propagate through the system in real-time. A centralized controller responsible for the aggregation of market demand and supply functions should be avoided and more innovative decentralized data flow should be considered. For example, a two-layer hierarchical data aggregation model could be employed where the global marketplace is decomposed to individual submarkets on the first layer and market information transferred from one market to the others on the second hierarchical layer.

Chapter 7

Energy Market-Based Control

The market-based control approach developed in Chapter 6 has proven to be very effective in limiting the deflection of structures during large seismic disturbances. Starting with the utility function of the market-buyers (actuators) and the profit function of the market-sellers (power sources), a static optimization problem is discretely solved at each time step, providing an approximate piecewise solution to the dynamic optimization problem.

The selection of the market utility and profit functions, as presented in the previous chapter, is rather ad-hoc, where a desire to yield linear demand and supply functions governed. The convenience provided by linear functions is an ability to solve for the competitive price of power algebraically. The only constraint in modeling the demand and supply functions was the intention to capture the intuitive behavior of buyers and sellers that would interact in a market centered on the commodity of control power. One shortcoming of market-based control, as previously derived, is the large number of weighting coefficients used to attain suitable control performances. For example, four coefficients (R, S, T, and Q) are included in Equation (6.37) to ensure flexibility in tuning the demand function for each implementation of market-based control.

In this chapter, the derivation of market-based control is revisited with two goals in mind. First, the approach is to be modeled in a more rational manner that will enhance its attractiveness to the structural engineering community. Second, a derivation is sought that is less dependent upon multiple tuning coefficients for the attainment of ideal control performance. To accomplish the first goal, measures of energy that exist within the dynamic system are used to model the market demand and supply functions. Using energy measures in the derivation also leads to fewer tuning constants to attain suitable performance. The new approach is termed energy market-based control (EMBC).

Once derived, the performance of EMBC will be explored to assess its performance during seismic excitations. The control method is implemented in both the Kajima-Shizuoka Building and the 20-story benchmark structure. One feature to be explored is the robustness of the EMBC approach. As the scale of the control solution grows with greater number of control devices used to limit system deflections, a situation of some devices not working properly or even at all, must be addressed. Hence, a control solution is sought such that the system suffers minimal degradation in performance during scenarios of actuation failure. It will be shown that the piecewise static optimization solution of energy market-based control is more robust than those provided by the traditional centralized linear feedback control approaches.

7.1 Structural Energy during Seismic Disturbances

The energy balance of a structural system during a seismic disturbance can easily be derived. First consider a control system for an *n* degrees-of-freedom structural system subjected to a seismic disturbance. The equation of motion can be written as:

$$\boldsymbol{M}\ddot{\boldsymbol{x}}(t) + \boldsymbol{C}\dot{\boldsymbol{x}}(t) + \boldsymbol{K}\boldsymbol{x}(t) = -\boldsymbol{M}\{\boldsymbol{1}\}\ddot{x}_g(t) + \boldsymbol{D}\boldsymbol{u}(t) \tag{7.1}$$

The displacement response vector of the system is $\boldsymbol{x}(t)$, the control forces applied to the system by *m* actuators are represented by $\boldsymbol{u}(t)$, and the scalar input ground displacement is $x_g(t)$. The mass, damping, and stiffness matrices are *n* x *n* in dimension and are denoted by $\boldsymbol{M}$, $\boldsymbol{C}$, and $\boldsymbol{K}$, respectively. It is assumed that the mass, damping and stiffness matrices are symmetric. $\boldsymbol{D}$ is the *n* x *m* location matrix for the application of control forces. A vector representing the absolute displacement of the system, $\boldsymbol{y}(t)$, is introduced.

The absolute displacement of the system is simply the input ground displacement, $x_g(t)$, added to each term of the relative displacement vector, $\boldsymbol{x}(t)$. The introduction of the relative acceleration response simplifies Equation (7.1).

$$\boldsymbol{M}\ddot{\boldsymbol{y}}(t) + \boldsymbol{C}\dot{\boldsymbol{x}}(t) + \boldsymbol{K}\boldsymbol{x}(t) = \boldsymbol{D}\boldsymbol{u}(t) \tag{7.2}$$

Equation (7.2) represents the equilibrium balance of forces in the structural system at any point in time. Integrating the forces over the response path from the initial position, $\boldsymbol{x}_o$, to the final position, $\boldsymbol{x}_f$, yields the energy of the balanced system (Wong and Yang 2001).

$$\int_{x_o}^{x_f} \ddot{\boldsymbol{y}}^T \boldsymbol{M} d\boldsymbol{x} + \int_{x_o}^{x_f} \dot{\boldsymbol{x}}^T \boldsymbol{C} d\boldsymbol{x} + \int_{x_o}^{x_f} \boldsymbol{x}^T \boldsymbol{K} d\boldsymbol{x} = \int_{x_o}^{x_f} \boldsymbol{u}^T \boldsymbol{D}^T d\boldsymbol{x} \tag{7.3}$$

The equation of balanced energy in the system is rewritten to reflect the relationship that exists between the derivative of the absolute response, $d\boldsymbol{y}$, the derivative of the relative response of the structure, $d\boldsymbol{x}$, and the vector derivative of the response of the ground, $d\boldsymbol{x}_{\boldsymbol{g}}$. The derivative, $d\boldsymbol{x}_{\boldsymbol{g}}$, is equal to $\{\mathbf{1}\}\mathrm{d}x_g$.

$$\int_{x_o}^{x_f} \ddot{\boldsymbol{y}}^T \boldsymbol{M}\left(d\boldsymbol{y} - d\boldsymbol{x}_g\right) + \int_{x_o}^{x_f} \dot{\boldsymbol{x}}^T \boldsymbol{C} d\boldsymbol{x} + \int_{x_o}^{x_f} \boldsymbol{x}^T \boldsymbol{K} d\boldsymbol{x} = \int_{x_o}^{x_f} \boldsymbol{u}^T \boldsymbol{D}^T d\boldsymbol{x} \tag{7.4}$$

The terms of Equation (7.4) can be reordered as:

$$\int_{x_o}^{x_f} \ddot{\boldsymbol{y}}^T \boldsymbol{M} d\boldsymbol{y} + \int_{x_o}^{x_f} \dot{\boldsymbol{x}}^T \boldsymbol{C} d\boldsymbol{x} + \int_{x_o}^{x_f} \boldsymbol{x}^T \boldsymbol{K} d\boldsymbol{x} - \int_{x_o}^{x_f} \boldsymbol{u}^T \boldsymbol{D}^T d\boldsymbol{x} = \int_{x_o}^{x_f} \ddot{\boldsymbol{y}}^T \boldsymbol{M} d\boldsymbol{x}_g \tag{7.5}$$

The first term on the left-hand side of Equation (7.5) reflects the kinetic energy of the system while the third term represents the strain energy of the system. Both measures of energy are based upon conservative forces and are therefore path independent. Their measure is only dependent upon current and initial positions of the system. Assuming the system is initially at rest, the kinetic and strain energy of the system can be rewritten and Equation (7.5) updated.

$$\frac{1}{2}\dot{\boldsymbol{y}}^T \boldsymbol{M}\dot{\boldsymbol{y}} + \int_{x_o}^{x_f} \dot{\boldsymbol{x}}^T \boldsymbol{C} d\boldsymbol{x} + \frac{1}{2}\boldsymbol{x}^T \boldsymbol{K}\boldsymbol{x} - \int_{x_o}^{x_f} \boldsymbol{u}^T \boldsymbol{D}^T d\boldsymbol{x} = \int_{x_o}^{x_f} \ddot{\boldsymbol{y}}^T \boldsymbol{M} d\boldsymbol{x}_g \tag{7.6}$$

The four terms of the left-hand side of Equation (7.6) represent, respectively, the kinetic (KE), damping energy (DE), strain energy (SE) and control energy (CE) of the system. These four energies balance the input energy (IE) resulting from the ground motion as shown on the right-hand side of Equation (7.6).

$$KE + DE + SE + CE = IE \tag{7.7}$$

7.2 Derivation of Energy Market-Based Control

The derivation of energy market-based control (EMBC) is centered upon a marketplace allocating the scarce commodity of control energy. The method begins with the selection of demand and supply functions that reflect measures of energy in the system. The demand and supply function will each contain one tuning constant that can be used to vary their sensitivities. To reflect the limited capacity of the system power sources in the EMBC approach, the supply function of the marketplace sellers will be a function of their available control energy. This is in contrast to the MBC approach where available control energy was assumed constant in time. The constant nature of the supply function is not accurate unless the market sellers possess a nearly infinite amount of power.

7.2.1 Demand and Supply Functions for EMBC

The form of the demand function is selected to reflect two intentions of the market buyers. First, when the price of control energy is zero, the demand of the market buyer is equal to the input energy applied at the buyer's degree-of-freedom. Second, the demands of the market buyers asymptotically converge toward zero at infinite prices. To encapsulate these two characteristics, an exponential demand function for the i^{th} market buyer, is proposed.

$$CE_i = W_i \left| \ddot{y}_i(t) m_i dx_g \right| e^{\frac{-2p\alpha}{\dot{y}_i^2 m_i + x_i^2 k_i}} \tag{7.8}$$

The y-axis intercept is equal to the instantaneous input energy of the ground motion at a particular degree-of-freedom multiplied by the market buyer's wealth, W_i. The exponential decay of demand is dependent upon the kinetic and strain energy of the system as depicted by the exponential term's denominator. As the response of the system increases due to greater kinetic and strain energy, the rate of decay decreases. The tuning constant, α, is provided to control the sensitivity of the demand function. As α increases, the demand function's decay becomes more rapid. Figure 7-1 serves as an illustration of the market demand function due to variations in the input ground motion and structural response.

The control system's power sources represent the market sellers whose actions are described by supply functions. Each market seller has in its possession a certain amount of control energy. Again, two observations of the market seller's behavior are required before specifying a suitable supply function. First, if the price of power is set to zero, no market seller is willing to sell. Second, as the price grows to infinity, each market seller would be willing to sell all of its remaining control energy, L_i. As a result, the following supply function is proposed:

$$CE_i = L_i \left(1 - e^{-\beta p}\right) \tag{7.9}$$

Equation (7.9) provides an origin intercept in addition to an asymptotic convergence to the remaining control energy at very large market prices. The constant β is used to provide a means of adjusting the supply function. Figure 7-2 graphically illustrates the market supply function.

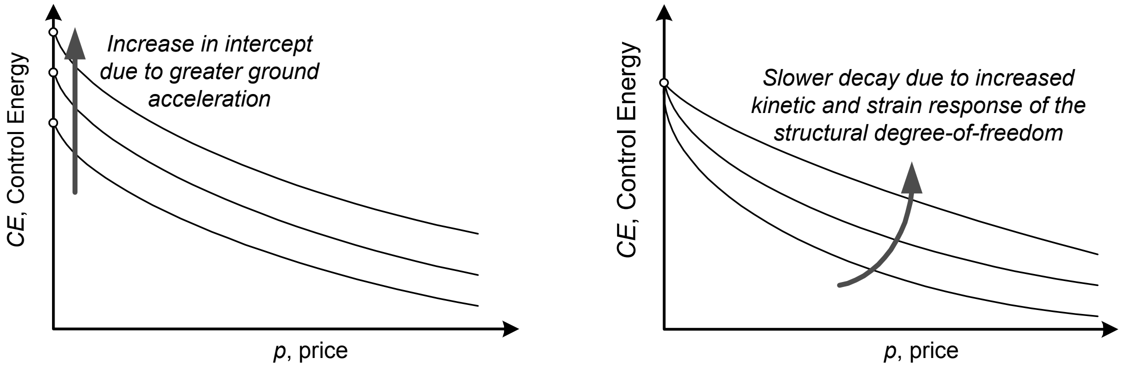

Figure 7-1: Demand function of the energy marketplace

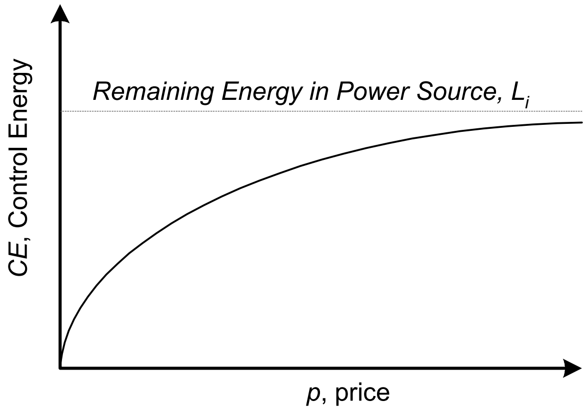

Figure 7-2: Supply function of the energy marketplace

7.2.2 Equilibrium Price of Power

With the demand and supply functions for all market participants established, the Pareto optimal price at each time step can be readily determined. First, the demand functions of all the market buyers are aggregated to make a single marketplace demand function. If the demand function of Equation (7.8) is reduced in notation to Ce^{-Ap}, then the aggregate demand of the N energy marketplace buyers is simply:

$$CE = C_1 e^{-A_1 p} + C_2 e^{-A_2 p} + \cdots + C_N e^{-A_N p} \tag{7.10}$$

In a similar fashion, the supply functions of the market sellers are aggregated to derive the total marketplace supply function.

$$CE = L_1\left(1 - e^{-\beta p}\right) + L_2\left(1 - e^{-\beta p}\right) + \cdots + L_N\left(1 - e^{-\beta p}\right) = L_T\left(1 - e^{-\beta p}\right) \tag{7.11}$$

Since the value of ($1-e^{-\beta p}$) is independent of the degree-of-freedom, the aggregate supply function reduces to the total remaining control energy contained within the marketplace, L_T, times the exponential function ($1-e^{-\beta p}$) as shown on the right-hand side of Equation (7.11). Hence, whether the supply side of the marketplace appears as one market seller or multiple market sellers, the end result of the aggregate supply function is the same. While control systems today typically employ a centralized power source, the market-based control approach can now accommodate systems with multiple distributed power sources.

The aggregate demand function is set equal to the aggregate supply function to determine the competitive equilibrium price of energy for a given time step. A graphical interpretation of the equilibrium solution is shown in Figure 7-3 as the price of power at the point of intersection between the global demand and supply functions. It can be shown that an intersection point always exists. The solution represents a Pareto optimal price of control energy for the marketplace.

At each time step, the market-based controller numerically determines the price of control energy. After the price has been determined, each market buyer determines how much control energy it purchases based on its individual demand function. In turn, the amount of control energy that is purchased by each system actuator is used to determine the applied control force. Given the instantaneous control energy purchased by an actuator, the control force u_i can be determined from Equation (7.12).

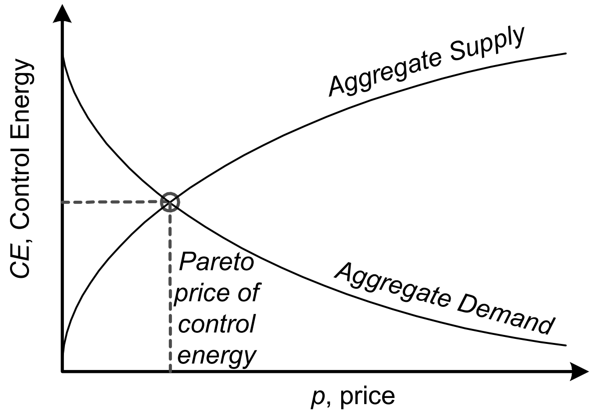

Figure 7-3: Determination of the competitive equilibrium price of control energy

$$CE = u_i \Delta x_i \tag{7.12}$$

After control energy has been purchased, the energy is subtracted from the system power sources. In a similar fashion, the amount of energy purchased by an actuator times the market price per unit power determines the amount of wealth removed from each actuator's total wealth. The money spent on purchasing control energy is then equally redistributed amongst the market buyers as labor income. If a potential market buyer has not taken part in purchasing control energy, then no money is spent by the buyer nor does the buyer receive income after the transaction.

7.2.3 EMBC Implementation in the Kajima-Shizuoka Building

With the EMBC marketplace clearly defined, the Kajima-Shizuoka Building is used to illustrate its implementation. The structural details of the building are summarized in Table 6-1. As illustrated in Figure 7-4, two additional semi-hydraulic damper (SHD) devices are added to the fifth story of the structure, resulting in a total of 10 SHD devices employed. To quantify the performance of the EMBC solution, the structure is controlled for the El Centro, Taft, and Northridge seismic disturbances. For the three earthquake records selected, peak absolute ground velocities are normalized to a value of 50 cm/s.

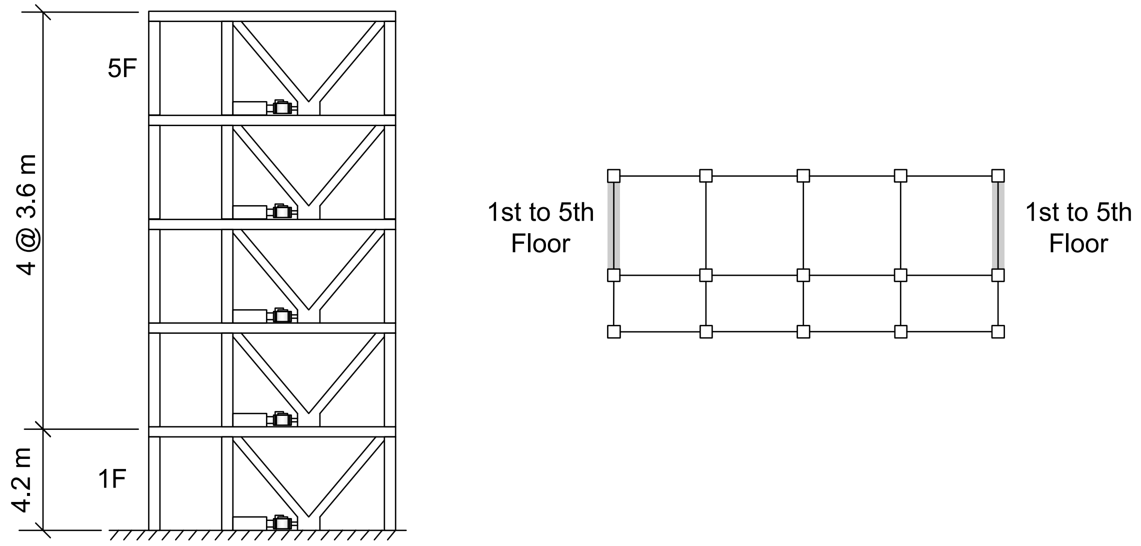

Figure 7-4: Modified Kajima-Shizuoka Building with 10 SHD devices

For the implementation of the EMBC controller, the demand and supply constants are set to unity.

$$\alpha = 1 \qquad \beta = 1 \tag{7.13}$$

It is determined that values of unity for these two constants make the supply and demand functions sufficiently sensitive to yield excellent control results. Coupling the two actuators of each story, the stories represent the market buyers of the marketplace and are provided with an equal amount of initial wealth.

$$W_1 = 1000; \quad W_2 = 1000; \quad W_3 = 1000; \quad W_4 = 1000; \quad W_5 = 1000 \tag{7.14}$$

The total amount of control energy initially provided by the system power source is calculated from observing that the battery installed in the Kajima-Shizuoka Building is designed to last for 8 continuous minutes with 8 SHD devices each drawing 70 W of power (Kurata et al. 1999). The total energy provided to the system power sources is thus set to 1.25 x 10^{10} Joules (J).

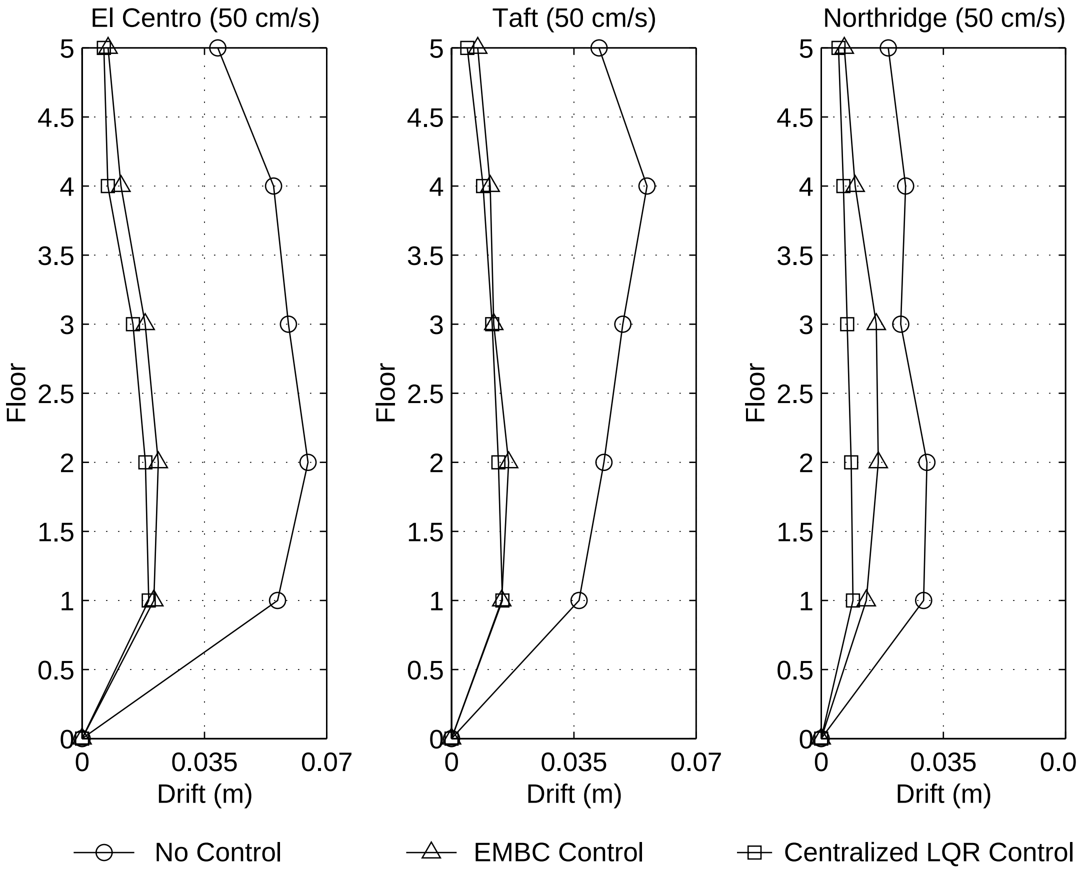

Figure 7-5: Shizuoka Building maximum interstory drifts (LQR, EMBC)

$$L_T = 1.25 \ x \ 10^{10} \ \text{J} \tag{7.15}$$

EMBC and LQR controllers are both implemented in the structure. The ***Q*** and ***R*** weighting matrices of the LQR controller are chosen to be the same as those used in the previous LQR design as shown in Equation (6.41). The SHD dampers added to the top story of the structure do not change the weighting matrices, but rather, only the actuation location matrix ***B*** of Equation (5.1) changes.

Figure 7-5 presents the maximum absolute interstory drift of the Kajima-Shizuoka structure when no control is used and when the LQR and EMBC controllers are employed. As clearly shown, both the LQR and EMBC controllers are effective in reducing the interstory drift response of the structure, with minimal differences between the two control performances. Only for the Northridge seismic disturbance does the LQR controller exhibit superior performance when compared to the drift response of the EMBC controller at the second and third stories.

The change in wealth of each market buyer over the entire El Centro seismic disturbance is presented in Figure 7-6. What is evident from the plot of wealth over time is the very fluid movement of wealth from one market buyer to another. At the conclusion of the analysis, some market buyers end with more wealth than they started at the expense of buyers who have less. The movement of wealth between market buyers can potentially provide insight to which market buyers consistently exhibit the greatest demand as manifested by the possession of less wealth at the end of the analysis. This type of market reasoning could potentially be helpful in solving the actuator placement problem.

Figure 7-7 plots the aggregate depletion of control energy from the system power source over time. Rapid drops in control energy are directly attributed to high structural responses resulting from extreme seismic input. Regions of minimal depletion correspond to times when the structural response is small with market buyers exhibiting minimal demand for control energy.

The locus of intersection points between the aggregate demand and supply functions of the energy marketplace is documented in Figure 7-8. The points close to the origin represent solutions where the seismic disturbance is small and the structure is not experiencing large responses. Conversely, the points furthest from the origin are solutions that result from high structural kinetic and strain energies. It is interesting to note the nearly linear nature of the marketplace pricing solution. This is directly attributed to the large reserve of control energy contained within the system power source. As the power source reduces in size, the equilibrium pricing solution would likely not behave in the same linear fashion observed.

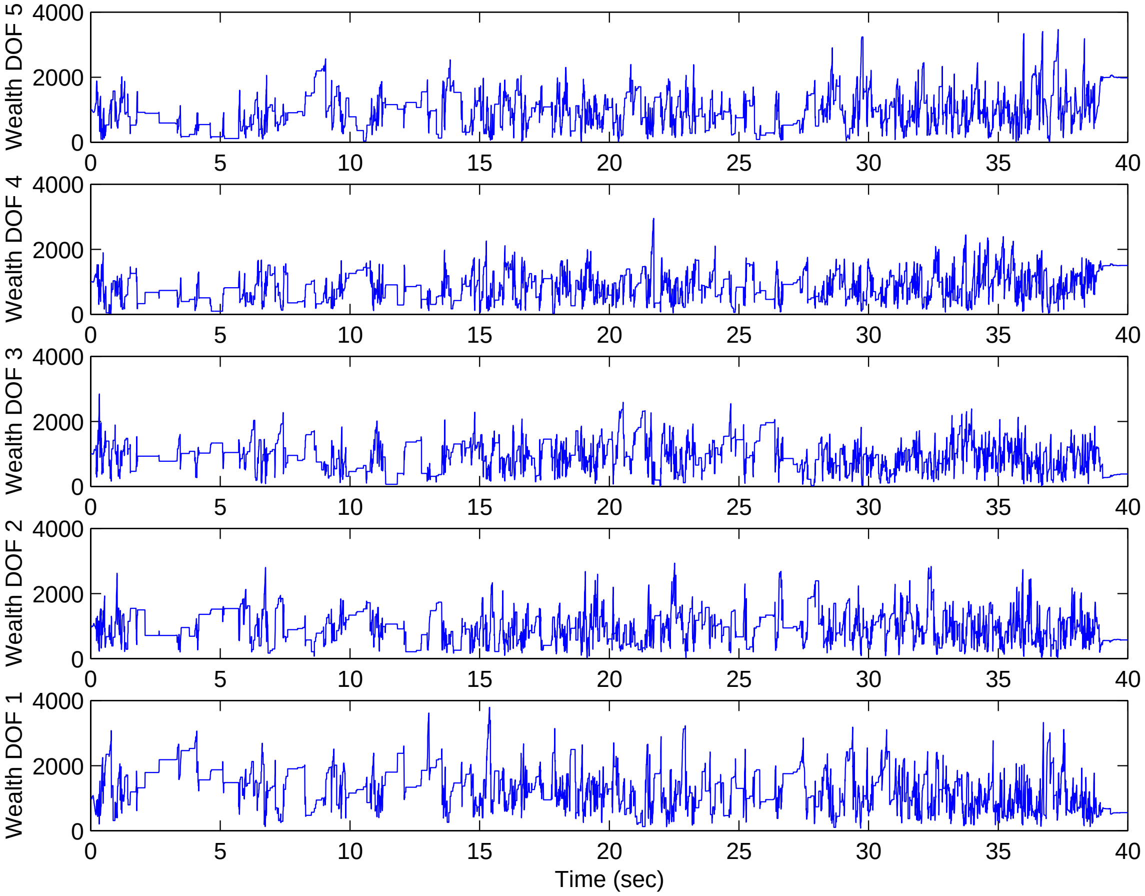

Figure 7-6: Time-history of Shizuoka Building EMBC agents' wealth

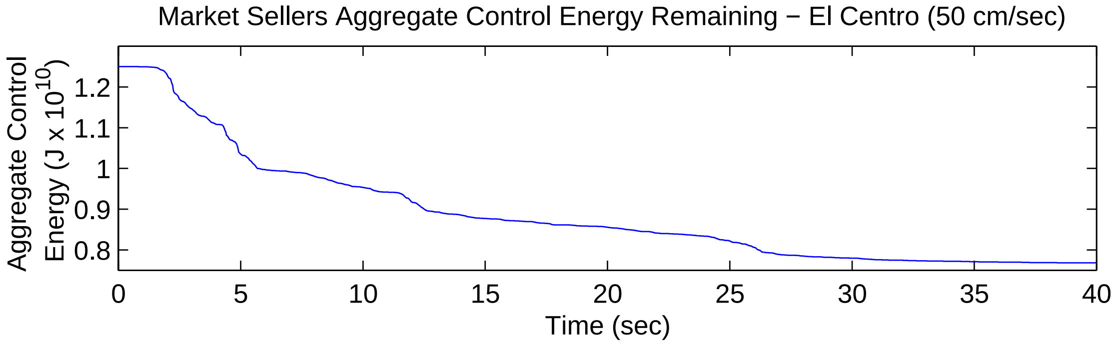

Figure 7-7: Shizuoka Building EMBC depletion of control energy

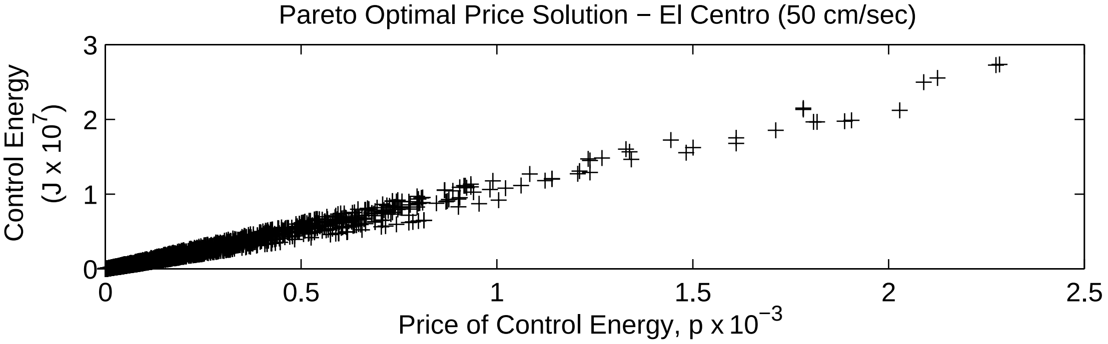

Figure 7-8: Locus of the Pareto optimal prices of the EMBC solution

7.2.4 EMBC Implementation in the 20-Story Benchmark Structure

EMBC and LQR solutions are implemented within the 20-story benchmark structure. The installation configuration of SHD devices is identical to that presented in Figure 5-4. The performance of the two controllers are observed during the El Centro, Taft and Northridge seismic disturbances that have all been normalized to peak ground velocities of 50 cm/s.

The constants for tuning the demand and supply functions of the energy marketplace are set to unity values.

$$\alpha = 1 \qquad \beta = 1 \tag{7.16}$$

Each floor of the structure containing actuators represents a market buyer and is provided with an initial wealth of 1000.

$$\begin{gathered} W_1 = 0; \quad W_2 = W_3 = W_4 = W_5 = 1000; \quad W_6 = 0; \\ W_7 = W_8 = W_9 = W_{10} = 1000; \quad W_{11} = 0; \quad W_{12} = W_{13} = W_{14} = W_{15} = 1000; \\ W_{16} = 0; \quad W_{17} = W_{18} = W_{19} = W_{20} = 1000; \end{gathered} \tag{7.17}$$

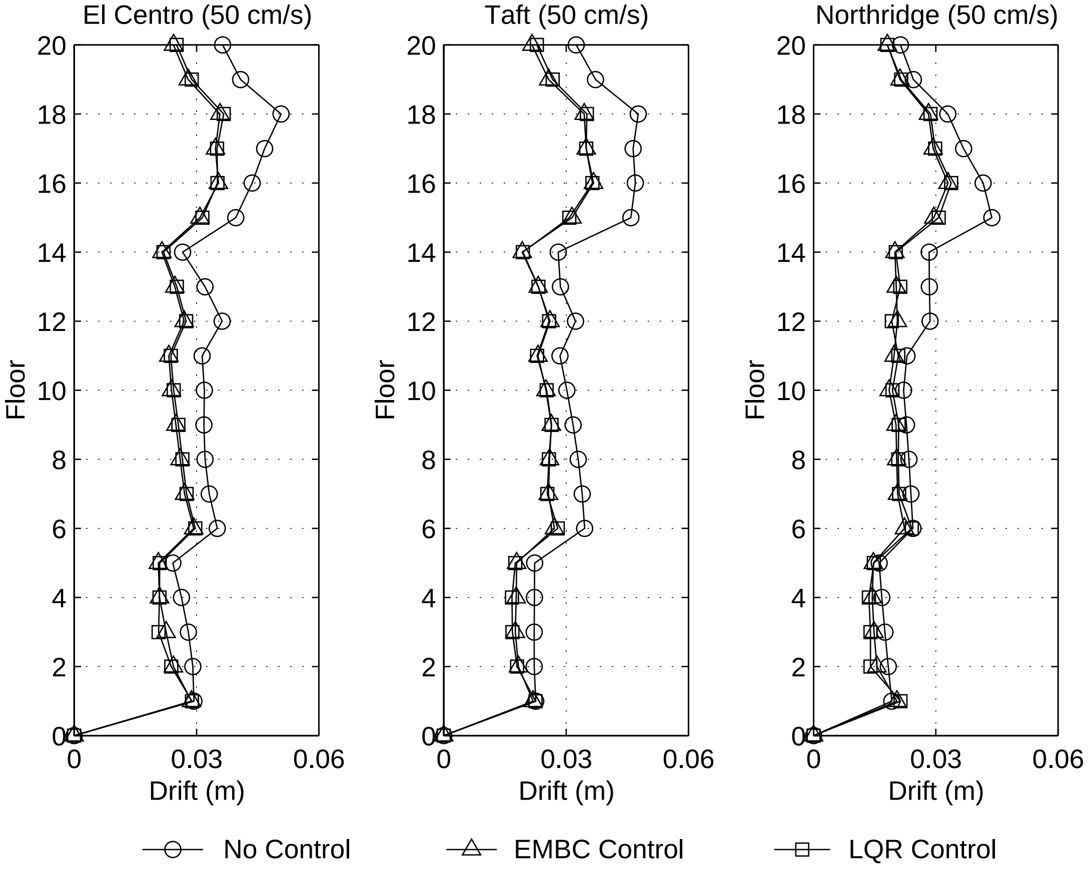

Figure 7-9: Benchmark structure maximum interstory drifts (LQR, EMBC)

The total control energy provided to the system power source is 8 x 10^{11} J. This amount of reserve power should be sufficient for roughly 5 minutes of continuous use by the system's 36 SHD devices.

$$L_T = 8 \;\; x \;\; 10^{11} \;\; \mathrm{J} \tag{7.18}$$

The LQR controller is designed using the ***Q*** and ***R*** weighting matrices previously selected for this structure as presented by Equation (6.44).

Figure 7-9 plots the maximum absolute interstory drift of the 20-story benchmark structure for the selected seismic disturbances. The EMBC controller exhibits excellent control results with a performance comparable to that of the centralized LQR controller. It can be observed that implementation of the EMBC solution is significantly easier with two tuning constants than in the previous MBC derivation where five constants are employed. The new rational derivation of EMBC, based on the natural measure of energy, is less sensitive to changes in the tuning constants than in the previous MBC approach.

7.3 Robustness of Large-Scale Control

While structural control was first introduced over three decades ago, the technology has yet to experience wide spread adoption. The large gap that exists between structural control research and full-scale industry implementation can be attributed to a belief that structural control systems would prove unreliable over their expected lifespan (Battaini et al. 2000).

An investigation into the reliability of structural control can be approached from different perspectives. In the first, the reliability of the control solution is evaluated with respect to uncertainties surrounding the structural properties of the system. Often termed robust control analysis, bounds are placed on the uncertainty of structural parameters with the bounds propagated through the design of the controller to arrive at a worst-case assessment of the control system's performance (Chandrasekharan 1996). Through this analysis, the robustness of the control solution to uncertainties can be ascertained. In other approaches, first and second order reliability methods (FORM/SORM) have been applied to the problem to make an assessment of the probability of instability that could result from the control solution (Spencer et al. 1994). Another approach to considering the robustness of the control solution is from the perspective of the reliability of the individual control devices. For example, some have taken a fault-tree approach in measuring the probability of actuation availability when the control system is activated (Battaini et al. 2000). While great strides have been made in determining the robustness and reliability of structural control, the techniques developed typically consider only systems characterized by small numbers of actuators and sensors.

The primary motivation for considering a decentralized control approach is the hypothesis that structural control systems of the future will have large number of sensors and actuators. Looking at the smart matter research community, it has been observed that a push for low cost MEMS actuation integrated within distributed mass systems has also resulted in large-scale control problems. In smart matter systems, the delicate nature of MEMS actuators results in the failure of some parts. However, it has been learned that the benefit of a low cost solution far exceeds the disadvantages of reduced reliability of individual parts. Furthermore, a high density of actuators in the system represents redundancy, thereby minimizing the impact of an individual actuator's low reliability. Researchers in the smart matter field have pursued using decentralized autonomous processes as providing robust solutions to large-scale control systems that are defined by potential actuation failures (Hogg and Huberman 1998).

Given the potential of actuation failure in a structural control system, robust structural control solutions that can deliver a superior control performance, even when control system components might fail, are sought. Such an environment is poorly suited for centralized control approaches that assume, at the outset of their design, complete knowledge of a fixed system. Drawing on the success of researchers in the smart matter field, a decentralized autonomous control solution is applied to the problem. EMBC is a decentralized autonomous process with autonomous market buyers competing with each other to determine their attainment of a scarce system resource (control energy). The adaptive nature of the EMBC control approach makes it a suitable candidate for serving as a robust control solution in systems where actuators could potentially fail. The candidacy of the EMBC solution is supported by its highly adaptive piecewise static optimization solution.

7.3.1 Robustness of Energy Market-Based Control

The centralized LQR control solution represents a fixed control solution based on the assumption of complete knowledge of a fixed parameter system. On the other hand, EMBC has the distinct advantage of performing an approximate dynamic optimization solution by solving a static optimization problem at each point in time. Therefore, the piecewise static optimization solution has an opportunity to account for changes in the system as they may arise, resulting in a robust control approach. The adaptive nature of the EMBC approach can potentially reap great benefits when the approach is applied to the robust control problem. When a component of the control system fails, the EMBC approach has indirect knowledge of the failure and will find an optimal solution for the new actuation configuration.

7.3.1.1 Measure of Optimality

Optimality measures of the control solution are required for robustness assessment of the EMBC method. In reference to the derivation of the LQR controller, optimality was measured with respect to a total control cost index, *J*, represented by the cost function of Equation (5.4). We will use the same optimality measure, *J*, with modifications made to the ***Q*** and ***R*** weighting matrices. In particular, the weighting matrices of Equation (5.4) are selected to represent total energy in the system. First, the cost function is divided into two components, J_X and J_U, respectively, representing energy of response and energy of the control forces. As presented by Equation (7.19), the first optimality measure, J_X, represents the total kinetic and strain energy of the system where $\boldsymbol{X}$ is a state space representation of the system response and $\boldsymbol{X} = \{\boldsymbol{x} \quad \dot{\boldsymbol{x}}\}^T$.

$$J_X = \sum_{i=1}^{N} \boldsymbol{X}^T \begin{bmatrix} \boldsymbol{K} & 0 \\ 0 & \boldsymbol{M} \end{bmatrix} \boldsymbol{X} \tag{7.19}$$

The second optimality measure, J_U, is the cost associated with the application of controls to the system. As shown in Equation (7.20), the cost of control is a function of the control energy applied by the system actuators (Wong and Yang 2001).

$$J_U = \sum_{i=1}^{N} \boldsymbol{U}^T \boldsymbol{K}^{-1} \boldsymbol{U} \tag{7.20}$$

The total measure of optimality is the sum of Equations (7.19) and (7.20) resulting in Equation (7.21).

$$J = J_X + J_U \tag{7.21}$$

The LQR solution is optimal because the solution derived represents a minimization of the cost function, *J*. However, even though the optimal cost index is originated from the LQR derivation, it can be applied to other control approaches as to measure optimality relative to the LQR solution.

7.3.1.2 Assessment of the Robustness of the Control Solution

In assessing the robustness of the EMBC solution, the Kajima-Shizuoka Building and the 20-story benchmark structure will both be used to simulate control systems that have partial actuation failure. Failure of a portion of the actuation system is applied to the model at the problem outset.

The behavior of the LQR control solution is well understood by a strong closed-form mathematical solution. Conversely, the derivation of the EMBC approach is more phenomenological. To assess the robustness of the EMBC controller, the LQR controller is used to observe its robust behavior during failures to the actuation system. By drawing a parallel to the LQR behavior, the robustness of the EMBC controller is proven.

The following analysis will be performed with respect to each structure in order to illustrate the robustness qualities of the EMBC solution. First, the robustness of the LQR solution is quantified by performing the following tasks:

1. An optimal LQR controller, reflected by the minimization of the cost index, *J*, is designed. Once the LQR solution is implemented, the cost index is computed and recorded for a seismic disturbance.

2. To represent a scenario of actuation failure, a portion of the control system's actuators is intentionally disabled before the seismic disturbance is applied. During the excitation, the control forces are determined by the controller's original feedback gain matrix but applied only by those actuators that are working. Using the original LQR gain matrix that was derived under the assumption that all actuators are working, the failed actuators result in a sub-optimal controller performance as observed by a change in the cost index value. Whether an increase or decrease of the cost index occurs cannot be conclusively stated in this case. If all actuators are properly functioning but the solution is sub-optimal, an increase in the cost index would be observed. However, as a result of some actuators not using control energy, the cost index might decrease even though it is a suboptimal solution.

3. The control solution can be re-optimized if a new LQR solution is calculated based on knowledge of the failed actuators. The performance of the new LQR controller is optimal for the current configuration of working and failed actuators. The seismic excitation is applied to the structure. A decrease in the cost index is noted in this LQR solution compared to that from the case of the original LQR solution applied to the failed actuation system in the previous step.

This analysis is purely academic since no mechanism exists for the LQR controller to recalculate an optimal feedback gain once the failure of actuators is identified. The intention is to show how the LQR solution behaves given failure in the system. This behavior will serve as a key component in assessing the robustness qualities of the EMBC approach.

Next, attention is turned to assessing the robustness of the EMBC controller:

1. An EMBC solution is devised under the assumption that all actuators are reliable and will work when required. The solution devised by the EMBC controller is optimal in a Pareto optimal sense. The same seismic disturbance used in the LQR analysis is imposed to the structural system and the cost index, *J*, is measured using Equation (7.21).

2. Next, actuators are purposely disabled prior to application of the seismic disturbance. The EMBC controller is artificially constrained to perform market competitions without awareness of the actuator failures; control energies purchased by defective actuators are not used for control. This is equivalent to step 2 of the LQR analysis where the original LQR controller is used to apply control forces only by actuators functioning properly. The result is a sub-optimal performance of the EMBC solution as manifested by a change in the cost index. Again, a decrease or increase in the cost index can occur as a result of the failed actuators not using control energy. Forcing the EMBC controller to behave in this manner during actuation failures is spurious and is done for illustration purposes only. Naturally, the marketplace can observe the loss of an actuator by seeing that control energy purchased is not being applied. In a situation where the actuator is not functioning, the actuator's market buyer would not spend its wealth nor receive income. The isolation of the market buyer associated with the failed actuator is the natural internal mechanism of the EMBC controller for indirect identification of failed actuators.

3. In the next set of analyses, the EMBC solution is allowed to behave as designed; market buyers associated with broken actuators are permitted to add their demand to the global market demand function, but no wealth is transferred from or to the failed market participant. The result is an EMBC solution that is Pareto optimal with respect to the loss of the actuators. This fact will be observed by a decrease in the optimal cost index, *J*, when compared to the cost index calculated for the spurious implementation of EMBC in the previous step.

In summary, the analysis will illustrate two important issues. First, when actuators fail in the control system, the original optimal LQR control solution has become sub-optimal reflected by a change in the cost index. To return to an optimal solution as reflected by a reduction in the suboptimal cost index value, a new LQR solution needs to be calculated with knowledge of the failed system actuators. Second, if the energy market-based control approach is forced to ignore the existence of failures in the control system's actuators, it too will experience a change in the cost index. By allowing the EMBC controller to behave as it is designed, a decrease in the cost index from the artificially constrained EMBC implementation can be achieved.

If the LQR controller could identify the existence of failed actuators in the system and recalculate its control solution, it would represent a robust controller with respect to actuation failures. Unfortunately, no implementation exists that allows the LQR controller to behave in this manner. On the other hand, EMBC has the unique ability to sense the existence of actuation failure by identifying market-participants that have become isolated in the market (no wealth is transferred between the buyer and the market). As a result, the EMBC solution optimizes around the isolated participant. Proof of the EMBC approach's optimization and subsequent robustness is supported solely by the behavior of the EMBC total cost index value, but the cost index's behavior is compared to that of the LQR controller in order to provide stronger support since the LQR controller is well understood. The unique behavior of the EMBC approach observed makes the approach robust in the face of system failures since it can optimize the control solution in real-time to account for failures. This is additional evidence of the advantages of performing an approximate dynamic optimization through recalculation of the static optimization problem at each time step.

7.3.1.3 The Kajima-Shizuoka Building

The analysis described above is applied to the controllers previously designed for implementation in the Kajima-Shizuoka Building whose configuration is shown in Figure 7-4. The El Centro seismic disturbance, normalized to a peak ground velocity of 50 cm/s, is selected as the external disturbance to the system. Actuation failure is introduced to the structure at the outset of the analysis. To reveal a complete picture of the robustness of the EMBC method, a total of seven actuation failure scenarios are considered. In the first five analyses, the actuators located on each of the five floors of the structure are assumed to have failed individually. The next analysis considers the actuators of the first, third and fifth floors failing together while the last analysis investigates the situation where the actuators on the second and fourth floor all fail in unison. Presentation of the maximum absolute interstory drifts of the building to the various failure scenarios are presented in Figure 7-10.

Assuming no actuation failures, the measure of solution optimality, *J*, is determined for the LQR controller previously designed using weighting terms for ***Q*** and ***R*** as described by Equation (6.41).

$$\begin{aligned} J_X &= 1.3155 \;\; x \;\; 10^5 \;\; \mathrm{J} \\ J_U &= 1.4428 \;\; x \;\; 10^6 \;\; \mathrm{J} \\ J &= 1.5744 \;\; x \;\; 10^6 \;\; \mathrm{J} \end{aligned} \tag{7.22}$$

Next, the seven actuation failure scenarios are implemented. The original controller gain of the LQR solution is employed with failed actuators applying no control force. Last, a new LQR controller is calculated that reflects an optimal solution with actuators absent in the location known to have failed. The optimality measures for these fourteen analyses are tabulated in Table 7-1.

Two trends are to be noted in considering the LQR solution performance when actuators fail. First, the reduction of the total number of actuators results in the cost index of response, J_X, to unconditionally increase while the cost index of control effort, J_U, to unconditionally decreases. This means the ability of the control system to limit structural responses decreases with a reduction in the number of actuators available in the system. The second trend is how the total cost indices, *J*, listed in column 4 of Table 7-1, changes

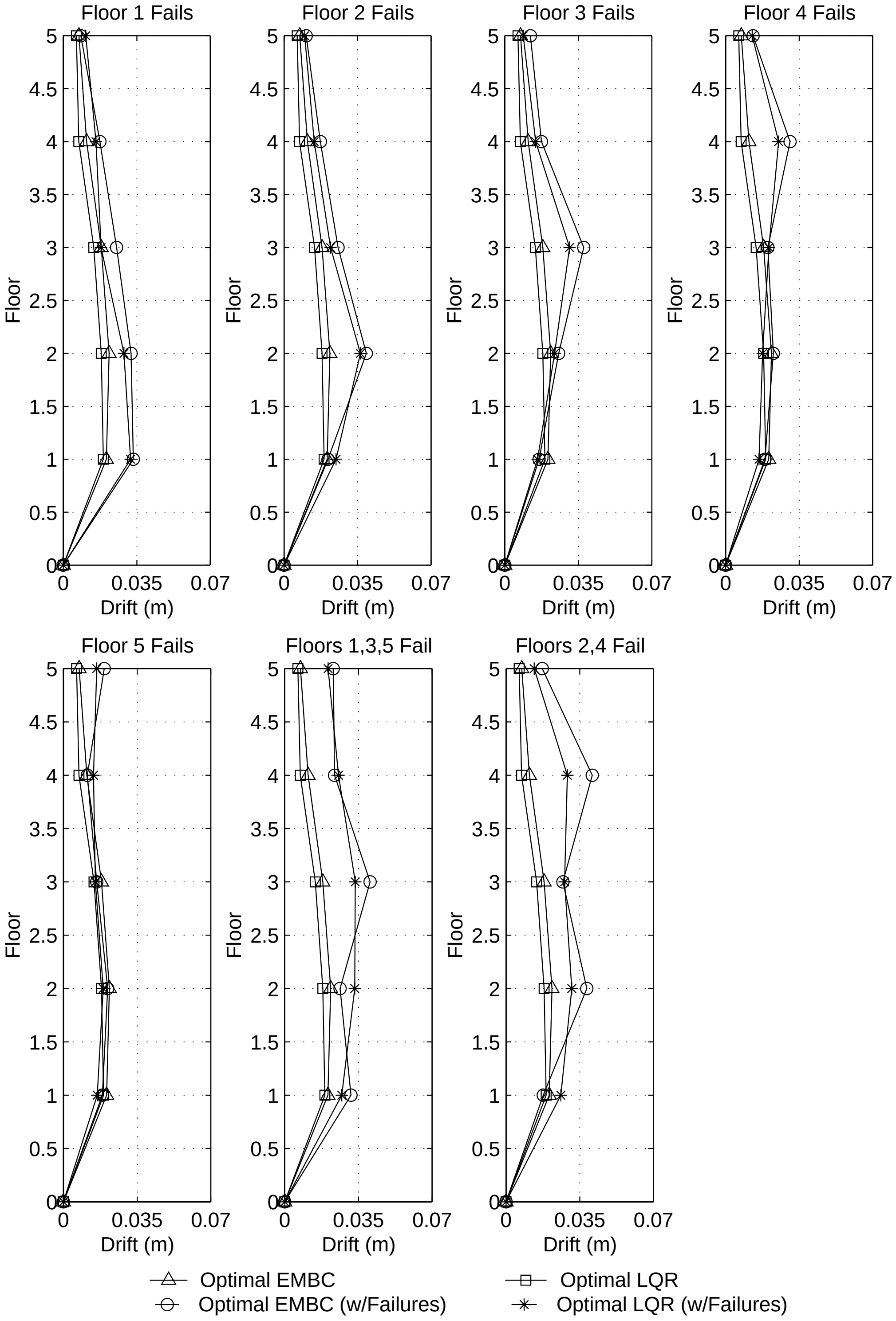

Figure 7-10: Shizuoka Building drift response to actuator failures (LQR, EMBC)

Table 7-1: Shizuoka Building LQR performance (actuation failure) – El Centro

Floor	J_X	J_U	$J = J_X + J_U$
Fail F1, Centralized LQR	4.1490×10^5 J	1.3989×10^6 J	1.8138×10^6 J
Re-optimized LQR (w/o F1)	3.9987×10^5 J	1.2840×10^6 J	1.6839×10^6 J
Fail F2, Centralized LQR	4.0440×10^5 J	1.1017×10^6 J	1.5061×10^6 J
Re-optimized LQR (w/o F2)	4.2009×10^5 J	0.8125×10^6 J	1.2326×10^6 J
Fail F3, Centralized LQR	3.3495×10^5 J	0.8456×10^6 J	1.1805×10^6 J
Re-optimized LQR (w/o F3)	3.2909×10^5 J	0.7407×10^6 J	1.0697×10^6 J
Fail F4, Centralized LQR	2.6670×10^5 J	0.8482×10^6 J	1.1149×10^6 J
Re-optimized LQR (w/o F4)	2.4948×10^5 J	0.8150×10^6 J	1.0644×10^6 J
Fail F5, Centralized LQR	1.9843×10^5 J	0.9975×10^6 J	1.1959×10^6 J
Re-optimized LQR (w/o F5)	1.8851×10^5 J	0.9345×10^6 J	1.1230×10^6 J
Fail F2,4 Centralized LQR	5.5834×10^5 J	0.6114×10^6 J	1.1697×10^6 J
Re-optimized LQR (w/o F2,F4)	5.9586×10^5 J	0.4674×10^6 J	1.0633×10^6 J
Fail F1,3,5, Centralized LQR	7.7250×10^5 J	0.5390×10^6 J	1.3115×10^6 J
Re-optimized LQR (w/o F1,F3,F5)	7.8508×10^5 J	0.3470×10^6 J	1.1320×10^6 J

for the same failure scenario between the original LQR solution and the reformulated LQR solution. In all cases, the cost indices will decrease for the reformulated LQR controller because the original controller is no longer optimal when actuators fail while the reformulation determines the optimal solution for the set of available actuators. The decrease in the total cost index, J, can come from a decrease in the system response as manifested by a decrease in J_X, a decrease in the control effort used as seen in a decrease in J_U, or from a combination of both. To identify which component of J is responsible for its overall reduction both J_X and J_U are presented in the second and third columns of Table 7-1.

The EMBC solution, using the market parameters set forth by Equations (7.13), (7.14) and (7.15), is implemented assuming all system actuators are working properly. The EMBC controller yields the following measures of optimality using Equations (7.19), (7.20) and (7.21):

$$J_X = 1.4992 \;\; x \;\; 10^5 \;\; \text{J}$$

$$J_U = 1.7324 \;\; x \;\; 10^6 \;\; \text{J} \tag{7.23}$$

$$J = 1.8823 \;\; x \;\; 10^6 \;\; \text{J}$$

The LQR controller is slightly more efficient with lower cost indices. The tuning coefficients of the EMBC controller could be altered to attain the same cost values.

The same failure scenarios described for the LQR analysis are used for the EMBC control solution as tabulated in Table 7-2 . First, the EMBC solution is forced to behave in an unnatural way with no knowledge of the actuation failures. Next, the EMBC marketplace performs as designed with isolation of failed market buyers.

Table 7-2: Shizuoka Building EMBC performance (actuation failure) – El Centro

Floor	J_X	J_U	$J = J_X + J_U$
Fail F1, EMBC Ignore Failure	4.2841 x 10^5 J	1.4663 x 10^6 J	1.8947 x 10^6 J
EMBC (w/o F1)	4.2174 x 10^5 J	1.4071 x 10^6 J	1.8288 x 10^6 J
Fail F2, EMBC Ignore Failure	4.7216 x 10^5 J	1.4583 x 10^6 J	1.9305 x 10^6 J
EMBC (w/o F2)	4.5897 x 10^5 J	1.4193 x 10^6 J	1.8783 x 10^6 J
Fail F3, EMBC Ignore Failure	4.0186 x 10^5 J	1.1773 x 10^6 J	1.5791 x 10^6 J
EMBC (w/o F3)	3.9040 x 10^5 J	1.1192 x 10^6 J	1.5096 x 10^6 J
Fail F4, EMBC Ignore Failure	3.1071 x 10^5 J	1.0462 x 10^6 J	1.3569 x 10^6 J
EMBC (w/o F4)	3.0935 x 10^5 J	1.0567 x 10^6 J	1.3660 x 10^6 J
Fail F5, EMBC Ignore Failure	2.1090 x 10^5 J	1.1741 x 10^6 J	1.3850 x 10^6 J
EMBC (w/o F5)	2.0536 x 10^5 J	1.2131 x 10^6 J	1.4184 x 10^6 J
Fail F2,4 EMBC Ignore Failures	7.0626 x 10^5 J	0.8439 x 10^6 J	1.5501 x 10^6 J
EMBC (w/o F2,F4)	7.0836 x 10^5 J	0.8158 x 10^6 J	1.5241 x 10^6 J
Fail F1,3,5, EMBC Ignore Failures	8.2253 x 10^5 J	0.5714 x 10^6 J	1.3940 x 10^6 J
EMBC (w/o F1,F3,F5)	8.0210 x 10^5 J	0.5804 x 10^6 J	1.3825 x 10^6 J

Similar to the trends of the LQR results, the cost index of the structural response, J_X, increases with actuation failings while the cost index on control effort, J_U, decreases. But the more significant trend is the reduction of the cost index between the case of enforced ignorance of actuation failure on the part of the EMBC controller (suboptimal) and the case where the EMBC operates by its natural design (optimal). When allowed to behave as it normally would, the EMBC solution is more optimal than when the EMBC is forced to ignore failures within the control system. This serves as evidence of the EMBC piecewise static solution optimizing to its given environment. If the control environment is lacking actuators, the solution is optimal in reference to the available actuators. This inevitably implies that the EMBC controller is more robust to potential actuation failures. This is one of the key benefits of EMBC control over the classical centralized LQR solution. One important observation that cannot be avoided is that the reduction in the cost index from the ignorant EMBC implementation to the one where the EMBC controller can compensate for the actuation failures is smaller than reductions seen in the LQR analysis. Future work is needed to potentially maximize the cost index reductions and hence arrive at the most optimal solution possible.

7.3.1.4 The 20-Story Benchmark Structure

To observe the robust behavior of the EMBC solution in a large-scale structure, the 20-story benchmark structure, as shown in Figure 5-4 is used. In contrast to the actuation failure scenarios of the Kajima-Shizuoka Building, actuation failures are grouped into larger regions that span multiple floors. For this set of analyses, the actuators located in the building are grouped into four zones. In the first zone, actuators on floors 2 through 5 are grouped. Likewise, the second, third and fourth zones group the actuators of floor 7 through 10, floors 12 through 15 and floors 16 through 20 respectively. A picture of the defined actuation zones are presented in Figure 7-11. A total of six failure scenarios are considered; the first four failure scenarios are of each of the zones experience total actuation failure, the fifth failure scenario is of the actuators in zones 2 and 3 all not working while the last scenario is of actuators in zones 1 and 4 all not working.

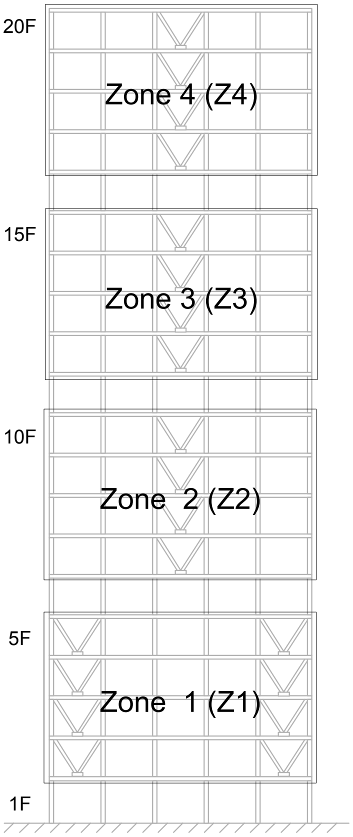

Figure 7-11: Zones of actuation failure of the 20-story benchmark structure

LQR and EMBC controllers are both implemented in the 20-story benchmark structure using the same configuration parameters as was used previously. For the EMBC controller, the market parameters employed are those presented in Equations (7.16), (7.17), and (7.18). The weighting matrices, $\boldsymbol{Q}$ and $\boldsymbol{R}$, of the LQR controller are selected as those presented in Equation (6.44). The maximum absolute interstory drift response of the benchmark structure to the scaled El Centro seismic record is presented in Figure 7-12. The actuation failure of the last two cases (multiple zone failures) is most dramatically felt by the structure with the EMBC controller outperforming the LQR controller for these cases.

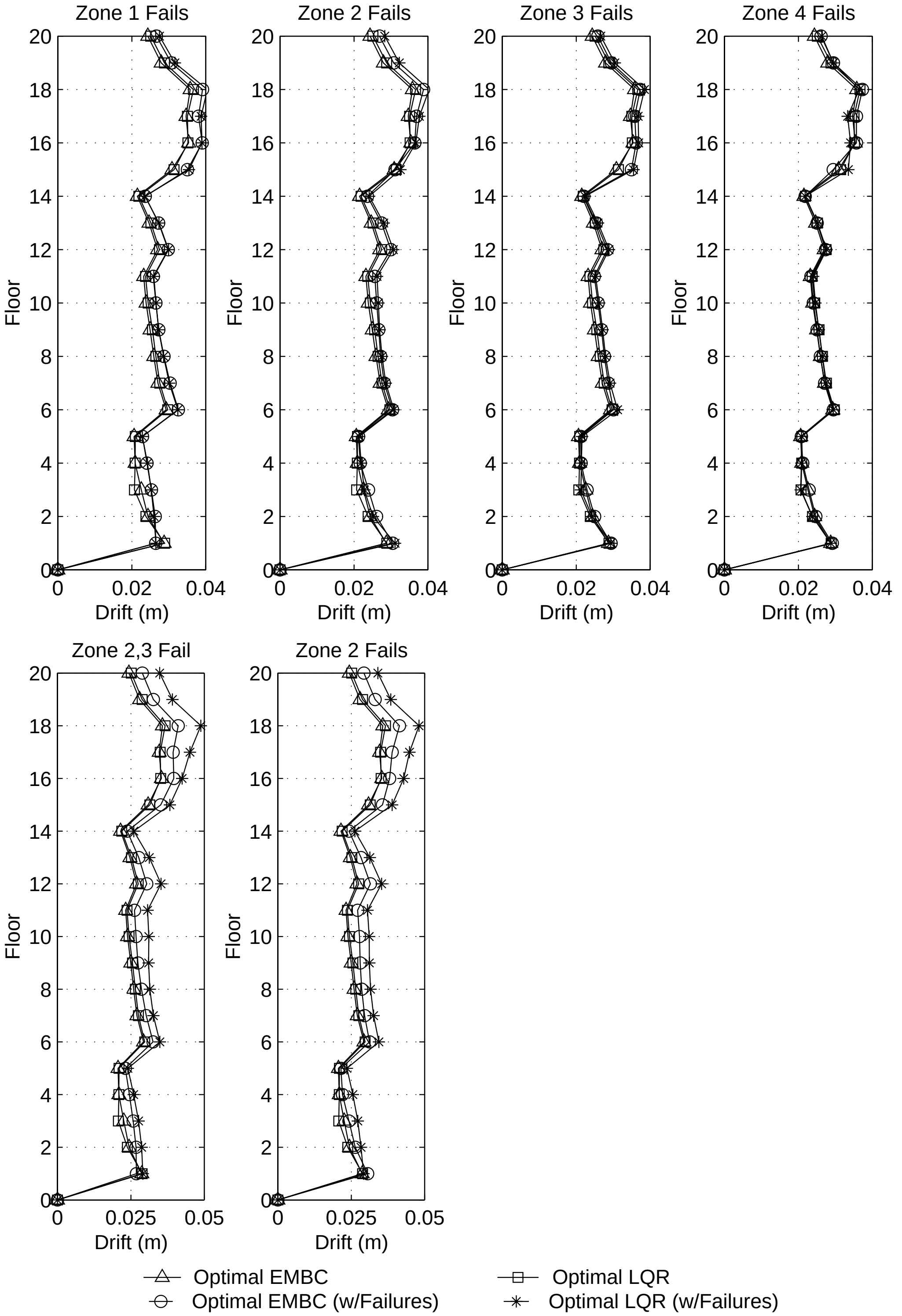

Figure 7-12: Benchmark structure drift response to actuator failures (LQR, EMBC)

Assuming no actuation failure, the cost indices for the LQR controller are:

$$\begin{aligned} J_X &= 3.7209 \;\; x \;\; 10^9 \;\; \mathrm{J} \\ J_U &= 3.7154 \;\; x \;\; 10^9 \;\; \mathrm{J} \\ J &= 7.4363 \;\; x \;\; 10^9 \;\; \mathrm{J} \end{aligned} \tag{7.24}$$

After determination of the initial cost index values, the actuation failure scenarios are applied to the benchmark structure. The analyses results for the normalized El Centro record are summarized in Table 7-3. Similar to the Kajima-Shizuoka Building's results, the cost index on structural response, J_X, increases and the cost index on control effort, J_U, decreases as a result of actuation failure. The trend of importance is the reduction of the total cost index, J, from application of the original controller to application of the re-optimized controller for each failure scenario.

In the next set of analyses, the EMBC solution is applied to the benchmark structure. With the actuators all working properly, the EMBC cost indices are determined from the response of the structure to the El Centro seismic record.

Table 7-3: Benchmark structure LQR performance (actuation failure) – El Centro

Floor	J_X	J_U	$J = J_X + J_U$
Fail Z1, Centralized LQR	4.5975 x 10^9 J	2.8078 x 10^9 J	7.4054 x 10^9 J
Re-optimized LQR (w/o Z1)	4.5778 x 10^9 J	2.8010 x 10^9 J	7.3789 x 10^9 J
Fail Z2, Centralized LQR	4.3681 x 10^9 J	2.1539 x 10^9 J	6.5219 x 10^9 J
Re-optimized LQR (w/o Z2)	4.3504 x 10^9 J	2.1270 x 10^9 J	6.4774 x 10^9 J
Fail Z3 Centralized LQR	4.3135 x 10^9 J	1.8665 x 10^9 J	6.1800 x 10^9 J
Re-optimized LQR (w/o Z3)	4.3211 x 10^9 J	1.8706 x 10^9 J	6.1917 x 10^9 J
Fail Z4 Centralized LQR	3.7829 x 10^9 J	3.5603 x 10^9 J	7.3432 x 10^9 J
Re-optimized LQR (w/o Z4)	3.7255 x 10^9 J	3.5931 x 10^9 J	7.3186 x 10^9 J
Fail Z1,Z4 Centralized LQR	5.0869 x 10^9 J	0.7080 x 10^9 J	5.7949 x 10^9 J
Re-optimized LQR (w/o Z1, Z4)	5.3092 x 10^9 J	0.0070 X 10^9 J	5.3172 x 10^9 J
Fail Z2,Z3 Centralized LQR	4.6583 x 10^9 J	2.7424 x 10^9 J	7.4007 x 10^9 J
Re-optimized LQR (w/o Z2, Z3)	6.2995 x 10^9 J	1.3479 x 10^9 J	6.3130 x 10^9 J

$$J_X = 3.7412 \;\; x \;\; 10^9 \;\; \mathrm{J}$$

$$J_U = 3.6391 \;\; x \;\; 10^9 \;\; \mathrm{J} \tag{7.25}$$

$$J = 7.3803 \;\; x \;\; 10^9 \;\; \mathrm{J}$$

To assess the robustness of the EMBC solution, the actuation failure scenarios are applied to the structure at the outset of the analysis. The artificially constrained and natural EMBC solutions are implemented and the cost indices calculated as presented in Table 7-4. Evident is a reduction in the total cost index, *J*, from the constrained to the natural EMBC implementations. With the reductions identical to those in the set of LQR analyses, it can be concluded that the EMBC solution is optimized to the current failed system configuration. Therefore, with real-time optimization capabilities, the energy market-based control solution exhibits an element of robustness that the centralized LQR solution is lacking. Again, it is also observed that the reductions of the LQR cost index appear to be more significant when compared to those of the EMBC controller.

Table 7-4: Benchmark structure EMBC performance (actuation failure) – El Centro

Floor	J_X	J_U	$J = J_X + J_U$
Fail Z1, EMBC Ignore Failure	4.6209×10^9 J	2.6854×10^9 J	7.3063×10^9 J
EMBC (w/o Z1)	4.6305×10^9 J	2.6739×10^9 J	7.3044×10^9 J
Fail Z2, EMBC Ignore Failure	4.3978×10^9 J	2.0015×10^9 J	6.3993×10^9 J
EMBC (w/o Z2)	4.3879×10^9 J	2.0002×10^9 J	6.3881×10^9 J
Fail Z3, EMBC Ignore Failure	4.2931×10^9 J	1.8446×10^9 J	6.1377×10^9 J
EMBC (w/o Z3)	4.2981×10^9 J	1.8537×10^9 J	6.1518×10^9 J
Fail Z4, EMBC Ignore Failure	3.8094×10^9 J	3.5111×10^9 J	7.3205×10^9 J
EMBC (w/o Z4)	3.7763×10^9 J	3.5046×10^9 J	7.2809×10^9 J
Fail Z1,Z4 EMBC Ignore Failure	5.0468×10^9 J	0.6752×10^9 J	5.7219×10^9 J
EMBC (w/o Z1, Z4)	5.0197×10^9 J	0.6947×10^9 J	5.7144×10^9 J
Fail Z2, Z3 EMBC Ignore Failure	4.6889×10^9 J	2.6213×10^9 J	7.3102×10^9 J
EMBC (w/o Z2, Z3)	4.6836×10^9 J	2.5860×10^9 J	7.2696×10^9 J

7.4 Summary

The chapter began with a reevaluation of the market based control (MBC) derivation. The original MBC derivation was a result of seeking linear demand and supply functions with a sufficient number of tuning constants for flexibility during implementation in a structural control system. An attempt was made to revisit the derivation of MBC using a more rational approach. As a result, energy market-based control (EMBC) was devised. Using the natural measures of energy in the dynamic structural system, a powerful control approach using fewer tuning constants appeared. The EMBC controller was implemented in both the Kajima-Shizuoka Building and the 20-story benchmark structure with excellent control results observed. While deriving the market-based control approach using measures of energy was very intuitive, other market models can be adopted that might provide superior control performances.

The robustness of the EMBC control approach was illustrated. Robustness with respect to actuation failures was illustrated for the EMBC approach by observing the behavior of the cost index, *J*, during the LQR and EMBC implementations and drawing parallels between the two controllers. Conceptually, the robustness of the EMBC approach is directly derived from the static optimization performed at each step in time. Changes in the system can be observed and incorporated in the static optimization solutions immediately. The failure of actuators in the system represents only one form of change in the system's properties. Therefore, the ability of the approximate dynamic optimization of the EMBC control problem could have potential in the realm of nonlinear controls which also represents property changes in the system.

Only the robustness qualities of the EMBC approach have been investigated. It is certain that the original MBC controllers would exhibit similar properties since both methods are based upon the same optimization mechanism from which the robustness qualities are derived.

Chapter 8

Summary and Discussion

The focus of this research was the introduction of decentralization to the realm of two categories of smart structure technologies: monitoring and control. Current state-of-practice employs highly centralized architectural designs for structural monitoring and control. As the cost of smart structure technologies decreases and their capabilities broaden, an opportunity exists to deploy larger numbers of sensors and actuators. The centralized architecture of current systems represents a limitation that retards the adoption of monitoring and control technologies in applications requiring high sensing and actuation densities. In response to this observation, decentralization has been proposed as a scalable architectural framework that enables the adoption of large-scale smart structure systems.

8.1 Decentralization of Wireless Structural Monitoring

Before the concepts of decentralization can be considered within the field of structural monitoring, a capable hardware infrastructure must first be developed. A novel sensing unit design was proposed to serve as a fundamental building block of structural monitoring systems of the future. Two enabling technologies were incorporated within the design of the novel sensing units: wireless communications and embedded microcontrollers. The introduction of wireless communications is of paramount importance because it significantly reduces the cost associated with installation and maintenance of wire-based monitoring systems. In addition, efficient data transfer is supported between sensing units through wireless peer-to-peer communications. Placing embedded microcontrollers at the unit's core permits on-board data processing and consolidation. The wireless sensing unit represents embedded intelligence for placement at each node of a monitoring system. Capable of autonomous or collaborative operation, tremendous synergies exist between the proposed units and decentralized monitoring schemes.

The hardware design of a prototype wireless sensing unit is presented in detail in Chapter 2. Components selected for inclusion into the wireless sensing unit's design represent the most advanced embedded system technologies currently available. Two important criteria were used in the component selection process; components with low unit costs and with low power consumption characteristics were sought. The result was a wireless sensing unit with versatile features for implementation in a broad set of applications. In particular, a multi-channel interface is provided to accommodate a variety of sensing transducers such as MEMS-based accelerometers and strain gages, just to name a few. The computational core of the wireless sensing unit was designed using two microcontrollers. An 8-bit microcontroller is included for overall unit operation including reading measurement data and sending it for transmission to the wireless modem. A second 32-bit microcontroller with floating-point computations supported in hardware, is included for computational intensive data processing. A wireless modem on the 2.4 GHz radio band serves as the wireless communication channel between units. Using spread spectrum encoding techniques, reliable communications of up to 1,000 ft. was attained.

The software embedded in the wireless sensing unit's computational core is the topic of Chapter 3. Careful attention was paid to using a modular approach to writing software, ensuring a flexible and scalable software structure. Software development efforts for the wireless sensing unit can be defined by two software abstraction levels. The first level of software was written for the operation of the hardware subsystems of the sensing unit.

The second level of software was written to reside on top of the first level and is intended to perform tasks specific to engineering applications such as system identification and structural health monitoring (damage detection). Decentralization of the structural monitoring system is defined by the embedded application software since it provides the capability of autonomous interrogation of measurement data with multiple sensing nodes performing computations in parallel.

With the design of the unit's hardware and software systems complete, a series of validation tests were performed on the wireless sensing unit in both the laboratory and field settings, as summarized in Chapter 4. The intention of the validation tests was to quantify the performance characteristics of the complete prototype design. The first set of validation tests assessed the performance of the wireless sensing unit hardware subsystems such as the resolution of the sensing interface's analog-to-digital conversion. The second set of validation tests centered upon interfacing low cost structural monitoring transducers. In particular, low cost MEMS-based accelerometers were interfaced and used in the laboratory to measure the response of a five degree-of-freedom structure excited by a shaking table. For the large acceleration responses (>1 g) exhibited by the test structure, the MEMS accelerometers were of sufficient accuracy to provide high-quality time-history response records. Also, a typical strain gage was successfully interfaced to the sensing unit to measure the strain induced upon a steel coupon sample cyclically loaded along its longitudinal axis. The last set of validation tests investigated the field deployment of the sensing units in a highway bridge. The Alamosa Canyon Bridge in New Mexico was instrumented with a wireless modular monitoring system (WiMMS) comprised of wireless sensing units. A classical wire-based monitoring system was installed in parallel to compare the performance of the wireless sensing system to that of a wire-based counterpart. The performance of the wireless sensing units was comparable to that of the tethered system with significant reductions in installation time gained.

8.2 Decentralization of Structural Control

The reduction in the size and cost of structural control devices will serve as a catalyst for wide-spread global adoption of structural control technologies. The recent adoption of semi-active structural control devices is evidence of the structural control industry progressing towards cheaper, smaller, and more power efficient devices. As a result, control systems of the future will grow into large-scale systems defined by hundreds of actuators and sensors. Large-scale control systems will overburden a centralized controller unless the computational capabilities of current controllers improve or new control system architectures are considered. One way of removing burden from the centralized controller is to employ decentralized control system architectures.

In Chapter 5, two control approaches were proposed that are decentralized in the *a posteriori* sense. In both approaches, the global control system was broken down to a series of subsystems, each with an autonomous controller. The first approach represented a suboptimal solution by modifying the optimal centralized linear quadratic regulator (LQR) gain matrix to fit the decentralized system architecture. Excellent control performance was attained using the modified LQR controller because actuators and sensors were assumed collocated. The second decentralized approach derived was based on the derivation of the LQR solution. This decentralized optimal controller produced excellent control results when compared to the results derived from the centralized LQR controller. Both decentralized control approaches were analytically applied to a 20-story benchmark structure with 36 semi-active actuators installed.

An *a priori* decentralized control approach with limited knowledge of the structural system was derived in Chapter 6. Termed market-based control (MBC), the control system was modeled as a free market economy with actuators acting as market buyers and power sources representing market sellers. The limited commodity of control power was introduced as the scarce market commodity to be efficiently allocated. The origins of MBC are from the realm of econometrics and represent the solution to the static optimization problem. This is in contrast to the LQR solution that represents an optimal solution to the dynamic optimization problem. The MBC static optimization is performed at each time step of the control system implementation and can be viewed as a piecewise solution to the dynamic optimization problem. As a result, the MBC solution is optimal in the Pareto optimal sense. Two structures were used for implementation of the MBC approach: the 5-story Kajima-Shizuoka Building and the 20-story benchmark structure. In both cases, MBC yielded excellent control results, nearly identical to those of the centralized LQR controller.

The MBC derivation of Chapter 6 was revisited in Chapter 7 to provide a more rational framework to the approach. Using the natural measures of energy in the dynamic structural system, energy market-based control (EMBC) was derived. These efforts resulted in a more rational context for the approach with easy to implement demand and supply functions defined by only one tuning coefficient each. Identical to MBC, EMBC represents a flexible piecewise static optimization solution. This fact indicates that EMBC is capable of exhibiting robust qualities. In the face of actuation failures, a robust control solution is desirable. To assess the robustness of the EMBC approach, the control approach was applied to the Kajima-Shizuoka Building and the 20-story benchmark structure during actuation failure scenarios. Unlike the centralized LQR controller, the EMBC approach can provide an optimal solution to the system even when faulty actuators exists.

8.3 Future Research

After introducing the concept of decentralization to the realm of smart structure technologies, it is evident that the concept holds great promise as a substitute to the current centralized approaches. It is shown in this thesis that decentralization can be applied to structural monitoring and control systems with great success. In all cases shown, decentralized system performance was comparable to that of centralized approaches. In some cases, decentralization provided additional benefit such as robustness of the control solution. This research only represents the first step in investigating decentralized concepts for adoption in smart structure systems. Clearly, additional work is required to further the concepts in this thesis towards implementation in real smart structure systems of tomorrow.

8.3.1 Wireless Monitoring

The wireless sensing unit is comprised of components found in the highly dynamic embedded system marketplace. With embedded system technology offerings improving and costs reducing, the wireless sensing unit design can benefit from new component adoption. In particular, improvements can be made to the wireless modem technology integrated. Currently, the Proxim RangeLAN2 modem is capable of communication ranges of 1,000 ft. and a data rate of 1.6 Mbps while drawing 160 mA from the unit power source. Greater ranges, higher data rates and lower power demands should be sought in future wireless modems. Wireless products compliant with the IEEE 802.11a standard are just starting to become available and could prove instrumental in improving the wireless communication capabilities of the unit. Operating in the 5 GHz radio band, IEEE 802.11a provides data rates as high as 54 Mbps, but communication ranges exceeding 1200 ft. can be attained outdoors at lower data rates (Netgear 2002).

This research only explored two analysis tasks for embedment in the wireless sensing unit. First, a fast Fourier transform was used to derive the frequency response function of measurement data. Second, a component of the statistical pattern recognition structural health monitoring method was locally implemented. The economic and life safety value associated with structural health monitoring is tremendous and promises to grow in the future. The goal of researchers is to develop robust structural health monitoring methods that can identify the onset of damage in addition to assessing its location and severity. It is envisioned that structural health monitoring methods will be deployed as autonomous systems in the future. The wireless sensing unit's ability to serve as a major component of an autonomous structural health monitoring system has been illustrated. Additional application software specific to structural health monitoring should be developed and incorporated in the sensing unit.

The operational and environmental variability of a structure still poses a significant problem that hinders the identification of damage from ambient structural responses. In response to this fact, the use of active sensing techniques is being explored for application in civil infrastructure (Wu and Chang 2001). Active sensing defines a monitoring system that employs actuation for excitation exertion. Often, a feedback loop exists between the actuation and sensing systems to ensure appropriate excitation signals are applied to the structure. The wireless sensing unit design can be upgraded to include an actuation interface to which multiple actuators could be connected. The computational core of the wireless sensing unit can accommodate rapid signal processing tasks associated with an active sensing feedback loop. The inclusion of active sensing in the unit will allow researchers to consider additional structural health monitoring methods for embedment that use the unit actuators for excitation.

8.3.2 Decentralized Control

The field of decentralized control theory is rich with methods that can be potentially applied to the structural control problem. This research only explored the adoption of two *a posteriori* methods: modified decentralized LQR and optimal decentralized control. Future research can focus upon the other available methods in order to assess which services structural control systems best.

With respect to market-based control (MBC) and energy market-based control (EMBC), additional work is required to ready these promising decentralized control methods for deployment in real structural control systems. In particular, implementation details represent a big challenge to be encountered. The real-time operation of the marketplace will require the coordinated effort of distributed controllers for the aggregation of global demand and supply functions.

The bounded-input bounded-output (BIBO) stability of semi-active control systems was convenient since the stability of the MBC and EMBC methods were not considered. However, adoption of these methods in systems that are not naturally BIBO stable will require a better understanding of the methods to ensure that instability does not result. A stronger mathematical framework will be required in order to prove the stability of MBC and EMBC.

The piecewise static optimization solution of MBC and EMBC holds great promise in applying these control solutions to the nonlinear control problem. The geometric and material nonlinear responses represent significant changes in the structural system that cannot be modeled at the problem outset. As a result, classical control solutions such as LQR have had difficulty in systems that experience nonlinear responses. The highly adaptive nature of MBC and EMBC can be leveraged to avoid having to model nonlinear responses at the problem outset. As nonlinearities occur, MBC and EMBC will re-optimize the control solution to reflect new system states.

Appendix A

Prototype Circuit Schematics

The design of the wireless sensing unit's AT90S8515-based data acquisition circuit is documented in this Appendix. The circuit is designed using the placement tools provided by CircuitMaker 6. In CircuitMaker 6, physical dimensions and pin information specific to each component package are required for placement on a printed circuit board.

The circuit design can be divided into five subsystem segments. The first circuit segment documents the power source interface of the circuit with a voltage regulator producing a regulated 5V power source (Figure A-1). The second circuit segment illustrates the setup of the AVR AT90S8515 microcontroller in the circuit (Figure A-2). This implementation provides power and grounding to the microcontroller's IC package, an external 4MHz crystal oscillator for the microcontroller's internal clock, a reset circuit, and port pin-outs. The third segment displays the installation of an RS232 serial port in the system (Figure A-3). The fourth and fifth circuit segments present the implementation of the ADS7821 A/D converter and the ADXL210 accelerometer within the circuit (Figure A-4 and Figure A-5 respectively). The two IC packages are interfaced directly to the AT90S8515 microcontroller.

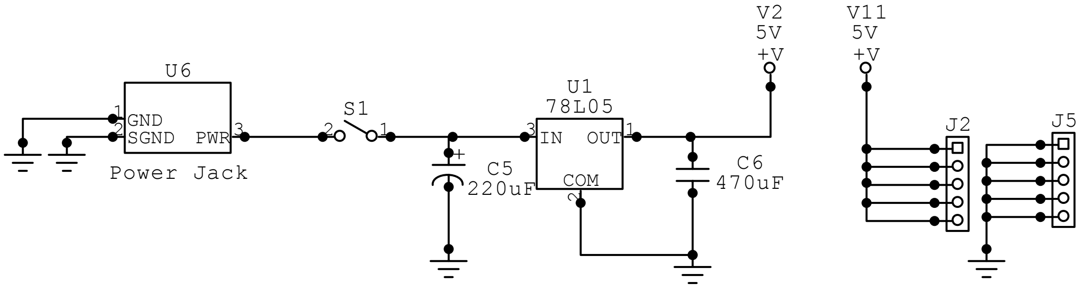

Figure A-1: Power input with 5V regulated voltage supply

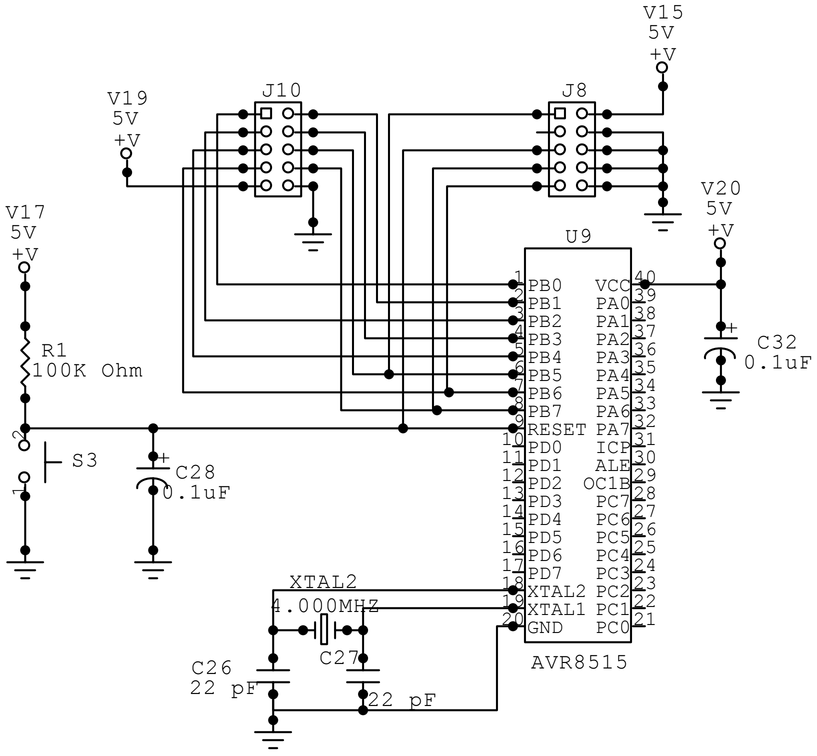

Figure A-2: Installation of the AT90S8515 microcontroller in the circuit

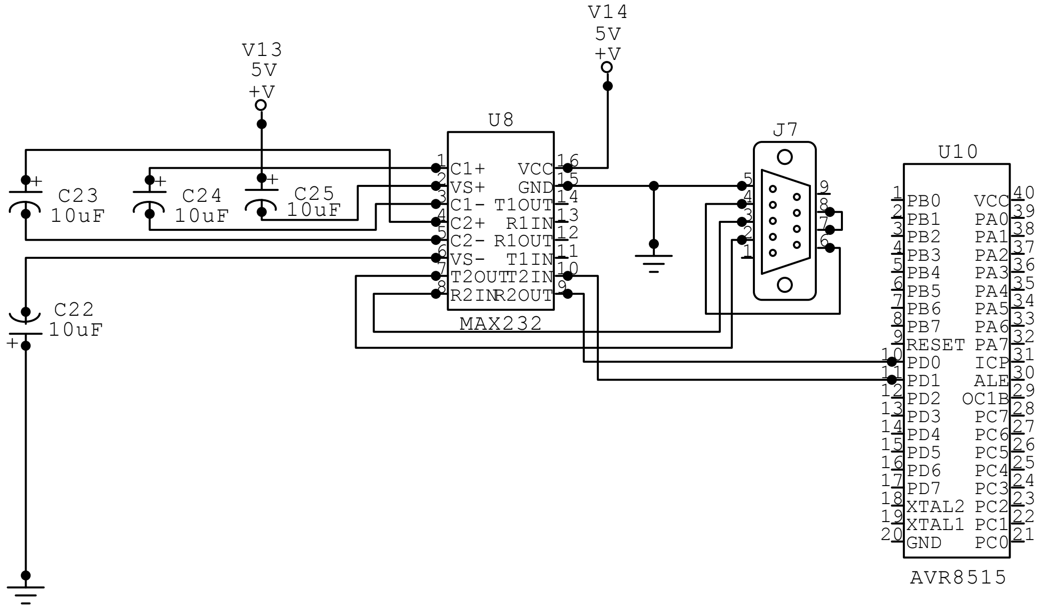

Figure A-3: Circuit RS232 Serial Port

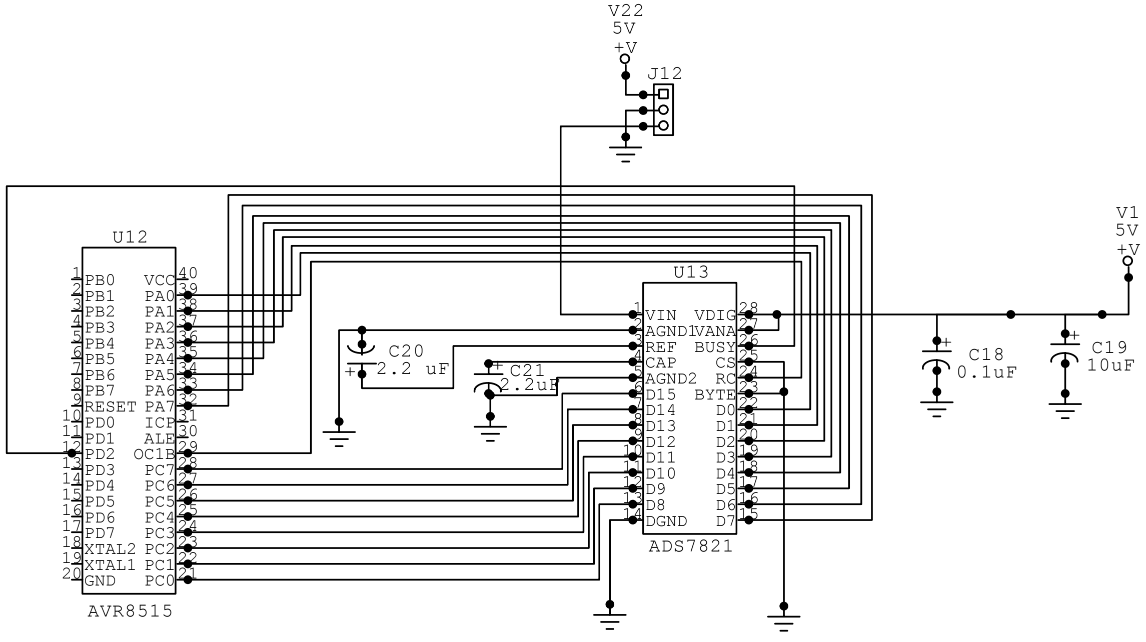

Figure A-4: ADS7821 A/D converter interfaced to the AT90S8515

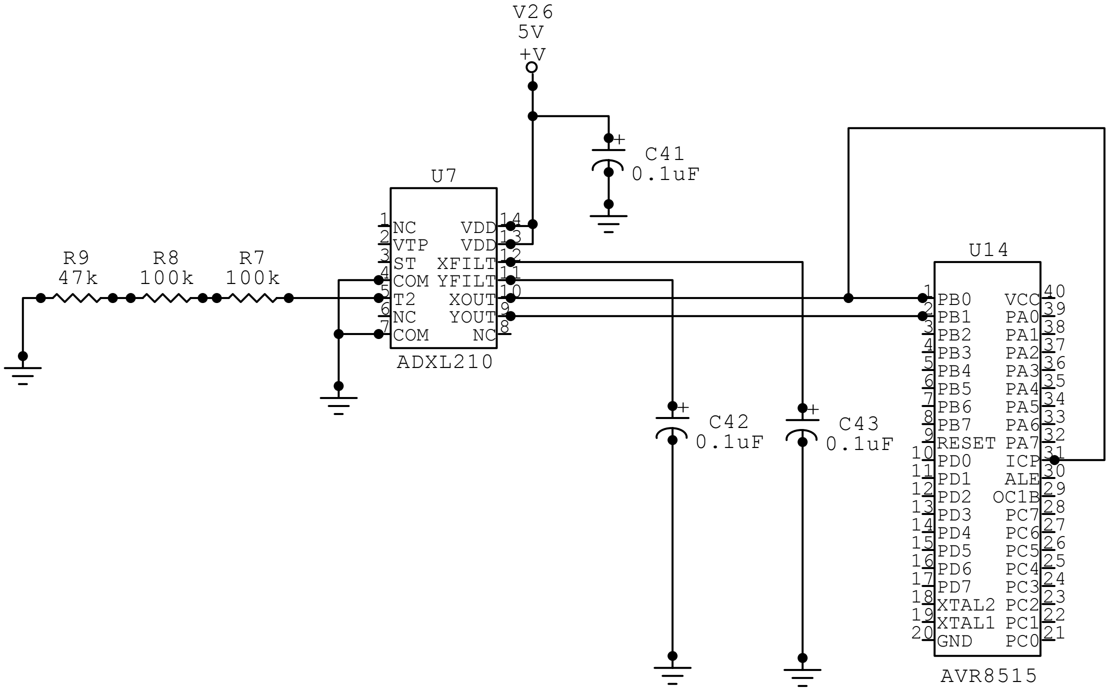

Figure A-5: ADXL210 accelerometer interfaced to the AT90S851

Bibliography

Analog Devices, Inc. (1999). *ADXL202/ADXL210 data sheet – low cost 2g/10g dual axis iMEMS accelerometers with digital outputs*. Norwood, MA.

Aoki, M. (1976). *Optimal control and system theory in dynamic economic analysis*. North-Holland, New York, NY.

Atmel Corporation. (2001). *Atmel AVR AT90S8515 data sheet – 8-bit AVR microcontroller with 8K bytes in-system programmable flash*. San Jose, CA.

Baker, A. D. (1992). "Case study results with the market-driven contract net manufacturing computer-control architecture." *Proceedings of AUTOFACT 1992 Conference*. Society of Manufacturing Engineers, Dearborn, MI, pp. 3117-3135.

Ball, S. (2001). "Analog-to-digital converters." *Embedded Systems Programming*, CMP Media LLC, 14(5): 10-25.

Barr, M. (2001). "Memory types." *Embedded Systems Programming*, CMP Media LLC, 14(5): 103-104.

Battaini, M., Casciati, F., and Faravelli, L. (2000). "Some reliability aspects in structural control." *Probabilistic Engineering Mechanics*, Elsevier, 15(1): 101-107.

Bergmeister, K. (2000). "Maintenance and repairs: an expert opinion." *Freyssinet Magazine*, Freyssinet, 10(209): 4-5.

Bergmeister, K., and Santa, U. (2001). "Global monitoring concepts for bridges." *Proceedings of Nondestructive Evaluation of Highways, Utilities, and Pipelines IV*, SPIE, Newport Beach, CA, v.3995, pp. 312-323.

Bogen, A. E., and Wollan, V. (1996). *AVR enhanced RISC microcontrollers*. Atmel Development Center, Trondheim, Norway.

Bolt, B. A. (2001). “Seismic instrumentation of bridges and dams: history and possibilities.” *Proceedings of Instrumental Systems for Diagnostics of Seismic Response of Bridges and Dams*, Consortium of Organizations for Strong-Motion Observation Systems, Richmond, CA, pp. 1-2.

Burr-Brown, Inc. (1996). *ADS7821 data sheet – 16-bit 10 μs sampling CMOS analog-to-digital converter*. Tucson, AZ.

Chandrasekharan, P. C. (1996). *Robust control of linear dynamical systems*. Academic Press, London, UK.

Chiang, A. C. (1992). *Elements of dynamic optimization*. McGraw-Hill, New York, NY.

Christenson, R. E., Spencer, B. F., and Johnson, E. A. (2001). “Experimental verification of semi-active damping of stay cables.” *Proceedings of the 2001 American Control Conference*, American Automatic Control Conference, Evanston, IL, pp. 5058-5063.

Clearwater, S. H. (1996). *Market-based control: a paradigm for distributed resource allocation*. World Scientific Press, Singapore.

Culshaw, B. (1996). *Smart structures and materials*. Artech House, Boston.

Davidson, A., and Hill, C. (1997). “Measurement of building penetration into medium buildings at 900 and 1500 MHz.” *IEEE Transactions on Vehicular Technology*, IEEE, 46(1): 161-168.

Doebling, S. W., Farrar, C. R., Prime, M. B., and Shevitz, D. W. (1996). *Damage identification and health monitoring of structural and mechanical systems from changes in their vibration characteristics: a literature review*. Report No. LA-13070-MS, Los Alamos National Laboratory, Los Alamos, NM.

Drouin, M., Abou-Kandil, H., and Mariton, M. (1991). *Control of complex systems*. Plenum Press, New York, NY.

Ewins, D. J. (1984). *Modal testing: theory and practice*. Research Studies Press, Letchworth, England.

Farrar, C. R. (2001). “Historical overview of structural health monitoring.” *Lecture Notes on Structural Health Monitoring using Statistical Pattern Recognition.* Los Alamos Dynamics, Los Alamos, NM.

Farrar, C. R., Doebling, S. W., Cornwell, P. J., and Straser, E. G. (1997). “Variability of modal parameters measured on the Alamosa Canyon Bridge.” *Proceedings of the*

15th International Modal Analysis Conference, Society of Engineering Mechanics, Bethel, CT, pp. 257-263.

Franklin, G. F., Powell, J. D., Emami-Naeini, A. (1994). *Feedback control of dynamic systems*. Addison-Wesley Publishing, Boston, MA.

Gelb, A. (1974). *Applied optimal estimation*. M.I.T. Press, Cambridge, MA.

Ginsberg, G. L. (1990). *Printed circuit design featuring computer-aided technologies*. McGraw-Hill Inc., New York, NY.

Glynne-Jones, P., Beeby, S. P., and White, N. M. (2001). "Towards a piezoelectric vibration-powered microgenerator." *IEE Proceedings of Science, Measurement and Technology*, IEE, 148(2): 68-72.

Guenther, O., Hogg, T., and Huberman, B. A. (1997). "Controls for unstable structures." *Proceedings of Smart Structures and Materials: Mathematics and Control in Smart Structures*, SPIE, San Diego, CA, v.3039, pp. 754-763.

Hatada, T., Kobori, T., Ishida, M., and Niwa, N. (2000). "Dynamic analysis of structures with Maxwell model." *Earthquake Engineering and Structural Dynamics*, John Wiley & Sons, 29(2): 159-176.

Hayes, J. R. (2001). "Modular programming in C." *Embedded Systems Programming*, CMP Media LLC, 14(13): 18-24.

Hintz, K., and Tabak, D. (1992). *Microcontrollers: architecture, implementation, & programming*. McGraw-Hill, New York, NY.

Hipley, P. (2001). "Caltrans' current state-of-practice." *Proceedings of Instrumental Systems for Diagnostics of Seismic Response of Bridges and Dams*, Consortium of Organizations for Strong-Motion Observation Systems, Richmond, CA, pp. 3-7.

Hogg, T., and Huberman, B. A. (1998). "Controlling smart matter." *Smart Materials and Structures*, Institute of Physics, 7(1): R1-R14.

Hooge, F. N. (1994). "1/f noise sources." *IEEE Transactions of Electron Devices*, IEEE, 41(11): 1926-1935.

Horowitz, P., and Hill, W. (1998). *The art of electronics*. Cambridge University Press, Cambridge, U.K.

Housner, G. W., Bergman, L. A., Caughey, T. K., Chassiakos, A. G., Claus, R. O., Masri, S. F., Skelton, R. E., Soong, T. T., Spencer, B. F., and Yao, J. T. P. (1997). "Structural control: past, present, and future." *Journal of Engineering Mechanics*, ASCE, 123(9): 897-971.

ImageCraft. (2001). *ICCAVR - ImageCraft C compiler and development environment for Atmel AVR version 6*. Palo Alto, CA.

Inaudi, D., and Vurpillot, S. (1999). "Monitoring of concrete bridges with long-gage fiber optic sensors." *Journal of Intelligent Material Systems and Structures*, Technomic Publishing, 10(4): 280-292.

Intriligator, M. D. (1971). *Mathematical optimization and economic theory*. Prentice-Hall, Englewood Cliffs, NJ.

Johnson, C. M. (Ed.) (2001). *Proceedings of Instrumental Systems for Diagnostics of Seismic Response of Bridges and Dams*, Consortium of Organizations for Strong-Motion Observation Systems (COSMOS), Richmond, CA.

Kajima Corporation. (1991). *Minimizing tremors by changing building stiffness – active variable stiffness system (AVS).* Technical Pamphlet 91-65E, Kajima Corporation, Tokyo, Japan.

Kernighan, B. W., and Ritchie, D. M. (1988). *The C programming language*, Prentice Hall PTR, Englewood Cliffs, NJ.

Kinemetrics, Inc. (2002). *ALTUS – Earthquake monitoring instruments and systems*. Pasadena, CA.

Kobori, T., Koshika, N., Yamada, K., and Ikeda, Y. (1991). "Seismic response controlled structure with active mass driver system – Part 1." *Earthquake Engineering and Structural Dynamics,* John Wiley & Sons, 20(2): 133-149.

Kurata, N., Kobori, T., Takahashi, M., Niwa, N., and Midorikawa, H. (1999). "Actual seismic response controlled building with semi-active damper system." *Earthquake Engineering and Structural Dynamics,* John Wiley & Sons, 28(11): 1427-1447.

Levine, W. S., and Athans, M. (1970). "On the determination of the optimal constant output feedback gains for linear multivariable systems." *IEEE Transactions on Automatic Control*, IEEE, 15(1): 42-48.

Luenberger, D. G. (1995). *Microeconomic theory*. McGraw-Hill, New York, NY.

Lunze, J. (1992). *Feedback control of large-scale systems*. Prentice Hall, New York, NY.

Lynch, J. P., and Law, K. H. (2000). "A market-based control solution for semi-active structural control." *Proceedings of the 8th International Conference on Computing in Civil and Building Engineering,* ASCE, Reston, VA, pp. 588-595.

Lynch, J. P., and Law, K. H., (2001). "Formulation of a market-based approach for structural control." *Proceedings of the 19th International Modal Analysis Conference*, Society of Engineering Mechanics, Bethel, CT, pp. 921-927.

Mas-Colell, A., Whinston, M. D., and Green, J. R. (1995). *Microeconomic theory*. Oxford University Press, New York, NY.

Measurements Group, Inc. (2000). *Precision strain gages engineering data sheet EP-08-250BG-120*. Micro-Measurements Division, Raleigh, NC.

Meninger, S., Mur-Mirands, J. O., Amirtharajah, R., Chandrakasan, A. P., and Lang, J. H. (2001). "Vibration-to-electric energy conversion." *IEEE Transactions on Very Large Scale Integration (VLSI) Systems,* IEEE, 9(1): 64-76.

Mittag, L. (2001). "Magic in the air," *Embedded Systems Programming*, CMP Media LLC, 14(10): 49-60.

Morton, T. D. (2001). *Embedded microcontrollers*. Prentice Hall, Upper Saddle River, NJ.

Motorola Corporation, Inc. (2000). *MPC555 user's manual*. Phoenix, AZ.

Netgear Corporation. (2002). *Model HA501 802.11a wireless 32-bit card bus adapter data sheet*. Santa Clara, CA.

Ni, Y. Q., Wang, B. S., and Ko, J. M. (2001). "Simulation studies of damage location in Tsing Ma Bridge deck." *Proceedings of Nondestructive Evaluation of Highways, Utilities, and Pipelines IV*, SPIE, Newport Beach, CA, v.3995, pp. 312-323.

Nishitani, A., and Inoue, Y. (2001). "Overview of the application of active/semi-active control to building structures in Japan." *Earthquake Engineering and Structural Dynamics,* John Wiley & Sons, 30(11): 1565-1574.

Norton, H. N. (1982). *Sensor and analyzer handbook*. Prentice Hall, Englewood Cliffs, NJ.

Partridge, A., Reynolds, J. K., Chui, B. W., Chow, E. M., Fitzgerald, A. M., Zhang, L., Maluf, N. I., and Kenny, T. W. (2000). "A high-performance planar piezoresistive accelerometer." *Journal of Microelectromechanical Systems*, IEEE, 9(1): 58-66.

Press, W. H., Teukolsky, S. A., Vetterling, W. T., and Flannery, B. P. (1992). *Numerical recipes in C: the art of scientific computing*. Cambridge University Press, Cambridge, U.K.

Proxim Corporation. (1994). *ProxLink PL and PL2 radio modem family user's manual*. Sunnyvale, CA.

Proxim Corporation. (1998). *RangeLAN2 serial adapter models 7910 and 7911 user's guide*. Sunnyvale, CA.

Roberts, E. S. (1998). *Programming abstractions in C.* Addison-Wesley, Reading, MA.

Roylance, L. M., and Angell, J. B. (1979). "A batch fabricated silicon accelerometer." *IEEE Transactions on Electron Devices,* IEEE, 26(12): 1911-1917.

Sandell, N., Varaiya, P., Athans, M., and Safonov, M. (1978). "Survey of decentralized control methods for large scale systems." *IEEE Transactions on Automatic Control,* IEEE, 23(2): 108-128.

Sasaki, A. (1998), Kobori Research Complex, Kajima Corporation, Japan, Personal Conversations.

Sastry, S. S. (1999). *Nonlinear systems: analysis, stability, and control*. Springer-Verlag, New York, NY.

Shakal, A. F. (2001). "Utilization of instrumental measurements in diagnostics for seismic response." *Proceedings of Instrumental Systems for Diagnostics of Seismic Response of Bridges and Dams*, Consortium of Organizations for Strong-Motion Observation Systems, Richmond, CA, pp. 21-22.

Siljak, D. D. (1991). *Decentralized control of complex systems*. Academic Press, Boston, MA.

Singh, M. G. (1981). *Decentralized control.* North-Holland Publishing, Amsterdam, Netherlands.

Smith, A. (1776). *An inquiry into the nature and cause of the wealth of nations*. Rowman and Littlefield, Baltimore, MD.

Sohn, H., Dzwonczyk, M., Straser, E. G., Kiremidjian, A. S., Law, K. H., and Meng, T. (1999). "An experimental study of temperature effect on modal parameters of the Alamosa Canyon Bridge." *Earthquake Engineering and Structural Dynamics,* John Wiley & Sons, 28(9): 879-897.

Sohn, H., and Farrar, C. R. (2001). "Damage diagnosis using time series analysis of vibration signals." *Smart Materials and Structures*, Institute of Physics, 10(2001): 446-451.

Sohn, H., Farrar, C. R., Hunter, N., and Worden, K. (2001). *Applying the LANL statistical pattern recognition paradigm for structural health monitoring to data from a surface-effect fast patrol boat*. Report No. LA-13761-MS, Los Alamos National Laboratory, Los Alamos, NM.

Soloman, S. (1998). *Sensors handbook*. McGraw-Hill, New York, NY.

Soong, T. T. (1990). *Active structural control: theory and practice*. Longman Scientific and Technical, Essex, England.

Spencer, B. F., Christenson, R. E., and Dyke, S. J. (1998). "Next generation of benchmark structural control problems for seismically excited buildings." *Second World Conference on Structural Control*, International Association for Structural Control, Kyoto, Japan, pp. 1351-1360.

Spencer, B. F., Sain, M. K., Won, C. H., Kaspari, D. C., and Sain, P. M. (1994). "Reliability based measures of structural control robustness." *Structural Safety*, Elsevier, 15(1): 111-129.

Spencer, B. F., Yang, G., Carlson, J. D., and Sain, M. K. (1998). "Smart dampers for seismic protection of structures: a full-scale study." *Second World Conference on Structural Control*, International Association for Structural Control, Kyoto, Japan, pp. 417-426.

Srinivasan, A. V., and McFarland, D. M. (2001). *Smart structures: analysis and design*. Cambridge University Press, Cambridge, England.

Staller, L. (2001). "Improving A/D converter resolution by oversampling and averaging." *Test and Measurement News*, CMP Media LLC, Online Tech Note (http://my.chipcenter.com/TestandMeasurement/tn033.html).

Stengel, R. (1994). *Optimal control and estimation*. Dover Publications, New York, NY.

Straser, E. G., and Kiremidjian, A. S. (1998). *A modular, wireless damage monitoring system for structures*. Report No. 128, John A. Blume Earthquake Engineering

Center, Department of Civil and Environmental Engineering, Stanford University, Stanford, CA.

Symans, M. D., and Constantinou, M. C. (1999). "Semi-active control systems for seismic protection of structures: a state-of-the-art review." *Engineering Structures*, Elsevier, 21(6): 469-487.

Takahashi, M., Kobori, T., Nasu, T., Niwa, N., and Kurata, N. (1998). "Active response control of buildings for large earthquakes – seismic response control systems with variable structural characteristics." *Smart Materials and Structures*, Institute of Physics, 7(4): 522-529.

Tamura, K. (2001). "Instrument systems of major bridges in Japan." *Proceedings of Instrumental Systems for Diagnostics of Seismic Response of Bridges and Dams*, Consortium of Organizations for Strong-Motion Observation Systems, Richmond, CA, pp. 10-18.

Texas Instruments. (1995). *Application report: understanding data converters*. Mixed-Signal Products Group, Dallas, TX.

Weinberg, H. (1999). "Dual axis low-g fully integrated accelerometers." *Analog Dialogues*, Analog Devices, 33(1): 1-2.

Wong, K. Y., Chan, W. Y. K., Man, K. L., Mak, W. P., and Lau, C. K. (2001). "Structural health monitoring results on Tsing Ma, Kap Shui Mun, and Ting Kau bridges." *Proceedings of Nondestructive Evaluation of Highways, Utilities, and Pipelines IV*, SPIE, Newport Beach, CA,v.3995, pp. 288-299.

Wong, K. F., and Yang, R. (2001). "Effectiveness of structural control based on control energy perspectives." *Earthquake Engineering and Structural Dynamics,* John Wiley & Sons, 30(12): 1747-1768.

Wu, F., and Chang, F. K. (2001). "A built-in active sensing diagnostic system for civil infrastructure systems." *Proceedings of Smart Systems for Bridges, Structures, and Highways,* SPIE, Newport Beach, CA, v.4330, pp. 27-35.

Yao, J. T. P. (1972). "Concept of structural control." *Journal of Structural Division*, ASCE, 98(7): 1567-1574.